REPORT DOCUMENTATION PAGE

Public reporting burden for this collection of information is estimated to average 1 hour per response, including the time for and maintaining the data needed, and completing and reviewing the collection of information. Send comments regard information, including suggestions for reducing this burden, to Washington Headquarters Services, Directorate for informa 1204, Arlington, VA 22202-4302, and to the Office of management and Budget, Paperwork Reduction Project (0704-0188)

AFRL-SR-BL-TR-98-

G439

1. AGENCY USE ONLY (Leave Blank)	2. REPORT DATE August 1995	3. REPORT TYF Final

4. TITLE AND SUBTITLE
Near-Wall Measurements of a Three-Dimensional Turbulent Boundary Layer

5. FUNDING NUMBERS

6. AUTHORS
Debora A. Compton and John K. Eaton

7. PERFORMING ORGANIZATION NAME(S) AND ADDRESS(ES)
Stanford University

8. PERFORMING ORGANIZATION REPORT NUMBER

9. SPONSORING/MONITORING AGENCY NAME(S) AND ADDRESS(ES)
AFOSR/NI
110 Duncan Avenue, Room B-115
Bolling Air Force Base, DC 20332-8080

10. SPONSORING/MONITORING AGENCY REPORT NUMBER

11. SUPPLEMENTARY NOTES

12a. DISTRIBUTION AVAILABILITY STATEMENT
Approved for Public Release

12b. DISTRIBUTION CODE

13. ABSTRACT *(Maximum 200 words)*
See attached.

14. SUBJECT TERMS

15. NUMBER OF PAGES

16. PRICE CODE

17. SECURITY CLASSIFICATION OF REPORT	18. SECURITY CLASSIFICATION OF THIS PAGE	19. SECURITY CLASSIFICATION OF ABSTRACT	20. LIMITATION OF ABSTRACT
Unclassified	Unclassified	Unclassified	UL

DTIC QUALITY INSPECTED 5

NEAR-WALL MEASUREMENTS OF A THREE-DIMENSIONAL TURBULENT BOUNDARY LAYER

by

Debora A. Compton and John K. Eaton

Report No. MD-72

Thermosciences Division
Department of Mechanical Engineering
Stanford University
Stanford, California 94305-3030

August 1995

Acknowledgments

Abstract

In order to improve predictions of flow behavior in numerous applications there is a great need to understand the physics of three-dimensional turbulent boundary layers, dominated by near-wall behavior. To that end, an experiment was performed to measure near-wall velocity and Reynolds stress profiles in a pressure-driven three-dimensional turbulent boundary layer. The flow was achieved by placing a 30° wedge in a straight duct in a wind tunnel, with additional pressure gradient control above the test surface. An initially two-dimensional boundary layer ($Re_\theta \approx 4000$) was exposed to a strong spanwise pressure gradient. At the furthest downstream measurement locations there was also a fairly strong favorable pressure gradient.

Measurements were made using a specially-designed near-wall laser Doppler anemometer (LDA), in addition to conventional methods. The LDA used short focal length optics, a mirror probe suspended in the flow, and side-scatter collection to achieve a nearly spherical measuring volume approximately 35μm in diameter. Good agreement with previous two-dimensional boundary layer data was achieved.

The three-dimensional turbulent boundary layer data presented include mean velocity measurements and Reynolds stresses, all extending well below $y^+ = 10$, at several profile locations. Terms of the Reynolds stress transport equations are calculated at two profile locations. The mean flow is nearly collateral at the wall. Turbulent kinetic energy is mildly suppressed in the near-wall region and the shear stress components are strongly affected by three-dimensionality. As a result, the ratio of shear stress to turbulent kinetic energy is suppressed throughout most of the boundary layer. The angles of stress and strain are misaligned, except very near the wall (around $y^+ = 10$) where the angles nearly coincide with the mean flow angle. Three-dimensionality appears to reduce the production of turbulent kinetic energy and, more strongly, the production of $-\overline{u'v'}$. A transport equation for a_1 is derived, and we find a dramatic decrease in the production of a_1, balanced by a decrease in the pressure-strain term.

Contents

v

Nomenclature

Roman Symbols

a_1	turbulence structure parameter: $a_1 \equiv \dfrac{\left(\overline{u'v'}^2 + \overline{v'w'}^2\right)^{1/2}}{\overline{u'^2} + \overline{v'^2} + \overline{w'^2}}$
C_f	skin friction coefficient
c_μ	constant in $k - \epsilon$ model
d	measuring volume diameter
$\mathcal{D}_{ij}$	viscous dissipation term in Reynolds stress transport equations
$\mathcal{D}$	homogeneous dissipation rate
$E_0{}^2$	calibration constant for hotwire anemometry
f	lens focal length, or:
f	frequency
f_{Bragg}	Bragg cell driver frequency
f_{downmix}	downmix frequency
$\mathcal{J}_{ijk}$	turbulent transport term in Reynolds stress transport equations
k	turbulent kinetic energy per unit mass: $k \equiv 1/2\overline{u'_i u'_i}$, or:
k	calibration constant for hotwire anemometry
n	exponent for hotwire anemometry
N, N_e	eddy viscosity ratios: $N \equiv \dfrac{\nu_{T_{\text{spanwise}}}}{\nu_{T_{\text{streamwise}}}}$
p	pressure
$\mathcal{P}_{ij}$	production term in Reynolds stress transport equations
Q	mean velocity magnitude in the plane of the wall: $Q^2 \equiv U^2 + W^2$
q^2	twice the turbulent kinetic energy: $q^2 \equiv \overline{u'_i u'_i}$
R, S	parameters in three-hole probe calibration
R_{th}	thermistor resistance
Re	Reynolds number
t	time
T	temperature

u	velocity
u_τ	friction velocity
u',v',w'	fluctuating velocity components
U	mean streamwise velocity in tunnel coordinates
U_e	freestream velocity
U_s	mean streamwise velocity in freestream streamline coordinates
U_n	mean spanwise velocity in freestream streamline coordinates
V	mean wall-normal velocity in tunnel coordinates
W	mean spanwise velocity in tunnel coordinates
$x,\ y,\ z$	streamwise, wall-normal, spanwise axes
y^+	nondimensional distance from wall: $y^+ \equiv y u_\tau / \nu$

Greek Symbols

α	laser beam crossing angle at measuring volume
β	Bragg angle, or:
β	freestream turning angle with respect to x-axis
γ	flow angle with respect to tunnel coordinates
γ_g	velocity gradient angle: $\gamma_g \equiv \tan^{-1}\left(\frac{\partial W}{\partial y}/\frac{\partial U}{\partial y}\right)$
γ_τ	shear stress angle
δ^*	boundary layer displacement thickness
δ_{99}	boundary layer thickness
θ	boundary layer momentum thickness
κ	constant in law of the wall equation; $\kappa = 0.41$
λ	wavelength
Λ	fringe spacing
μ	absolute viscosity
ν	kinematic viscosity
ν_τ	eddy viscosity
ρ	fluid density

σ	standard deviation
τ	shear stress
ϕ	grazing beam angle for LDA
Φ_{ij}	pressure-strain redistribution term in Reynolds stress transport equations
Ψ	wire angle for X-array hotwire

Chapter 1

Introduction

Three-dimensional turbulent boundary layers exist in nearly every wall-bounded turbulent flow of interest, but they are surprisingly poorly understood. Calculation methods for three-dimensional turbulent boundary layers use empirical constants derived from two-dimensional flows, because there is not sufficient information available to properly model the three-dimensional cases. A better understanding of the physics of three-dimensional boundary layers would provide the means to better predict flows in turbomachinery, aerodynamics, and environmental fluid applications. Although recent advances have been made in the understanding of three-dimensional turbulent boundary layers, a gap remains in near-wall data. Very near the wall, the turbulence production in the boundary layer is strongest, and the near-wall region accounts for the majority of the boundary layer displacement thickness. However, there have been only a few experiments in which measurements extend into the near-wall region. The aims of the present work are to develop techniques and to provide new measurements which will help us understand the near-wall region of three-dimensional turbulent boundary layers in considerably more detail than was previously possible.

1.1 Three-dimensional boundary layer background

When a flow has curving streamlines that lie in a plane parallel to a wall, the shear layer adjacent to the wall is a three-dimensional boundary layer. Simple examples of three-dimensional turbulent boundary layer flows include the flow on the end wall of a curved duct of rectangular cross-section, flow over a skewed aircraft wing, and a boundary layer approaching a three-dimensional obstacle. See figure 1.1 for examples of three-dimensional turbulent boundary layer geometries. Streamline curvature in these cases is caused by pressure gradients normal to the streamline. The fluid in

1

the boundary layer is acted upon by viscosity and turbulent stresses in addition to the pressure field. The slow-moving fluid in the boundary layer reacts to a spanwise pressure gradient by turning more strongly than the fluid outside the boundary layer. Looking at the boundary layer in coordinates aligned with the local free-stream velocity, we see a crossflow velocity component U_n which varies continually throughout the boundary layer, as shown in figure 1.2. The U_n component, like the U_s component, is zero at the wall due to the no-slip boundary condition. U_n increases rapidly to a maximum which occurs close to the wall. We may expect that the crossflow has its strongest effect in this region, and we refer to $y^+ < 100$ as the near-wall region.

Three-dimensional turbulent boundary layers may also be formed by shearing. A simple example of a shear-driven three-dimensional turbulent boundary layer is an initially two-dimensional boundary layer which encounters a section of the wall which is moving normal to the freestream flow direction. We will not discuss this type of flow in great detail.

1.1.1 Governing equations

Here we describe the basic equations which apply to three-dimensional boundary layers, in order to introduce some terminology and to explain the terms that must be measured. The Navier-Stokes equations describing an incompressible flow of a Newtonian fluid with constant density and viscosity, are:

$$\frac{\partial u_i}{\partial t} + u_j \frac{\partial u_i}{\partial x_j} = -\frac{1}{\rho} \frac{\partial p}{\partial x_i} + \nu \frac{\partial^2 u_i}{\partial x_j x_j} \tag{1.1}$$

Together with the continuity equation $\frac{\partial u_i}{\partial x_i} = 0$ the flow is completely described.

We apply the Reynolds decomposition, splitting velocity components into mean (U_i) and fluctuating (u_i') parts and then time-averaging to yield the mean momentum equations:[1]

$$U_j \frac{\partial U_i}{\partial x_j} = -\frac{1}{\rho} \frac{\partial p}{\partial x_i} + \frac{\partial}{\partial x_j} \left(\nu \frac{\partial U_i}{\partial x_j} - \overline{u_i' u_j'} \right) \tag{1.2}$$

---

[1]We break pressure into mean and fluctuating terms also, but choose to use lower case p to represent time-averaged pressure from this point forward.

The quantity $-\overline{u_i' u_j'}$ is grouped with the stress term $\nu \frac{\partial U_i}{\partial x_j}$. It is considered an effective stress caused by the turbulence, and is called the Reynolds stress tensor. Dimensionally, the stress is $-\rho \overline{u_i' u_j'}$ but we will refer to $-\overline{u_i' u_j'}$ as a stress per unit volume. The set of equations for mean velocity is not closed, since introducing the Reynolds stresses adds six additional unknowns. Transport equations for the Reynolds stresses may be derived (see chapter 6) but these transport equations introduce yet more unknown quantities, including triple products (*i.e.*, $\overline{u_i' u_j' u_k'}$) and terms involving pressure fluctuation correlations.

We next apply "thin shear layer" assumptions. For three-dimensional boundary layers these assumptions are that V is small compared to both U and W and that wall-normal derivatives are large compared to streamwise and spanwise derivatives. Doing this yields the following momentum equations for the mean velocities U and W in a three-dimensional boundary layer:

$$U\frac{\partial U}{\partial x} + V\frac{\partial U}{\partial y} + W\frac{\partial U}{\partial z} = -\frac{1}{\rho}\frac{\partial p}{\partial x} + \frac{1}{\rho}\frac{\partial}{\partial y}\left(\mu\frac{\partial U}{\partial y} - \rho\overline{u'v'}\right) \qquad (1.3)$$

$$U\frac{\partial W}{\partial x} + V\frac{\partial W}{\partial y} + W\frac{\partial W}{\partial z} = -\frac{1}{\rho}\frac{\partial p}{\partial z} + \frac{1}{\rho}\frac{\partial}{\partial y}\left(\mu\frac{\partial W}{\partial y} - \rho\overline{v'w'}\right) \qquad (1.4)$$

Thus, we see that prediction of the quantities $-\overline{u'v'}$ and $-\overline{v'w'}$ is critical to the prediction of the mean velocity field in a three-dimensional boundary layer. Many models reduce the Reynolds stress tensor into normal stresses and a shear stress "vector". The shear stress is defined by its x and z components, $\overline{u'v'}$ and $\overline{v'w'}$; its magnitude τ/ρ and angle γ_τ are

$$\tau/\rho = \left(\overline{u'v'}^2 + \overline{v'w'}^2\right)^{1/2}; \qquad (1.5)$$

$$\gamma_\tau = \tan^{-1}\left(-\overline{v'w'}/-\overline{u'v'}\right). \qquad (1.6)$$

The rate of strain angle, similarly, is defined as

$$\gamma_g = \tan^{-1}\left(\frac{\partial W}{\partial y} \middle/ \frac{\partial U}{\partial y}\right) \qquad (1.7)$$

1.1.2 Differences from 2D

Two-dimensional turbulent boundary layers have been studied for many years now (a classic text is that of Schlichting (1960)) and are for the most part well understood. We can predict with reasonable accuracy the mean flow in a two-dimensional turbulent boundary layer using well-tested correlations and models, even in the presence of transpiration, streamwise pressure gradient, or wall curvature. However, these correlations fail when the streamlines curve relative to the wall.

A simple closure model for equation 1.3 for two-dimensional boundary layers is to let $\overline{u'v'}$ scale on $\frac{\partial U}{\partial y}$. This is known as an eddy viscosity model. Scalar eddy viscosity models do not work for three-dimensional turbulent boundary layers since the vector defined by the quantities $\overline{u'v'}$ and $\overline{v'w'}$ is usually misaligned with the vector defined by the quantities $\frac{\partial U}{\partial y}$ and $\frac{\partial W}{\partial y}$; that is, $\gamma_\tau \neq \gamma_g$. We will discuss refinements to the eddy viscosity model later in this chapter.

Arguments can be made to scale the magnitude of the Reynolds shear stresses on the turbulent kinetic energy. (See Bradshaw (1967), or Nash and Patel (1972) for reasoning.) The ratio of shear stress to twice the turbulent kinetic energy — the a_1 parameter — has been found to be consistently around 0.15 for two-dimensional boundary layers in the absence of strong pressure gradients. For a three-dimensional turbulent boundary layer, a_1 is defined as:

$$a_1 \equiv \frac{\left(\overline{u'v'}^2 + \overline{v'w'}^2\right)^{1/2}}{\overline{u'^2} + \overline{v'^2} + \overline{w'^2}} \tag{1.8}$$

Experiments in three-dimensional turbulent boundary layers have found that the a_1 parameter is not constant, and is usually well below the standard value of 0.15.

Another critical difference between two- and three- dimensional turbulent boundary layers is perhaps obvious but worth mentioning. At any particular (x, z) location in a three-dimensional turbulent boundary layer, the mean streamline is turning as a function of distance from the wall. The implication which is often neglected is that the fluid which comprises this profile has experienced a broad range of pressure gradient histories — the domain of influence for each (x, z) position is therefore much broader than for any given location in a two-dimensional boundary layer.

1.2 Previous experiments

We review the existing literature on three-dimensional turbulent boundary layer experiments, beginning with the early experiments. Our discussion is roughly chronological, pointing out the most significant studies.

1.2.1 Early experiments

Johnston (1960) performed an experiment on the boundary layer caused by a two-dimensional jet impinging on an end wall. He claimed to present the third reasonably complete and accurate experiment in three-dimensional turbulent boundary layers, after Gruschwitz in 1935 and Kuethe *et al.* in 1949. He introduced a model of a universal crossflow (W) boundary layer profile, which seemed appropriate to the three data sets available. Central to this model was that the velocity below the location of peak crossflow was considered to be collateral; *i.e.* $W = e * U$.

By the mid-1970's, three-dimensional turbulent boundary layers had been studied in more detail, and we use as a starting point Johnston's (1976) review of three-dimensional turbulent boundary layer experiments, which discusses the early experiments in the field as well as the state of the art of experimental methods in three-dimensional boundary layers at that time. By the time of Johnston's writing, there were nine three-dimensional turbulent boundary layer experiments which included detailed Reynolds stress measurements. The geometries of these experiments varied broadly, and there were only a few qualitative points on which they agreed. He concluded that there was no hope of finding a universal crossflow profile. He noted the discrepancy between the angles of turbulent shear stress and mean strain rate, and mapped out N, an anisotropic eddy viscosity ratio.

$$N \equiv \frac{\nu_{\tau_{\text{spanwise}}}}{\nu_{\tau_{\text{streamwise}}}} = \left(-\overline{v'w'} \bigg/ \frac{\partial W}{\partial y} \right) \bigg/ \left(-\overline{u'v'} \bigg/ \frac{\partial U}{\partial y} \right) = \frac{\tan \gamma_\tau}{\tan \gamma_g} \qquad (1.9)$$

He noted that flows with strong skewing seemed to have lower values of N than "near-equilibrium" flows, but demonstrated that this ratio is not constant, as it ranges widely within and across experiments. The experiments demonstrated various relations between the shear stress angle and the strain rate angle. Some showed γ_τ

lagging γ_g, while others showed the opposite. A continual theme in Johnston's review is that history effects are critical in three-dimensional turbulent boundary layers. He also pointed out that as of 1976, in the region $y^+ \leq 100$ mean velocity data were rare and turbulence data were nonexistent.

Among these early experiments, the study by Bradshaw and Terrell (1969) is noteworthy in that it was the first three-dimensional turbulent boundary layer study to include all the Reynolds stresses. Bradshaw and Terrell studied the relaxing three-dimensional turbulent boundary layer on an "infinite" swept wing. The term "infinite" implies that end effects are minimal, so that the flow depends only on two coordinates. Flows of this sort should be easier to calculate than fully three-dimensional flows. The study of flow approaching a 45 degree, infinite, swept step is reported by Johnston (1970). This is a rapidly-turned flow which approaches separation. Having measured the Reynolds shear stresses in this flow, Johnston noted that the difference in angle between γ_τ and γ_g was as great as 15 to 20 degrees, with γ_τ lagging γ_g. Pierce and Duerson (1975) measured the boundary layer on the end wall of a 60 degree bend, using hot-film anemometers. They concluded that the $\overline{u'w'}$ stress was of greater magnitude than the $\overline{u'v'}$ stress, and questioned the wisdom of ignoring $\overline{u'w'}$ in models. Then, Pierce and Ezekewe (1976) made approximate measurements of the gradients of the shear stresses, and demonstrated that the terms $\frac{\partial \overline{u'w'}}{\partial x}$ and $\frac{\partial \overline{u'w'}}{\partial z}$ were as small as one-tenth the size of $\frac{\partial \overline{u'v'}}{\partial y}$ and $\frac{\partial \overline{v'w'}}{\partial y}$, which means that the role of $\overline{u'w'}$ in the production terms of the Reynolds stress transport equations is much smaller than the roles of $\overline{u'v'}$ and $\overline{v'w'}$. These findings are important to the current study because we choose not to measure the $\overline{u'w'}$ shear stress.

Pierce and East (1971) are worth adding to these early experiments for casting doubt on Johnston's theory of collateral flow at the wall. Using a finite-difference eddy viscosity calculation of Johnston's 1960 experiment, they predicted that W would not be a simple scalar product of U near the wall.

1.2.2 Post-1976 experiments

Several studies appeared in the following years, with measurements of the Reynolds stresses. Dechow and Felsch (1977) investigated a boundary layer approaching an obstacle, reporting the six Reynolds stresses as close to the wall as 2 mm. Contrary to most of the early studies, they reported that the shear stress angle led the velocity gradient angle for most of the flow. Fernholz and Vagt (1981) reported behavior of the shear stress angle for the flow over an axisymmetric body, with a swept backplate that created a strong, asymmetric pressure gradient. This pressure gradient produced a three-dimensional turbulent boundary layer in the vicinity of separation. They emphasized the need to measure near-wall Reynolds stresses, and succeeded in measuring $\overline{u'^2}$ with a single hotwire as close as $y^+ = 4$, but could only measure the shear stresses down to $y = 2$ mm ($y^+ = 35$ to 100). They noted a reduction in a_1 with increasing three-dimensionality. Pierce and McAllister (1982) performed two experiments, with geometries like those of Dechow and Felsch (1977) and Johnston (1970). They measured only mean flow and wall shear stress, and noted that the mean velocity appeared to be turning all the way to the wall. Müller (1982) measured flow turned spanwise by vanes, in a geometry similar to the current experiment. He reported that the shear stress angle lagged the velocity gradient vector, in a flow with a fairly strong adverse pressure gradient.

Bradshaw and Pontikos (1985) revisited an experiment by Elsenaar and Boelsma (1974) in which flow over an infinite swept wing was simulated. They noted two general trends in three-dimensional turbulent boundary layers: the shear stress angle lagging the velocity gradient angle, and the reduction of a_1. They suggested that the tilting sideways, or "toppling", of large eddies is the physical mechanism by which the shear stress is reduced relative to the turbulent kinetic energy, attributing this three-dimensional effect to outer-layer phenomena. They also suggested that the angle lag is due to changes in the pressure-strain redistribution term in the Reynolds stress transport equations.

In the late 1980's, the possibility of computing complex flows like three-dimensional turbulent boundary layers became evident. A number of experimental studies had as a primary goal to be test cases for computations.

Anderson and Eaton (1989) (see also Anderson and Eaton (1987) for complete data) investigated the flow in a Y-shaped duct. Their objective was to vary a single parameter, the ratio of spanwise to streamwise pressure gradient. Measuring fluctuating quantities as close to the wall as $y^+ = 50$, they found a_1 dropping in the outer part of the boundary layer. They suggested that the near wall region, especially in the vicinity of $y^+ = 20$, would hold the key to the decrease in a_1, since the peak of shear stress production should be there. They also postulated that the crossflow may serve to stabilize longitudinal vortices whose vorticity opposes the crossflow vorticity. Shizawa and Eaton (1991) introduced a longitudinal vortex into the Anderson and Eaton flow, to test this theory. The vortices were of the same size as the boundary layer, and the crossflow was seen to suppress a_1. Maps of eddy viscosity in this study dramatically capture the futility of that type of model in capturing the details of the boundary layer – vortex interaction.

Pierce, along with Harsh and Menna (Pierce and Harsh (1988), Menna and Pierce (1988)) studied another obstacle flow, attempting to produce a complete, fully-documented flowfield. Their turbulence data reach only as close to the wall as 1.3mm, which for their flow is $y^+ \approx 60$.

Özcan (1988) measured the axial flow over a cylinder with a swept bump, using a laser Doppler anemometer. The flow reverses directions three times over the bump, creating considerable confusion. He reports that a_1 ranges from 0.1 to 0.2. This is the highest reported a_1 in the literature; perhaps it is anomalous.

A European collaborative study began in the mid 1980's to fully describe the three-dimensional turbulent boundary layer flow over a swept wing. Van den Berg (1988) described the inception of the project; Gleyzes, *et al.* (1993) described some of the early results. They found a peak in turbulent kinetic energy away from the wall on the suction side of the wing, which they credited to the adverse pressure gradient. When complete, the European collaborative study should offer an enormous dataset for comparison to computations.

Baskaran, Pontikis, and Bradshaw (1989) extended the infinite swept wing study of Bradshaw and Pontikos, by adding surface curvature, both concave and convex. Lest we forget that the phenomena in question are highly nonlinear, they discovered

that the combined effects of spanwise and longitudinal curvature appeared to be less than the effect of each curvature on its own.

Schwarz and Bradshaw (1992), (1993), (1994) measured the three-dimensional turbulent boundary layer on the end wall of a 30 degree bend, concentrating on the centerline of the flow in order to study the effects of spanwise pressure gradient essentially free from streamwise pressure gradient. They measured only the outer part of the boundary layer. Throughout both the development and the decay of the three-dimensionality, they found a_1 suppressed. They found the shear stress to lag the strain rate, siding with the majority of the studies mentioned so far, and further learned that the flow angles were slower to recover than to develop. They measured some of the terms of the Reynolds stress transport equation, and compared several current models for turbulent transport and for the pressure-strain term against the data. They concluded that the models for the turbulent transport terms all had significant errors, but that those errors were small compared to the pressure-strain term. The pressure-strain models tested were all found to be reasonably accurate, with the nonlinear models providing no significant advantage over the linear models for this particular flow.

Chesnakas and Simpson (1994) reported near-wall measurements in the three-dimensional turbulent boundary layer over an inclined prolate spheroid. Using a unique laser Doppler anemometer, they measured the Reynolds stresses as close to the wall as $y^+ = 7$. They also analyzed the turbulent kinetic energy budget and found the structure parameter to decrease with increasing three-dimensionality, and proposed an empirical relation to describe the shape of the a_1 profile. Their measurement techniques are described in Chesnakas and Simpson (1992), and will be discussed in Chapter 3. Kreplin and Stäger (1993) also reported on a prolate spheroid geometry. They found the usual lag between γ_τ and γ_g, and suppression of a_1 in the outer part of the boundary layer, but their detailed data are highly suspect, for they used a four-sensor hotwire anemometer with poor resolution, prone to errors where there is strong velocity gradient.

Pompeo, Bettelini, and Thomann (1993) measured the effects of diverging and converging streamlines in the presence of constant-velocity outer flow. Streamline

convergence or divergence is present in most three-dimensional turbulent boundary layer geometries. They concentrated their efforts on the plane of symmetry, but the study is worth including here because of a computational difficulty it points out: small errors in the crossflow in the neighborhood of the plane of symmetry lead to large errors in the momentum thickness on the plane of symmetry. Thomann (1994) later reported that this difficulty is due to singularities which appear in integral and finite-difference methods, which utilize the boundary layer assumptions.

1.2.2.1 Shear-driven experiments

We will briefly mention a few noteworthy shear-driven three-dimensional turbulent boundary layer experiments. The earlier studies of Bissonette and Mellor (1974) and Lohmann (1976) both examined axial flow over rotating cylinders. Driver and Hebbar (1987) studied the axial flow over a rotating cylinder followed by a stationary section. Driver and Johnston (1990) expanded that study to include an adverse pressure gradient. The geometry produced a highly skewed three-dimensional turbulent boundary layer at the start of the spinning section, which gradually relaxed back to two-dimensional. They observed the shear stress angle lagging the mean strain rate angle, along with suppressed values of a_1. The suppression of a_1 was stronger for the cases of high adverse pressure gradient.

1.2.3 Structure experiments

Several recent studies of three-dimensional turbulent boundary layers have examined turbulence structure, using flow visualization and multi-point measurements.

Littell and Eaton (1991a), (1991b) investigated the turbulent boundary layer on a disk rotating in an otherwise quiescent environment. The disk boundary layer is three-dimensional because the low momentum fluid near the surface is flung outward by centrifugal acceleration. The study is notable for being the first three-dimensional turbulent boundary layer experiment to include two-point correlations. From the two-point correlations, Littell and Eaton inferred that there were strong asymmetries in the structure of the three-dimensional turbulent boundary layer. Conditional

sampling of the shear-stress-producing events indicated that longitudinal vortices of either sign occurred with equal frequency. However, the ability of one sign of vortex to generate strong ejections was suppressed.

Chiang and Eaton (1993) also investigated a disk boundary layer, using a water flow apparatus and relatively low Reynolds numbers to facilitate flow visualization. Their mean flow data agreed well with Littell's. Using flow visualization of longitudinal vortex structures very close to the wall, they observed that both signs of longitudinal vortices produce ejections at the same rate, but that one sign of vortex produced stronger ejections.

Eaton (1994) concluded from his group's studies that it is indeed appropriate to interpret the structure of three-dimensional turbulent boundary layers as a distorted version of two-dimensional boundary layers. He cited the turning of the mean velocity in the region $y^+ < 100$ as a major factor in producing this distortion.

Ha and Simpson (1993) investigated length scales of flow structures in a three-dimensional turbulent boundary layer. They looked into the spatial structure of the flow in a wing-body junction geometry previously studied by various members of Simpson's group. They used an array of hotwires at varying heights from the wall to find a coherence length scale based on two-point correlations of u. The near-wall coherence length scale was reduced by increasing three-dimensionality. Fleming and Simpson (1994) performed hydrogen bubble flow visualization in a flow of the same geometry, yet at much lower Reynolds numbers. They estimated the Reynolds number based on momentum thickness to be around 500 to 800. They discovered two main differences from two-dimensional boundary layers: The three-dimensional flow appeared qualitatively *more* stable and organized than two-dimensional flow at $5 < y^+ < 30$, and there was a 10% decrease in the spacing of the streaky structures.

Flack and Johnston (1993a), (1993b) investigated the near-wall region of two three-dimensional turbulent boundary layers. They reproduced the experiments of Schwarz and Bradshaw (1992) and Johnston (1970) at an initial Re_θ around 1400. They concluded that there is no near-wall collateral region, and that rapid turning seems to have less effect on a_1 than does gradual turning. Flack and Johnston (1995) reported from investigation of flow visualization of the same flow that the streak

spacing was reduced by three-dimensionality, agreeing with the findings of Fleming and Simpson (1994).

Worth mentioning here is an analytical study by Bassom and Hall (1991). They investigated the receptivity of Görtler vortices to roughness in situations where a turbulent boundary layer is very mildly three-dimensional and at very low Reynolds number. Their linear stability analysis demonstrated that crossflow can have a stabilizing effect upon vortical structures.

1.3 Computations

Direct numerical simulation (DNS) of turbulent flows has only recently been made possible, thanks to the continual development of supercomputers. These calculations can rightly be grouped with experiments, for they represent exact solutions of the time-dependent Navier-Stokes equations. Unfortunately, solutions are only available at low Reynolds numbers and for simplified boundary conditions. Direct numerical simulations have the distinct advantage of the possibility of measuring all the terms in the Reynolds stress transport equations.

The earliest three-dimensional turbulent boundary layer studied via DNS was by Spalart (1989). A half-plane of fluid bounded by a wall had its freestream velocity vector continually rotating but of constant magnitude. The flow was similar to an Ekman (infinite rotating disk) boundary layer, and is referred to as a "scrubbing" flow. The scrubbing flow did not demonstrate strong three-dimensionality in that $\gamma_\tau - \gamma_g$ was small, and the Reynolds number was low, but the study may prove useful because it provided a look at the Reynolds stress budget near the wall, where physical experiments have not reached.

Moin, Shih, Driver, and Mansour (1990) applied three-dimensionality to the fully developed turbulent channel flow of Kim, Moin, and Moser (1987). The three-dimensionality was in the form of a spanwise pressure gradient. Moin *et al.* likened their study to an infinite swept wing, but pointed out that an essential difference is that their channel experienced temporally evolving three-dimensionality which has no streamwise velocity gradients. They credited a decrease in the production term and

a decrease in the dissipation term of the Reynolds stress transport equations with causing an observable reduction in the turbulent kinetic energy.

Sendstad and Moin (1992) looked in detail at the same flow, investigating structures in the instantaneous flow fields. They found that vortices of the same sign as the crossflow vorticity are weakened, and that the streaky structures at $y^+ = 10$ are broken up when three-dimensionality is applied.

1.4 Modeling concepts

For engineering purposes, the goal in modeling three-dimensional turbulent boundary layers is to predict boundary layer displacement thickness, wall shear stress magnitude and direction, and mean flow profiles. As we saw in the earliest experiments, attempts were made to determine some sort of universal crossflow profile. Those attempts have essentially been abandoned, though theoretical limits have been addressed. Ölçmen and Simpson (1992) present a brief review of experimentally measured three-dimensional turbulent boundary layers, and apply a number of variations of "law of the wall" logarithmic formulas to the mean velocities. As might be guessed by the discussions to this point, none of the relations adequately described all of the flows. Degani, Smith and Walker (1992) performed an asymptotic study of the mean crossflow profile in a three-dimensional turbulent boundary layer with small crossflow at high Reynolds number. They found that the near-wall flow should be collateral to leading order, and that W profiles should display a logarithmic region at high Reynolds number. Degani, Smith and Walker (1993) extended that study to fully three-dimensional boundary layers, again seeking a functional form for the W profile. They found a theoretical W profile, but cautioned that it would not be expected to apply to a flow approaching separation.

The next step is an eddy viscosity model. Ölçmen and Simpson (1993) used the same datasets as before to evaluate eddy viscosity models, reporting on the models' ability to predict the magnitude and direction of the Reynolds shear stresses. Though they slightly favored a model by Johnson and King they discovered that these simple models were consistently wrong. Bettelini and Fanneløp (1993) offered a very similar

review and came to similar conclusions, offering adaptations to the Johnson-King eddy viscosity model.

Rotta (1977) offered an adaptation of eddy viscosity modeling for three-dimensional boundary layers. His widely-tested (but not wildly successful) "Rotta T" model introduces an anisotropic eddy viscosity which depends on a new parameter T, which is equivalent to the ratio N discussed earlier, and depends on the direction of the local free-stream velocity. It has a major flaw in that it is not translationally invariant.

A step up in complexity from algebraic eddy viscosity modeling is $k - \epsilon$ modeling. Transport equations are made for the turbulent kinetic energy and the dissipation; then an eddy viscosity is defined:

$$\nu_T = c_\mu k^2 / \epsilon \tag{1.10}$$

The eddy viscosity varies throughout the flow but is still assumed to be isotropic, so $k - \epsilon$ methods encounter the same difficulty as simple eddy viscosity methods.

Reynolds stress transport models, or "second-moment closure" models, rely on approximations for certain terms of the Reynolds stress transport equations (c.f. Launder (1988)). A difficulty near the wall where all turbulent boundary layers are concerned is the anisotropy in the dissipation. Most second-moment closure models take as an essential assumption that the dissipation is isotropic.

1.5 A note on choice of coordinate system

It is appropriate at this stage to include a brief discussion on coordinate systems. In three-dimensional turbulent boundary layer research, data are presented and discussed in a number of systems, and there is considerable disagreement as to which system is the most logical. All the coordinate systems are orthogonal, with the wall-normal coordinate designated as y, and the streamwise and spanwise coordinates designated as x and z. It is not clear as to which direction is best called "streamwise," however.

Aligning the coordinates with the physical axis of the wind tunnel, upstream of any three-dimensionality, is a logical first choice for many experiments. Viewing data

in these coordinates allows us to see the global development of three-dimensionality and the flow history, which Johnston cites as important in his 1976 review.

The local freestream streamline defines a second coordinate system. For some studies this is the logical physical choice, especially in rotating flows. We can better see the effects of three-dimensionality in this system, where W is by definition zero in the freestream.

Some researchers choose the direction of the wall shear stress as the direction of the x axis. This system is consistent with the concept that quantities in the boundary layer scale with the wall shear stress. Many experimental studies have difficulty presenting data in this coordinate system because of large uncertainties in measuring the angle of the wall shear stress.

Another popular coordinate system in the early studies is obtained by aligning the x axis with the *local* mean velocity vector. This is certainly convenient for displaying crosswire data, in the coordinate system of the probe stem, but it is not possible to derive simple transport equations in a coordinate system that has a different orientation at every point in the flowfield.

Occasionally, alternative coordinate systems are chosen. Ölçmen and Simpson (1994), for example, have selected coordinates aligned with the direction of maximum normal stress, claiming this as the intuitive choice for capturing the interaction between near-wall and outer region flow.

Whichever coordinate system is chosen, it is essential that a model be at least translationally and rotationally invariant.

1.6 Near-wall experimental methods

It is apparent from the experimental data sets available that there is a serious gap in data in the region of high skewing in three-dimensional turbulent boundary layers, below $y^+ = 100$. The primary reason for the lack of data near the wall is the need for high spatial resolution instrumentation where the velocity gradients are large. Two approaches may be taken to acquiring high-quality near-wall data. The first option is to increase the length scales in the boundary layer; the second is to decrease the

length scale of the measuring instrument.

The study of Flack and Johnston (1993a) is a good example of increasing the length scales to acquire near-wall data. They used a large water channel in which the boundary layer developed over a distance of 3 meters before entering the three-dimensional test section. They also ran the experiments at very low Reynolds number to further thicken the near wall layer. Perhaps more three-dimensional turbulent boundary layer experiments should be run in large facilities. However, many of the flow geometries studied to date would be very difficult and expensive to implement in a large wind tunnel or water channel. An alternative is to use a very viscous fluid. Fontaine and Deutsch (1995) used a conventional laser Doppler velocimeter (measuring volume 80μm x 820μm) in the glycerin tunnel at Pennsylvania State University, to measure shear stresses down to $y^+ = 3$ in a turbulent pipe flow, $Re_\theta = 720$. Johansson and Karlsson (1989) reported data down to $y^+ = 5$ in a two-dimensional boundary layer $Re_\theta = 2420$, using a similar-sized measuring volume. Such highly specialized facilities are rare, though, and to date none have been used for three-dimensional turbulent boundary layer research.

To measure Reynolds stresses near the wall in a moderate Reynolds number three-dimensional turbulent boundary layer it is generally necessary to increase the spatial resolution of the instrumentation. Johansson and Alfredsson (1983) illustrated this fact by measuring velocity fluctuations with hot film probes of various lengths. They showed that the maximum measured turbulence intensity (around $y^+ = 10$) is a strong function of L^+, the probe sensing length in wall units. In air, at a moderate Re_θ, we might expect $y^+ = 1$ to correspond to 30μm. Measurements below $y^+ = 10$ would require instrument length scales significantly less than 0.3 mm. This type of resolution is impossible with hotwire anemometry.

1.7 Motivation for the current study

There are a significant number of critical issues to be addressed in three-dimensional turbulent boundary layer research. A picture is beginning to emerge of the behavior of three-dimensional turbulent boundary layers, but relatively few accurate data sets

are available. High Reynolds number studies are nonexistent at this point, but we will not address that gap in this study. Critical to the understanding of the budget of shear stresses and turbulent kinetic energy is the near-wall region. Specifically, we would like to know what happens to the Reynolds stresses $\overline{u'v'}$ and $\overline{v'w'}$ in the region near the peak cross-stream velocity and approaching the wall, in a moderate Reynolds number boundary layer.

1.8 Specific objectives of this study

Based on the above motivations, our objectives are:

- Develop, construct and test a near-wall laser Doppler anemometer.
- Generate a simple three-dimensional turbulent boundary layer with well-understood pressure gradients at a moderate Reynolds number.
- Map the upstream boundary layer, as well as the outer layer, using conventional instrumentation.
- Measure several full profiles of the mean and fluctuating velocities, along two lines, as close to the wall as we can.
- Arrange to measure streamwise and spanwise derivatives of the quantities measured, in order to evaluate terms of the Reynolds stress transport equations.
- Interpret the data in terms of structure parameters, turning angles, and contributions to the development of shear stress and turbulent kinetic energy.
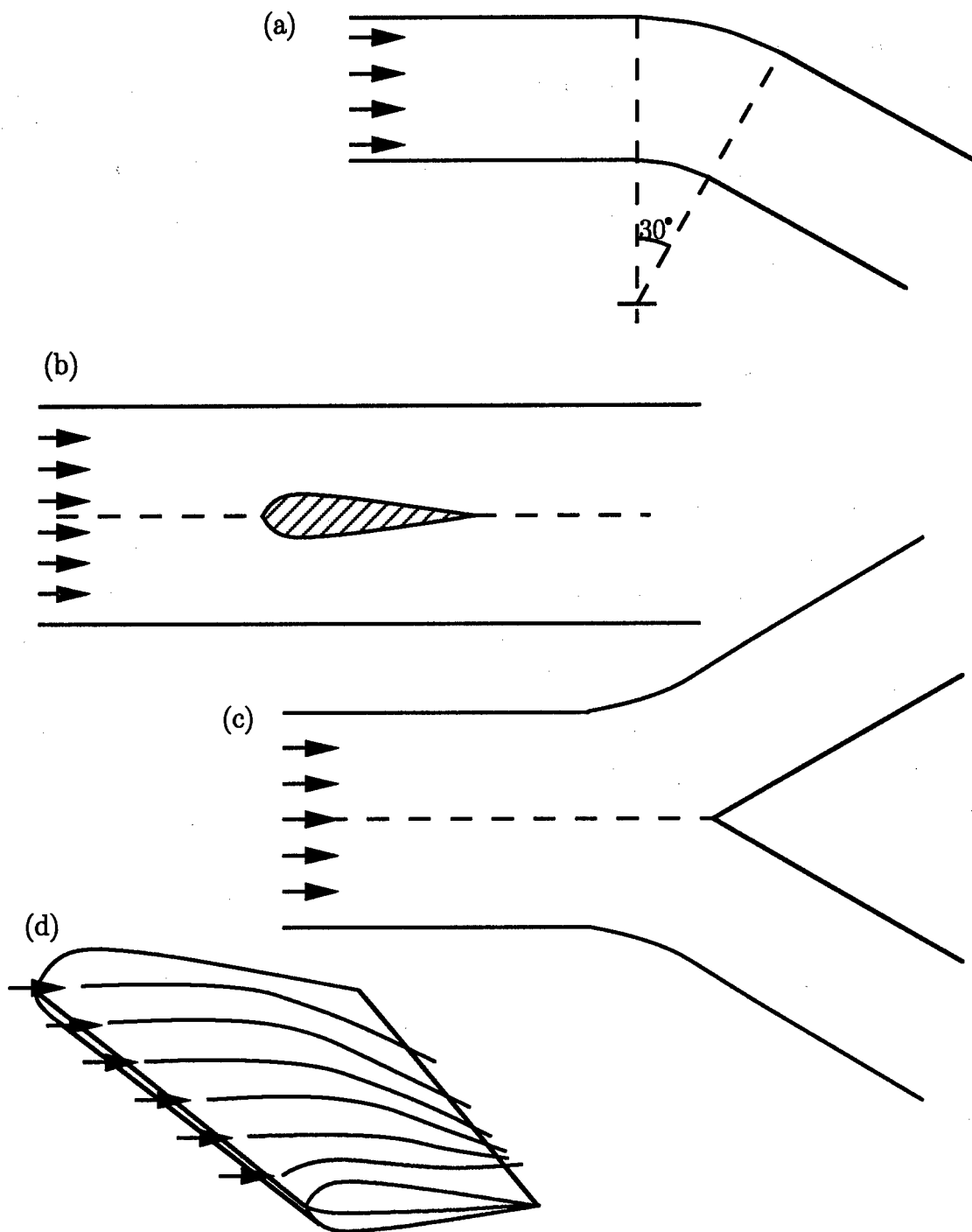- Test current models for the Reynolds stresses against the experimental data.

Figure 1.1. Examples of three-dimensional turbulent boundary layer geometries: (a) Schwarz & Bradshaw bend; (b) obstacle of Simpson *et al.* ; (c) Anderson & Eaton wedge; (d) swept wing.
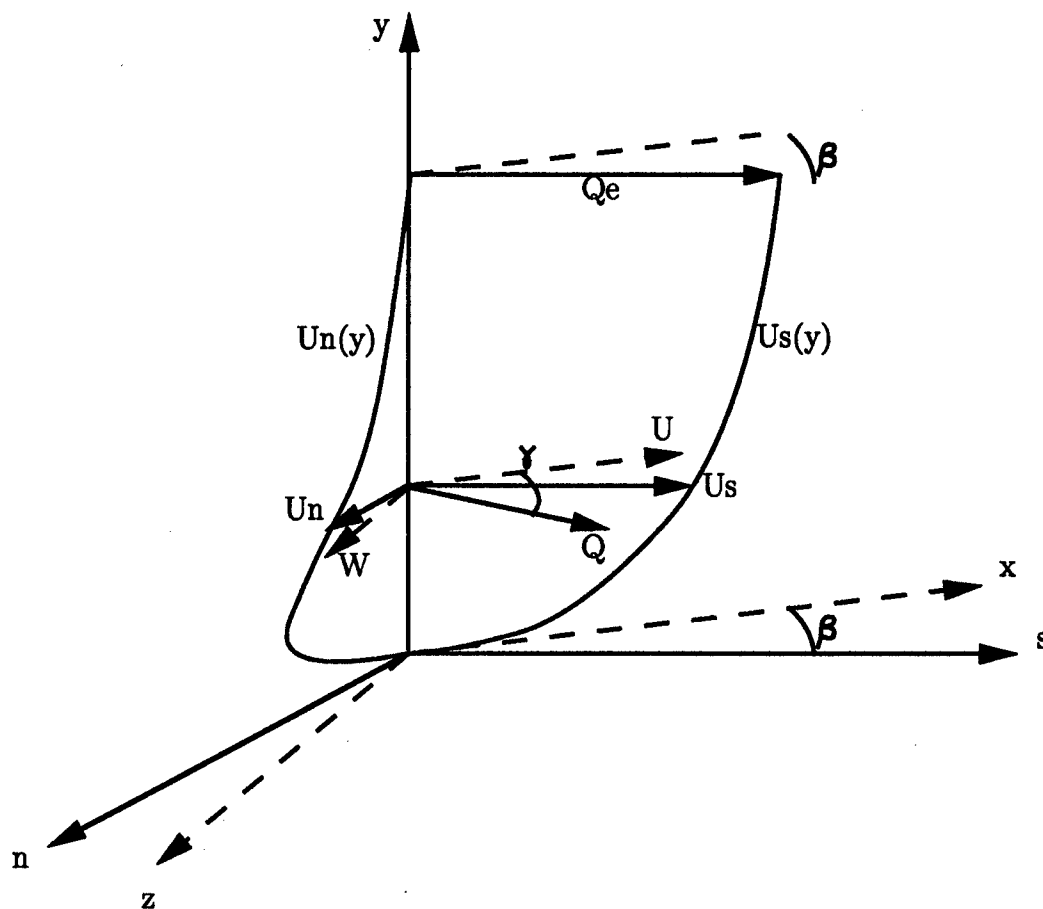
Figure 1.2. The canonical three-dimensional boundary layer. This figure serves to identify much of the nomenclature.

Chapter 2

Facility and Conventional Experimental Methods

2.1 Wind tunnel

The wind tunnel used in this experiment was originally built to study control of separated flow and dynamic stall, in Stanford University's Heat Transfer and Turbulence Mechanics Laboratory. The wind tunnel provides a steady, low freestream turbulence environment. We chose to use this facility because in addition to these properties it has a long test section with Plexiglas walls, allowing the moderately large Reynolds numbers and the optical access necessary for this experiment.

The closed circuit tunnel, shown in figure 2.1, has a centrifugal blower (New York AcoustaFoil), rated for 30,000 cfm, driven by a 40 horsepower motor with eddy-current clutch. The inlet to the blower is vented to the room; this ensures that the test section pressure is greater than atmospheric. Following the blower is a three-dimensional diffuser, which leads to a settling chamber. Flow conditioning consisting of a honeycomb and four screens precedes the three-dimensional contraction. The test section is 12 ft long, with a 24 in × 36 in cross-section. The boundary layer studied grows on a Plexiglas test surface 12 in above the floor of the tunnel.

After the test section, the flow passes through a two-dimensional diffuser and two 90° bends. The return leg of the tunnel contains a second Plexiglas test section. Access to this second test section in the return leg of the tunnel allows for introduction of seed particles for the laser Doppler anemometer without disturbing the boundary layer in the primary test section.

The temperature in the tunnel is maintained at a constant level of approximately 295 K by a heat exchanger mounted between the two bends downstream of the test section. A 100 gallon reservoir is filled with cold tap water before running the tunnel.

A water pump, with a user-set regulator and valve sends 3.0 gallons per minute of water from the reservoir through the heat exchanger and then to a floor drain. Make-up water is added continuously to the reservoir. The tunnel temperature reaches equilibrium within 30 minutes of starting.

The wind tunnel speed is set to within 0.05 m/s of the desired speed by a closed-loop controller implemented in the laboratory computer. Velocity is measured using a keil probe suspended from the top of the test section 24 in downstream of the start of the test section. The tunnel velocity is set at least as often as once before each data acquisition run. The tunnel speed remains constant over long periods of time: the maximum drift over a several-hour data acquisition run was approximately 0.05 m/s. The freestream turbulence intensity $\sqrt{\overline{u'^2}/U^2}$, well upstream of the wedge, is less than 0.6 percent.

2.1.1 Test section

The test section is constructed of 0.75 in Plexiglas walls with an aluminum frame. The side walls of the test section are removable, to allow for the introduction of new test surfaces and other equipment. An 18 in wide section of the side wall allows quick access; this section can be placed in the center of the test section or at the rear. The side port was kept in the rear position for this study, and was removed frequently for probe access and for adjustment of optical components below the test surface. Additionally, three rectangular ports in the floor of the test section allow for access to pressure tap connections and for various cables to exit the test section.

The test surface is a horizontal plexiglas plate, 0.75 in thick, held on six legs at 12 in above the floor of the test section. The leading edge of the plate is a 3:2 elliptical nose. Weatherstripping along the edges of the test surface isolates the flow above the test surface from the flow below.

A boundary layer trip was placed 15 cm downstream of the leading edge of the test surface. The trip consists of a 0.25 in × 0.625 in length of styrene. We were concerned with two criteria for boundary layer trips. First, the momentum thickness Reynolds number should be at least 200 upstream of the trip. Based on laminar

boundary layer development before the trip, we calculate Re_θ to be approximately 240 at $x = 15$ cm (c.f. Kays and Crawford (1980), equation 7-20). Second, the trip height should be of the same order of magnitude as the displacement thickness of the boundary layer. We estimate the displacement thickness at the trip location to be 0.7 mm. According to these criteria, the boundary layer trip was of proper size and placement. A third criterion, mentioned by White (1974), is that the Reynolds number based on trip height be at least 826. This criterion is also met by the boundary layer trip. In addition to the trip on the test surface, all sides of the inlet to the tunnel are equipped with "Dymo-V"[1] boundary layer trips, to provide a stationary transition site.

A spoiler flap at the end of the test plate is used to control the location of the stagnation point on the leading edge of the test surface. The spoiler flap was only necessary when we studied two-dimensional boundary layers. We attempted to use a pair of Preston tubes mounted just after the leading edge of the test surface to fine-tune the spoiler flap, but the results were unreliable. We found that the seed particles for the laser Doppler anemometer act as an excellent indicator: They collect at the stagnation line at the leading edge of the plate, showing clearly that there is no region of separation on the top of the test surface.

Two separate test surfaces were used. One has static pressure taps at the locations shown in figure 2.5. The other is clear, for optical access at the same locations as the pressure taps. The tubing from the static taps exits the tunnel through a bottom port. In order to minimize blockage from tubing, we make a maximum of six static pressure measurements at a time.

2.1.2 Three-dimensional boundary layer configuration

One of our goals is to generate a simple three-dimensional boundary layer, at a moderately high Reynolds number. A 30° Plexiglas wedge placed in the rear of the test section as shown in figure 2.2 produces the spanwise pressure gradient to turn

---

[1]Dymo brand labelers create plastic strips with raised letters. The letter V, evenly-spaced, with the top pointed downstream, is commonly used as a boundary layer trip. Its length is approximately 4 mm and its height approximately 0.4 mm.

the streamlines. The wedge spans the entire working height of the test section and blocks exactly half of the test section exit area. The leading edge of the wedge is at $x = 122.3$ in, allowing the two-dimensional boundary layer to develop to a moderate Reynolds number at a fairly low velocity. Potential flow calculations indicate freestream turning angles between 0° and 30°, but we planned to measure only the region where the turning angle is around 15 degrees or less. This constitutes a flow field which turns more rapidly than that studied by Schwarz and Bradshaw and less rapidly than the Anderson and Eaton wedge flow.

In order to relieve some of the favorable pressure gradient set up by the presence of the wedge, a fairing is added to the top of the test section, as indicated in the side view of figure 2.2. The fairing geometry is shown in more detail in figure 2.3. The idea was to allow the height of the test section to increase in the region where the width is decreasing, in the presence of the wedge. Contracting the test section early allows the boundary layer to grow to a reasonable thickness.

Several iterations were made on the design, each successive design relieving more of the favorable pressure gradient. The final design, depicted in figure 2.3, is 9.125 in high and spans the entire 12 ft length of the test section. The initial section is a smooth contraction formed over a length of 15.12 in. Following the contraction is a 108.10 in development section, where the fairing is flat. The remainder of the fairing increases test section height linearly, where the wedge is decreasing the width linearly. Transitions between the sections are smoothed as indicated in figure 2.3.

2.2 Laboratory computers

Almost all of the data acquisition and control is performed by laboratory computers. The primary computer was an IBM PC-AT (80286 microprocessor) equipped with an IBM DACA card for analog and digital input/output, and with a National Instruments GPIB card. The DACA card has four differential-input analog-to-digital (A-to-D) channels, with a range of ±10 Volts and 12 bit resolution. Prior to each day of data acquisition the voltage offset of each A-to-D channel is measured by shorting the input channels; the offset is subsequently subtracted from all voltages measured.

All data acquisition programming on the IBM is written in Microsoft QuickBasic 4.5.

In addition to the IBM PC, a Macintosh Quadra 650 is used for crosswire measurements, when it is necessary to collect multi-channel data simultaneously. The Macintosh is equipped with a National Instruments NB-MIO-16L I/O card, with eight differential-input A-to-D channels with 12 bit resolution. The A-to-D channels have selectable ranges; we used ranges of ± 1 and ± 10 Volts. All programming on the Macintosh is done in LabView 3.0.

2.3 Motor-controlled traverses

All wall-normal traversing is performed by using traverses driven by stepper motors. The probe traverse is mounted on rails above the test section. It is a Unislide linear traverse, with a 20 thread per inch lead screw and over 24 inches of travel. The motor can be stepped at 200 steps per revolution, so vertical traversing is in increments of 0.00025 in (0.00635 mm). A second vertical traverse sits in the test section under the test surface and translates optical components for the laser Doppler anemometer; this smaller Unislide has a 40 thread per inch lead screw, allowing 0.003175 mm resolution.

Two motor controllers drive the motors, a Superior Electric Translator Drive, model 230, and a SLO-SYN model TBM 105-6209. Both controllers supply the necessary current to turn the motors, based on square waves fed to them by the DACA card's binary output channels.

Traversing in the streamwise (x) direction is performed manually, facilitated by the top traverse mounted on rails in that direction. Traversing in the spanwise direction is limited to two discrete locations, corresponding to two slots in the top wall of the tunnel at $z = 0$ (the centerline) and $z = -3.5$ in. The vertical traverse is not moved in the spanwise direction; the probe holder adapts to hold the probe in either of the two slots. The center slot is sealed using a pair of spring-loaded metal tape measures which lie in a groove. Additional sealing is provided by weatherstripping in the slot. The off-center slot is sealed with tape. The fairing has slots which correspond to the slots in the top wall of the test section.

One probe holder was fabricated to accommodate all the probes used to traverse the boundary layer. The probe holder is depicted in figure 2.4. The apparatus accommodates 0.3125 in diameter probe shafts; a fairly large diameter was chosen because stiffness was a consideration in probe design, since the probes are subject to a crosswind along the length extended into the wind tunnel, up to 24 inches. The probe holder may be yawed about the probe axis manually, and is equipped with a dial indicator and vernier, providing 0.2° resolution.

2.4 Temperature and pressure

An Omega ON-910-44007 thermistor probe is used with a homemade voltage divider network to determine the air temperature in the tunnel. The thermistor sits inside the test section, below the test surface. The laboratory computer supplies the excitation voltage to the voltage divider circuit through one D-to-A channel, and measures both the thermistor voltage and the excitation voltage with two separate A-to-D channels. Once we determine the thermistor resistance, R_{th}, measured in Ohms, we use the following relation to determine the temperature in Kelvins:

$$T_{[Kelvins]} = 1/(A + B\log_{10}(R_{th}) + C(\log_{10}(R_{th}))^3), \qquad (2.1)$$

where

$$A = 1.2858 \times 10^{-3} \qquad (2.2)$$
$$B = 2.3599 \times 10^{-4} \qquad (2.3)$$
$$C = 9.4329 \times 10^{-8}, \qquad (2.4)$$

as given by Simonich and Moffat (1982), accurate to within 0.01 K of the Omega table.

Two Setra pressure transducers (model 239 and model 264) are connected to the laboratory computer and used for the pressure measurements necessary to the study. Both measure a range of ±0.5 in of water, over a 5 Volt output range. These transducers were calibrated on a daily basis against a Combist micromanometer, which has a resolution of 0.0005 inches of water. The measurements taken during the

two-point calibrations were averages of 6000 samples over 30 seconds; care was made to assure that the transducers had settled before making calibration measurements.

Atmospheric pressure was checked daily, and accounted for in gas density calculations.

2.5 Three-hole probe

A three-hole, or Conrad, pressure probe, is used to measure mean velocity and skew angle. The three-hole probe is similar to that used by Anderson and Eaton (1987). Anderson found that using tubes chamfered at $40°$ provides for strong sensitivity to yaw angle while being relatively insensitive to small changes in pitch. The tubes used for this three-hole probe are hypodermic needles with an outer diameter of 0.8 mm. The probe has a gooseneck shape, so that the tip of the probe is aligned with the probe stem axis.

To calibrate the three-hole probe, we placed the probe in the freestream of the wind tunnel, without the three-dimensional wedge installed. We ran the tunnel at four different speeds and varied the angle of the probe, γ, defined in figure 2.6. Note that if the probe is aligned with the x-axis, the angle reported is of opposite sign as the flow angle in a right-handed coordinate system. The calibration data are presented in figures 2.7 and 2.8 as dimensionless variables:

$$R = \frac{p_2 - p_3}{p_1 - p_s} \tag{2.5}$$

$$S = \frac{p_2 - p_s}{(p_2 - p_s)_{\gamma=0}}, \tag{2.6}$$

where p_1 and p_3 are the pressures in the side tubes, p_2 is the center tube pressure, and p_s is the static pressure. The data from all four speeds collapse on R vs. γ and γ vs. S curves. The four sets were averaged, then a fourth order polynomial curve was fit to R; three separate polynomials were fit to S. The polynomials are:

$$\gamma = r_0 + r_1 R + r_2 R^2 + r_3 R^3 + r_4 R^4 \tag{2.7}$$

$$S = s_0 + s_1 \gamma + s_2 \gamma^2 + s_3 \gamma^3 + s_4 \gamma^4 \tag{2.8}$$

The coefficients for these equations are found in table 2.1.

Yaw calibration		Magnitude calibration			
		$-30° \leq \gamma \leq -6°$	$-6° < \gamma < 6°$	$6° \leq \gamma \leq 30°$	
r_0	.273349613	s_0	.988815069	1.000429630	1.003293037
r_1	20.373661041	s_1	-.004214720	-.000208973	-.000346008
r_2	.000813345	s_2	-.000535055	-.000132969	-.000122061
r_3	-1.065526605	s_3	-.000005085	n/a	-.000011138
r_4	-.012972006	s_4	-.000000062	n/a	.000000165

Table 2.1. Three-hole probe calibration coefficients.

Near the wall, pressure probes are prone to error. This error was well-documented for single pitot tubes by Young & Maas (1936). The proximity of the three-hole probe to the wall causes the streamlines to be diverted, and we effectively measure at a height slightly above the physical probe location. The correction is based on the outer diameter (OD) of the tubes:

$$y_{corrected} = \begin{cases} y + 0.18 \text{ OD} & m \geq 0.1 \\ y + 1.8m \text{ OD} & m < 0.1 \end{cases} \qquad (2.9)$$

$$m = \text{OD}\frac{1}{U}\frac{\partial U}{\partial y} \qquad (2.10)$$

For the lowest points measured, this correction is 0.014 mm, and it tapers to at the edge of the boundary layer. The correction changes the lowest point reported by only 2%. An asymmetric probe is susceptible to misreporting the flow angle near the wall. We measured a two-dimensional boundary layer with this probe and found that its maximum angle error was 1.5°, at a height of 1 mm from the wall. There was virtually no error in reported angle above $y = 6$ mm.

The probe is used in "non-nulling mode"; i.e., the probe is not necessarily aligned with the local mean velocity at each position. Rather, the calibration constants are used to determine the angle and velocity of the approaching flow. The probe

was always rotated so as to keep the measured velocity angles within the range of calibration, and roughly centered in the range of calibration. Profiles acquired using the three-hole probe utilized a secondary static port with known pressure difference from the local reference static pressure, in order to prevent the probe's presence from altering the measured local static pressure.

The probe was aligned in the x direction by using the static pressure taps as markers; misalignment in x was no more than 1 mm. The probe holder controlled the z alignment. Placement in y was done by traversing the probe toward the wall and monitoring the probe tip visually. With practice, we found we could visually determine when the probe was between 0 and 0.2 mm ($y^+ \approx 6$) from the wall.

Each three-hole pressure data point was acquired over a period of 30 seconds, with 6000 samples each of $(p_1 - p_3)$ and $(p_2 - p_s)$, acquired at a rate of 200 Hz. A 30 second pause between moving the probe to a new location and acquiring pressure samples assured that the pressure had settled. Averages were made in software; individual samples were not kept.

Anderson and Eaton (1987) used a three-hole pressure probe of identical design. They analyzed the uncertainties in the measurements, citing three main sources for uncertainty: uncertainties in the probe response calibration, in the two differential pressures measured, and and in the local static pressure, measured separately from the other pressure measurements. Combined, these uncertainties are ± 0.2 m/s in velocity magnitude and $\pm 1.0°$ in direction.

2.6 Hotwire anemometry

An X-array hotwire probe (crosswire) shown in Figure 2.9 was used for turbulence measurements in the outer part of the boundary layer. We used the same crosswire used by Anderson and Eaton (1987), with minor modifications for use in a larger wind tunnel. A DISA 55-P-51 dual-sensor hotwire tip forms the sensor. It is mounted in a gooseneck probe configuration, which allows the probe tip to be rotated about the y-axis, while remaining in the same (x, z) position. The probe tip rotates about its own axis, also, to enable the four wire positions necessary to find the full Reynolds stress

tensor. One position is used to measure u and w simultaneously, and a second position measures u and v simultaneously. These two positions yield the mean flow and five of the six Reynolds stress components. Two additional positions are used to indirectly measure $\overline{v'w'}$. A pin through holes on the back of the hotwire tip allows indexing at 45° increments. The pin is spring-loaded, and rotation is controlled through the use of actuators at the top of the probe shaft, so rotation about this axis may be controlled from outside the tunnel.

The sensor is comprised of two tungsten wires with gold-plated ends. The wires are 5 mm long, with an active length of 1.25 mm, and 5μm in diameter, giving a length-to-diameter ratio of 250. The two wires are spaced approximately 1.0 mm apart. The sensor is tilted toward the wall at a grazing angle of 0.75°, measured optically.

A TSI IFA-100 unit is used as the constant temperature bridge electronics for the crosswire. The IFA-100 contains all the traditional components of hotwire circuitry: a bridge, filters, and offset and gain electronics. We chose unity gain for the signals, using the -1 to 1 Volt range on the A-to-D card on the Macintosh. The final signal was low-pass filtered at 20 kHz to remove spurious high frequency noise.

Calibration of the crosswire is a two-step process. First, the velocity response of the two individual wires is determined. Then, the angle of the wires is inferred. A new calibration was performed for each boundary layer profile, typically after two hours of data acquisition. After each profile, the crosswire probe was recalibrated. The difference between calibrations before and after profiles was typically around 1.5%. Calibration was performed with the crosswire in the wind tunnel, at the furthest upstream location in the slot in which the profile was to be taken, at a height $y = 75$ mm above the wall. Prior to calibrating the hotwire, the three-hole probe was used to determine the correlation between the local total pressure at the calibration site and the pressure difference between the keil probe and reference static port. A linear fit correlating the two pressure data sets had mean squared error of 1.00×10^{-6}. This function was used during the hotwire calibration.

We operated the tunnel at twelve preset (increasing) velocities to find the correlation between velocity and bridge voltage. A linear least squares fit to "King's

law,"

$$u = k(e^2 - E_0^2)^{1/n} \qquad (2.11)$$

was performed to determine the quantities k and E_0^2 at each calibration. The rms error between the fit and the measured u^n was typically around 1×10^{-7}. We found that using the exponent $n = 0.43$ the calibration was most linear.

A temperature correction is often included in hotwire calibration schemes. With the tunnel temperature remaining constant, we did not need to use such a correction. The maximum temperature change we see over the course of a profile is 1K. We use Littell's temperature correction scheme to predict the error due to this change in temperature, and find that the measured velocity would change by approximately 1% due to one degree change in ambient temperature.

The angular sensitivity of the hotwires is assumed to be a cosine response. Although earlier studies cite a minimum length-to-diameter ratio of 600 for cosine response, Littell and Eaton (1991) investigated the angular response of a single 2.5μm diameter wire, $l/d = 255$, finding its response over $\pm 60°$ to match a cosine curve almost perfectly:

$$u_{measured} = u \cos \psi, \qquad (2.12)$$

where ψ is the angle between the wire and the mean velocity vector. We therefore assume these wires also exhibit cosine response.

In order to determine the angles of the wires, the probe is placed in the $\overline{u'w'}$ position, with both wires essentially parallel to the test surface, but well out of the boundary layer. Because we assume a cosine response, we may use any two positions with a known offset angle $\Delta\psi$ to estimate the wire's angle with respect to the flow.

$$U_0 = U_e \cos \psi_0 \qquad (2.13)$$

$$U_1 = U_e \cos(\psi_0 + \Delta\psi) \qquad (2.14)$$

Combining and solving for ψ_0, we find

$$\psi_0 = \tan^{-1} \left(\cot \Delta\psi - \frac{1}{\sin \Delta\psi} \frac{U_1}{U_0} \right) \qquad (2.15)$$

Following the example of Littell and Eaton, we rotate the probe stem through five positions: $\gamma = -10°$, $\gamma = -5°$, $\gamma = 0°$, $\gamma = 5°$, and $\gamma = 10°$. For each position of

the probe, we solve the above equation four times, corresponding to the other four positions, using known $\Delta\psi$ angles. We average the results, and thus have an estimate for each of the five positions. Then, we subtract off the known offsets and average again to yield the angle of the wire. This entire process is repeated for the second wire. The two wire angles are called Ψ_1 and Ψ_2. Ψ_2 is negative.

Finally, we correct the originally measured k for each wire based on the cosine of the wire's angle, to reflect the fact that the velocity calibration is performed with the wires angled with respect to the flow.

2.6.1 Data acquisition and reduction

The crosswire probe is aligned with the mean flow at every point in the profile, during data acquisition. We acquire a profile of the boundary layer in four of the probe's "roll" positions in order to obtain all the components of the Reynolds stress tensor; $\overline{u'v'}$ and $\overline{u'w'}$ are measured directly but $\overline{v'w'}$ is measured indirectly. The $\overline{u'w'}$ stress is likely to have high uncertainties near the wall since the two wires are at different heights.

At each location, we collect 4000 samples from each wire at a rate of approximately 200 Hz with a time separation of $20\mu s$ between wires. Appendix A describes the data reduction in detail.

2.6.2 Uncertainty

We used the same probe tip as Anderson and Eaton (1987), and we should expect similar overall uncertainties. They catalogued a number of sources of uncertainty: probe misalignment during calibration or data acquisition, temperature variation, uncertainties in voltage measurement, global uncertainties in the calibration procedure, and uncertainties due to violations of the assumptions mentioned in section §2.6. They assigned the uncertainty levels listed in table 2.2. They cited Müller (1982b), who estimated that the $\overline{v'w'}$ Reynolds stress could be off by as much as 15% of $\overline{u'v'}$. We note that the uncertainties must be highest near the wall, especially for the quantities $\overline{u'w'}$ and $\overline{v'w'}$ in regions of large wall-normal gradients, where the probe

Error in	percentage	of Quantity
U, V, W	$\pm 3\%$	U
$\overline{u'^2}, \overline{v'^2}, \overline{w'^2}$	$\pm 5\%$	$\overline{u'^2}$
$\overline{u'v'}, \overline{u'w'}$	$\pm 10\%$	$\overline{u'v'}$
$\overline{v'w'}$	$\pm 15\%$	$\overline{u'v'}$

Table 2.2. Crosswire uncertainties, from Anderson and Eaton (1987).

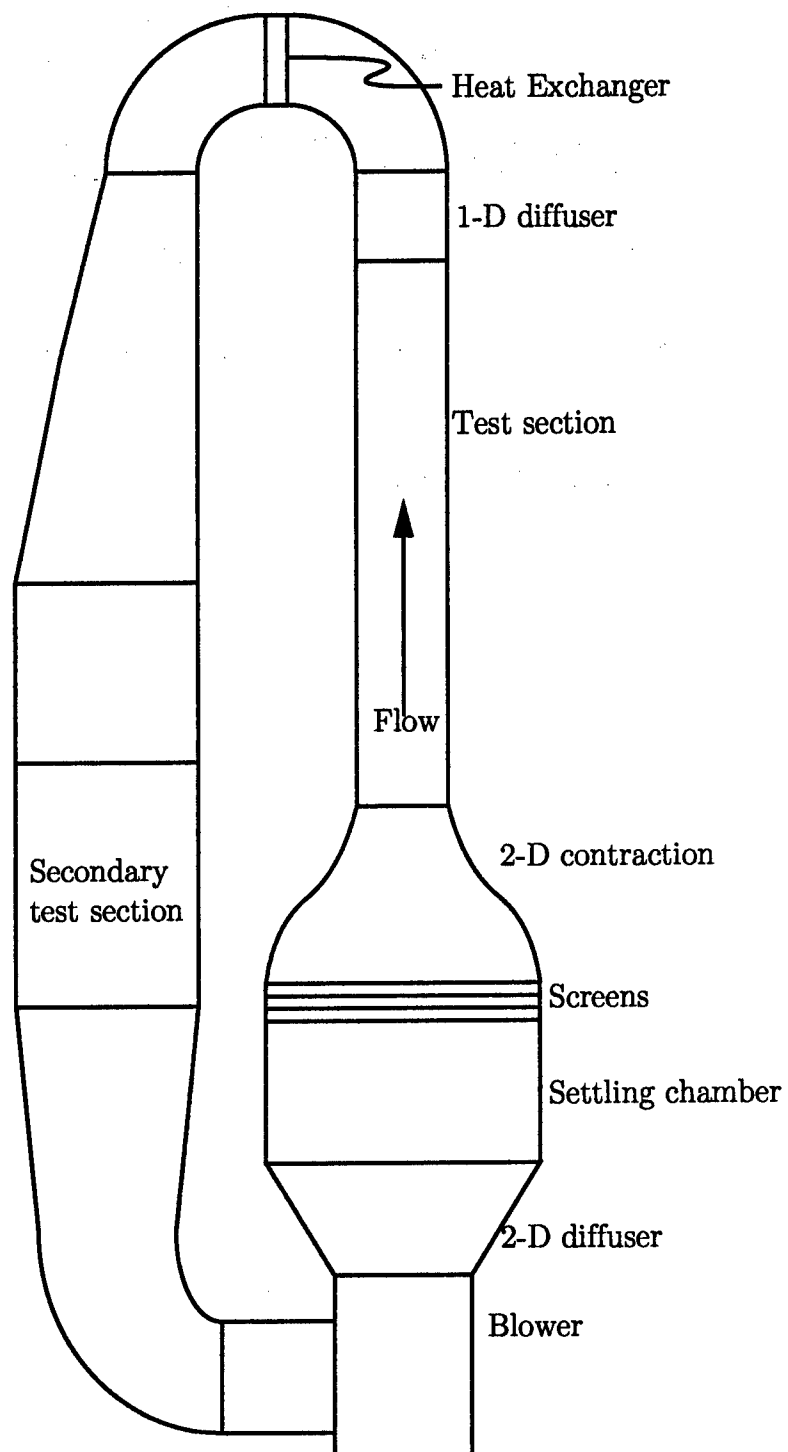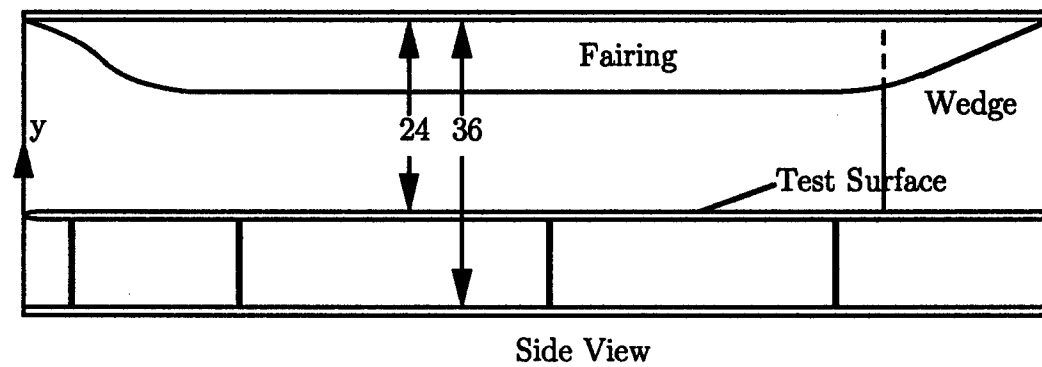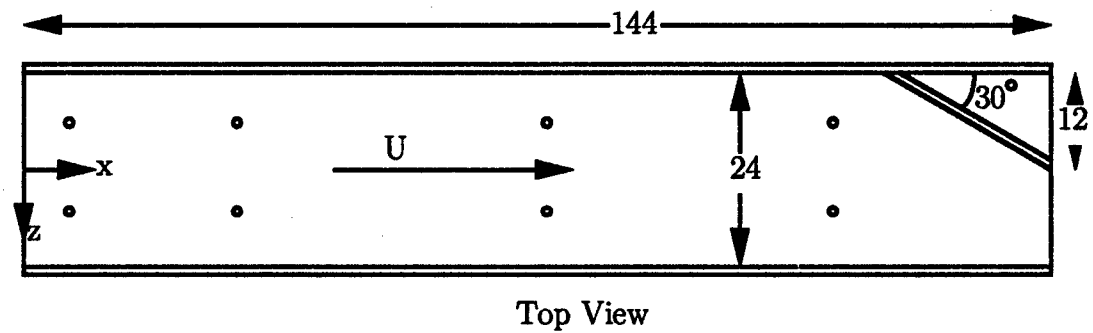spatial resolution, as determined by the spacing of the wires, is necessarily poor.

Heat Exchanger

1-D diffuser

Test section

Flow

2-D contraction

Secondary
test section

Screens

Settling chamber

2-D diffuser

Blower

Figure 2.1. Wind tunnel outline.

Figure 2.2. Test section (dimensions in inches).
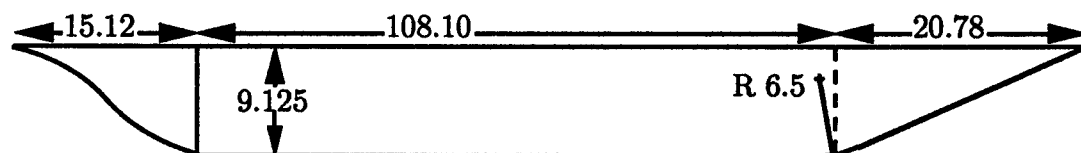
Figure 2.3. Fairing detail, side view (dimensions in inches).

A. probe shaft
B. dial
C. vernier
D. secondary mounting holes
E. attachment to traverse
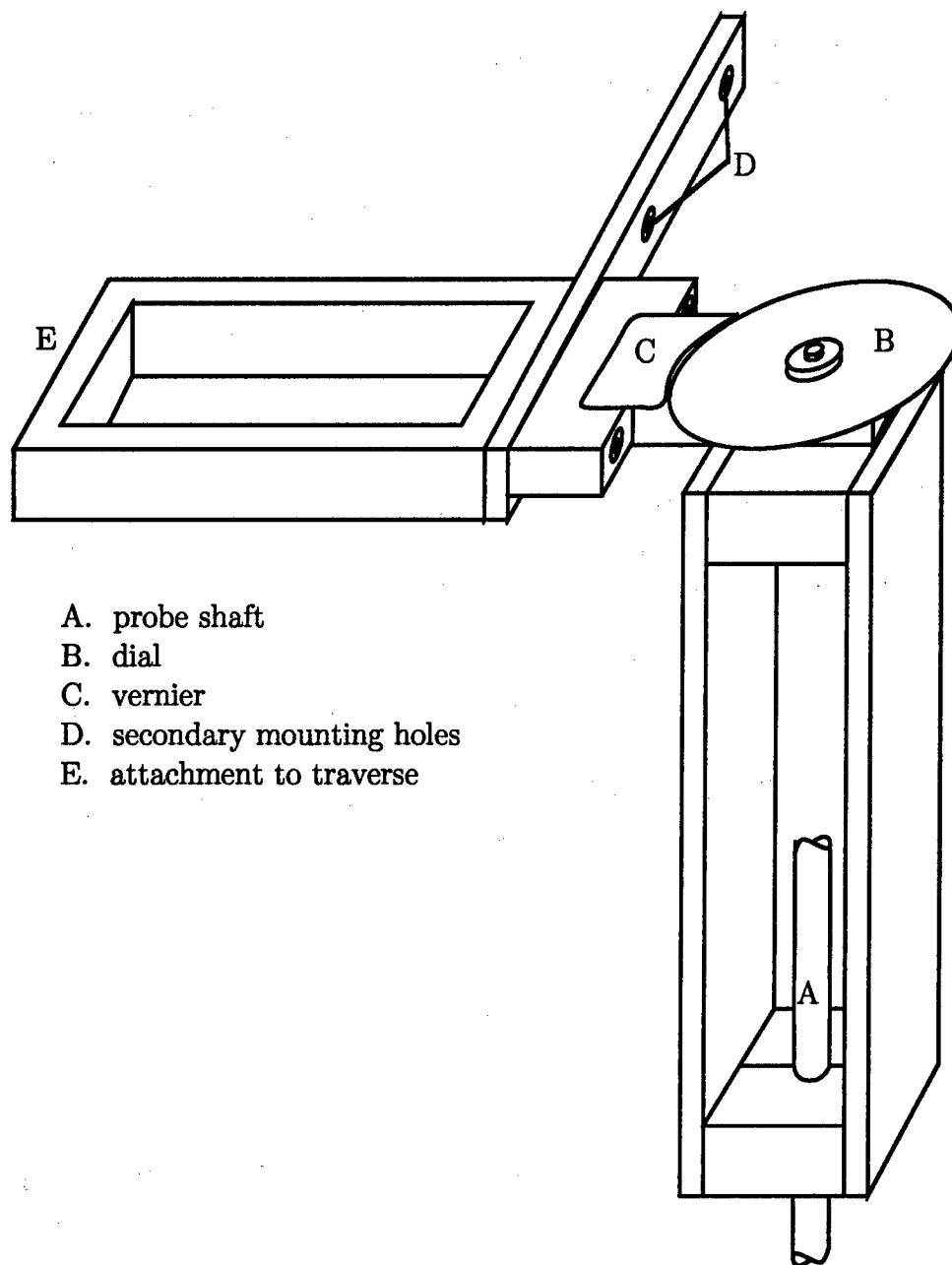
Figure 2.4. Rotating probe holder.
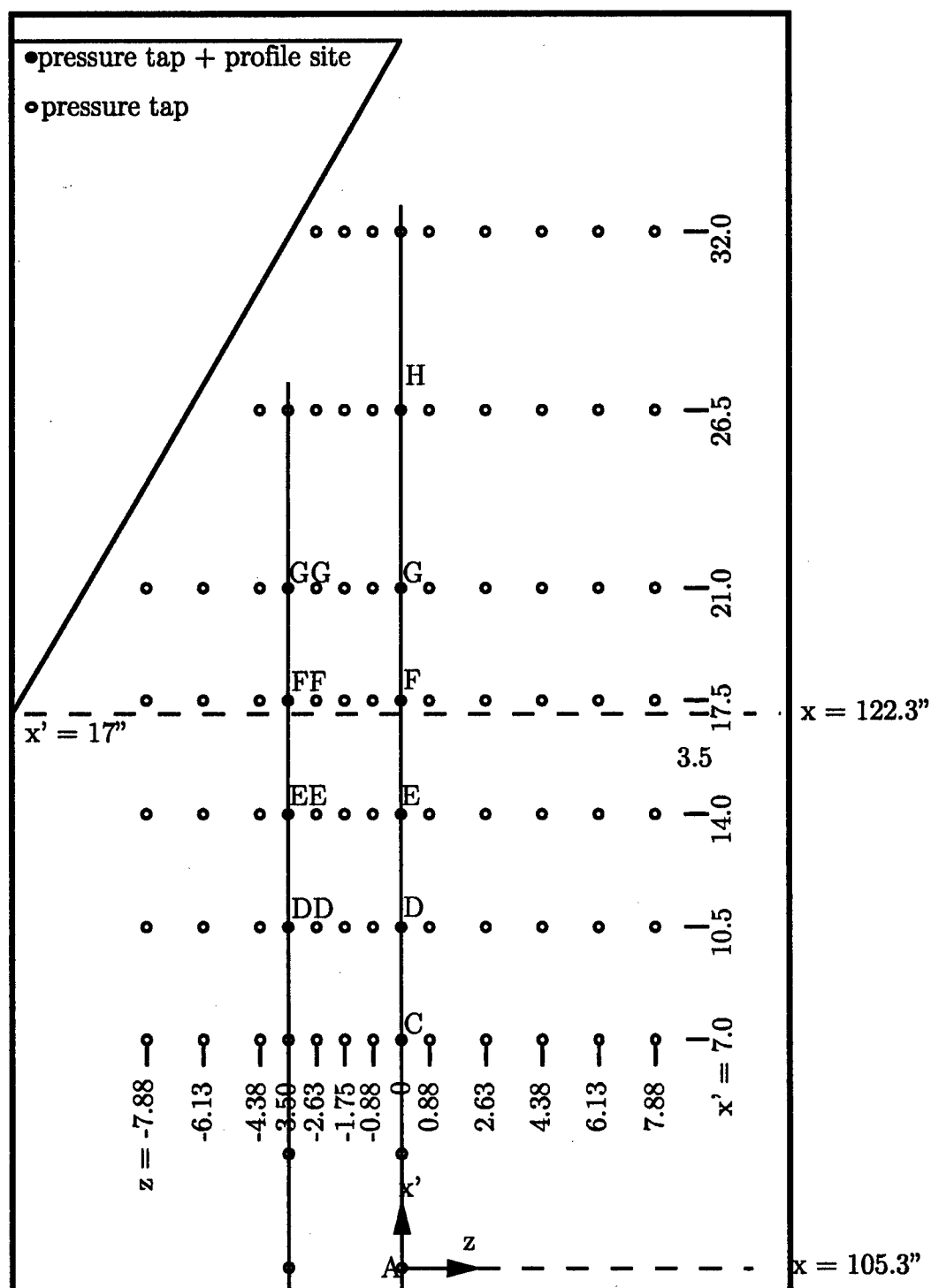
Figure 2.5. Map of pressure tap locations in 3-D section.

Gooseneck   Probe tip detail
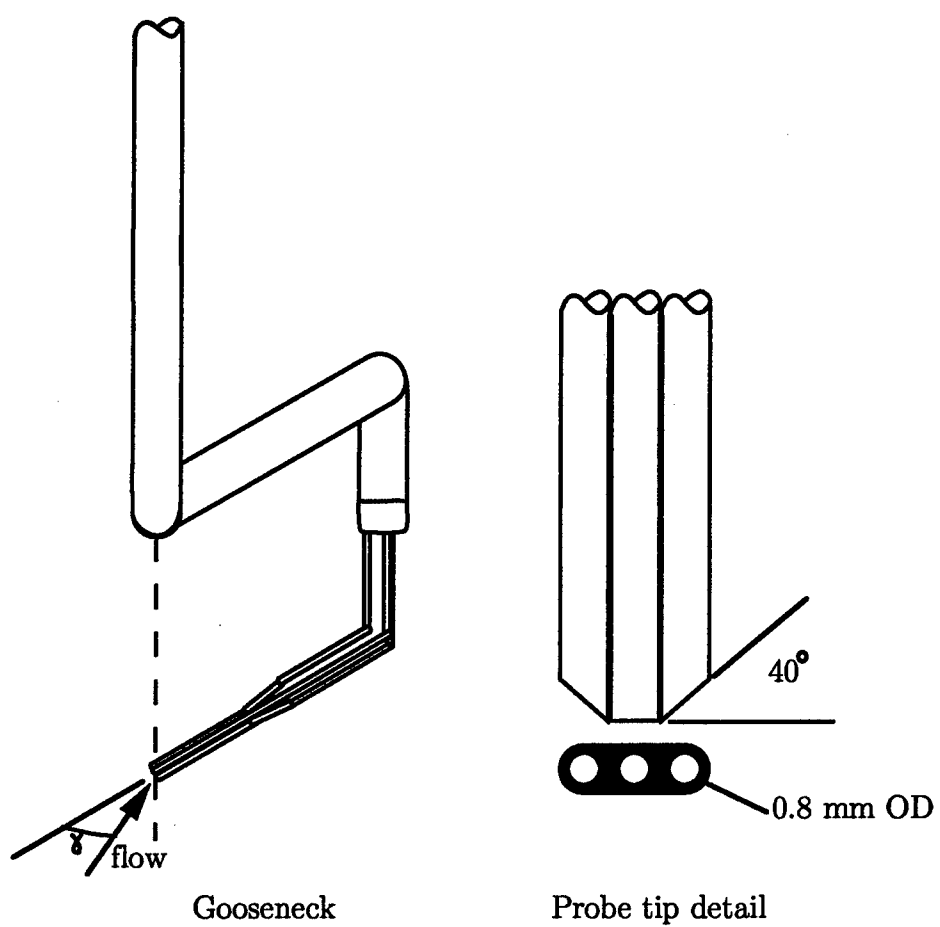
Figure 2.6. Three-hole probe detail.
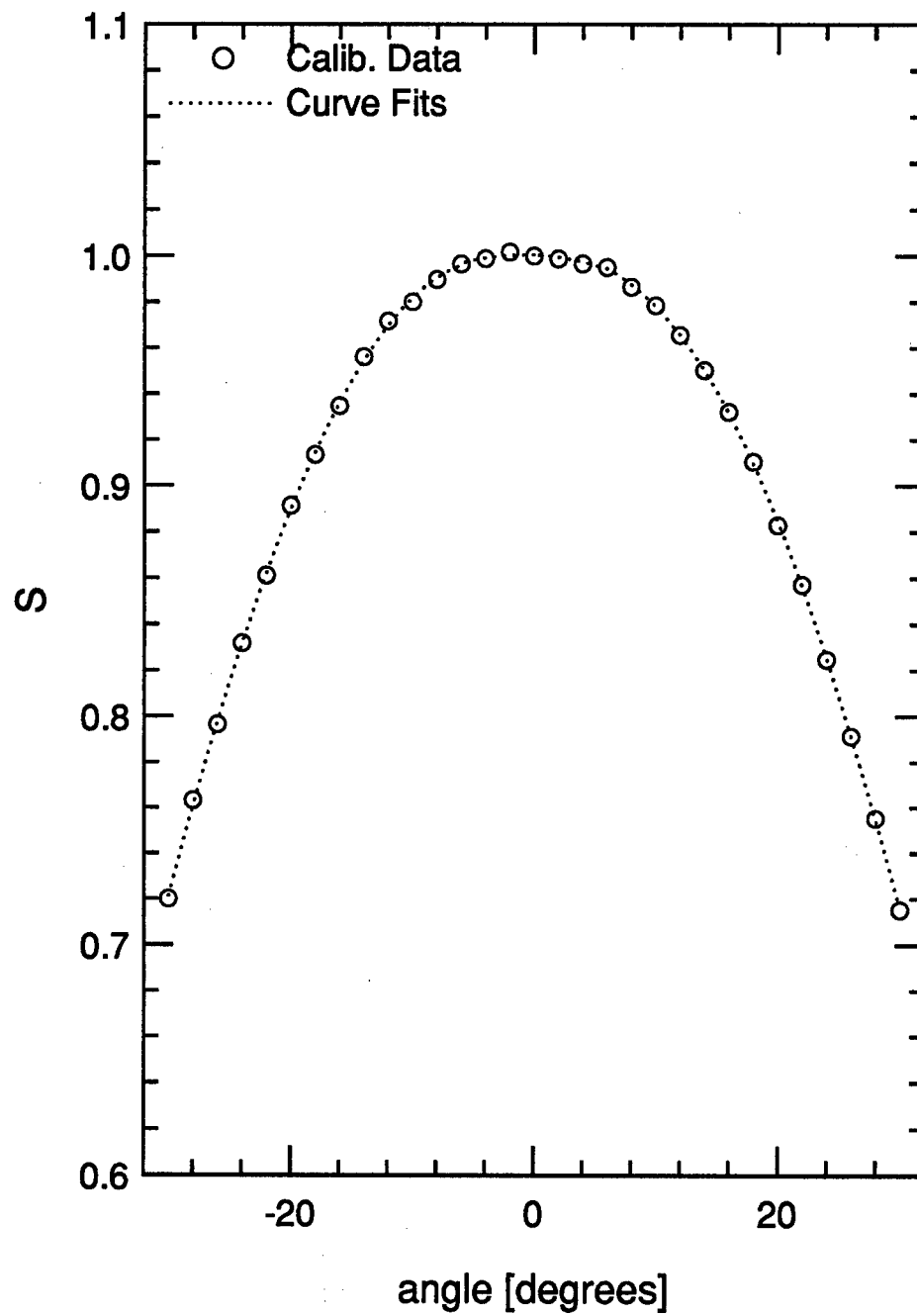
Figure 2.7. Three-hole probe magnitude vs. angle.
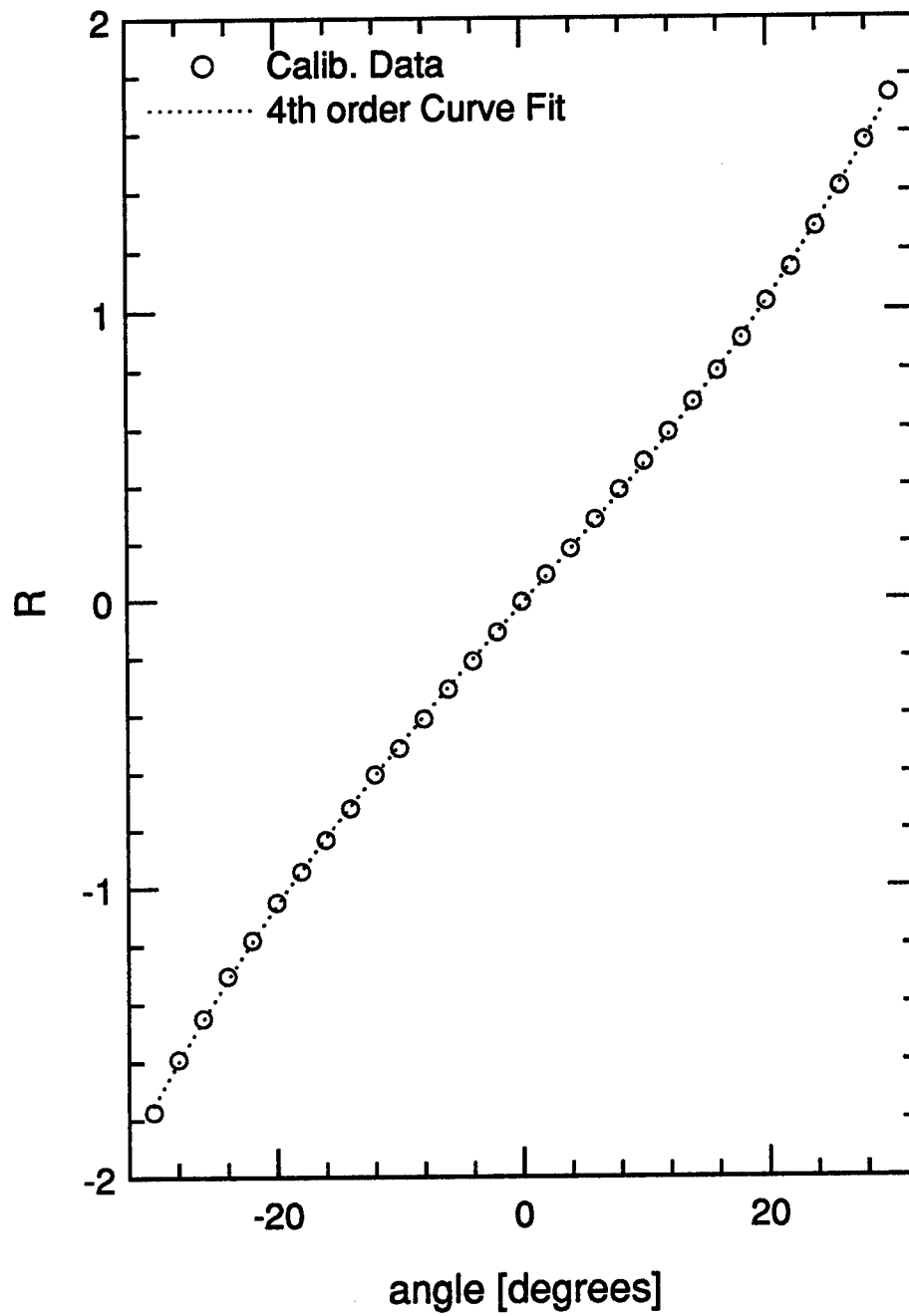
Figure 2.8. Three-hole calibration: yaw parameter vs. angle.
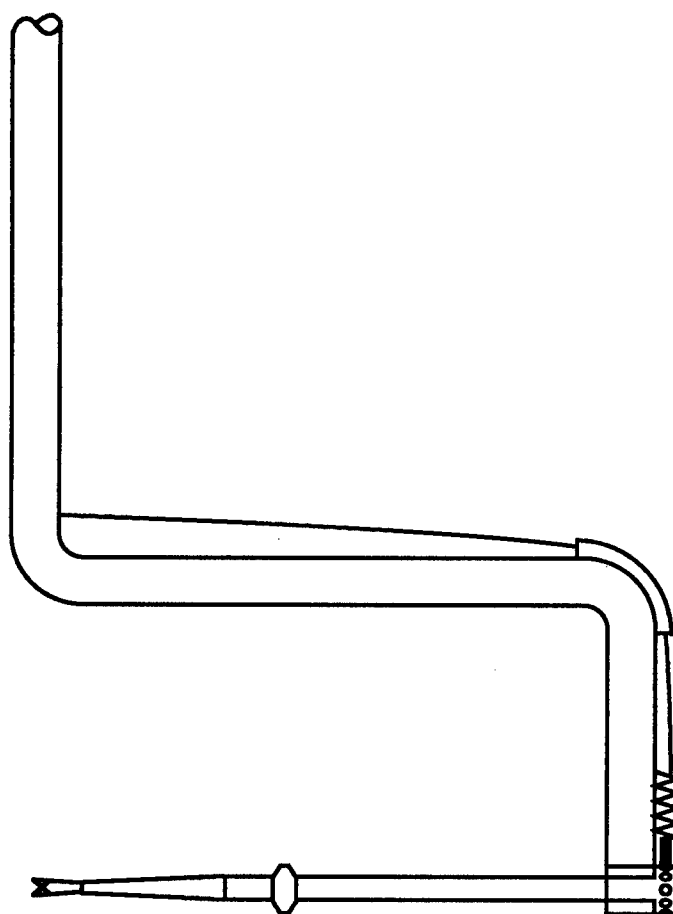
Figure 2.9. Crosswire probe.

Chapter 3

Near-wall Laser Doppler Anemometer

3.1 Introduction

A clear understanding of the near-wall behavior of velocities and Reynolds stresses is crucial to the future of predictive models for wall-bounded turbulent flows. Very few reliable Reynolds stress data exist below $y^+ = 100$ for three-dimensional turbulent boundary layers, leaving open for speculation questions regarding the behavior of the shear stress angle compared to the mean strain angle, and the behavior of the shear stress magnitude.

The scale of subsonic three-dimensional boundary layers studied in laboratory settings is somewhat restricted. In typical laboratory wind tunnels, the viscous length scale ν/u_τ is around $10 - 40\mu$m. It would be desirable but costly to build larger-scale facilities with thick boundary layers. In order to capture flow physics in the viscous sublayer, the spatial resolution of the instrument — at least in the wall-normal direction — must be comparable to this length scale.

Single-wire hotwires have been built with diameters as small as 0.6 μm and active length 0.2 mm (c.f. Westphal *et al.* (1988)). Adding a second wire to capture shear stress information, however, necessarily increases the effective size of the interrogation volume. Even the smallest X-array hotwire probes can have wires spaced as much as 0.5 mm apart. In three-dimensional turbulent boundary layers, the two relevant Reynolds shear stresses are $\overline{u'v'}$ and $\overline{v'w'}$. The shear stresses measured directly by X-array hotwire probes are $\overline{u'v'}$ and $\overline{u'w'}$; $\overline{v'w'}$ must be inferred from measurements from two positions, and therefore has high uncertainty. With conventional laser Doppler anemometry it is possible to overlap the measuring volumes for different velocity components. However, the smallest measuring volumes are typically 0.1 mm in diameter and as much as 1 mm long. These dimensions are to some extent a function of

the size of the experimental facility, since large-scale facilities generally require long focal-length optics, which generate large measuring volumes.

Johnson and Abrahamson (1989) proposed a near-wall laser Doppler anemometer for use in boundary layer flows. They relied on short focal-length optics and a mirror probe inside the flow to minimize probe volume. They reported mean velocities and normal stresses as close to the wall as 150 μm. Their work is the inspiration for our laser Doppler anemometer. Ölçmen and Simpson (1994) presented preliminary data from another laser Doppler system which relied on short focal-length optics. They used inclined 60 μm diameter measuring volumes, relying on time-coincident measurements to measure three components of velocity, down to $y^+ = 4$. They reported 7% repeatability in U/u_τ. Naqwi and Reynolds (1991) reported a measurement method which does not require high spatial resolution near the wall. They formed an interferometric measuring volume with fringes whose spacing varied linearly with distance from the wall. The Doppler signal frequency was therefore proportional to $\frac{\partial U}{\partial y}$. Use of such an instrument in a three-dimensional turbulent boundary layer would require the assumption that the flow is collateral near the wall. However, the velocity profiles measured to date cannot justify such an assumption.

Laser Doppler anemometry is becoming an increasingly popular method to measure turbulent flows, especially in regions of high turbulence intensity and reversing flows, since the method is generally non-intrusive. Durst *et al.* (1981) offer a fairly complete description of laser anemometry and its implementation. In its most common form, a laser Doppler anemometer (LDA) consists of a pair of laser beams which cross at an angle α to form an interference pattern. Particles that are small enough to follow the flow pass through the crossing region, known as the measuring volume. A sensor collects light scattered from the particles, and the frequency of the collected "burst" signal is a function of the particle's velocity as follows:

$$f = u/\Lambda, \quad \text{where} \quad \Lambda = \frac{\lambda}{2\sin\frac{\alpha}{2}}. \tag{3.1}$$

A signal processor is required to measure the dominant frequency in the scattered light signal for each burst. In order to resolve low or reversing velocities it is common to add a known offset to the frequency by frequency-shifting one of the two laser

beams. This is done using an acousto-optic modulator, called a Bragg cell. Another typical variation is to measure a second velocity component by introducing laser light of another color to generate a second measuring volume orthogonal to the first volume. The scattered light is split using a prism and color filters, and then each signal is processed separately to determine the two independent velocity components.

Based on our need to understand the physics of the near-wall region of three-dimensional turbulent boundary layers, our aim was to develop and test a high spatial resolution, two-component laser Doppler anemometer which would simultaneously measure either the v and w velocity components or the u and v velocity components. Desirable secondary attributes were low cost and portability. The first task for the LDA would be to document the Reynolds stresses in a two-dimensional turbulent boundary layer, to validate its capabilities.

The present LDA system was developed to make near-wall measurements in a wind tunnel which has a cross section of 2 ft × 3 ft and a boundary layer which has a viscous length scale ν/u_τ of approximately 35μm. This requires an LDA measuring volume with dimensions of the same order; a very difficult task given the long focal length optics implied by the scale of the test section. The LDA optics described below produce a measuring volume that is 35μm in diameter and approximately 66μm long. This high resolution is achieved by placing the transmitting and receiving optics immediately below the test plate and reflecting the transmitted beams from a mirror which is suspended in the flow. This allows the use of short focal length lenses and side scatter collection, both of which serve to minimize the measuring volume. The use of a mirror within the flow seems like a simple solution. However, the very short focal length produces some complexity beyond that found in ordinary LDA systems. This chapter discusses our solutions to some of the more difficult problems, and provides data which demonstrate the utility of the system.

3.2 The laser anemometer hardware

Figure 3.1 shows a simplified sketch of the optical train for the LDA system. The light source is an argon-ion laser operated in single line mode at a wavelength of

514.5 nm (green), and at a power level of 2.5 W. The second optical element is a 500 mm focal length "collimating" lens, to bring the laser beam to a second waist. A two-dimensional Bragg cell is placed near the second beam waist on a 3-axis rotation stage, and is used to split and shift the laser beam. Three useful beams exit the Bragg cell; all other beams are masked off. The first beam, unshifted, is a continuation of the beam which enters the Bragg cell. The second is shifted by 41 MHz, at a small angle β_{41} to the side of the primary beam. The third, shifted by 40 MHz and at the angle β_{40}, exits below the primary beam. These beams will be made to cross to form two orthogonal measuring volumes. After exiting the Bragg cell, the beams pass through the 100 mm focal length transmitting lens and the horizontal test surface. Just above the test surface, they reflect off the mirror probe, a 1.0 cm × 1.0 cm mirror. This mirror and all other mirrors used have $\lambda/10$ smoothness and are coated to optimize reflections at 45° incidence.

The theory of Gaussian optics was applied to the analysis and design of the transmitting optics. The primary objective was to obtain a locally small beam radius ("waist") and to place the waist at the beam crossing. We assume that the laser is operating in the TEM_{00} mode, so the beam amplitude is a Gaussian function of its radius. The lenses preserve the Gaussian beam profile.

The beam waist, w_0, is defined as the radius of the laser beam at the location where the beam is locally smallest. At a distance $r = w_0$ from the center of the laser beam, the intensity (the amplitude squared) is e^{-2} times that at the center of the beam. The Rayleigh range, z_0, is the length of the laser beam over which the beam's radius is no greater than $\sqrt{2}w_0$. The waist, wavelength, and Rayleigh range are related through the formula:

$$w_0 \equiv \sqrt{\frac{\lambda z_0}{\pi}}. \tag{3.2}$$

The first beam waist is determined by the laser cavity geometry and its size is provided by the laser manufacturer. The rear mirror of a Lexel 95 laser is flat and is therefore the location of the first beam waist. The collimating lens is placed a distance S from this first waist. A second waist is formed a distance S' from the lens where S' is found

from the Gaussian beam imaging relation[1]:

$$S' = f + \frac{f^2(S - f)}{(S - f)^2 + z_0^2}$$ (3.3)

The Rayleigh range at this second waist is:

$$z_0' = \frac{z_0 f^2}{(S - f)^2 + z_0^2}$$ (3.4)

The Bragg cell is placed near the second beam waist and has no effect on the beam diameter. The beam then passes through the transmitting lens and is focused to the final beam waist in the measuring volume. The distance to this waist is calculated using equation 3.3, and the Rayleigh range is calculated using equation 3.4. Finally, equation 3.2 is used to calculate the beam waist at the measurement position.

It is essential that the beams cross to form the measuring volume where they are narrowest. To accomplish this we use the geometrical optics imaging relation:

$$\frac{1}{s} + \frac{1}{s'} = \frac{1}{f} \; ,$$ (3.5)

where s' is the distance from the transmitting lens to the beam waist, and f is the focal length of the transmitting lens. Solving for s, the distance from the Bragg cell to the transmitting lens, we place the Bragg cell such that the beams converge at their waists after the transmitting lens. We also check that this Bragg cell placement puts the Bragg cell within the Rayleigh range of the second waist. The lens positions were chosen iteratively to obtain the desired measuring volume size. The final parameters of the LDA system are shown in table 3.1.

Conventional LDA systems use beam steering to force the measuring volumes to coincide, but that is not required here because the beams emanate from a single point and encounter all the same optical components, so they automatically converge to the same point.

The measuring volume is formed by beams crossing at the relatively small angle of approximately 2°, which has two effects: the fringe spacing is large (14.7μm) and the measuring volume is long. The fringe spacing is large compared to the measuring

---

[1]We use the sign convention that $S > 0$, $S' > 0$, and $f > 0$, as in figure 3.2.

	coordinate [m]	w_0 [mm]	z_0 [mm]
Back mirror of laser	0	0.650	2580
Collimating lens	1.138		
Bragg cell	1.649		
Second waist	1.661	0.122	90.9
Transmitting lens	2.461		
Third waist	2.575	0.0173	1.83

parameter	length[m]
Laser wavelength λ	514.5 e-9
Focal length collimating lens	.500
Focal length transmitting lens	.100

Table 3.1. Optical parameters and coordinates of transmitting optics.

volume diameter, but there is a significant bias velocity added by the frequency shifting. For a particle which passes through the widest part of the measuring volume, the number of cycles in a burst is

$$N = \frac{d}{\Lambda} + \frac{d(f_{\text{Bragg}} - f_{\text{downmix}})}{u} \tag{3.6}$$

so a velocity of 10 m/s would have a burst of at least 12 cycles.

The measuring volume length is effectively reduced by using side-scatter receiving optics. The receiving lens has a focal length of 30 mm and is positioned 40 mm away from the measuring volume to achieve 3× magnification. The collection fiber tip is placed 120 mm below the receiving lens, at the location of the magnified image of the measuring volume (satisfying equation 3.5). The fiber tip is the field stop — the stop which limits the angle of rays emanating from off-axis. The image of the field stop in the object plane is the entrance window, which limits the extent of the measuring volume which can be detected by the receiving fiber, as illustrated in figure 3.3. Since the fiber diameter is 200 μm and the system magnification is 3, the size of the entrance window is 66μm. Note that side-scatter collection efficiency is low, so this is one source for a low data rate.

Generally in laser Doppler anemometry, we consider the wave fronts of the laser beam to be planar. When the beam waist is small and the beams cross at a small angle, we can no longer consider the wave fronts to be planar, and the wave radii

change over the length of the measuring volume. Consider figure 3.4, which is a cartoon of two laser beams crossing at their waists. The wavefronts far from the waist behave as though they emerge from a point source at the waist. Interference fringes, which appear as dark vertical lines, are formed by the superposition of the fields from the two laser beams. The figure illustrates that the interference fringe spacing varies with the closest spacing at the waist. In practice, we are able to interrogate a small portion of this measuring volume, so we scan the length of the measuring volume to find the point of local maximum measured velocity. This is the location of minimum fringe spacing.[2] The fringe spacing varies as much as 5% along its length, so it is easy to discern changes in fringe spacing. The measuring volume is inclined, so we perform this scan near the uuper limit of the LDA's travel to minimize the variation in U along the measuring volume. This variation is only about 0.1%, so it does not interfere with our finding the beam waists.

The practical optical setup is shown in figure 3.5. The components are mounted to three distinct bases. The first is an optical table that sits below the wind tunnel test section, holding the laser, collimating lens, and Bragg cell. A small wall-normal traverse mounted inside the wind tunnel below the test surface holds the transmitting lens and receiving optics. The proximity of the lenses to the test surface limits the wall-normal traversing range to approximately 25 mm. The mirror probe is suspended from the top of the test section on a second traverse. The mirror is 54 mm off-axis, and does not cause measurable disturbances to the flow. For wall-normal traversing we do not move the bench; consequences of this are discussed in section §3.4.

In order to obtain the third velocity component, the measuring volumes may be rotated by 90° about a vertical axis through the measurement location. The lens mount allows the transmitting lens to be rotated about the vertical axis. The mirror probe has a spring-loaded tip, as seen in figure 3.7, which allows it to be rotated easily. With the two configurations, we directly measure the mean velocity, the Reynolds normal stresses, and the $\overline{u'v'}$ and $\overline{v'w'}$ shear stresses. A 45° rotation is also possible, for extracting information about $\overline{u'w'}$, but we took no data at this position.

---

[2]If the beams do not cross at their waists, the fringe spacing will vary monotonically along the length of the measuring volume. The fact that we find a local maximum velocity indicates that the beam crossing does coincide with the beam waist.

The hardware is also equipped with the ability to easily translate to three alternate positions in order to measure streamwise and spanwise derivatives. Jigs on the optical bench allow for movement of the vertical axis (see figure 3.6) ; optional mounting holes for the small traverse allow for its translation. The probe tip mechanism rotates about a secondary vertical axis and locks in place at four different positions.

The light is collected into a 200 micron diameter fiber optic cable, which interfaces to a photomultiplier tube (PMT). A pair of RF amplifiers in series converts the PMT current to a measurable voltage and a downmixer subtracts 38 MHz from the signal. The amplified and downmixed signal is passed through an 8 MHz 8-pole LC Butterworth low pass filter. The downmixed signal contains the frequencies corresponding to two components of velocity, one centered at 2 MHz (40 MHz Bragg shift − 38 MHz downmix) and the other centered at 3 MHz.

The filtered signal is analyzed by a Macrodyne 3102 frequency-domain LDA signal processor, which finds the frequency components in user-specified frequency ranges. The concept of using one frequency-domain processor for multiple velocity components was suggested by Johnson (1990) as a way to significantly reduce cost in LDA systems. The two components are distinct because the lower-frequency signal always remains significantly below 3 MHz. The signal processor passes frequency information from each burst to an IBM PC via GPIB. Specific components for the LDA are listed in table 3.2.

3.3 Operating procedures

We align the optics such that the primary (unshifted) beam forms 90° angles at all mirror interfaces except at the final mirror, intersects the center of the Bragg cell as defined by the Bragg cell's apertures, and intersects the transmitting lens at its center. This alignment minimizes cross-contamination between velocity components.

The receiving fiber is mounted on a three-axis stage allowing accurate positioning of the fiber tip. The position in the horizontal direction perpendicular to the transmitted beams is chosen by moving the fiber tip to obtain the maximum data rate. Translating the fiber tip in the direction along the beam path means interrogating

different sections of the long measuring volume. We choose this location by scanning the fiber tip with the tunnel running and finding the location where the fringe spacing appears to be a minimum. We use a small port in the tunnel's floor to gain access to the knobs. We find that it is not possible to maintain alignment if we remove and replace a surface through which the beam passes.

Locating the wall with the measuring volume is done with the tunnel running at test speed, since everything exhibits small deflections in the presence of the flow. We translate the system in the wall-normal direction with the laser power set very low until a sharp image of the measuring volume is visible, centered on the tip of the fiber, and clear signal from both channels is obtained, indicating that the measuring volume is scattering off the wall.

Seed particles are introduced in the return leg of the closed circuit wind tunnel, upstream of the blower. The seed particles are titanium dioxide (diameter $\approx 1\mu m$), carried in a solution of ethyl alcohol, and propelled by compressed air at about 40 psig through an airbrush. The container of TiO_2-alcohol mixture is kept on a magnetic stirrer to maintain the suspension. We found that using pure alcohol was best: the particles are hydrophilic and tend to agglomerate when in 99% alcohol. The seeding system is run continuously during data acquisition. Due to the extremely small measuring volume, seeding is critical and the maximum data rate achieved was approximately 50 Hz. One positive side effect of low data rate is that it is extremely unlikely to measure multiple particles in one time window. This is borne out by our observations of the individual bursts.

3.4 Data reduction

The most difficult problem with the present LDA system is that we do not know the fringe spacing precisely. With the two-dimensional Bragg cell we cannot predict exactly at what point within the Bragg cell the beams will diverge. This point is determined by both the angle of the Bragg cell and the driver power level. Also, as discussed above, the fringe spacing depends on the positioning of the receiving optics since the fringe spacing varies along the length of the measuring volume. Therefore,

we are forced to calibrate the fringe spacing against known velocity data. The Bragg cell settings are held fixed throughout the study. The receiving optics' alignment is held fixed for each velocity profile. For three-dimensional boundary layers we match the U and W mean velocities to the the velocity measured with a three-hole probe, using the outermost point to match U and a point near the peak W (specifically at $y = 1.6$ mm) to match W. To fix the V fringe spacing we match measurements of $\overline{v'^2}$ from a crosswire over the range 7 mm $\leq y \leq$ 16 mm.

Traversing in y alters the fringe spacing slightly, as a consequence of not moving the Bragg cell. We calculate the fringe spacing as a function of y using geometrical optics. The fringe spacing changes by only 3% over the operating range of the LDA because the transmitting lens is placed very far from the Bragg cell.

Figure 3.8 shows the laser beam orientations for the two main configurations. The measuring volumes are pitched toward the wall by 6°, resulting in a small contamination of each velocity component by the other components. Transformation of the data into the wind tunnel coordinate system is straightforward. Details are discussed in Appendix B. There is a small contribution of $\overline{u'w'}$ to some of the other Reynolds stresses. For a two-dimensional boundary layer these contributions are zero, but for a strongly skewed three-dimensional turbulent boundary layer $\overline{u'w'}$ can be larger than $\overline{v'w'}$. We chose not to measure $\overline{u'w'}$, so we cite the following offsets: $\overline{v'^2}$ is off systematically by 3% of $\overline{u'w'}$, and the $\overline{u'v'}$ and $\overline{v'w'}$ shear stresses are off by approximately 10% of $\overline{u'w'}$. These estimates are discussed in detail in Appendix B.

As a final step in processing the data, we correct for small errors in locating the measuring volume relative to the wall. A small offset, not exceeding 80μm, is added to the y value for each point. The offset is chosen to minimize the mean squared difference from $u^+ = y^+$ for the data points below $y^+ = 7$.

3.5 Validation in a two-dimensional boundary layer

We present data from the LDA along with crosswire and pressure probe data for comparison. These data are for a two-dimensional turbulent boundary layer, with Reynolds number based on momentum thickness of approximately 3800. Table 3.3

lists the descriptive parameters for the boundary layer, as calculated from the pressure probe data. We use the experimental facility described in Chapter 2, with the wedge removed and the fairing extended to cover the space left by the wedge. Data are acquired on the centerline of the tunnel, 129.3 in downstream of the leading edge of the test surface. The freestream velocity is 12.5 m/s.

Figure 3.9 shows the mean velocity measured by the LDA and compared to data from the three-hole pressure probe. Two independent sets of LDA data are presented. The agreement is good: maximum deviation between the LDA and pressure data is approximately 0.05 m/s.

The LDA data are compared to crosswire measurements of the normal stresses in figure 3.10 and the shear stress in figure 3.11. All of the data are normalized using the friction velocity inferred from the pressure probe mean velocity measurements. We observe the expected peak in $\overline{u'^2}$ stress around $y^+ = 10$. The $\overline{w'^2}$ stress has greater scatter in the region below $y^+ = 20$; this may indicate that we have a small error in the height of the (U,W) volume. The $\overline{u'v'}$ shear stress reaches a peak somewhere between $y^+ = 80$ and $y^+ = 100$. This agrees qualitatively with the expected behavior, though there are few data sets to compare to our near-wall data. The $\overline{v'w'}$ shear stress measurements are plotted alongside the $\overline{u'v'}$ shear stress. In a two-dimensional boundary layer, $\overline{v'w'}$ is zero, so both instruments demonstrate small errors by measuring non-zero correlations between v and w.

3.6 Uncertainty analysis

The first consideration in the uncertainty analysis is the statistical uncertainty due to a finite sample size. Typically, we acquire at least 5000 samples per point, calculate the mean and standard deviation, then discard the data outside 3σ to remove any extraneous data, and recalculate the statistics. The statistical uncertainty in the mean at 95% confidence is then 2.8% of the standard deviation, which amounts to less than 1% of the mean velocity even in the region of highest relative turbulence intensity. The statistical uncertainty in the Reynolds stresses is approximately 4% of the measured stress.

Velocity bias occurs when the arrival rate of particles is correlated to the velocity. Mean velocity measurements can be significantly biased where the turbulent fluctuations are high. Gould and Loseke (1993) described four techniques to correct for this velocity bias. They recommended a correction scheme based on generating a Gaussian pdf shape, which is perhaps inappropriate for wall-bounded turbulence, but they also recommended that no correction scheme be implemented below a turbulence intensity $\frac{\sqrt{\overline{u'^2}}}{U}$ of 15%. We recognize that our uncorrected data may exhibit some velocity bias below $y^+ = 30$, where $\frac{\sqrt{\overline{u'^2}}}{U} \geq 15\%$. Adams, Eaton, and Johnston (1984) also quantified the effects of velocity bias, stating that velocity bias is strongest in regions of both high mean velocity and high turbulence. They developed a "worst case" analysis of velocity bias. Applying their analysis to the present 2D boundary layer data yields a peak error in the measured U of $0.8u_\tau$ at $y^+ = 7$. Their analysis is excessively conservative and the true bias errors are likely to be much smaller.

Finally, we must consider the effect of the finite spatial extent of the measuring volume. A detailed analysis of this effect is presented in Appendix C. The error in mean velocity is proportional to $d^2 \frac{\partial^2 U}{\partial y^2}$ while the error in Reynolds normal stress is proportional to $d^2 \left[2 \left(\frac{\partial U}{\partial y} \right)^2 + \frac{\partial^2 \overline{u'^2}}{\partial y^2} \right]$. Using Spalding's (1961) law of the wall equation and Spalart's (1988) two-dimensional boundary layer data, we find that the error due to the finite extent of the measuring volume is responsible for peak errors of approximately $0.1u_\tau^2$ in the normal stresses, and of $0.003u_\tau$ in the mean velocity near the wall.

3.7 Conclusions

The new LDA has proven to produce accurate mean velocity and Reynolds stresses well into the viscous sublayer of a moderate Re_θ two-dimensional boundary layer. In addition, the use of the two-dimensional Bragg cell to do both beam splitting and frequency shifting, and the use of a single frequency-domain processor have lowered the cost of the LDA substantially. Several factors make the LDA difficult to use. The biggest problem is the non-uniform fringe spacing, requiring careful alignment of the receiving optics and calibration of the LDA system. In addition, the small measuring

volume size and side-scatter receiving lead to low data rates.

Item	Brand and model
laser	Lexel 95-4
optical bench	Newport XSN-14
2D Bragg cell	Intra-Action F2M40/45
Bragg cell drivers	Intra-Action ME-40
photomultiplier tube	Thorn EMI model 9818B
PMT power supply	Thorn EMI model PM28RA
RF amplifier unit	Avantek GPD-201
downmixer	TSI 9186
collimating lens	Melles Griot 01LA0346 achromat
transmitting lens	Melles Griot 01LA0123 achromat
receiving lens	Melles Griot 01LA0024 achromat
probe mirror	Melles Griot 02MPG002/001
other mirrors	Melles Griot 02MPG001/001
optical fiber	Newport UV-NIR cable
LDA processor	Macrodyne FDP3102
airbrush (for seed)	Paasche-H

Table 3.2. Specific equipment for LDA.

$C_f/2$	0.001582
u_τ	0.5015 m/s
U_e	12.61
Re_θ	3792
$Re_\delta*$	5267
H	1.389

Table 3.3. Two-dimensional boundary layer parameters.

A. Laser
B. Collimating lens, f .500 m
C. 2D Bragg cell
D. Transmitting lens, f .100 m
E. Test surface
F. Mirror probe
G. Measuring volume
H. Receiving lens, f .030 m
J. Fiber tip
K. PMT
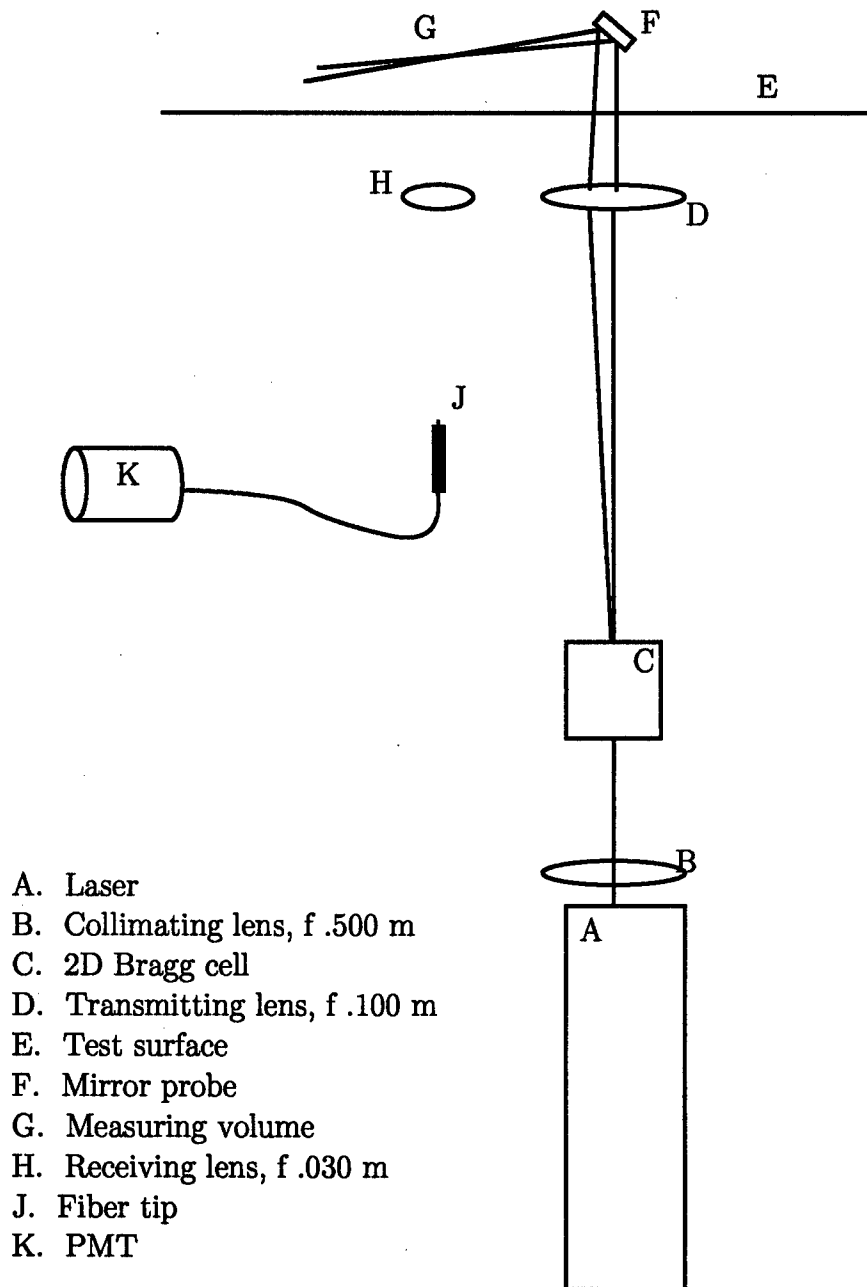
Figure 3.1. LDA optical path: sketch of essential elements.
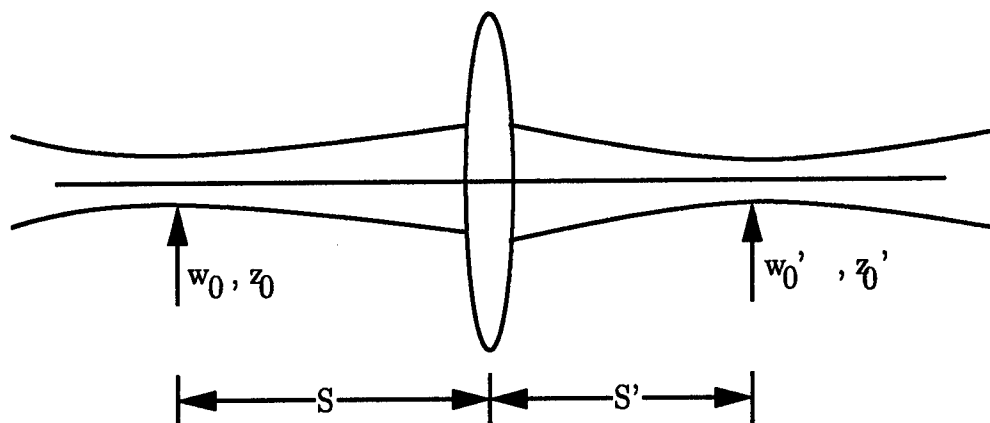
Figure 3.2. Gaussian beam propagating through a lens.

A. Measuring volume
B. Receiving lens (f=30mm)
C. Receiving fiber
D. Focus
E. Aperture stop
F. Field stop
G. Entrance window
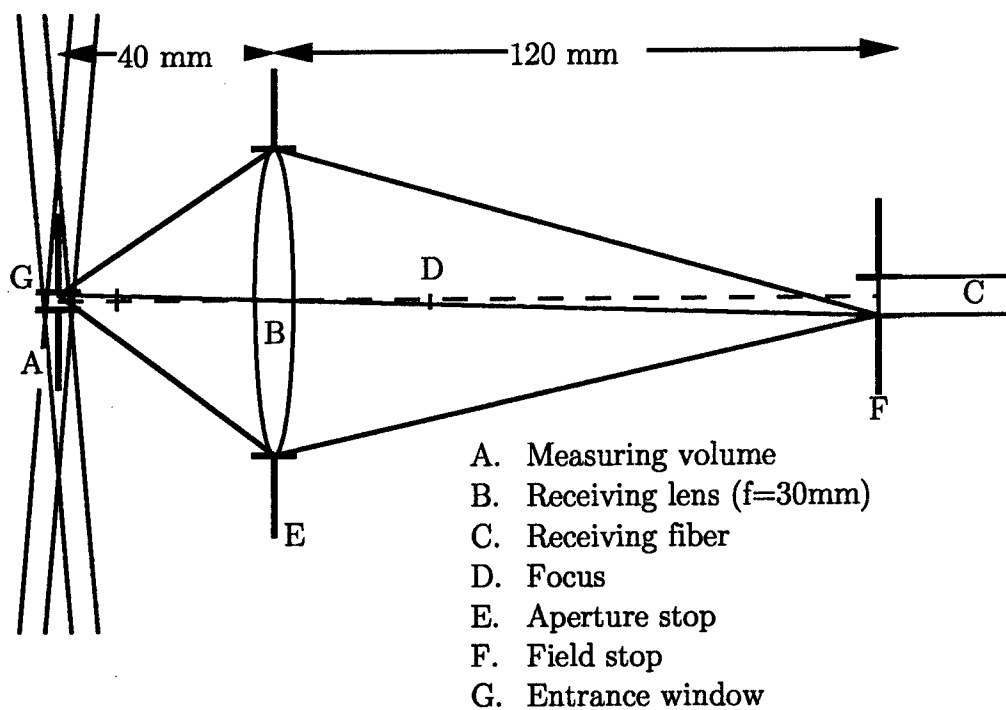
Figure 3.3. Stops in receiving optics. Vertical scale exaggerated.
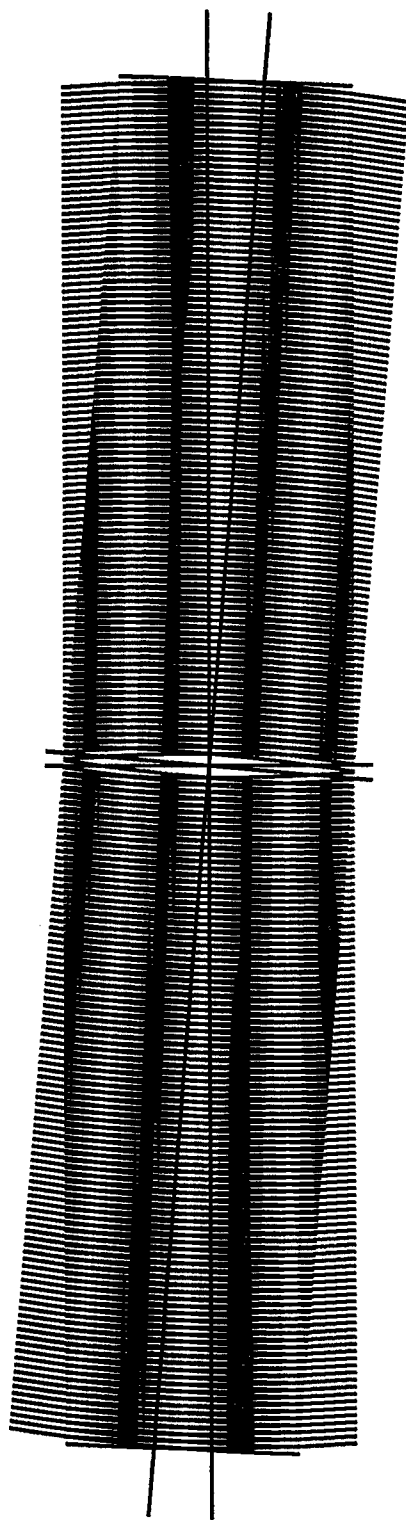
Figure 3.4. Fringe illustration.

Flow

A. Laser
B. Collimating lens, f= .500 m
C. 2D Bragg cell
D. Transmitting lens, f= .100 m
E. Test surface
F. Mirror probe
G. Measuring volume
H. Receiving lens, f= .030 m
J. Fiber tip
K. PMT
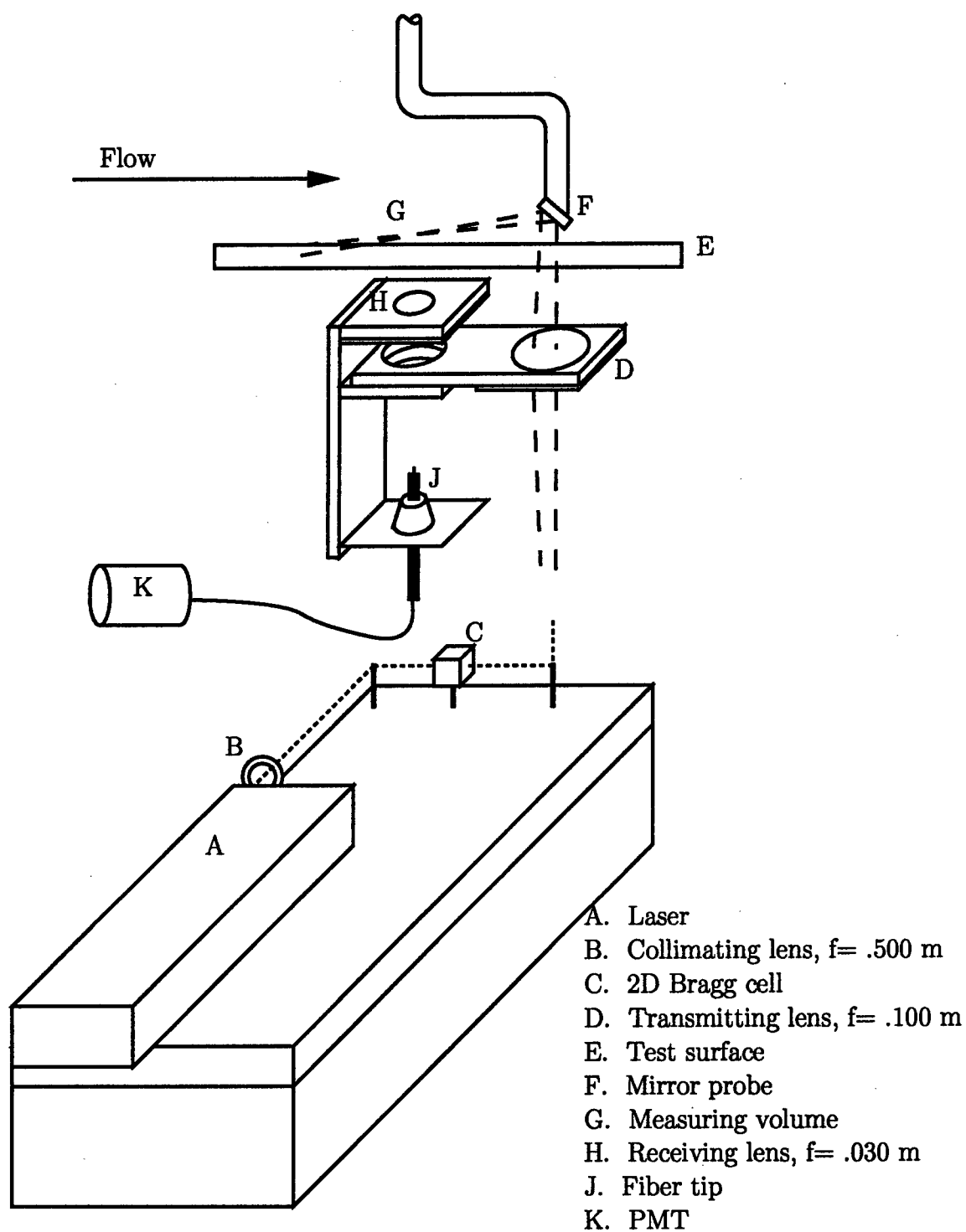
Figure 3.5. LDA optical path. Not to scale.

from laser

A. First mirror
B. 2D Bragg cell
C. Removable mirror (for rotation)
D. Probe axis
E. (v,w) mirror
F. (u,v) mirror
G. Plate for mirrors and Bragg cell
H. Positions for plate G
J. Positions for mirror A
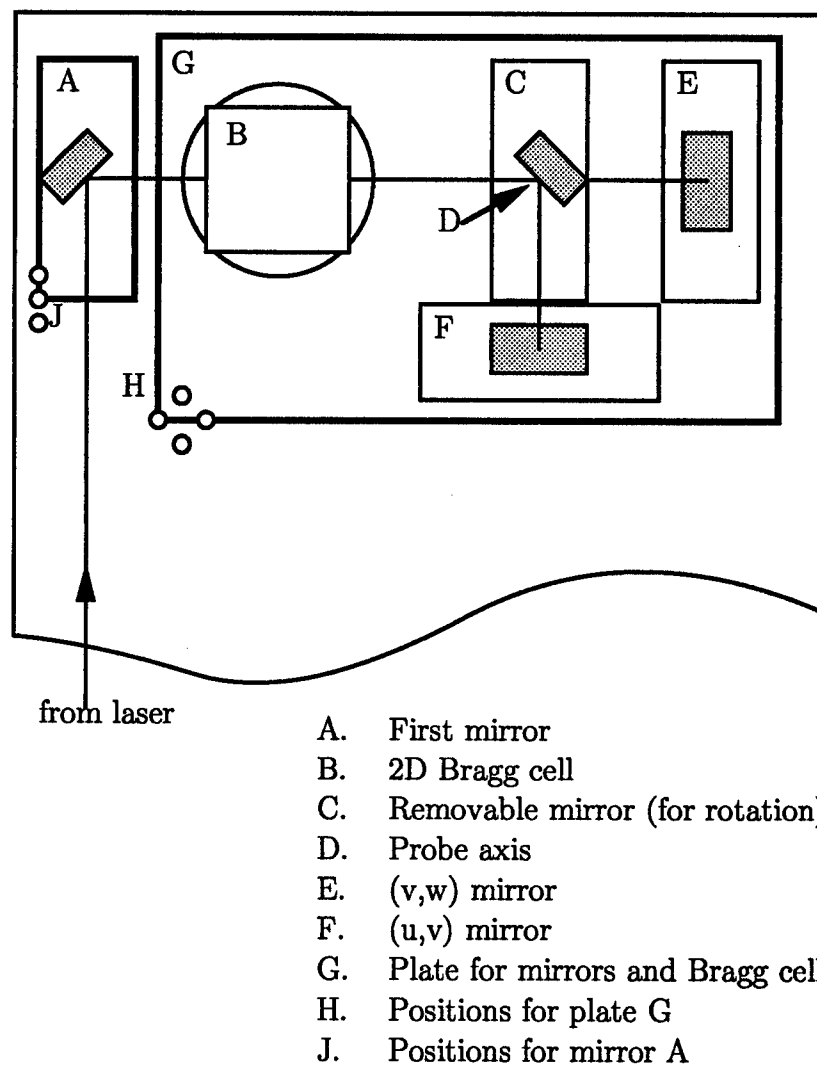
Figure 3.6. Detail of optical bench, indicating options for (x,z) translation and system rotation.

(a)

(b)
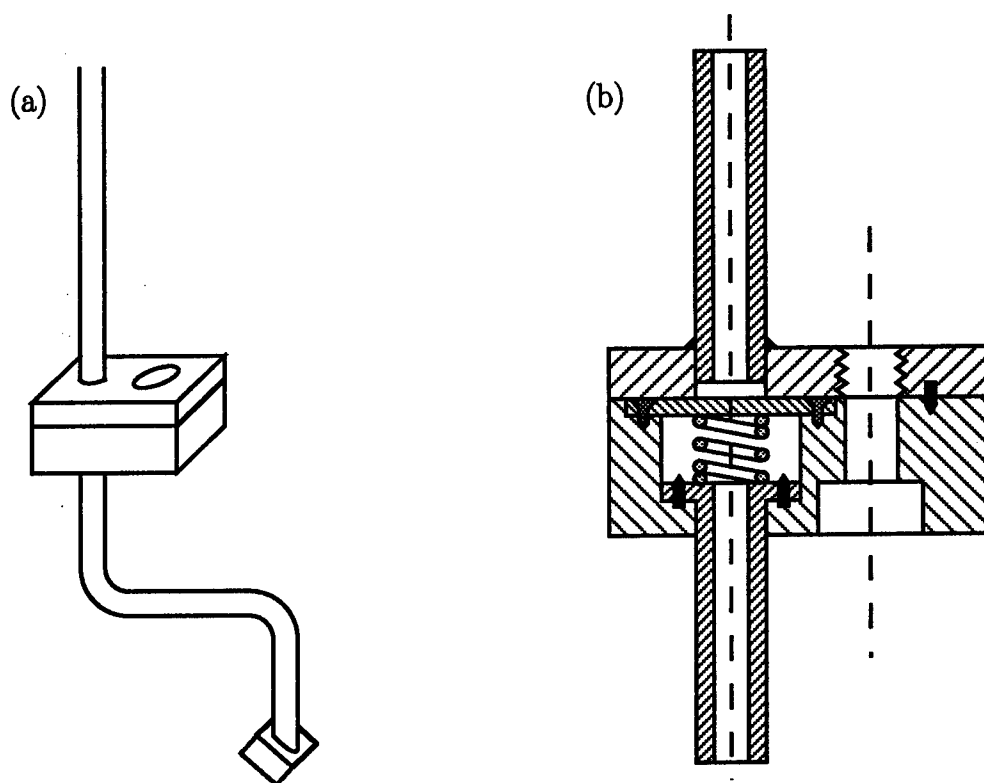
Figure 3.7. Mirror probe detail. (a) Probe (b) Mechanism section detail.

(U,V) Position

TOP VIEW

z

x

u$_{meas}$

+41 MHz

unshifted

SIDE VIEW

y

z

v$_{meas}$

unshifted

+40 MHz

(V, W) Position

z

x

w$_{meas}$

TOP VIEW

unshifted

+41 MHz

SIDE VIEW

y

x

v$_{meas}$

unshifted

+40 MHz
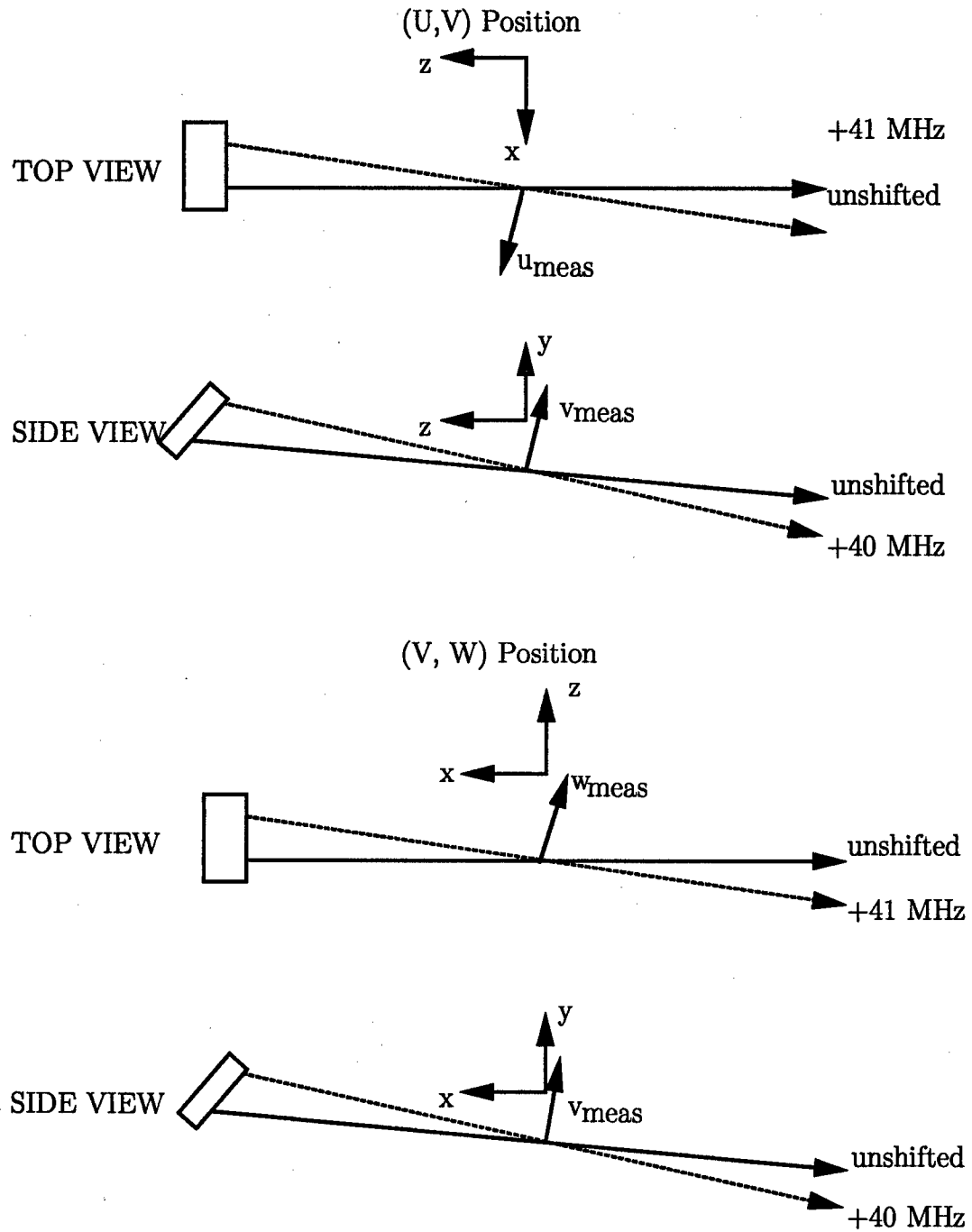
Figure 3.8. Beam orientations for measuring volumes.
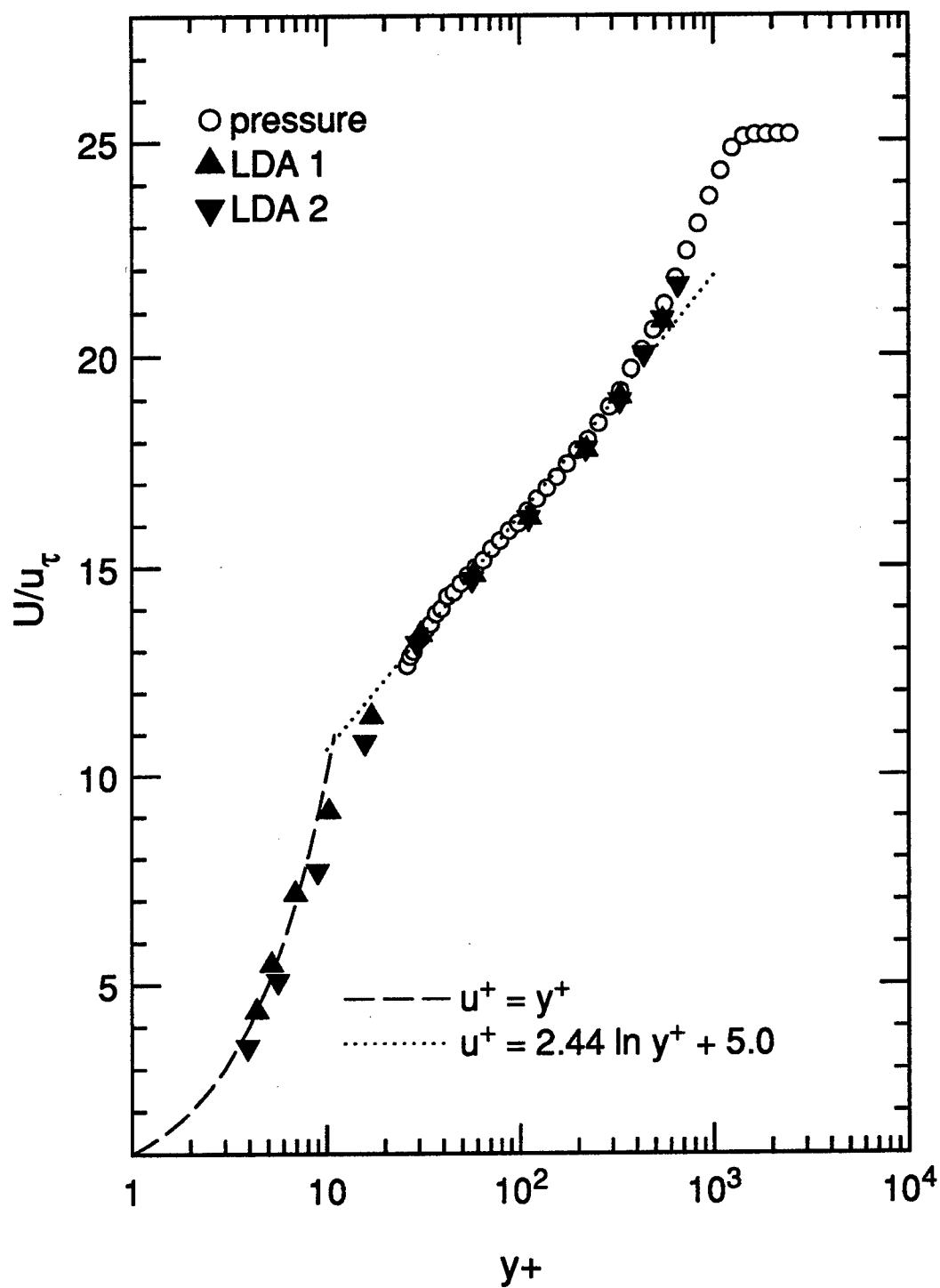
Figure 3.9. Mean velocity (2D): LDA vs pressure, scaled on u_τ.
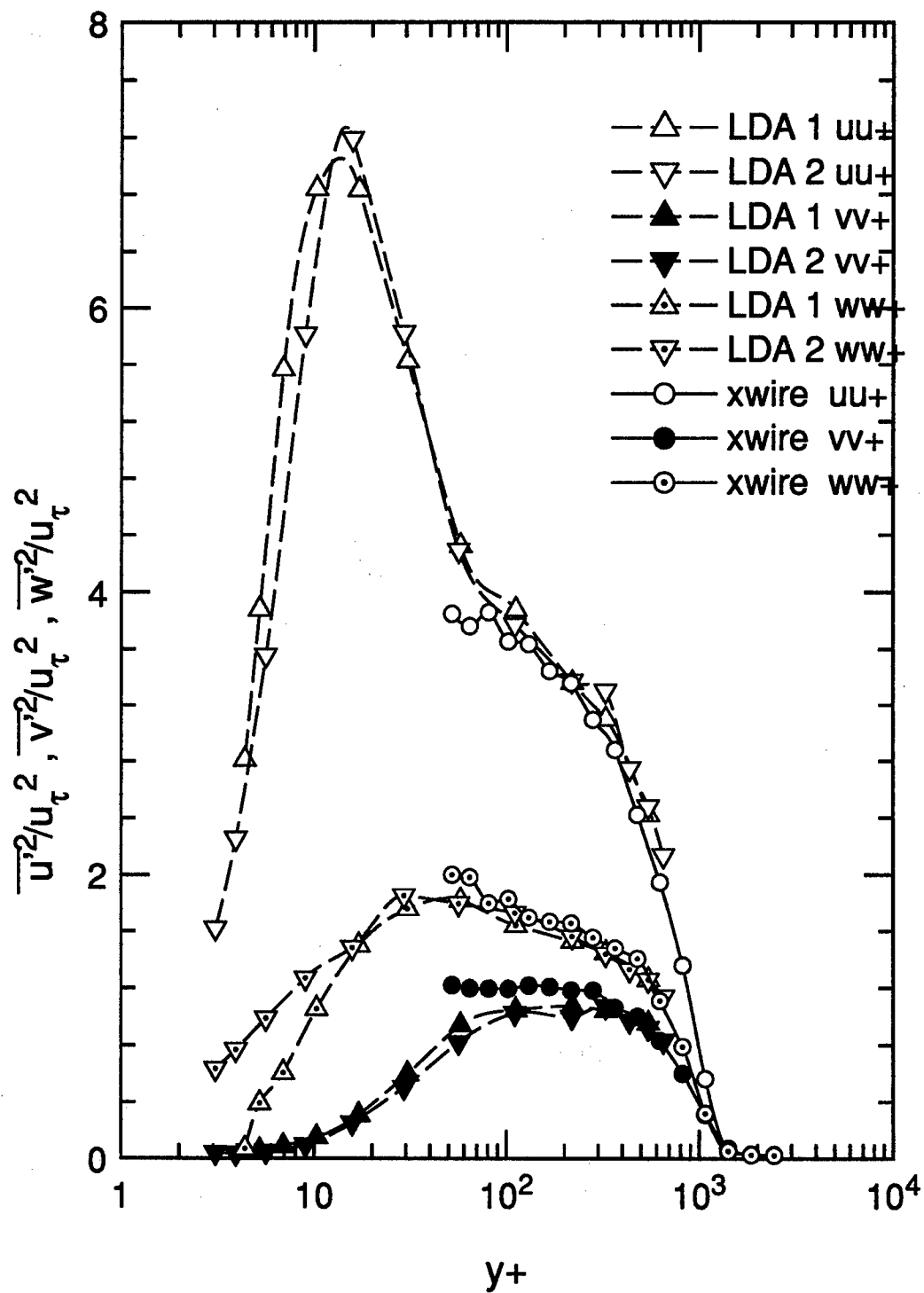
Figure 3.10. Normal stresses (2D): LDA vs crosswire.
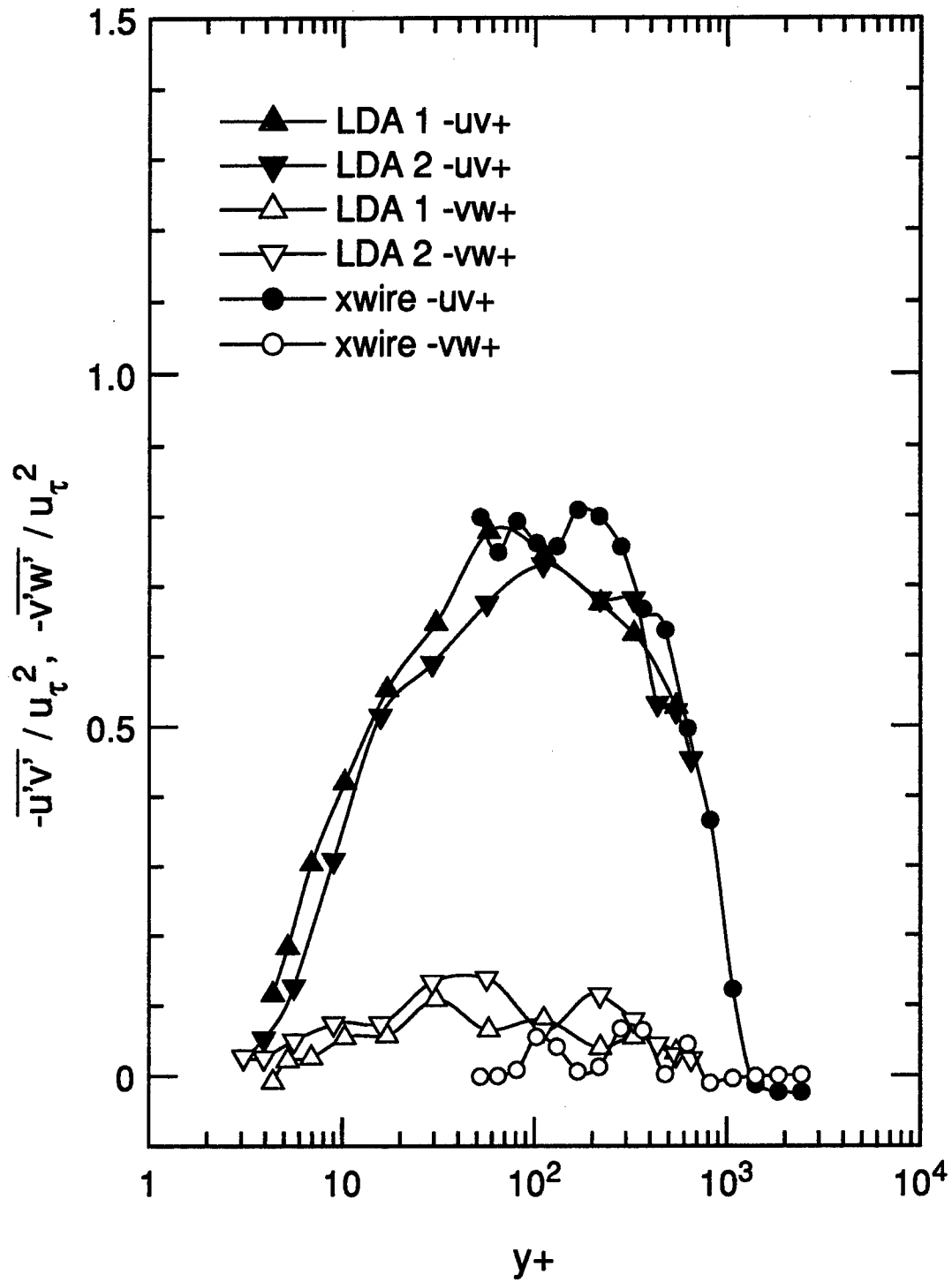
Figure 3.11. Shear stress (2D): LDA vs crosswire.

Chapter 4

Mean Flow Results

This chapter presents the mean velocity field in the three-dimensional turbulent boundary layer. We acquired profiles at several distinct locations in the boundary layer, and profile locations referred to in this chapter are indicated in figure 2.5 and in table 4.1 below. Profiles of mean velocity were acquired using the three-hole probe, the crosswire probe, and the LDA. We use the three-hole pressure probe data and the static pressure distribution to determine the global features of the boundary layer, then use the LDA data to describe the near-wall behavior. Most of the data are presented in the tunnel coordinate system, aligned with the upstream boundary layer.

$x' \setminus z$	0	-3.5
0	A	
7	C	
10.5	D	DD
14	E	EE
17.5	F	FF
21	G	GG
26.5	H	

Table 4.1. Profile location labels (dimensions in inches).

4.1 Static pressure field

The static pressure distribution is represented in terms of the pressure coefficient in figure 4.1.

$$C_p = \frac{p - p_{\text{ref}}}{\frac{1}{2}\rho U_{\text{ref}}^2},\qquad(4.1)$$

where p_{ref} and U_{ref} are the static pressure and freestream velocity at $(x', z) = (0, 0)$. The data are plotted along lines of constant z with the two lines selected for detailed study ($z = 0$ and $z = -3.5$ in) highlighted. In this coordinate system, $z = 0$ is the tunnel centerline and the wedge is on the $-z$ side of the tunnel. The leading edge of the wedge is at $x' = 17$ in. The pressure rises approaching the wedge for negative values of z. Along the centerline, the pressure is nearly constant until approximately $x' = 17$ before falling off as the area narrows and the flow accelerates past the wedge.

There is a strong spanwise pressure gradient upstream of the wedge, which acts to turn the flow into the angled exit passage. The freestream turning angle (as found using the three-hole probe) is depicted in figure 4.2. In the region where we measure boundary layer profiles, the turning angle varies from 0 to $14.5°$. Along the $z = -3.5$ line, the flow is turned more strongly than along the $z = 0$ line.

Figure 4.3 presents the derivatives of the static pressure in the tunnel coordinate system, normalized by δ_{99} at $(x', z) = (10.5, 0)$. The derivatives were calculated from the C_p data displayed in figure 4.1. We derived a central difference formula for unevenly spaced data, by fitting a parabola through three points:

$$\frac{df}{dx}_{(x=x_i)} = \frac{(x_{i-1} - x_i)^2(f_{i+1} - f_i) - (x_{i+1} - x_i)^2(f_{i-1} - f_i)}{(x_{i-1} - x_i)^2(x_{i+1} - x_i) - (x_{i+1} - x_i)^2(x_{i-1} - x_i)} \tag{4.2}$$

The plot shows that for most of the boundary layer, $\left|\frac{\partial C_p}{\partial z}\right|$ is greater than $\left|\frac{\partial C_p}{\partial x}\right|$, demonstrating that we have accomplished the goal of generating a flow dominated by the spanwise pressure gradient. The streamwise pressure gradient is nearly zero through the fourth measurement station (E) along the centerline and remains small up to the fifth station. The pressure gradient is initially mildly adverse along the $z = -3.5$ line then crosses zero near the wedge tip. The pressure gradient is strongly favorable beyond the wedge tip for both measurement lines.

Figure 4.4 shows the pressure gradients in the coordinate system aligned with the local freestream. The streamwise pressure gradient in this coordinate system, $\frac{\partial C_p}{\partial s}$, is small compared to $\frac{\partial C_p}{\partial n}$, except toward the exit where the pressure gradient is predominantly streamwise.[1] We note that along the $z = -3.5$ line the streamwise pressure gradient is initially adverse, but becomes favorable beginning with station

---

[1] We have defined (s, y, n) coordinates to be right-handed, a rotated version of the (x, y, z) tunnel

FF. Along the $z = 0$ line the streamwise pressure gradient is favorable from station F downstream. At the locations where we acquire pressure profiles, the strongest curvature is at station EE, where $\delta_{99}\frac{\partial C_p}{\partial n} = 0.042$ and $\delta_{99}\frac{\partial C_p}{\partial s} = 0.004$. This is stronger turning than in the experiment of Schwarz and Bradshaw, which had a maximum $\delta_{99}\frac{\partial C_p}{\partial z} \approx -0.032$. The study of Anderson and Eaton had stronger turning and stronger acceleration: their $\delta_{99}\frac{\partial C_p}{\partial z} \approx -0.1$, with $\frac{\partial C_p}{\partial x}$ approaching 80% of $\frac{\partial C_p}{\partial z}$. They cited a non-dimensional turning ratio δ/R which reached as high as 0.055.

4.2 Three-hole probe profiles

Profiles were acquired with the three-hole probe at all eleven stations tabulated in table 4.1. Profiles at $z = 0$ are plotted separately from profiles at $z = -3.5$. The resulting velocity magnitude profiles are featured in figures 4.5 and 4.6, which show that the boundary layer is accelerated only mildly, and show the boundary layer thickness increasing. We see the profiles growing "fuller" in the favorable pressure gradient region, with relatively higher velocities near the wall. The boundary layer skewing is represented in figures 4.7 and 4.8. The turning angle $\gamma - \beta$ is positive, indicating that the flow near the wall is rotated at a greater angle than the freestream, as should be expected. At the farthest downstream stations (H and GG), the skewing through the boundary layer is as much as 24 degrees. It is interesting to note that the turning angle actually decreases approaching the wall at these two measurement stations. This is related to the rapid reduction in the cross stream pressure gradient.

We align local axes with the freestream and break the velocity into local streamwise and spanwise components, U_s and U_n:

$$U_s = U\cos\beta + W\sin\beta \tag{4.3}$$

$$U_n = W\cos\beta - U\sin\beta. \tag{4.4}$$

The streamwise component is represented in figures 4.9 and 4.10. Figures 4.11

---

coordinates. This makes n point inward toward the center of curvature, which is not consistent with the usual casting of the Euler's equation in streamline coordinates.

and 4.12 show the spanwise component, which is seen to reach a maximum at increasingly large y values. The maximum spanwise velocity is as much as 28% of the freestream velocity. We also represent the mean velocities using a "hodograph", seen in figures 4.13 and 4.14. This plot shows the spanwise component of velocity as a function of the streamwise component. The hodograph accentuates the near-wall region's absence in the three-hole probe data. Figures 4.15 and 4.16 compare the outer part of the boundary layer to the angles predicted by the inviscid Squire-Winter-Hawthorne (SWH) theory (see, for example, Squire and Winter (1951)), which implies that for small freestream turning angles, the slope of the outer edge of the hodograph is 2β:

$$\frac{U_n}{U_e} = 2\beta \left(1 - \frac{U_s}{U_e}\right) \tag{4.5}$$

The data for the upstream stations (A – D) follow reasonably straight lines although there is small disagreement between the measured $\frac{U_n}{U_s}$ and the $\frac{U_n}{U_s}$ implied by SWH. Further downstream, the data exhibit some curvature. This curvature is an effect of the streamwise pressure gradient, which is not accounted for by SWH.

There has been considerable debate as to whether it is appropriate to expect a "law of the wall" for three-dimensional boundary layers. Figures 4.17 and 4.18 are a relatively unbiased representation of the fit to the law of the wall. To calculate the friction velocity, Q_τ, we assume that the law of the wall holds for the velocity magnitude:

$$Q/Q_\tau = \frac{1}{\kappa} ln(yQ_\tau/\nu) + B \tag{4.6}$$

We use the values generally accepted for two-dimensional boundary layers, $\kappa = .41$ and $B = 5.0$. Our analysis program iterates to find a region between $y^+ = 40$ and $y^+ = 150$ where the value of Q_τ found from the law of the wall is constant. The profiles are shown against equation 4.6. All the profiles tend to rise above the line slightly at first, then dip below it. They then rise well above the line to form a "wake" region. The upstream boundary layer (station A) agrees qualitatively with the mean flow reported by Murlis, Tsai and Bradshaw (1982) for a two-dimensional boundary layer at similar Re_θ. The furthest downstream profiles are severely distorted. They may be contaminated by flow that has swept across from near the wedge-floor corner. We use the friction velocity to find the wall skin friction and thus the skin friction

coefficient, C_f:

$$u_\tau{}^2 = \frac{\tau_0}{\rho} = \frac{C_f U_e^2}{2} \tag{4.7}$$

The skin friction coefficient is the quantity chosen for non-dimensionalizing other profiles at the same location. Figure 4.19 shows the skin friction determined in this way, compared to the analytically predicted value for two-dimensional boundary layers (Kays and Crawford (1980) equation 10-20),

$$C_f/2 = 0.0125 Re_\theta{}^{-0.25}. \tag{4.8}$$

The good agreement between the measured and predicted C_f at small turning angles indicates that we may expect some two-dimensional correlations to work in this region of three-dimensionality. The points farther downstream have skin friction coefficients greater than the two-dimensional correlation, indicating the favorable streamwise pressure gradient's influence on the mean velocity profiles.

The boundary layer integral parameters from the pressure data are tabulated in table 4.2. The displacement thickness is based on the streamwise velocity U_s, since there is no true physical analogy for three-dimensional boundary layers for a displacement thickness based on Q. The displacement thickness, δ^*, is also known in three-dimensional turbulent boundary layer literature as δ_1^*, where 1 denotes the mass flow in the streamwise direction. Similarly, for the momentum thickness θ we choose the streamwise momentum, and in other works this quantity is sometimes called θ_{11}.

$$\delta^* = \int_0^\infty \left(1 - \frac{U_s}{U_e}\right) dy \tag{4.9}$$

$$\theta = \int_0^\infty \frac{U_s}{U_e} \left(1 - \frac{U_s}{U_e}\right) dy \tag{4.10}$$

To aid in integration, we first fit a natural cubic spline to the velocity data, then integrate that spline. The ratio between the displacement thickness and the momentum thickness is called the boundary layer shape factor, H.

$$H = \frac{\delta^*}{\theta} \tag{4.11}$$

	Profile										
	A	C	D	E	F	G	H	DD	EE	FF	GG
x' [in]	0.0	7.0	10.5	14.0	17.5	21.0	26.5	10.5	14.0	17.5	21.0
z [in]	0.0	0.0	0.0	0.0	0.0	0.0	0.0	-3.5	-3.5	-3.5	-3.5
β [deg]	0.14	1.81	3.52	5.63	7.90	10.57	14.36	3.98	6.86	10.40	14.16
Q_e [m/s]	12.43	12.40	12.40	12.37	12.35	12.47	13.08	12.23	12.14	12.13	12.34
δ_{99} [mm]	36.3	38.5	41.6	43.1	45.2	49.5	56.5	38.9	41.9	44.7	49.3
δ^* [mm]	5.78	6.24	6.74	7.13	7.60	8.51	9.52	6.43	7.00	7.78	8.90
θ [mm]	4.22	4.56	4.90	5.19	5.53	6.19	7.04	4.67	5.06	5.61	6.19
H	1.37	1.37	1.38	1.38	1.38	1.37	1.35	1.38	1.38	1.39	1.44
Re_{δ^*}	4692	5058	5458	5766	6136	6931	8139	5160	5570	6186	7200
Re_θ	3431	3693	3968	4192	4460	5047	6016	3746	4031	4457	5009
Q_τ [m/s]	0.506	0.499	0.491	0.489	0.488	0.500	0.558	0.490	0.482	0.484	0.504
$C_f/2$ $\times 10^{-3}$	1.66	1.62	1.57	1.57	1.56	1.61	1.82	1.60	1.58	1.59	1.67

Table 4.2. Boundary layer parameters from pressure data.

4.3 Crosswire and three-hole probe data compared

The hotwire mean velocity magnitude data are compared to the pressure data for two different profiles, in figure 4.20. This figure indicates that the hotwire data agree well, within 0.03 Q/Q_e. There is some discrepancy near the wall, indicating either an error in the distance from the wall of the crosswire (a correction of 0.9 mm would significantly improve the agreement) or overprediction of the velocity magnitude near the wall. The hotwire probe was aligned with the local flow direction previously measured using the three-hole probe. Thus, the flow angle was assumed to be the same, as is common practice.

4.4 The near-wall mean flow: LDA data

Now we describe the inner part of the boundary layer, using the LDA profiles. Profiles were acquired with the LDA at seven stations (D, E, F, G, DD, EE, and FF). We begin by comparing the LDA data to the three-hole data. Figures 4.21 and 4.22 show the streamwise and spanwise velocity profiles at two locations, showing the agreement between the instruments. In Chapter 3 we decribed the LDA fringe calibration method, in which U is matched to the outermost three-hole probe point and W is matched where W is relatively large. This calibration is the cause for the good fit at the edge of the LDA data in figure 4.21 and the good fit near the peak crossflow in figure 4.22. The maximum deviation in the velocity magnitude between LDA data and the pressure probe data is approximately $0.015Q_e$.

The boundary layer skewing is represented in figures 4.23 and 4.24. For the most part, $\gamma - \beta$ increases monotonically toward the wall down to about $y^+ = 20$. Along the $z = 0$ line the angle is approximately constant below $y^+ = 20$ indicating the presence of a near-wall collateral region. At the most downstream location (G) the trend of the angle reverses below $y^+ = 20$ with the angle decreasing toward the wall. The flow angle data show considerable scatter in the one or two points nearest the wall. This is because different LDA setups are used to measure the U and W velocity components. A slight offset in the vertical positioning can result in significant error

in the angle because of the steep velocity gradients near the wall. The angle trends for the profiles along $z = -3.5$ are not as clear. All three profiles show a monotonic increase in the flow angle approaching the wall above $y^+ = 10$. The trend below that point is inconsistent, possibly due to high uncertainty. The furthest downstream profile may be affected by flow sweeping over from the wedge corner.

The hodographs (figures 4.25 and 4.26) show clearly that the LDA has captured the near-wall behavior of the mean flow, with the profiles extending toward the origin. These plots show an approximately triangular shape. The three-hole probe data are plotted alongside the LDA data. These coordinates tend to highlight differences between the two instruments, since errors in U_n are accentuated. There is excellent agreement between the LDA data and the three-hole probe data throughout most of the boundary layer. Near the inner edge of the pressure profiles, agreement is not as good, most likely due to small angle errors in the three-hole probe data as the probe approaches the wall.

Figures 4.27 and 4.28 represent the LDA data in the log-law coordinates. In reducing the data, we determined the wall offset by optimizing the data's fit to $u^+ = y^+$ (as discussed in detail in Chapter 3), so we should not be too surprised by the profiles' collapse in this region.
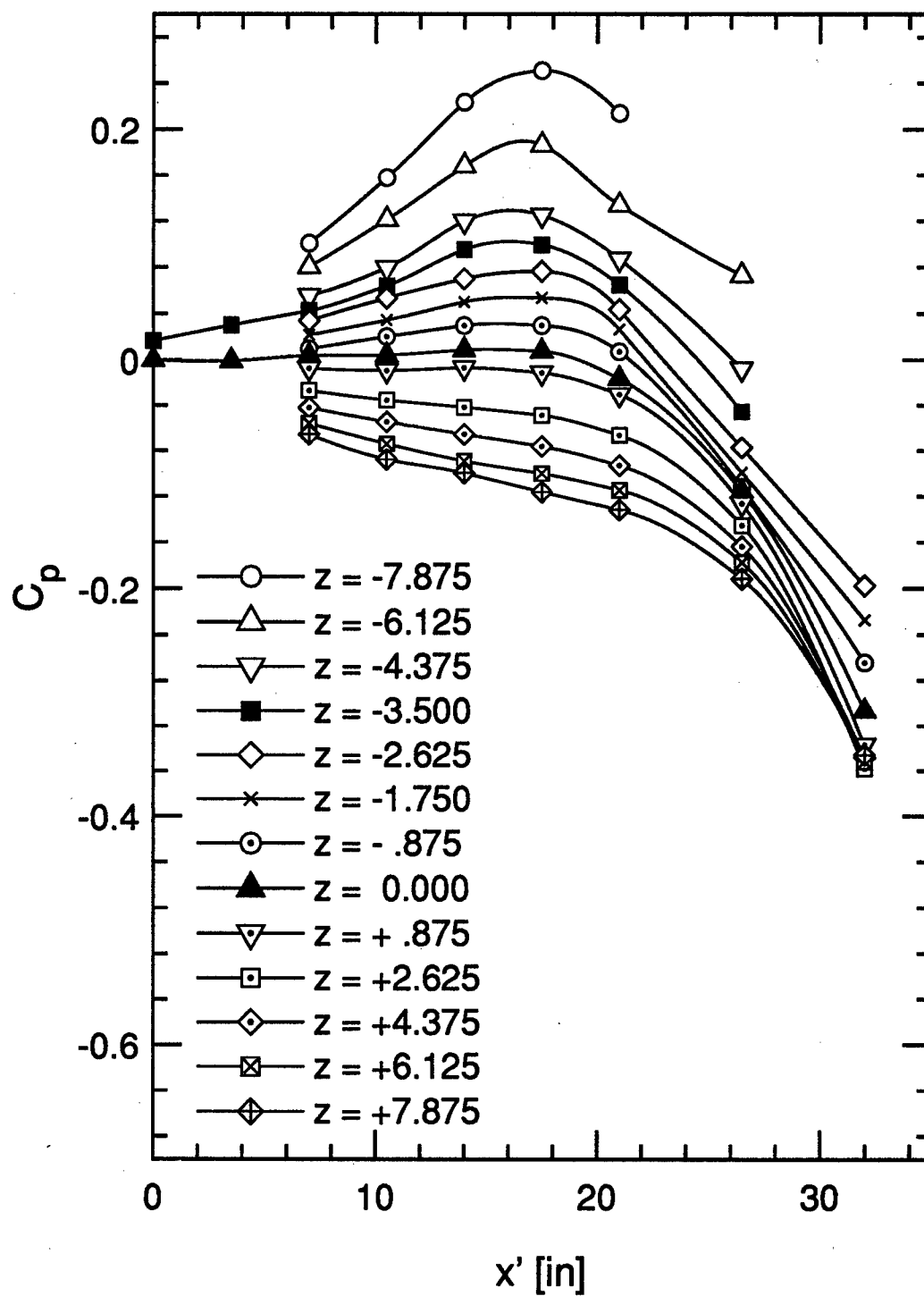
Figure 4.1. Static pressure distribution near the wedge.
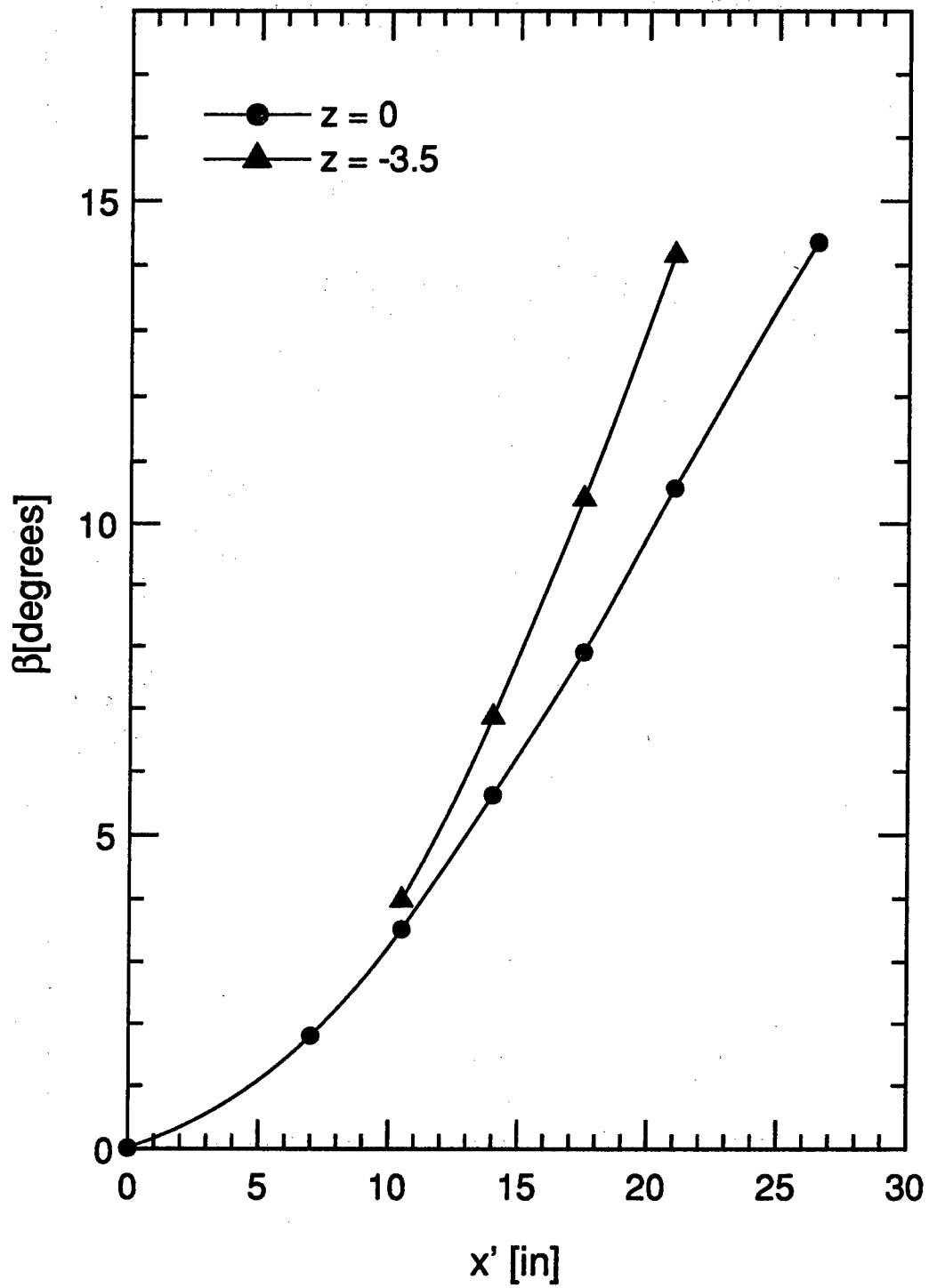
Figure 4.2. Freestream turning angle at all profile locations.
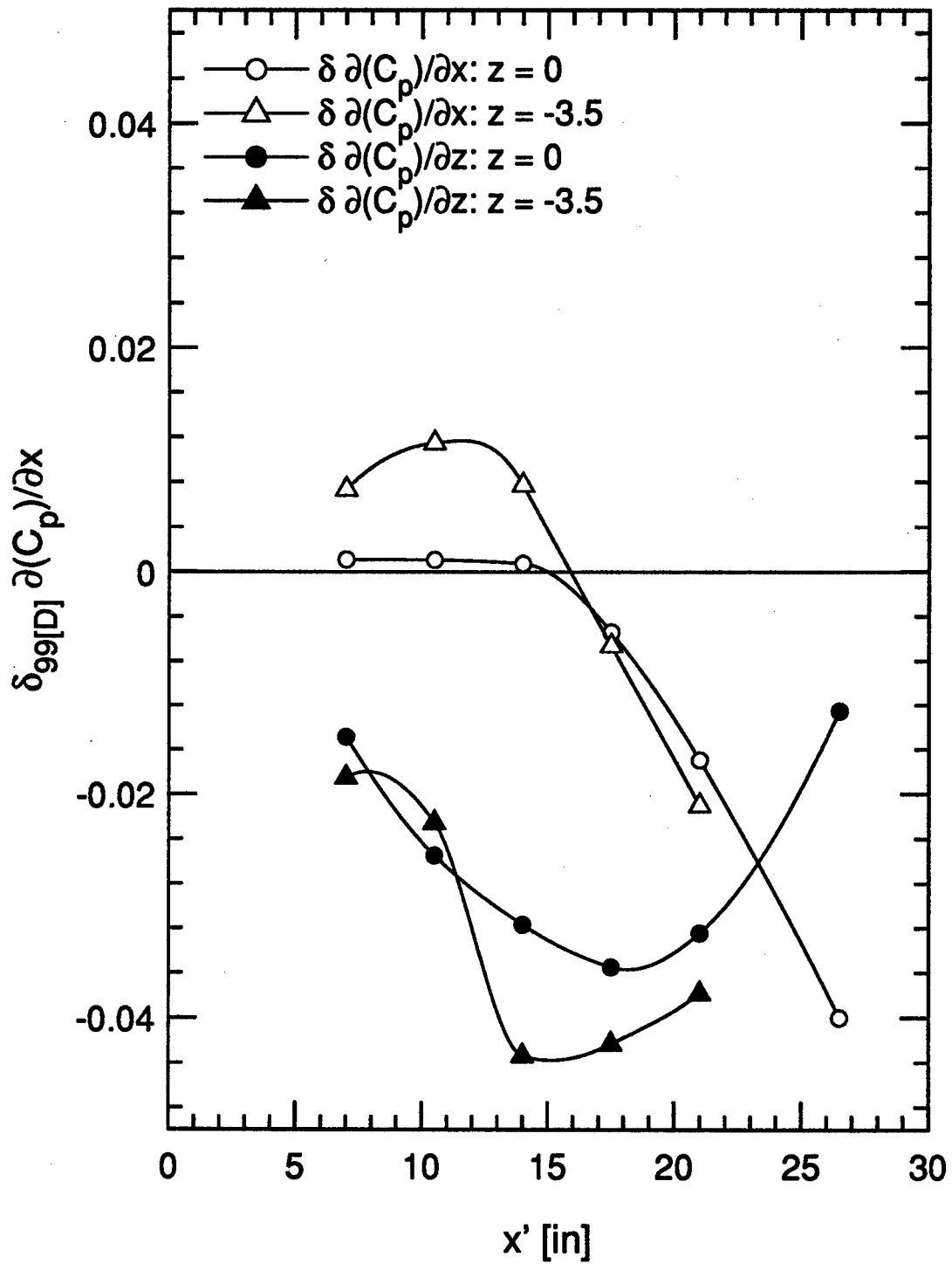
Figure 4.3. Static pressure derivatives with respect to x and z, normalized by δ_{99} at $(x', z) = (10.5, 0)$.
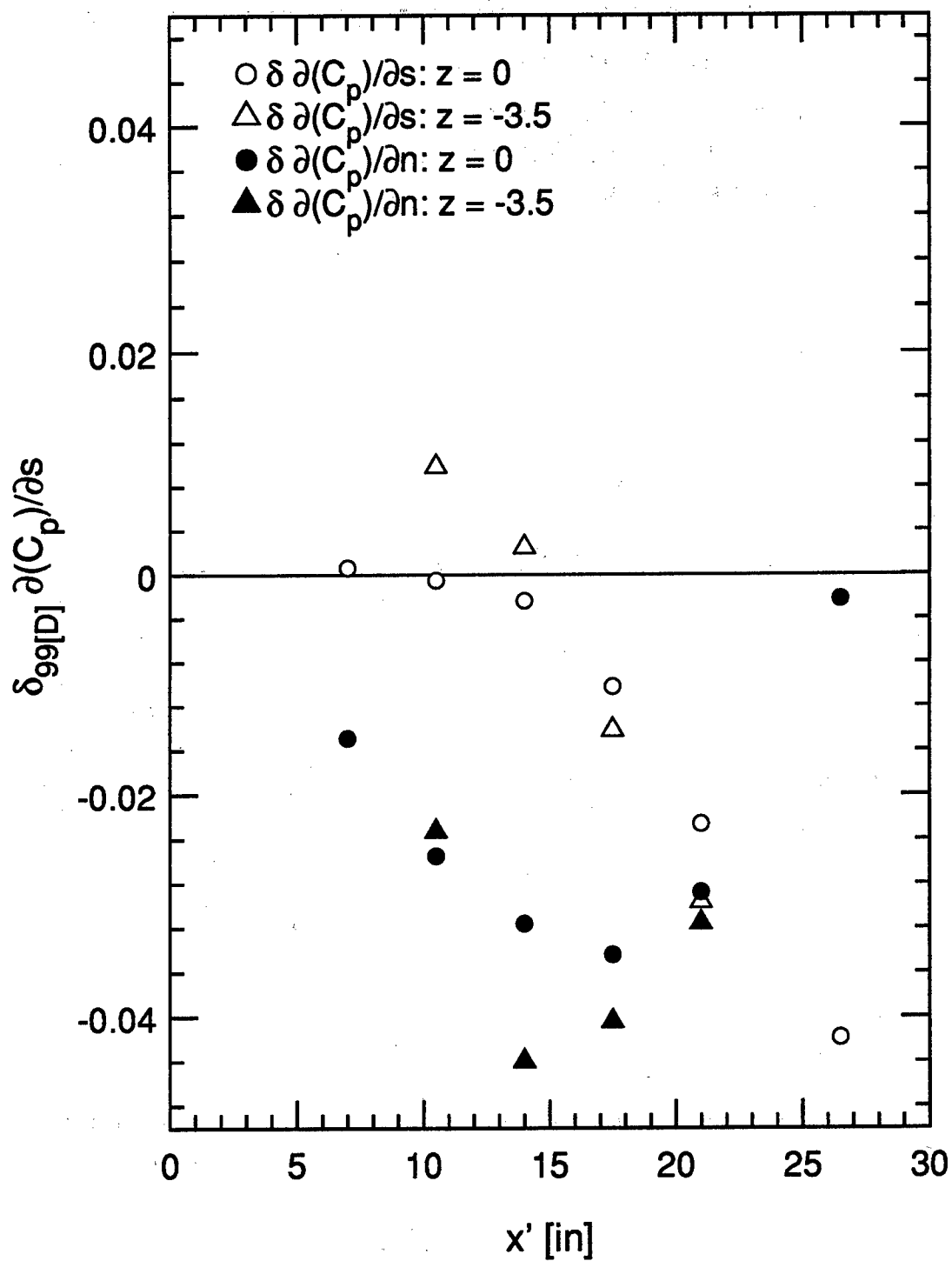
Figure 4.4. Static pressure derivatives with respect to s and n, normalized by δ_{99} at $(x', z) = (10.5, 0)$
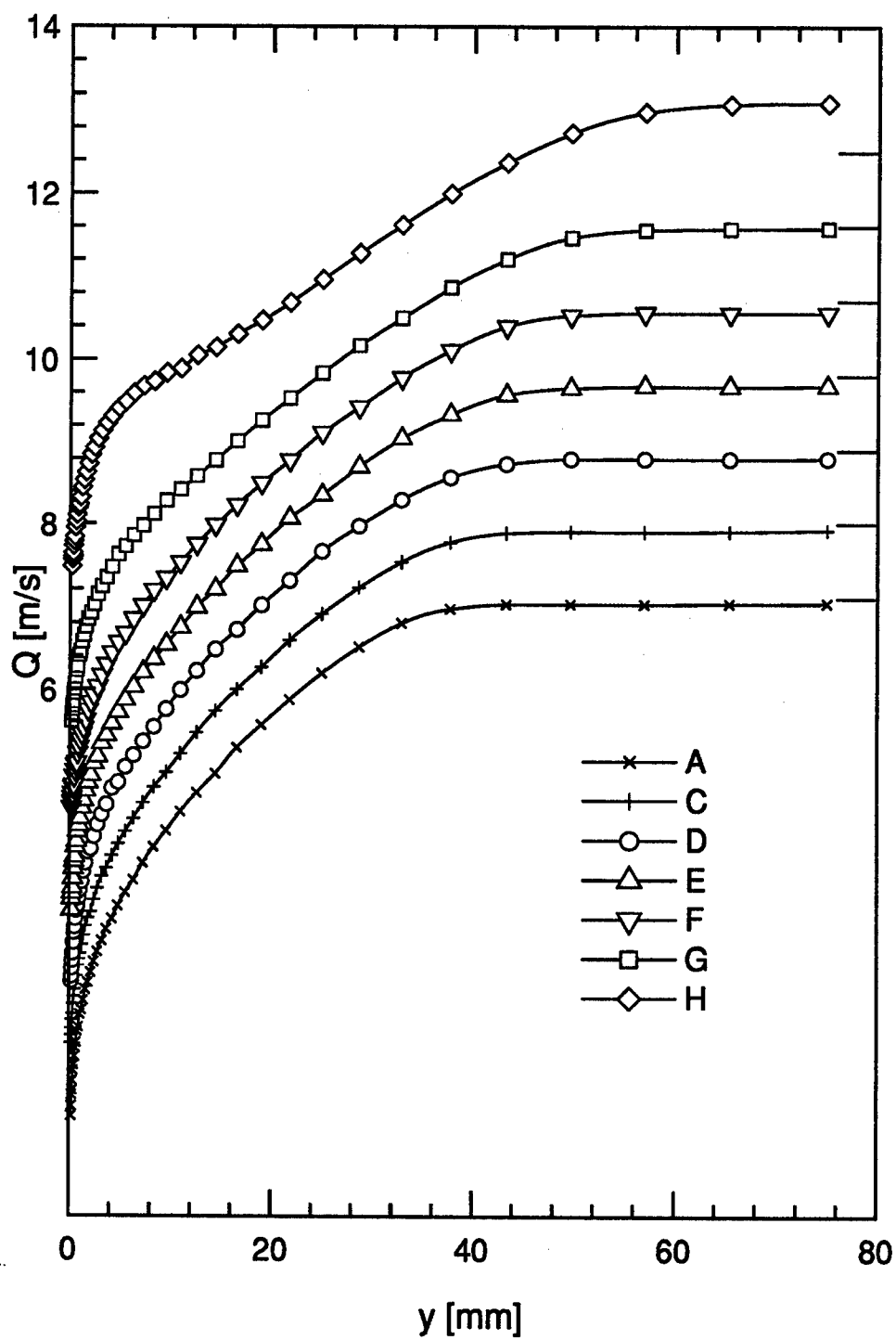
Figure 4.5. Dimensional velocity magnitude. $z = 0$. Staggered axis; ticks on right axis indicate 12.5 m/s.
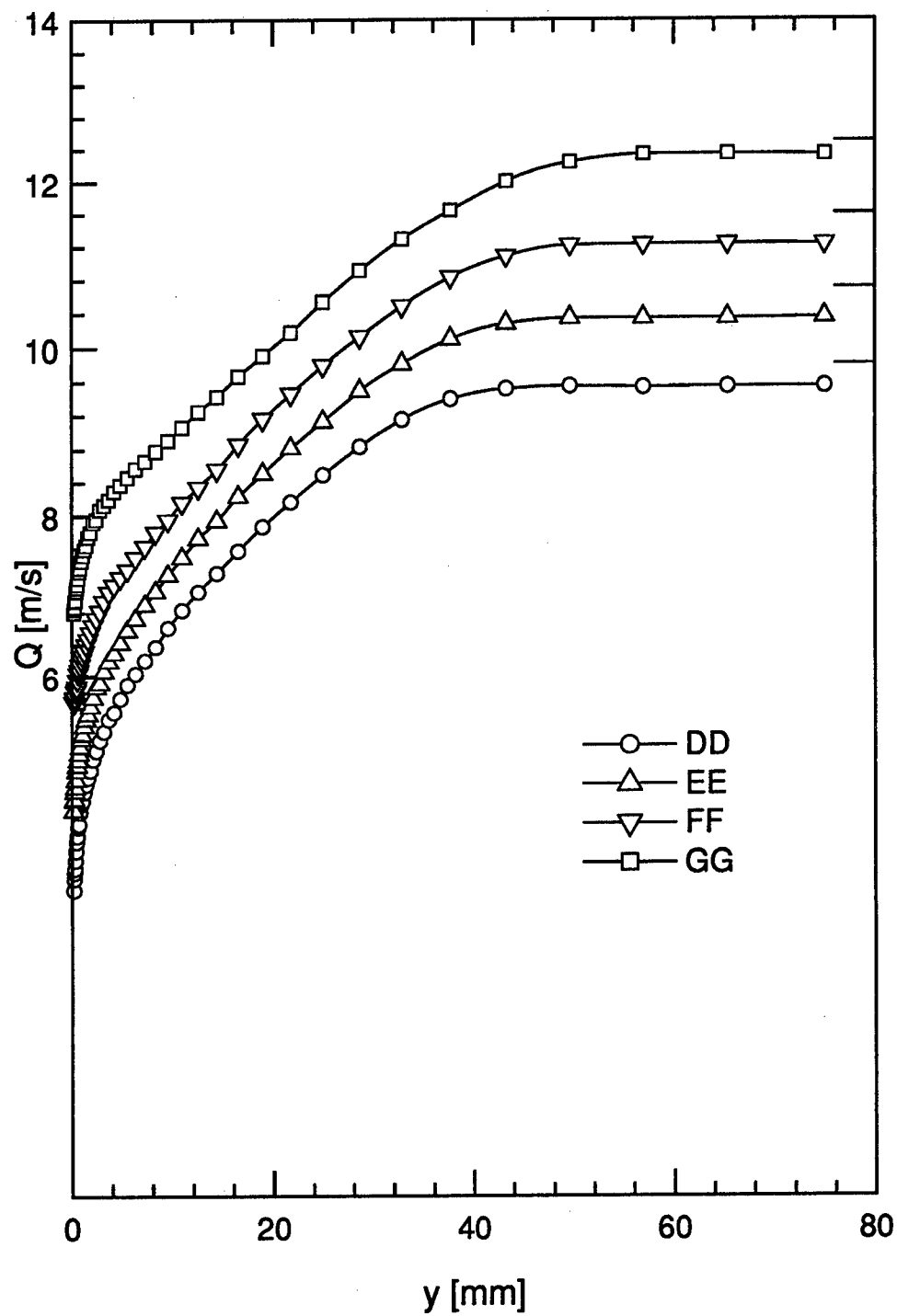
Figure 4.6. Dimensional velocity magnitude. $z = -3.5$. Staggered axis; ticks on right axis indicate 12.5 m/s.
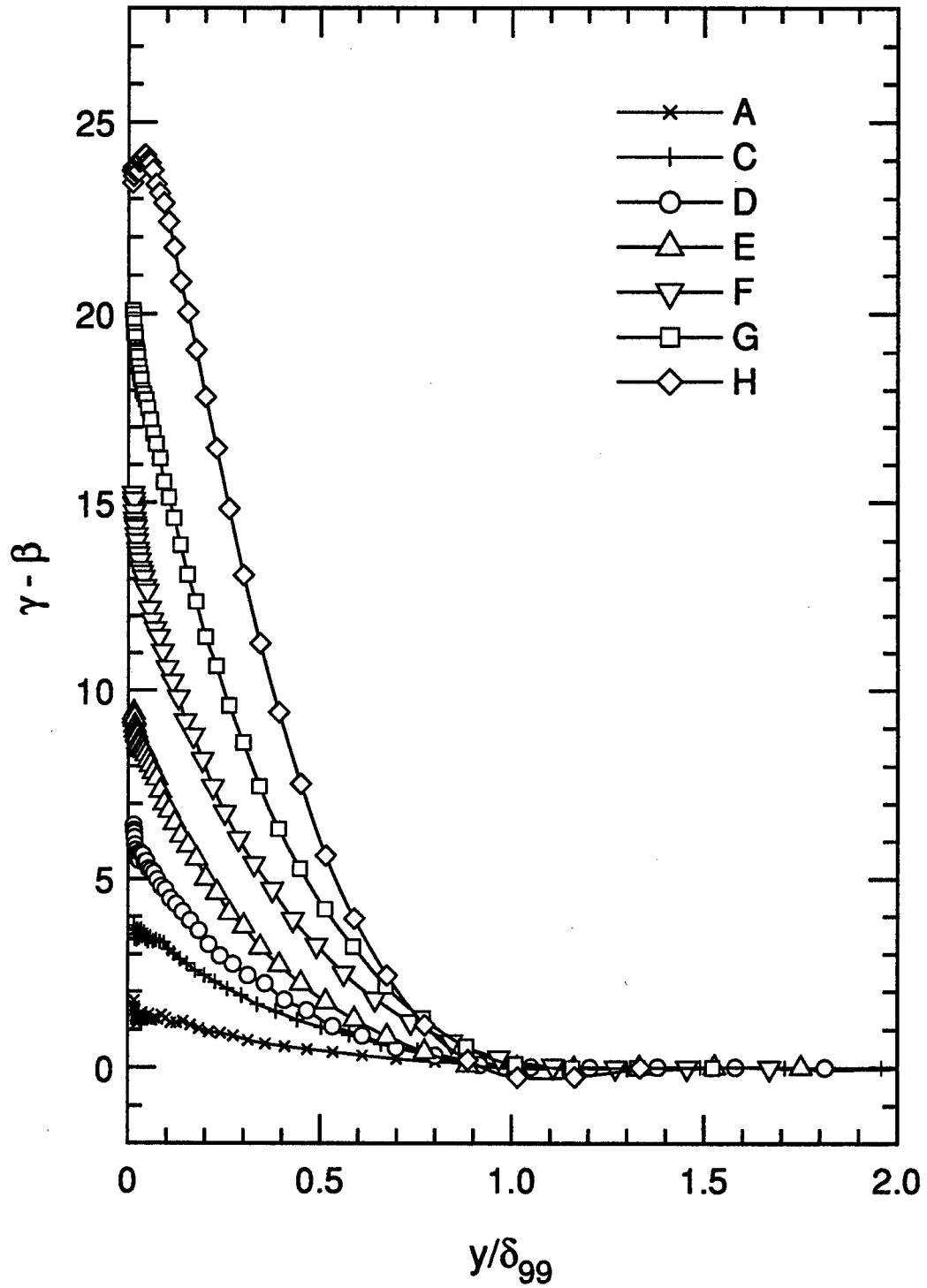
Figure 4.7. Mean velocity angle. $z = 0$.
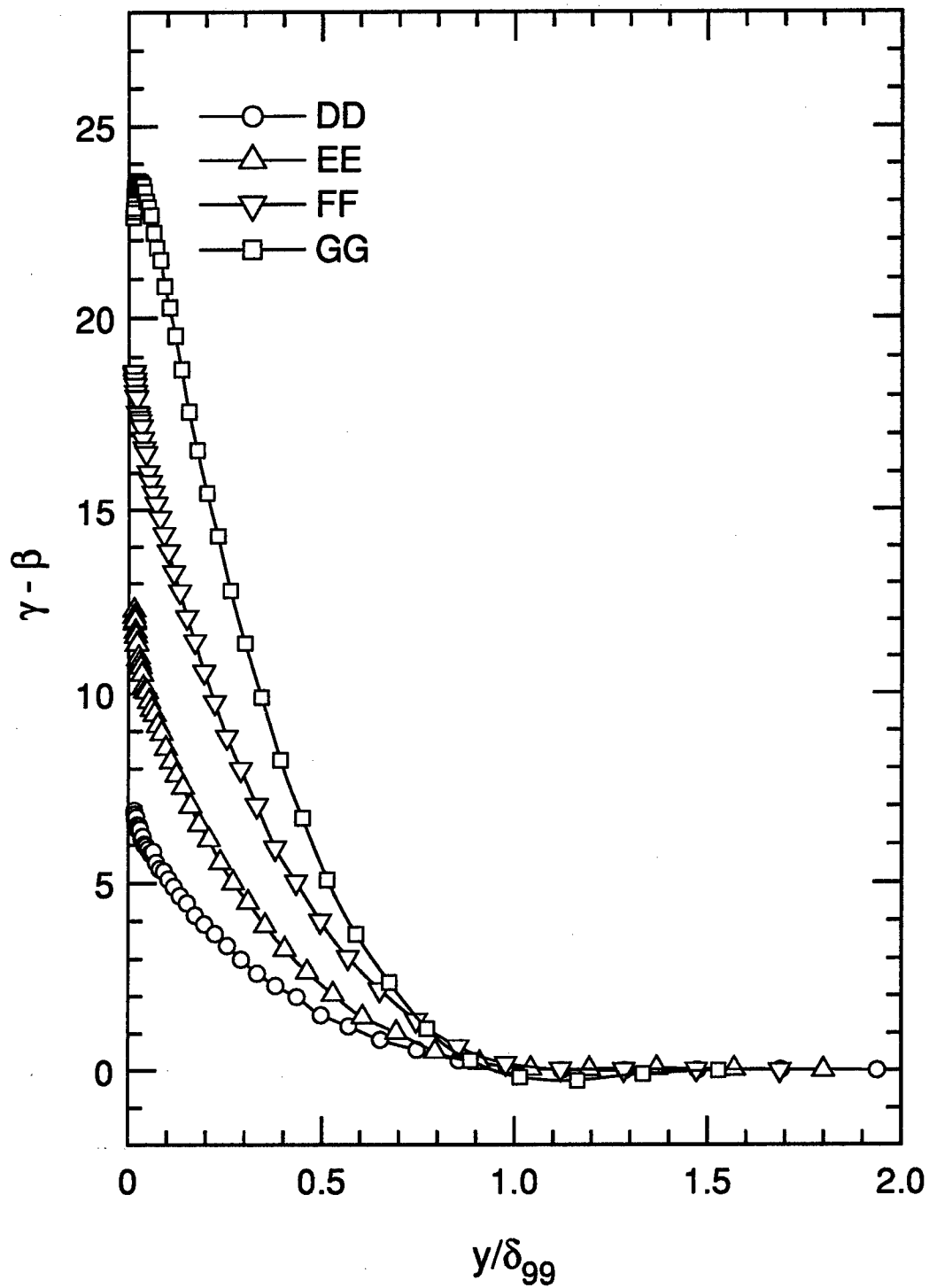
Figure 4.8. Mean velocity angle. $z = -3.5$.
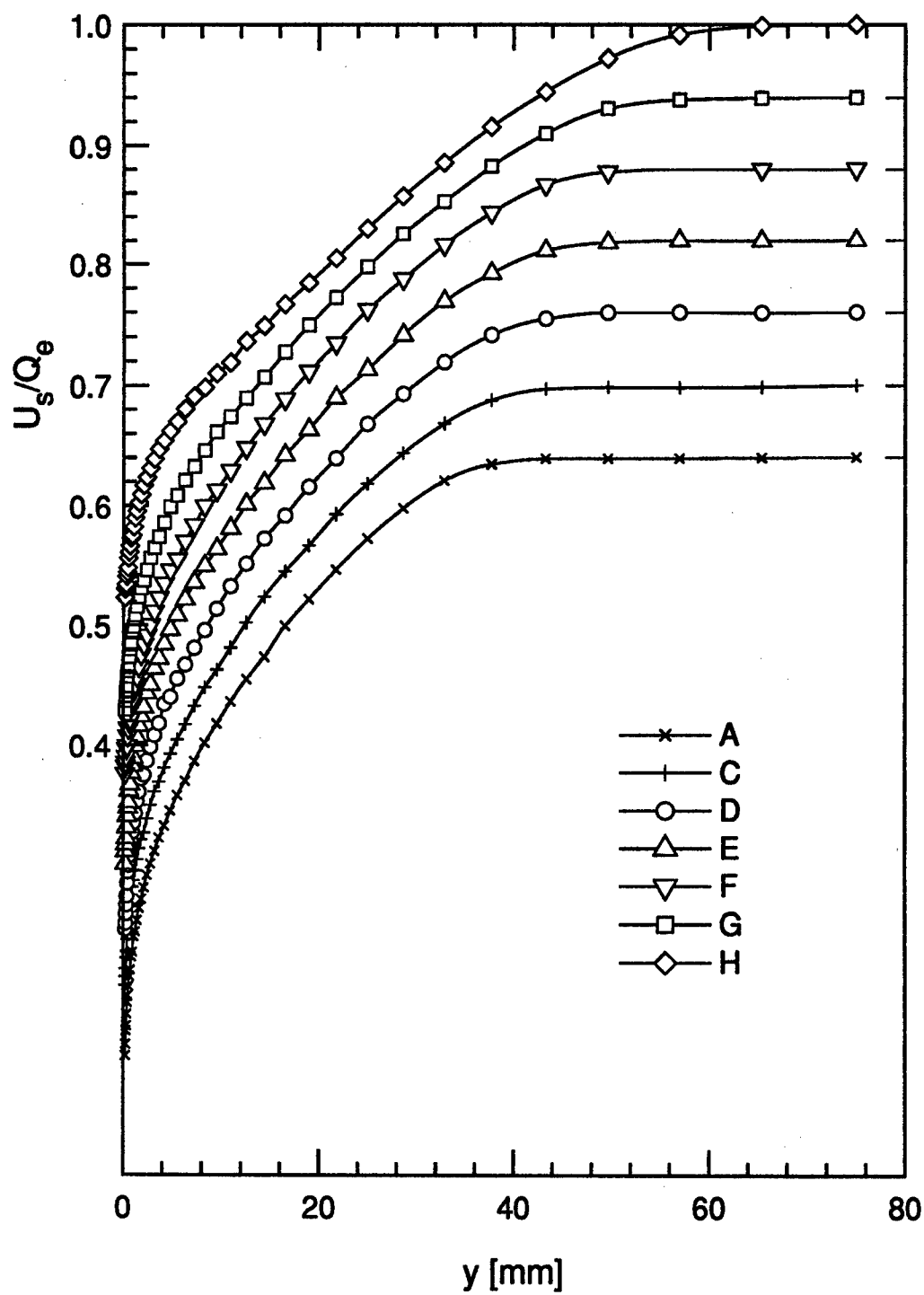
Figure 4.9. Streamwise velocity. $z = 0$. Staggered axis.
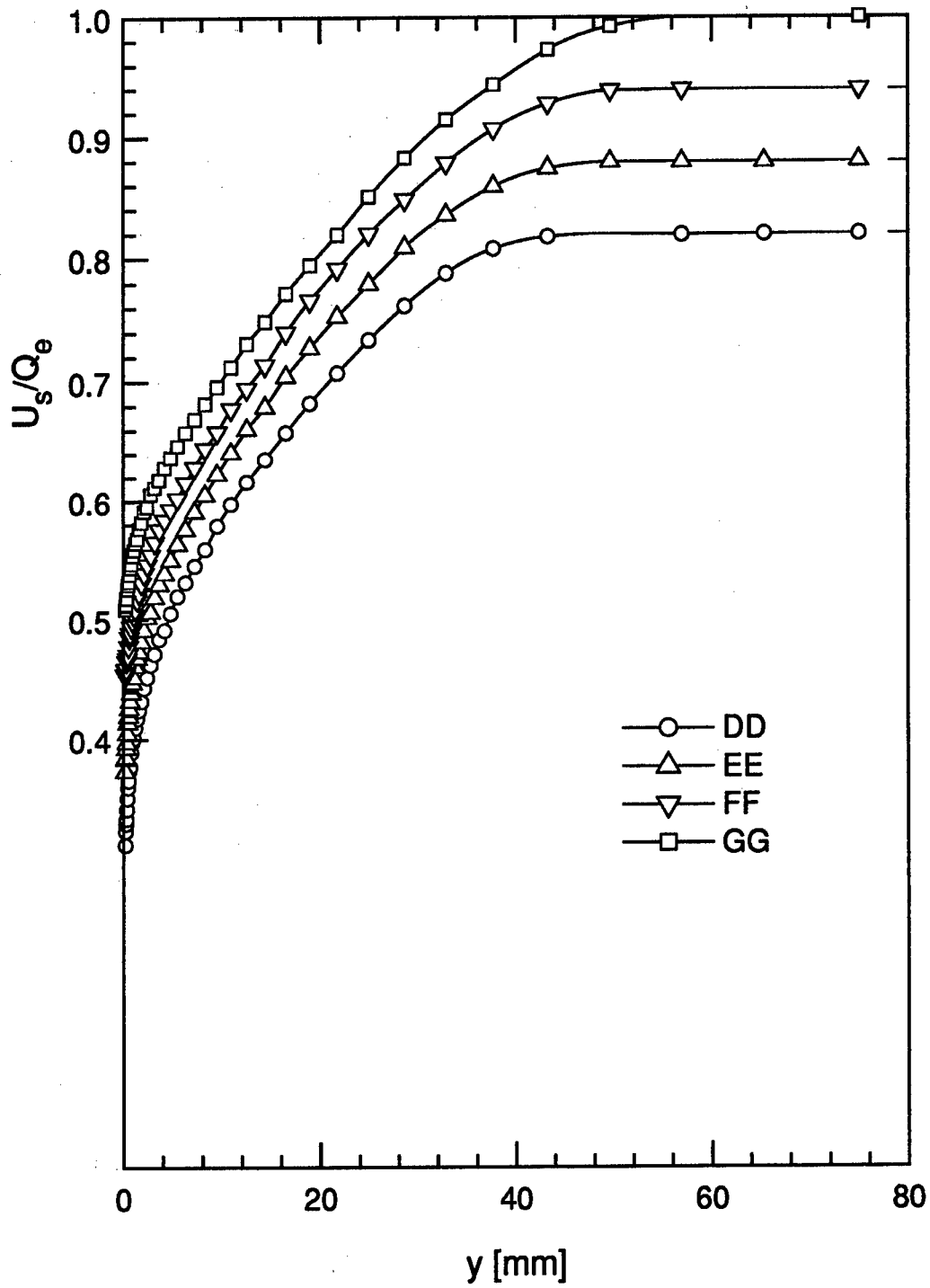
Figure 4.10. Streamwise velocity. $z = -3.5$. Staggered axis.
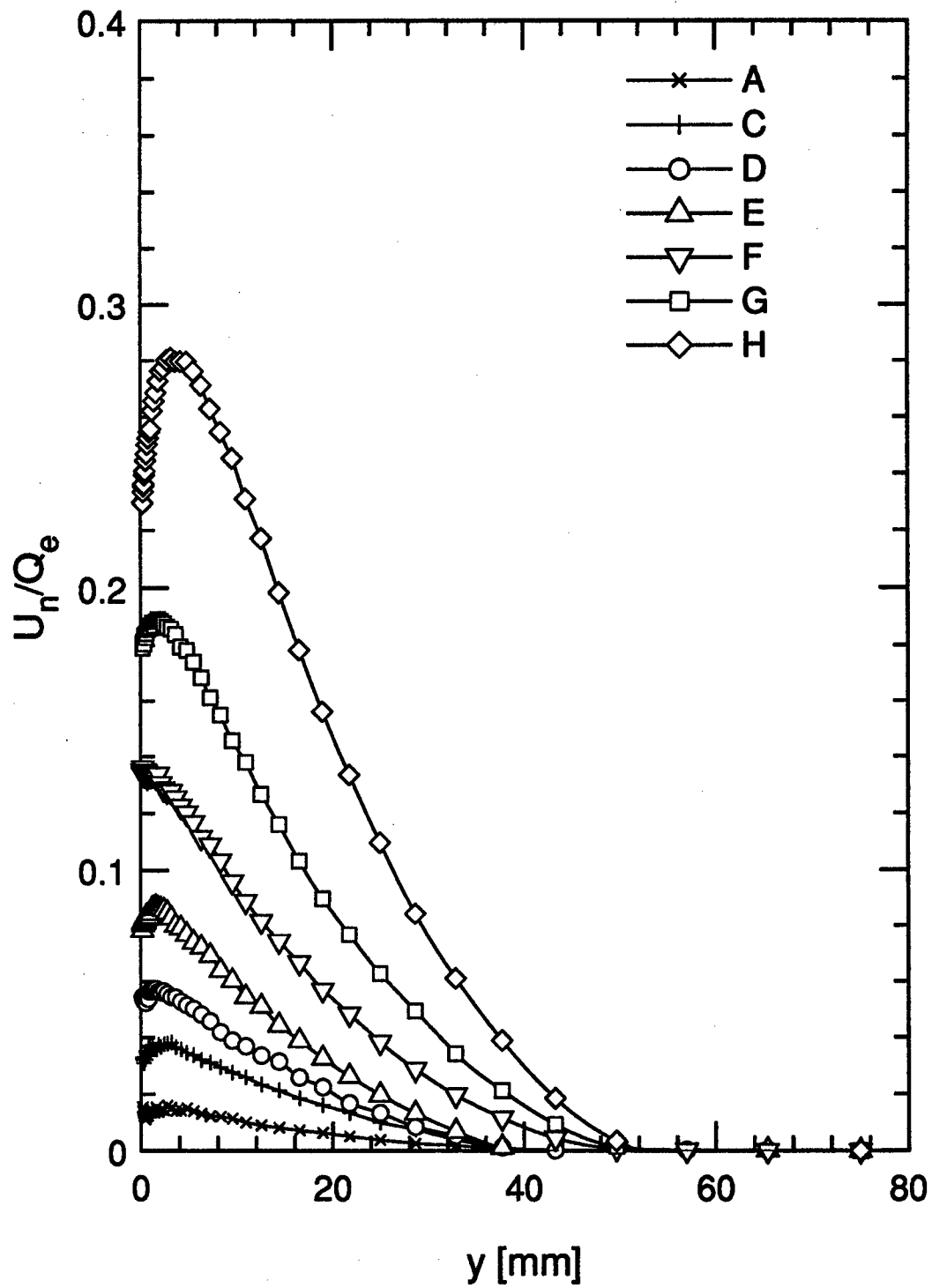
Figure 4.11. Spanwise velocity. $z = 0$.
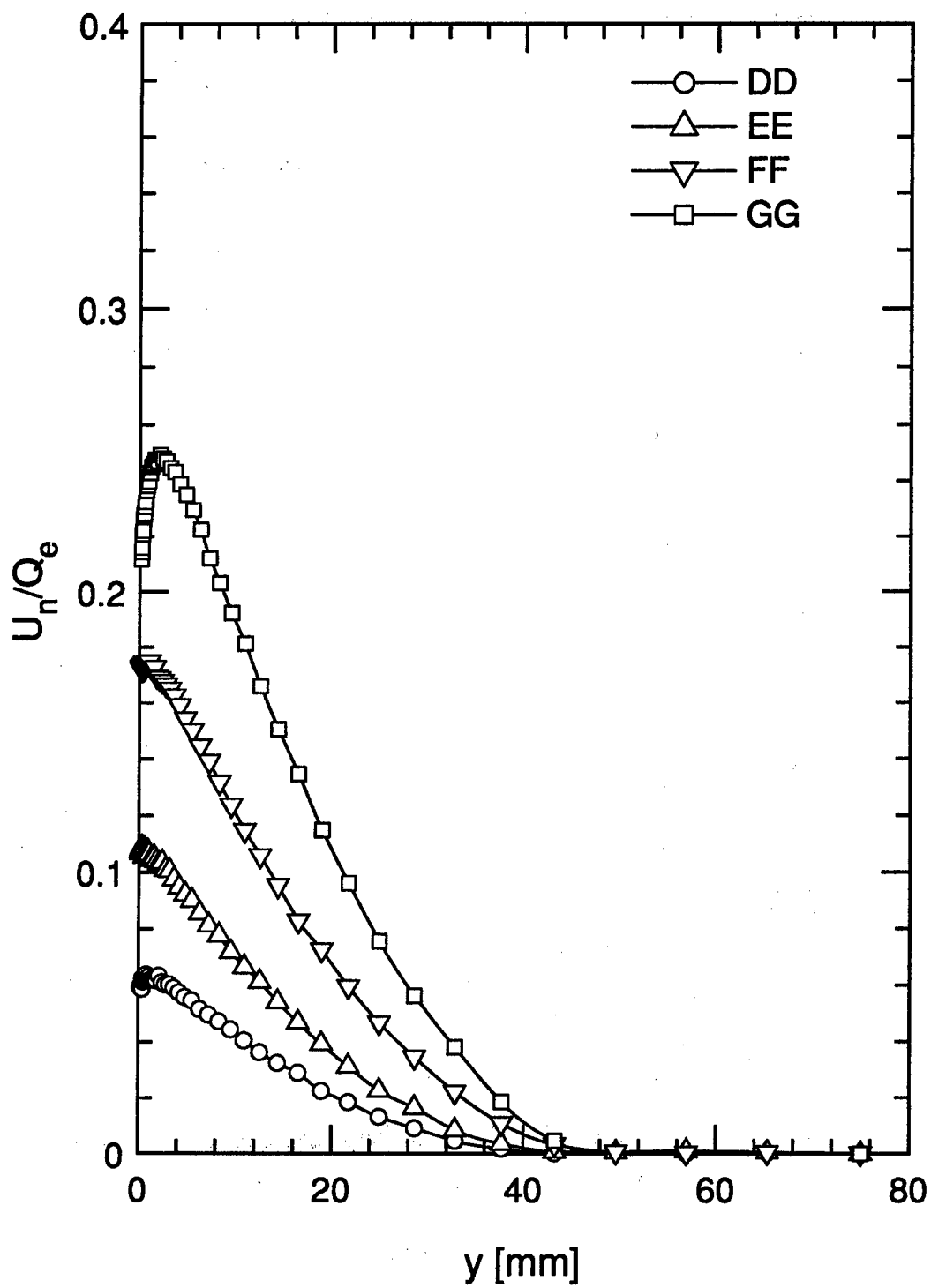
Figure 4.12. Spanwise velocity. $z = -3.5$.
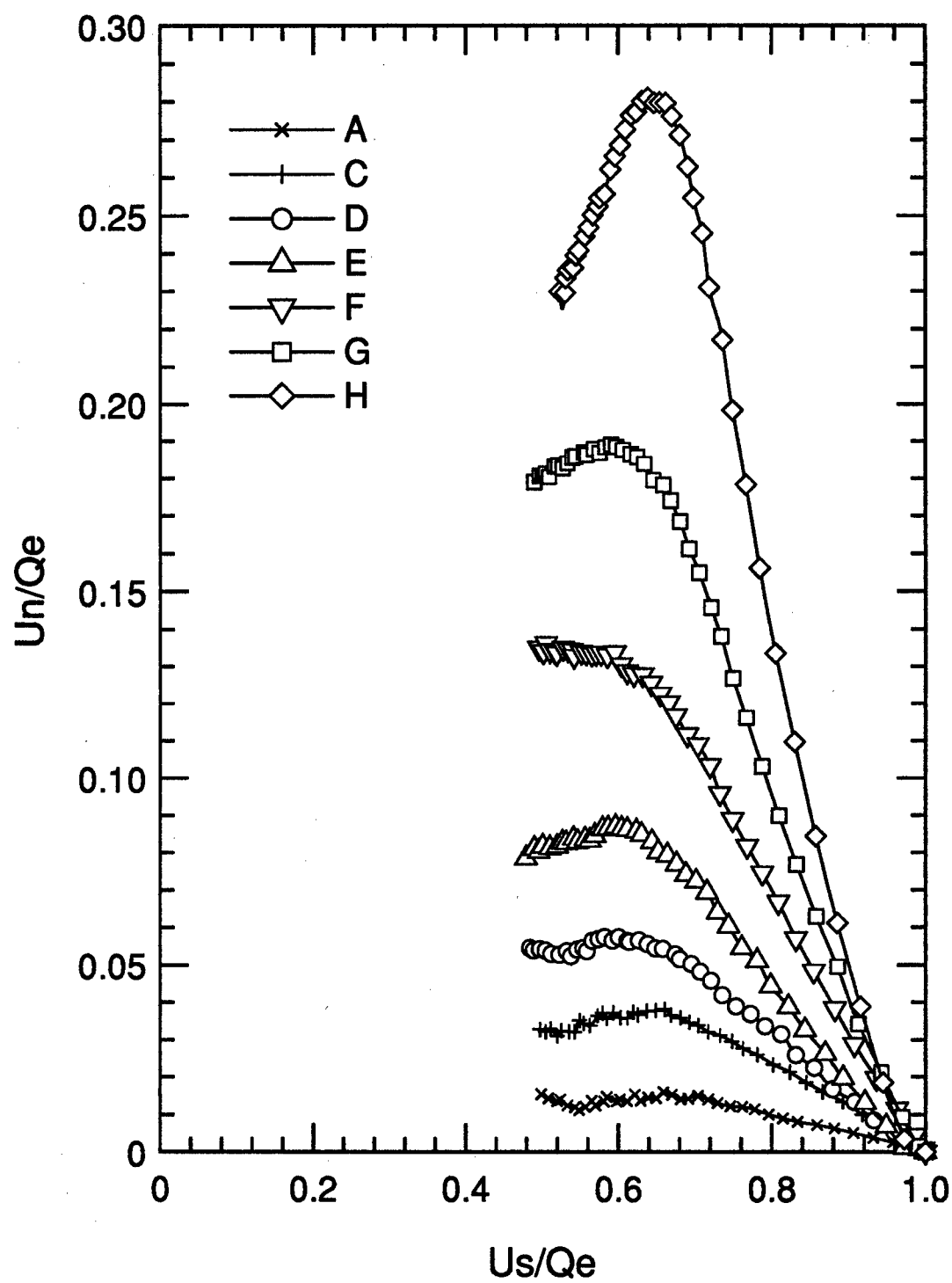
Figure 4.13. Hodograph. $z = 0$.
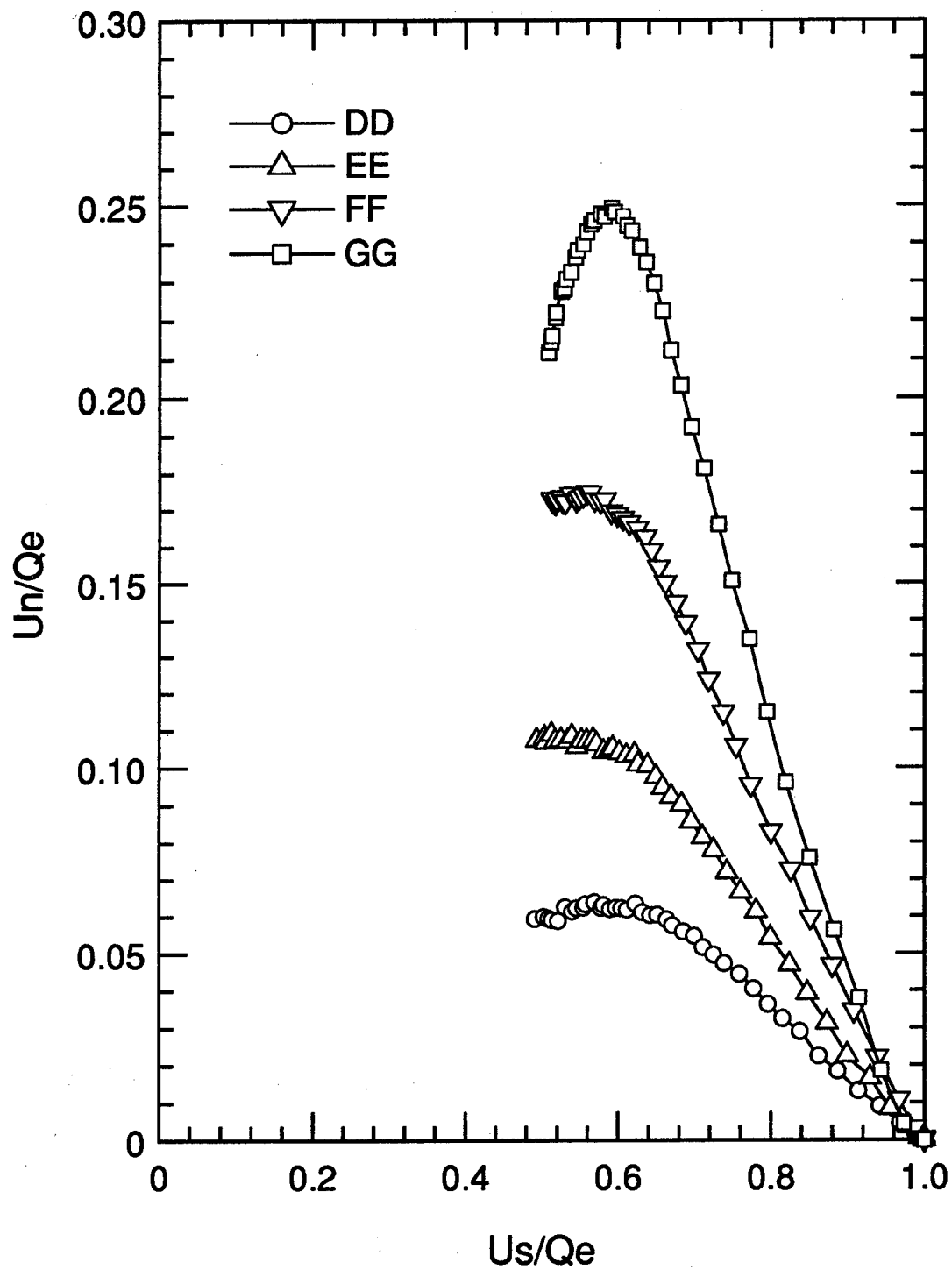
Figure 4.14. Hodograph. $z = -3.5$.
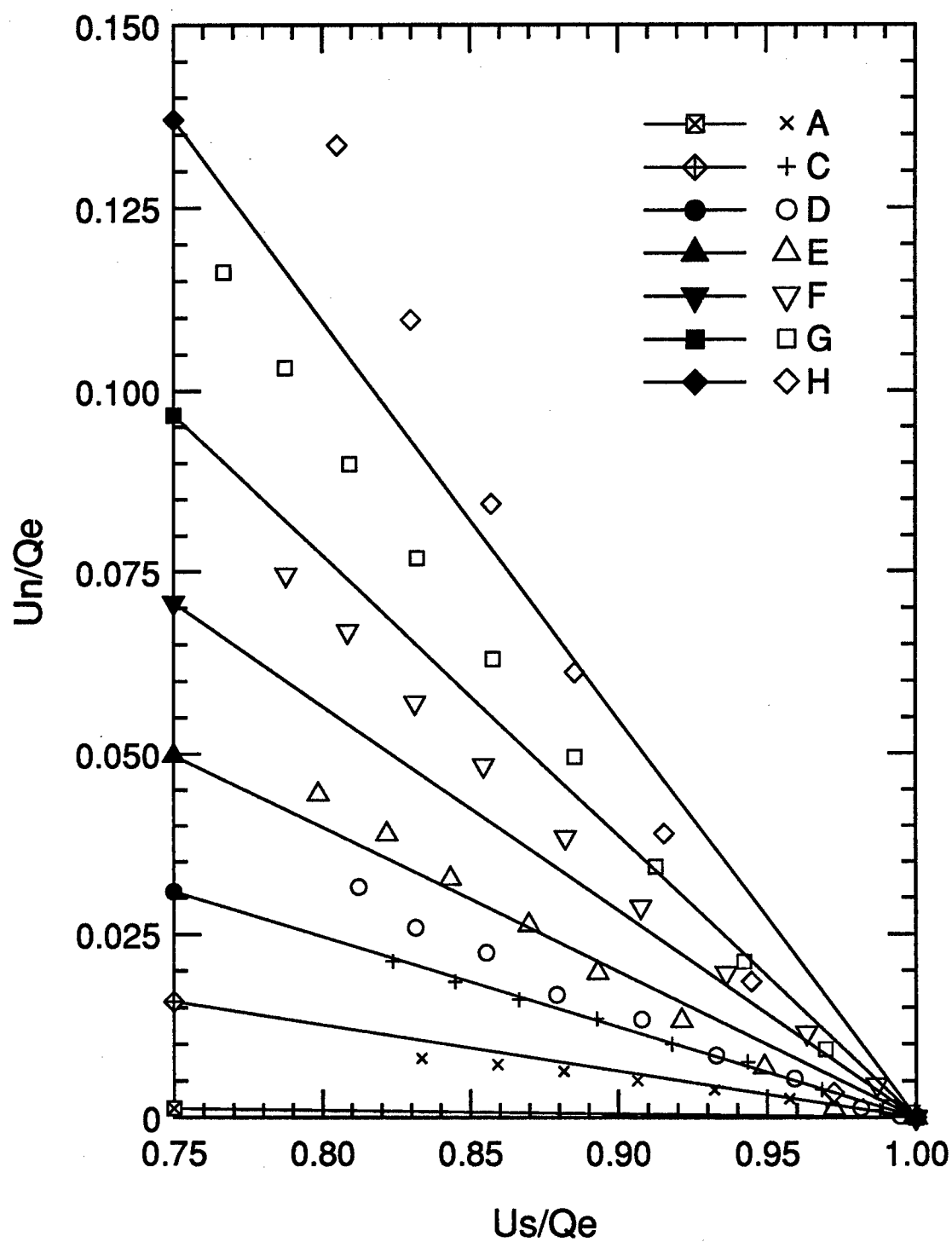
Figure 4.15.   Comparison of hodograph to angles predicted by Squire-Winter-Hawthorne theory. $z = 0$.
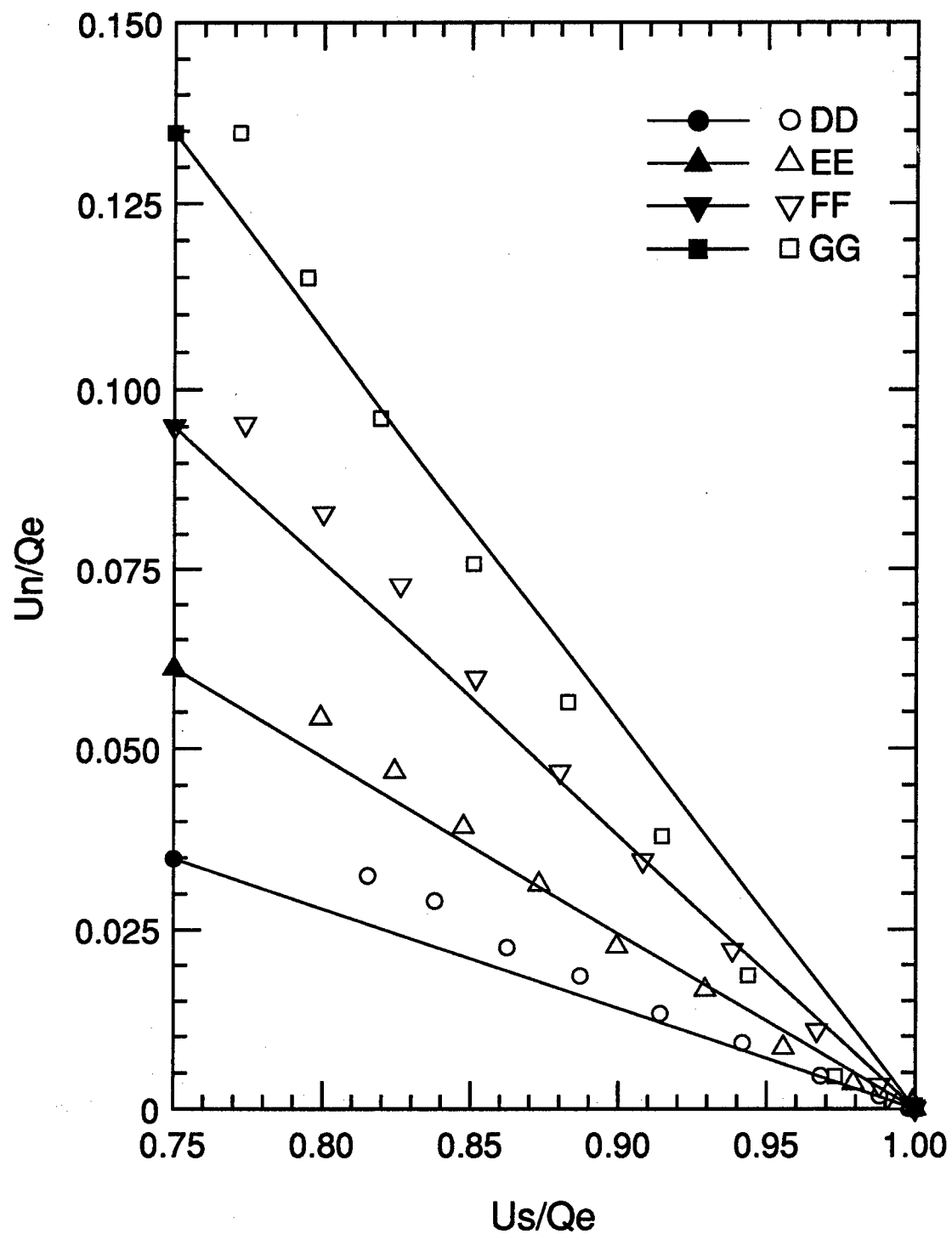
Figure 4.16. Comparison of hodograph to angles predicted by Squire-Winter-Hawthorne theory. $z = -3.5$.
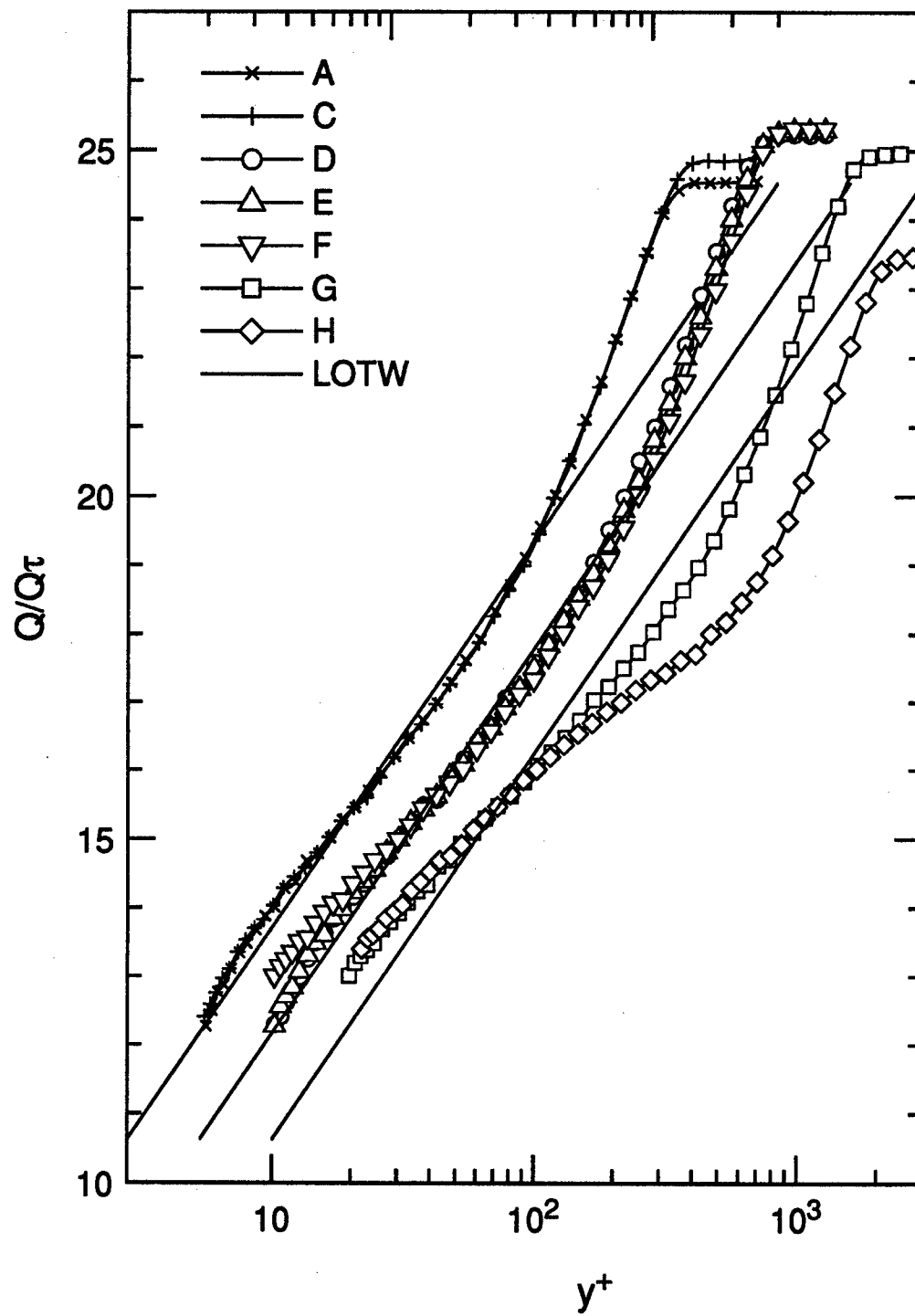
Figure 4.17. Law-of-the-wall representation. $z = 0$. Staggered axis.
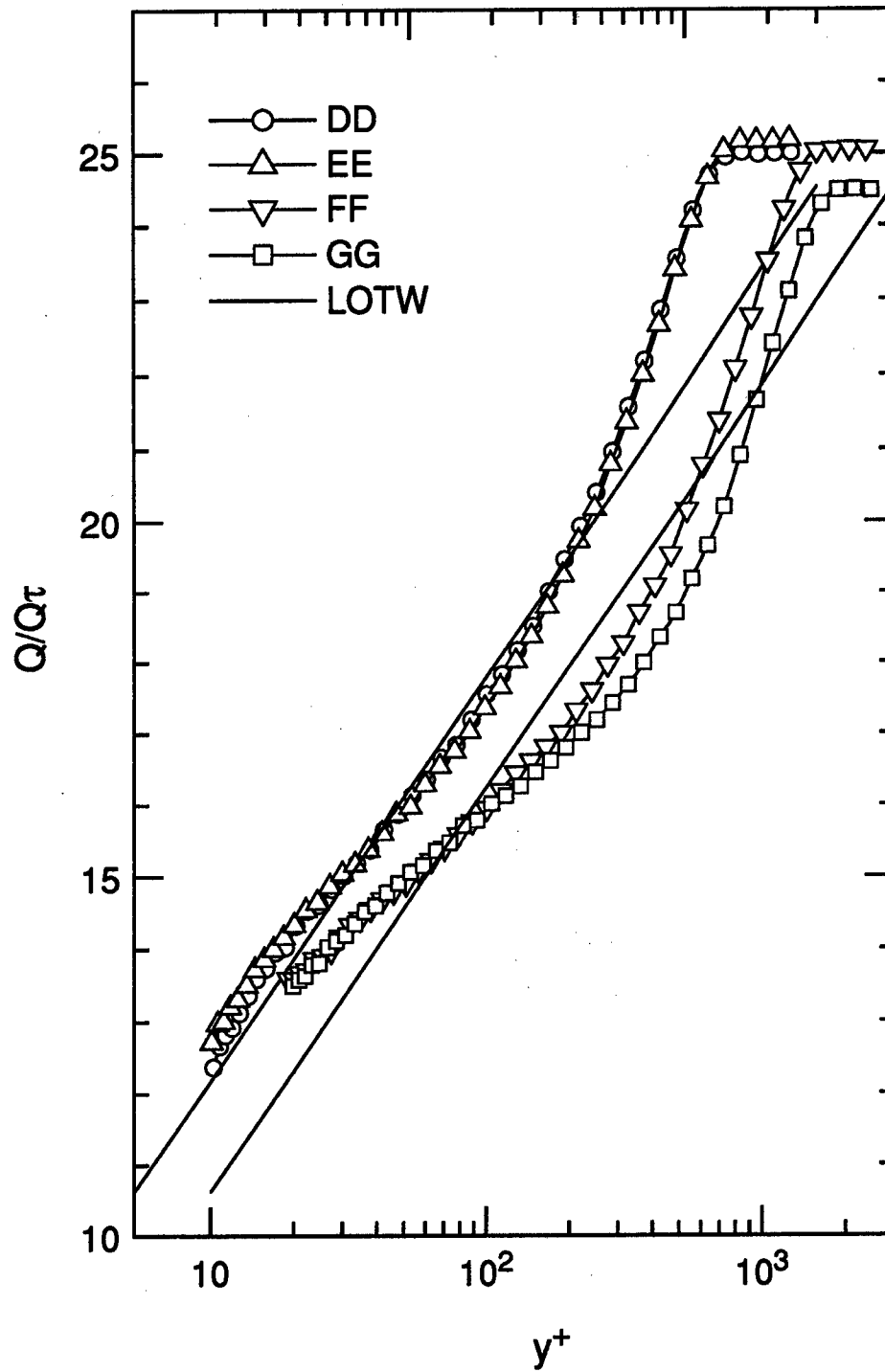
Figure 4.18. Law-of-the-wall representation. $z = -3.5$. Staggered axis.
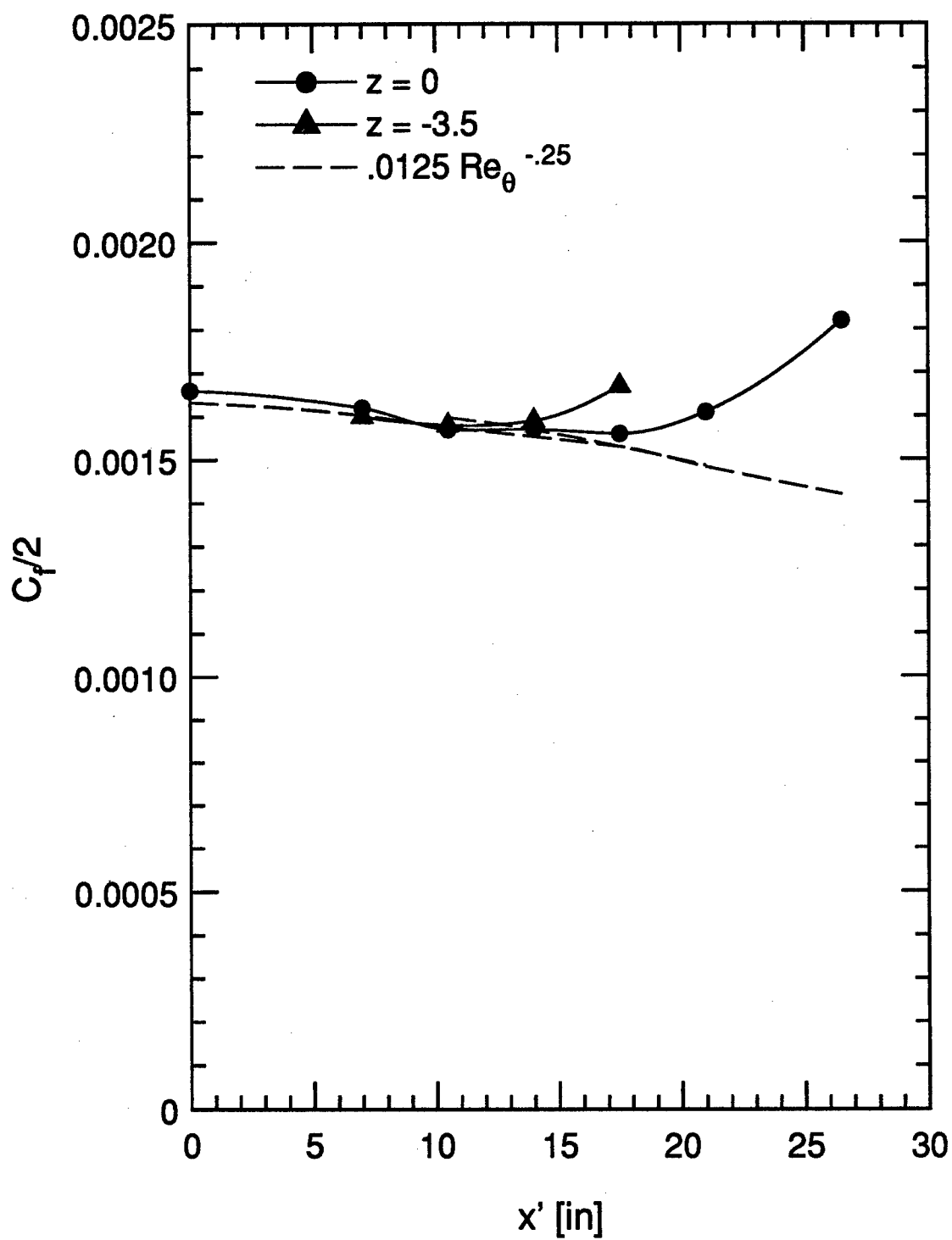
Figure 4.19. Skin friction at all stations.
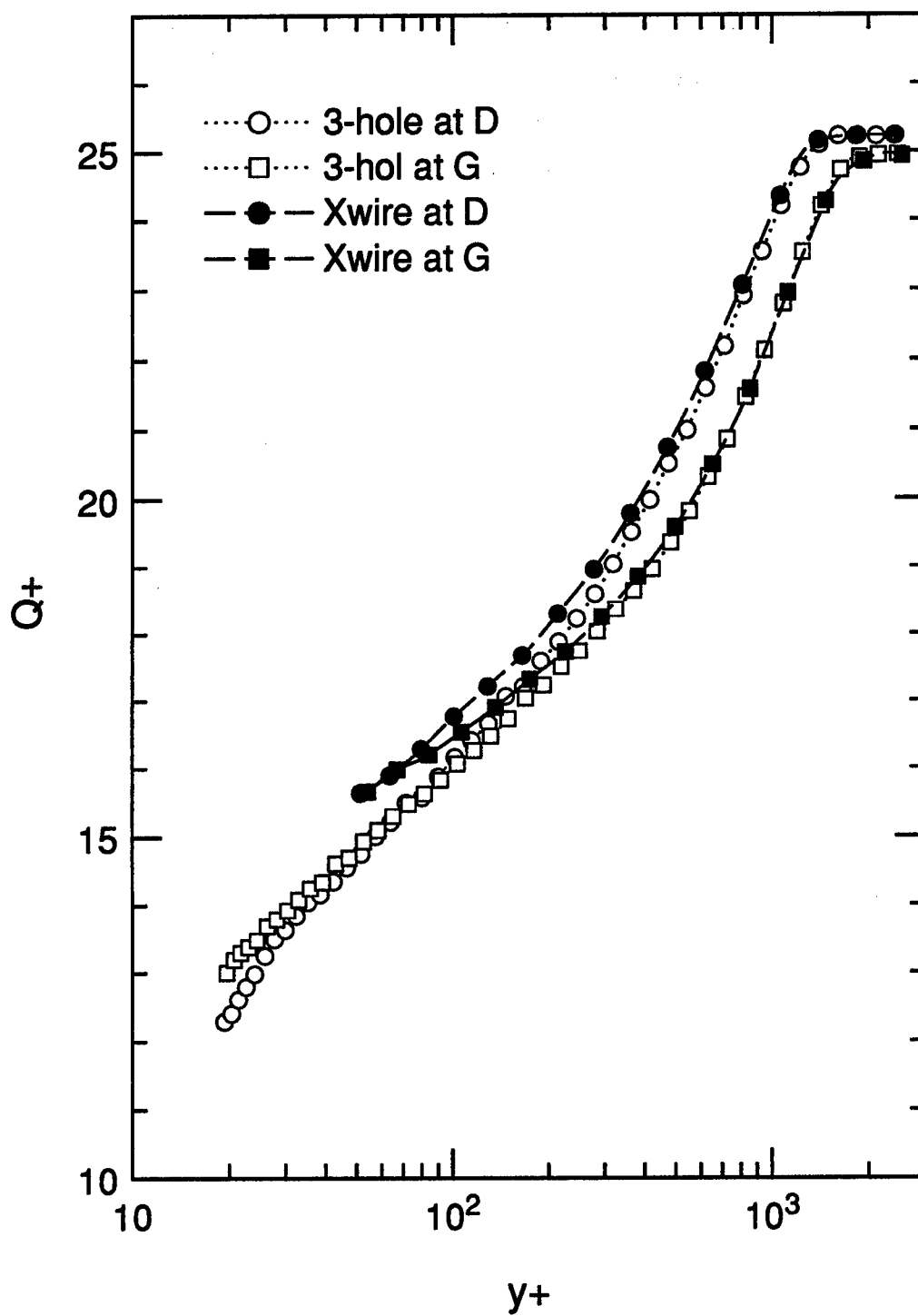
Figure 4.20. Crosswire data compared to three-hole probe data: mean velocity magnitude.
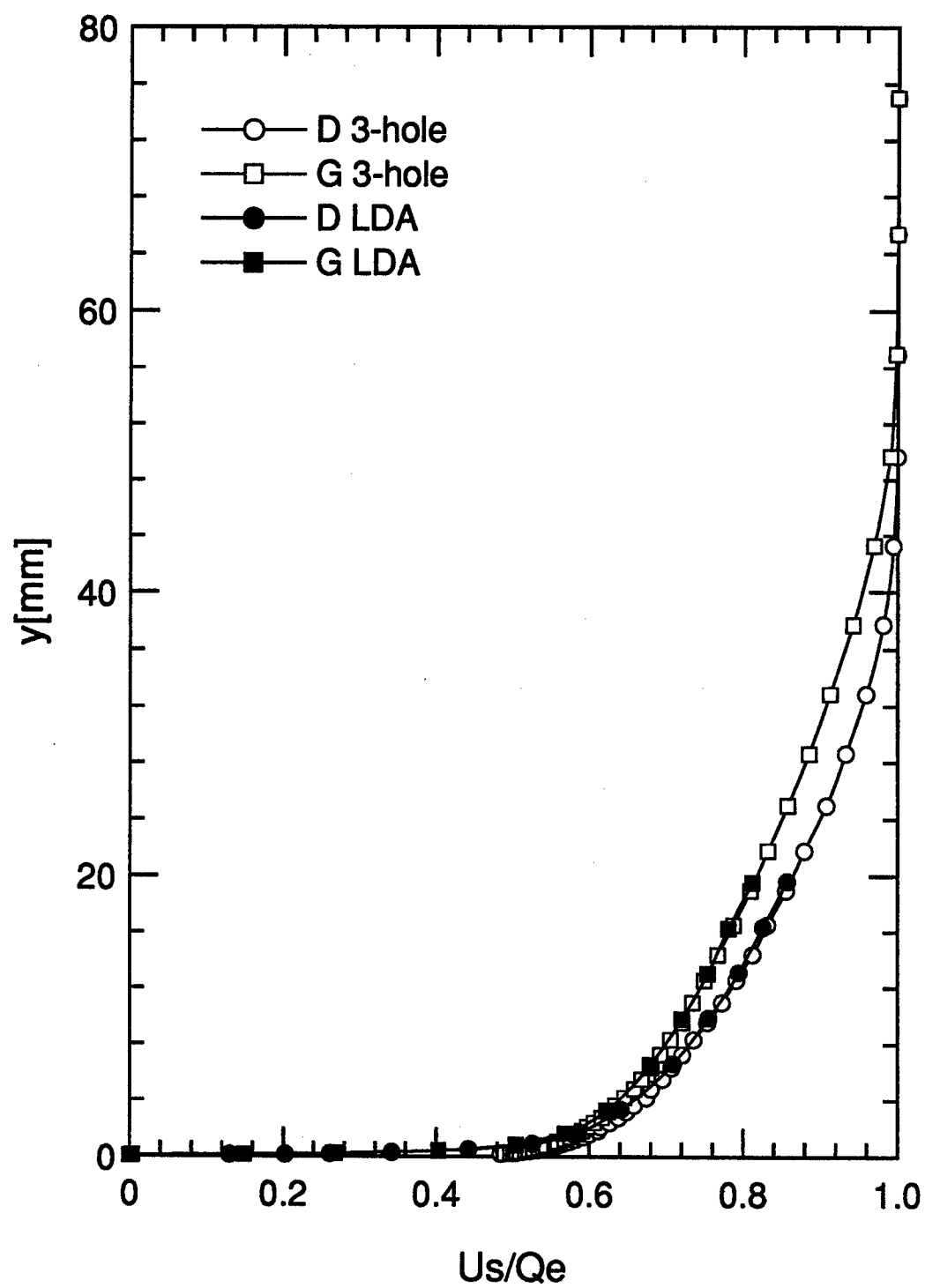
Figure 4.21. LDA data compared to three-hole probe data: Streamwise velocity.
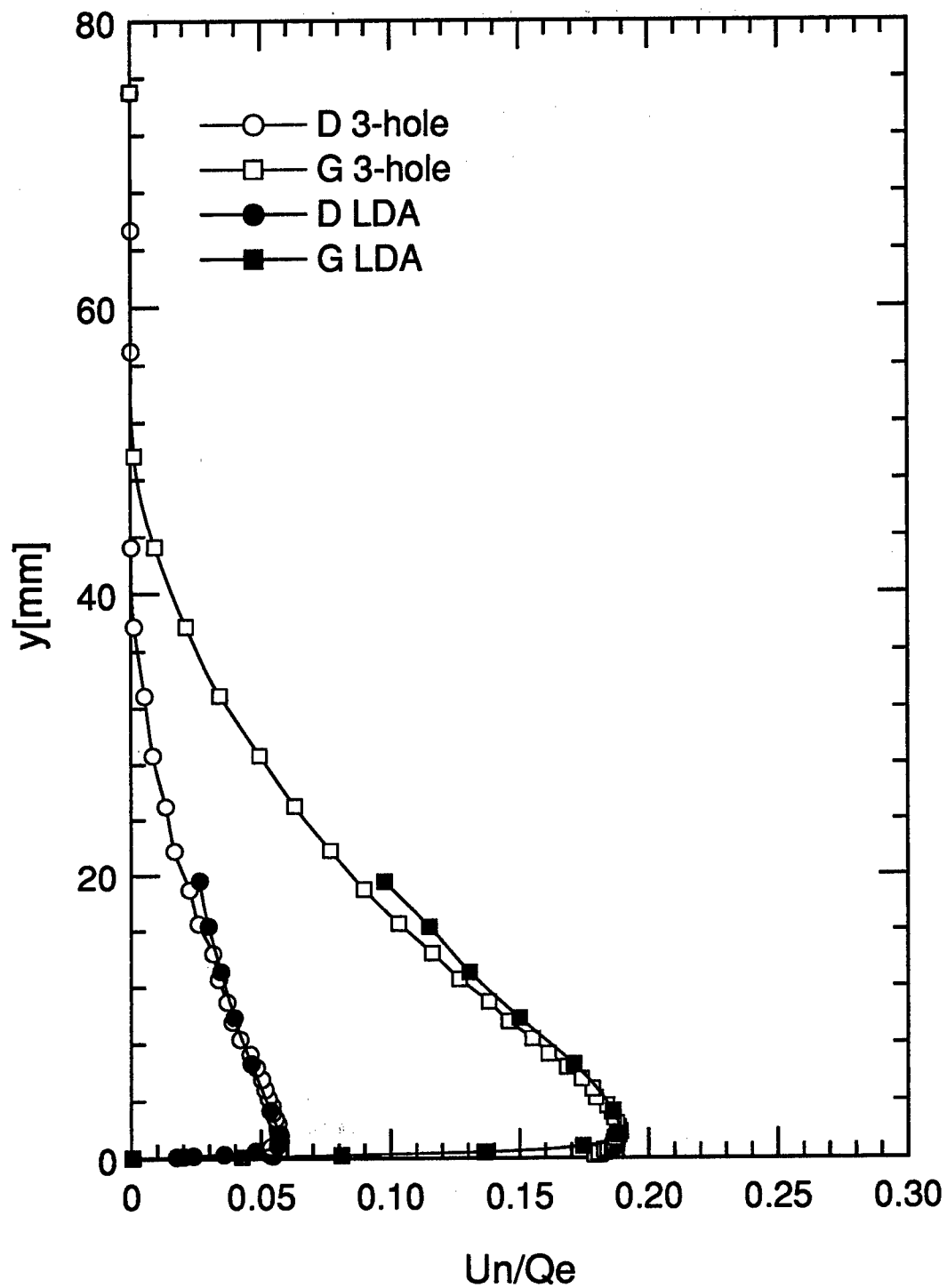
Figure 4.22. LDA data compared to three-hole probe data: Spanwise velocity.
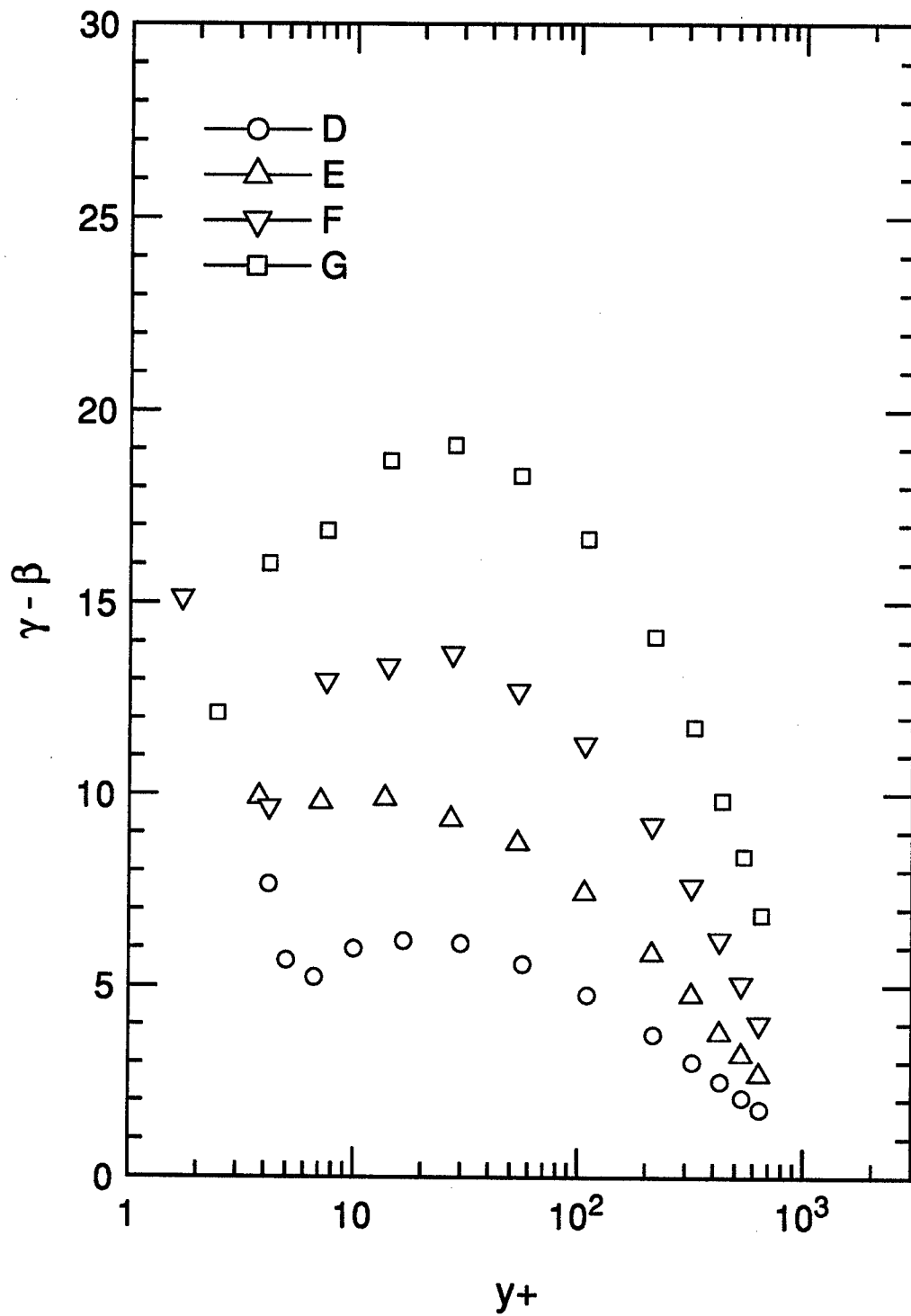
Figure 4.23. Near-wall mean velocity angle. $z = 0$.
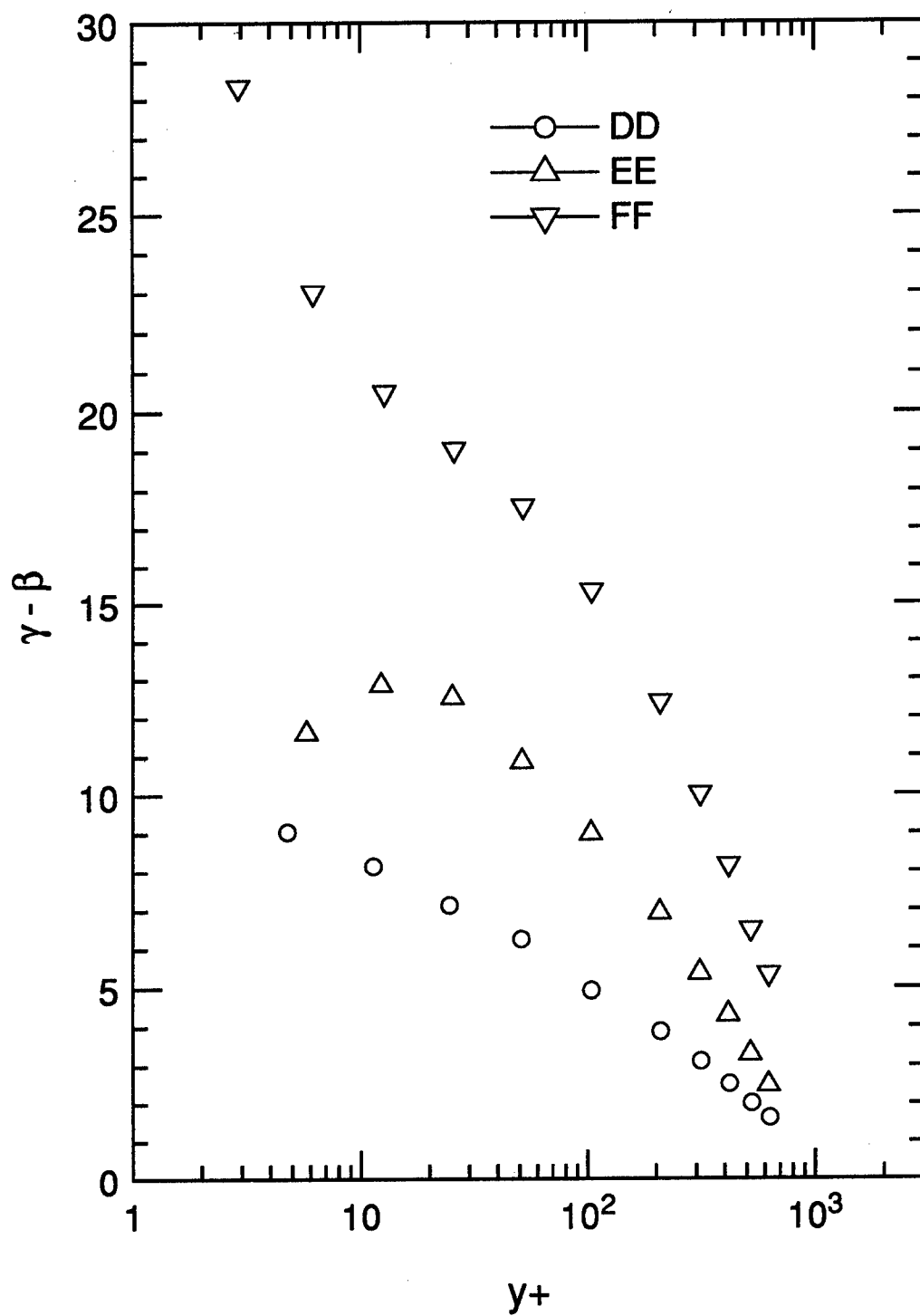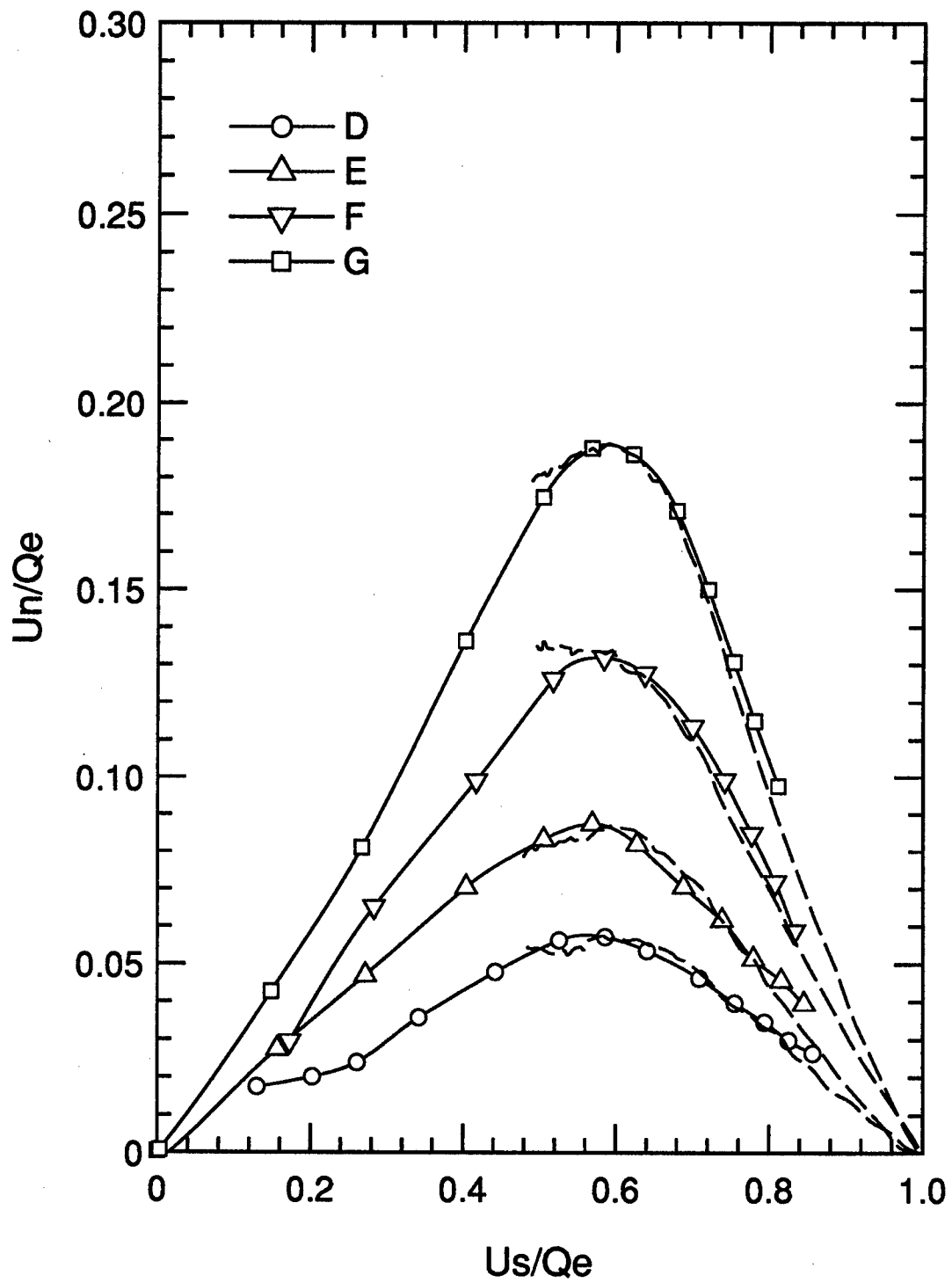
Figure 4.24. Near-wall mean velocity angle. $z = -3.5$.

Figure 4.25. Hodograph, LDA data. Dashed curves represent three-hole probe data. $z = 0$.
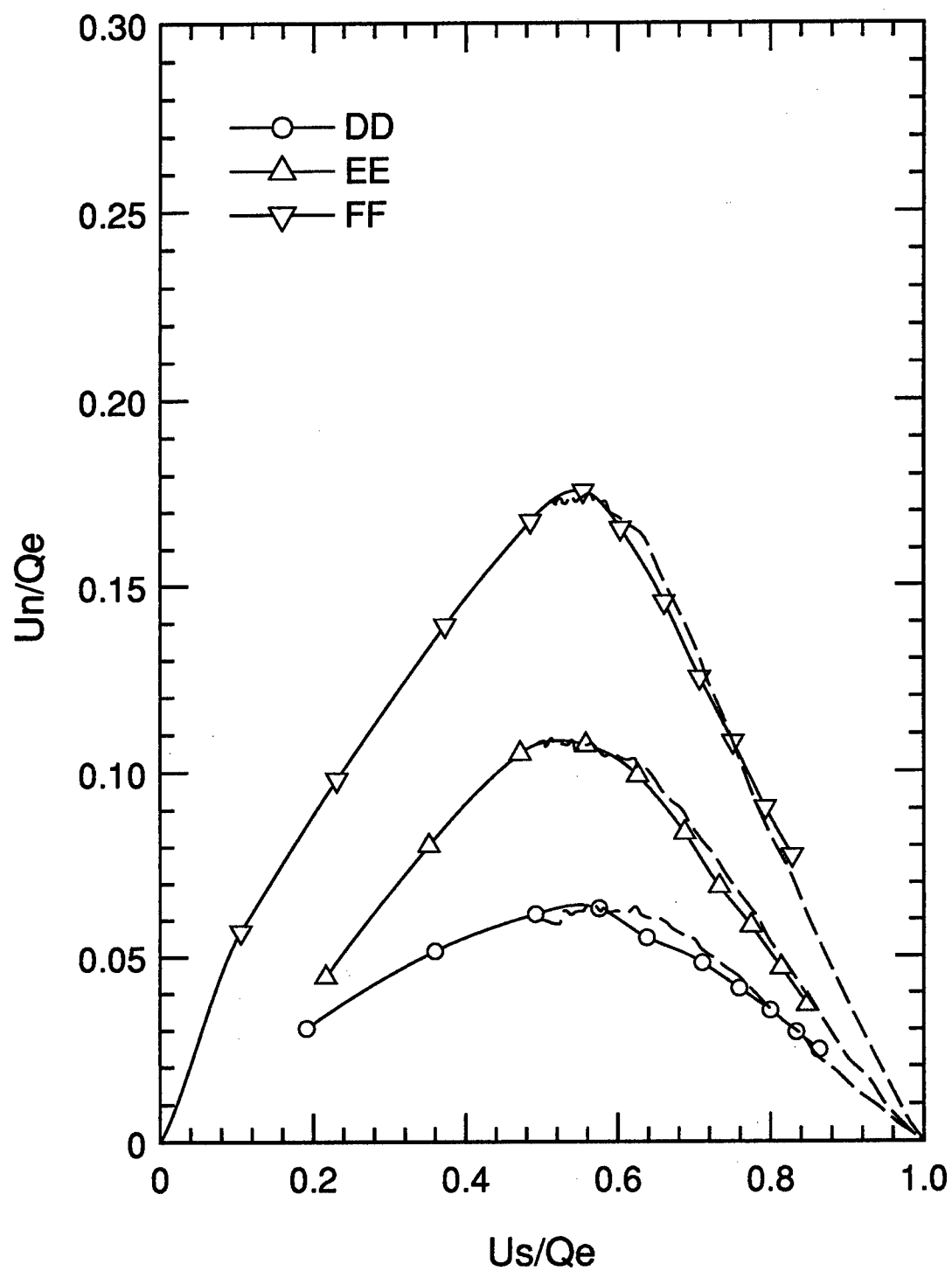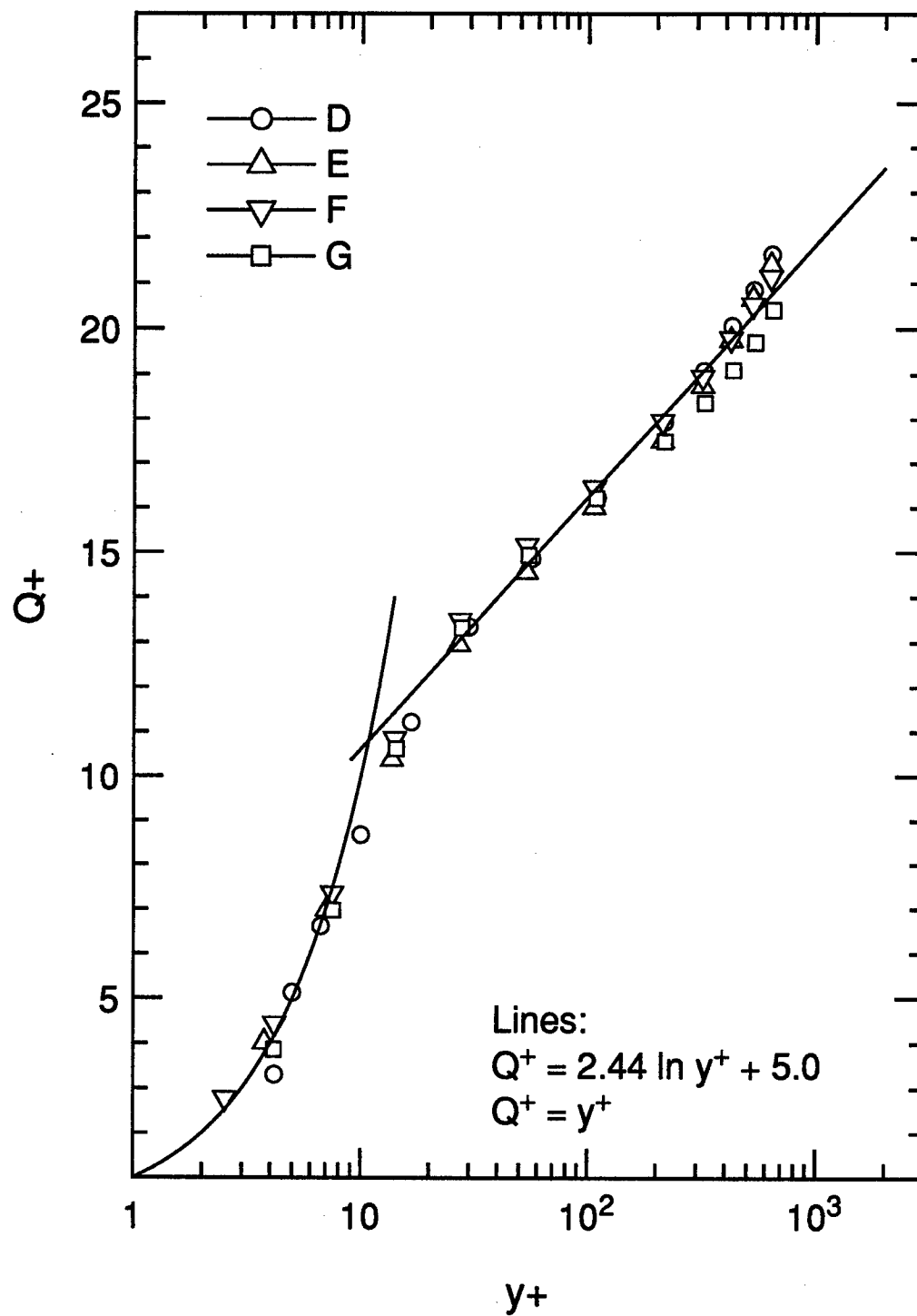
Figure 4.26. Hodograph, LDA data. Dashed curves represent three-hole probe data. $z = -3.5.$

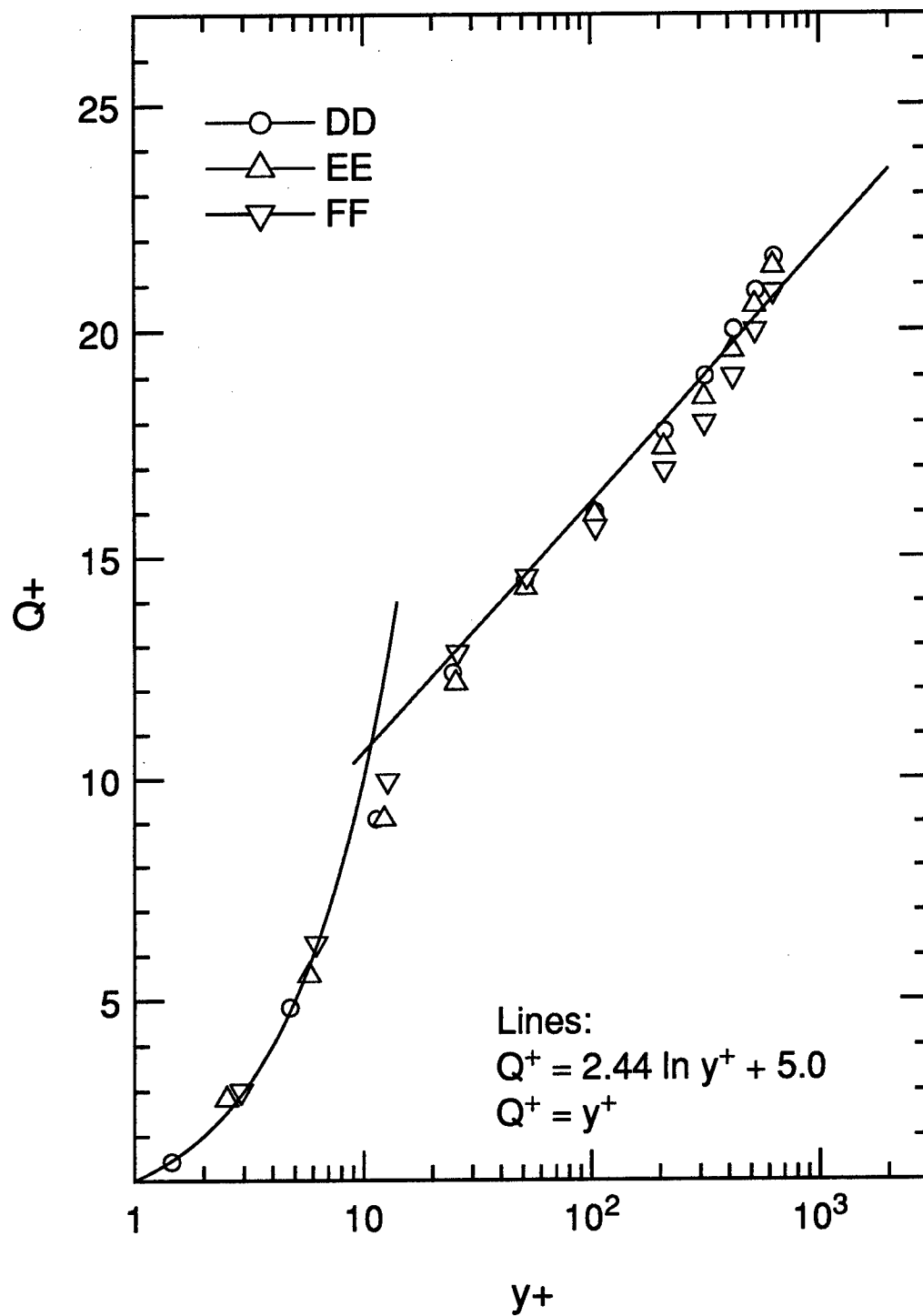Figure 4.27. Law-of-the-wall representation, LDA data. $z = 0$.

Figure 4.28. Law-of-the-wall representation, LDA data. $z = -3.5$.

Chapter 5

Turbulence Results

In this chapter we discuss the turbulence quantities in the three-dimensional turbulent boundary layer, as measured by the LDA and by the crosswire. We examine the components of the Reynolds stress tensor and at the angles of stress and strain. We also discuss some turbulence modeling quantities. The triple products were calculated and are included in the tabulated data but are not presented here; they are used in calculating vertical transport velocities and Reynolds stress transport equation balances, presented in the following chapter.

Data are presented for stations D, E, F, G, DD, EE, and FF, as indicated in figure 2.5 and table 4.1. The data are grouped into two sets: the four stations at $z = 0$ and the three stations at $z = -3.5$. The latter are the more strongly turned profile locations. We present the data in the coordinate system aligned with the wind tunnel.

5.1 Reynolds normal stresses

The Reynolds stresses are normalized by the friction velocity, and plotted in profiles as functions of y^+, in semi-log coordinates to emphasize near-wall features. The crosswire data are plotted alongside the LDA data, to complete the profiles.

Figures 5.1 and 5.2 show the $\overline{u'^2}$ normal stress consistently reaching a peak near $y^+ = 10$. Similar peak locations and values have been found in two-dimensional boundary layer studies (see, for example, Purtell et al. (1981) or Spalart (1988)). This peak diminishes in amplitude at the farthest downstream stations. Station FF demonstrates the suppressed values of $\overline{u'^2}$ in this region quite strongly, though the data are not spaced closely enough to determine the exact location and magnitude of the peak. There is a plateau in $\overline{u'^2}$ centered around $y^+ = 100$ followed by a rapid drop to nearly zero at the edge of the boundary layer. The fall-off happens at increasing

103

values of y^+, as occurs with increasing Reynolds number in two-dimensional boundary layers. There appears to be general collapse between all the data in the region below $y^+ = 10$. The agreement is quite good between the LDA data and the crosswire data in the region where the two datasets overlap. This comparison is sensitive to error in fringe spacing (Λ), since the measured Reynolds stresses are proportional to Λ^2.

The $\overline{v'^2}$ normal stress is displayed in figures 5.3 and 5.4. This stress is considerably smaller than $\overline{u'^2}$, and again takes on a profile shape similar to $\overline{v'^2}$ for two-dimensional boundary layers. There is an excellent collapse of the data scaled in wall coordinates. The three-dimensionality does not have a strong effect on $\overline{v'^2}$, but the data do indicate that there is a small increase in $\overline{v'^2}$ in the further downstream stations.

Figures 5.5 and 5.6 show the $\overline{w'^2}$ normal stress. The upstream profiles look similar to two-dimensional boundary layer $\overline{w'^2}$ profiles, with the highest point around $y^+ = 50$ and a steep drop off at the outer edge of the boundary layer. As the flow develops, the level of $\overline{w'^2}$ gradually increases. A peak appears near $y^+ = 10$ as the mean three-dimensionality develops. The peak in the $\overline{u'^2}$ stress diminishes as the flow develops, though, so it is possible that we are seeing the "streamwise" peak in rotated coordinates. The agreement between the LDA and crosswire data for $\overline{w'^2}$ is not as good as for $\overline{u'^2}$.

Also included are the crosswire data normalized by the "outer" parameters U_{ref} (= 12.5 m/s) and δ_{99}, in figures 5.7 and 5.8. These plots are dominated by the wake behavior of the boundary layer and show and excellect collapse in outer layer coordinates.

5.2 Turbulent kinetic energy

Figures 5.9 and 5.10 show the development of twice the turbulent kinetic energy, plotting $q^2 \equiv \overline{u'^2} + \overline{v'^2} + \overline{w'^2}$ against y^+. The turbulent kinetic energy is coordinate-invariant. It is clear that q^2 begins at zero at the wall, reaches a peak near $y^+ = 10$, falls to a plateau approximately in the range $40 < y^+ < 300$, and falls off steeply at the edge of the boundary layer. We see a few trends with increasing three-dimensionality. Most notably, the plateau region appears to grow flatter. At station FF, there is even

a local minimum in q^2 near $y^+ = 100$. In the outer part of the boundary layer, we see a mild increase in turbulent kinetic energy with increasing three-dimensionality. In the inner part of the boundary layer (below $y^+ = 100$) the trend is not as marked, but the turbulent kinetic energy seems to decrease with increasing three-dimensionality.

5.3 Reynolds shear stresses

One of the strengths of this study is our ability to directly measure the $-\overline{u'v'}$ and $-\overline{v'w'}$ shear stresses with the near-wall LDA. We chose not to measure the less important $\overline{u'w'}$ stress with the LDA, but do have $\overline{u'w'}$ data from the crosswire. Figures 5.11 and 5.12 show the streamwise $-\overline{u'v'}$ shear stress. This shear stress does not collapse as well in the region $y^+ < 10$ as the normal stresses do. Collapse of $-\overline{u'v'}$ in the near-wall region is not necessarily expected, since the streamwise pressure gradient will affect the shear stress. We note that there is a distinct decrease in $-\overline{u'v'}$ with increasing three-dimensionality.

A "Couette flow" approximation can be used to analytically predict the behavior of the shear stresses near the wall in a nearly equilibrium flow. Estimating that U and W are functions of y only leads to the conclusion that

$$- \rho\overline{u'v'} + \mu\frac{\partial u}{\partial y} = y\frac{\partial p}{\partial x} + \tau_{0x}. \tag{5.1}$$

We compared our data to the above equation and found that there was poor agreement. This lack of agreement is probably due to the rapidly changing pressure gradients.

The spanwise $-\overline{v'w'}$ shear stress is represented in figures 5.13 and 5.14. For a two-dimensional boundary layer, $\overline{v'w'}$ is zero; we see increasing $-\overline{v'w'}$ with increasing three-dimensionality. The peak $\frac{-\overline{v'w'}}{u_\tau^2}$ is about 0.5, near $y^+ = 10$ to 20, which is almost as large as $-\overline{u'v'}$ at that point.

Perhaps the most striking feature of these figures is that the crosswire fails to capture the major part of the $\overline{v'w'}$ stress. We must be very careful not to draw too-broad conclusions from studies which barely capture the behavior of $\overline{v'w'}$.

We include the crosswire data normalized by "outer" parameters in figures 5.15 and 5.16. These figures include $\overline{u'w'}$ data from the crosswire. Near the wall $\overline{u'w'}$ is positive, but $\overline{u'w'}$ is negative for most of the boundary layer. $|\overline{u'w'}|$ is generally larger than $|\overline{v'w'}|$, as is commonly found in other three-dimensional turbulent boundary layer experiments. We see that $\overline{u'w'}$ increases as the flow becomes more three-dimensional, with a maximum value of approximately 0.035% of U_{ref}^2, or about 50% of the local $\overline{u'v'}$.

The LDA data as presented are slightly contaminated by $\overline{u'w'}$. The contamination of $\overline{u'^2}$ and $\overline{w'^2}$ is negligible (0.3% of $\overline{u'w'}$) and the contamination of $\overline{v'^2}$ is zero. However, the shear stresses need further discussion. The error in $\overline{u'v'}$ and $\overline{v'w'}$ is equal to $0.123\overline{u'w'}$. For two-dimensional boundary layers $\overline{u'w'}$ is identically zero, so initally the effect of $\overline{u'w'}$ on $\overline{u'v'}$ is negligible. For three-dimensional turbulent boundary layers, this error is small above $y^+ = 50$, with errors in $\overline{u'v'}$ averaging 3%. Near the wall in a strongly turned boundary layer, $\overline{u'w'}$ can become as large as $\overline{u'v'}$, so $\overline{u'v'}$ and $\overline{v'w'}$ could be underreported by as much as 12% of $\overline{u'v'}$. Effects of $\overline{u'w'}$ on the LDA data are discussed in detail in Appendix B.

5.4 Angles of stress and strain

An isotropic eddy viscosity formulation is only valid if the shear stress angle γ_τ is identical to the mean strain angle, γ_g.

$$\gamma_\tau \equiv \tan^{-1}\left(-\overline{v'w'}/-\overline{u'v'}\right); \qquad (5.2)$$

$$\gamma_g \equiv \tan^{-1}\left(\frac{\partial W}{\partial y}\bigg/\frac{\partial U}{\partial y}\right). \qquad (5.3)$$

These angles, along with the mean flow angle γ, are indicated in figures 5.17 through 5.23. We have calculated γ_g by differentiating the data, using a parabolic fit to the unevenly spaced data to estimate the first derivatives.

$$\frac{df}{dy}_{(y=y_i)} = \frac{(y_{i-1} - y_i)^2(f_{i+1} - f_i) - (y_{i+1} - y_i)^2(f_{i-1} - f_i)}{(y_{i-1} - y_i)^2(y_{i+1} - y_i) - (y_{i+1} - y_i)^2(y_{i-1} - y_i)}. \qquad (5.4)$$

For very closely spaced data with some uncertainty, the first derivative becomes very jagged, so when differentiating the hotwire data we chose to replace y_{i+1} by y_{i+2},

y_{i-1} by y_{i-2}, f_{i+1} by f_{i+2}, and f_{i-1} by f_{i-2} in the above equation, in order to obtain smooth yet accurate derivatives. The γ_τ data also tend to be noisy, because of the noise in $\overline{v'w'}$.

Agreement between the flow angle γ and the gradient angle γ_g is not expected. However, if the flow is collateral at the wall, as conjectured in Chapter 4, there would be some agreement in the viscous sublayer. To see this, suppose $U = c_1 y$ and $W = c_2 y$: Then $\gamma = \gamma_g = \tan^{-1}(\frac{c_2}{c_1})$. The angle data uphold this idea of collateral flow at the wall, showing close agreement at all stations around $y^+ = 8$. Below $y^+ = 8$ scatter prevents us from making further conclusions.

Throughout most of the boundary layer, the angles of stress and strain do not agree with each other. Based on the results of other experiments, we expect this misalignment. Most of the experiments which we discussed in Chapter 1 demonstrated that the shear stress vector lagged the mean strain vector. Our data demonstrate the same lag through most of the boundary layer, especially in the outer part. Station FF shows that $(\gamma_\tau - \gamma)$ is less than $(\gamma_g - \gamma)$ by as much as 25 degrees. However, close to the wall the angles nearly coincide, and the difference between γ_τ and γ_g below $y^+ = 10$ seems to become negligible, although noise at very low y hides the pattern.

5.5 Structural parameters

Townsend's structure parameter a_1 is shown in figures 5.24 and 5.25. Considerable attention has been paid to a_1 in previous studies. It can be thought of as the "efficiency" of the turbulence in generating shear stress. As discussed in Chapter 1, the value of a_1 is generally accepted to be around 0.15 for two-dimensional boundary layers, even in the presence of moderate pressure gradient, but many three-dimensional turbulent boundary layer studies have found a_1 to drop below that value. The cross-wire data show the behavior of a_1 in the outer part of the boundary layer. Near $y^+ = 1000$, a_1 is at its highest, ranging between 0.12 and 0.14. Profile G has the lowest values of a_1. Surprisingly, the data on the $z = -3.5$ line show less spread than the data on the $z = 0$ line. The LDA data are noisier but also indicate suppressed values of a_1. Looking back at figure 5.11 it appears that reduced values of shear stress

are the cause for the suppression of a_1. Flack and Johnston observed that for their 30 degree bend flow, a_1 took on a consistent profile from the wall to about $y^+ = 50$, then fell to values around 0.11. We do not observe this near-wall agreement. This may be due to our experiment's higher Reynolds number and stronger curvature. We observed divergent behavior of the shear stresses as low as $y^+ = 10$, while their shear stresses behaved similarly up to $y^+ = 50$. The experimental uncertainty in the measurement of a_1 is quite high, so it is difficult to draw broader conclusions.

In section §5.3 we discussed the influence of $\overline{u'w'}$ on the reported values of the Reynolds stresses. The aggregate effect on the turbulent kinetic energy is zero, but the shear stress magnitude is altered by approximately 12% of $\overline{u'w'}$. This causes the LDA data to underestimate a_1 when $\overline{u'w'}$ is strongly negative, specifically toward the outer edge of the LDA data for cases of strong three-dimensionality, and to overestimate a_1 in the near-wall region.

The ratio of the normal stresses in the plane of the wall to the wall-normal normal stress, $\frac{\overline{u'^2} + \overline{w'^2}}{\overline{v'^2}}$ is displayed in figures 5.26 and 5.27. A value of 2 is consistent with equipartition of turbulent kinetic energy between $\overline{u'^2}$, $\overline{v'^2}$, and $\overline{w'^2}$, which we expect the data to approach in the freestream. The wall forces $\overline{v'^2}$ to approach zero faster than $\overline{u'^2}$ and $\overline{w'^2}$, so we expect to see the value of $\frac{\overline{u'^2} + \overline{w'^2}}{\overline{v'^2}}$ to be higher in the boundary layer. This turbulence parameter grows considerably less steep as the flow develops.

Eddy viscosity formulations are commonly used to relate the shear stress in a boundary layer to the mean velocity gradient. The misalignment of the shear stress and the strain rate vectors shown above indicates that a scalar eddy viscosity is not appropriate in three-dimensional turbulent boundary layers. The eddy viscosity ratio N_e is used as a measure of the anisotropy of the turbulence. Usually, N_e is defined as the ratio of the spanwise eddy viscosity to the streamwise eddy viscosity in a coordinate system aligned with the local mean flow. Relating N_e to the quantities we have already defined, it can be represented as

$$N_e \equiv \frac{\tan(\gamma_\tau - \gamma)}{\tan(\gamma_g - \gamma)}. \tag{5.5}$$

There are serious flaws with the concept: first, that two misaligned vector quantities should be related by a simple scalar proportion, and second, that the coordinate

system could everywhere have a different orientation throughout the flowfield. Nevertheless, the eddy viscosity ratio holds some meaning in that it represents in a single parameter the extent of misalignment of the stress and strain vectors.

We plot N_e for the LDA data in figures 5.28 and 5.29. The values of N_e are determined from the angle data presented in figures 5.17 through 5.23, and necessarily have high uncertainties. The measured N_e is always less than 0.8, and a large fraction of the values are between 0.2 and 0.4.

Flack and Johnston measured as close to the wall as the present experiment and found that they had to disregard all values of N_e below $y^+ = 20$ due to high uncertainties. They found about as much scatter in the values of N_e as are seen in the present study. They concluded that an isotropic eddy viscosity could model their flow from the wall through the inner buffer region (i.e. for $y^+ \leq 50$). Such a model is not supported by the present data. Other earlier experiments have shown the eddy viscosity ratio ranging between 0.1 and 1.2. Anderson and Eaton (1989) postulated that the level of suppression of N_e below unity is somehow a function of the turning rate, defined by the boundary layer thickness divided by the radius of curvature. As seen in figure 4.4 this nondimensional turning rate, which is approximately equal to $\delta_{99}\frac{\partial C_p}{\partial n}$ is between 0.02 and 0.04 for most of the stations studied. A comparison of 5.28 to 5.29 does indicate that the more strongly turned stations — those along the $z = -3.5$ line — have lower values of N_e.
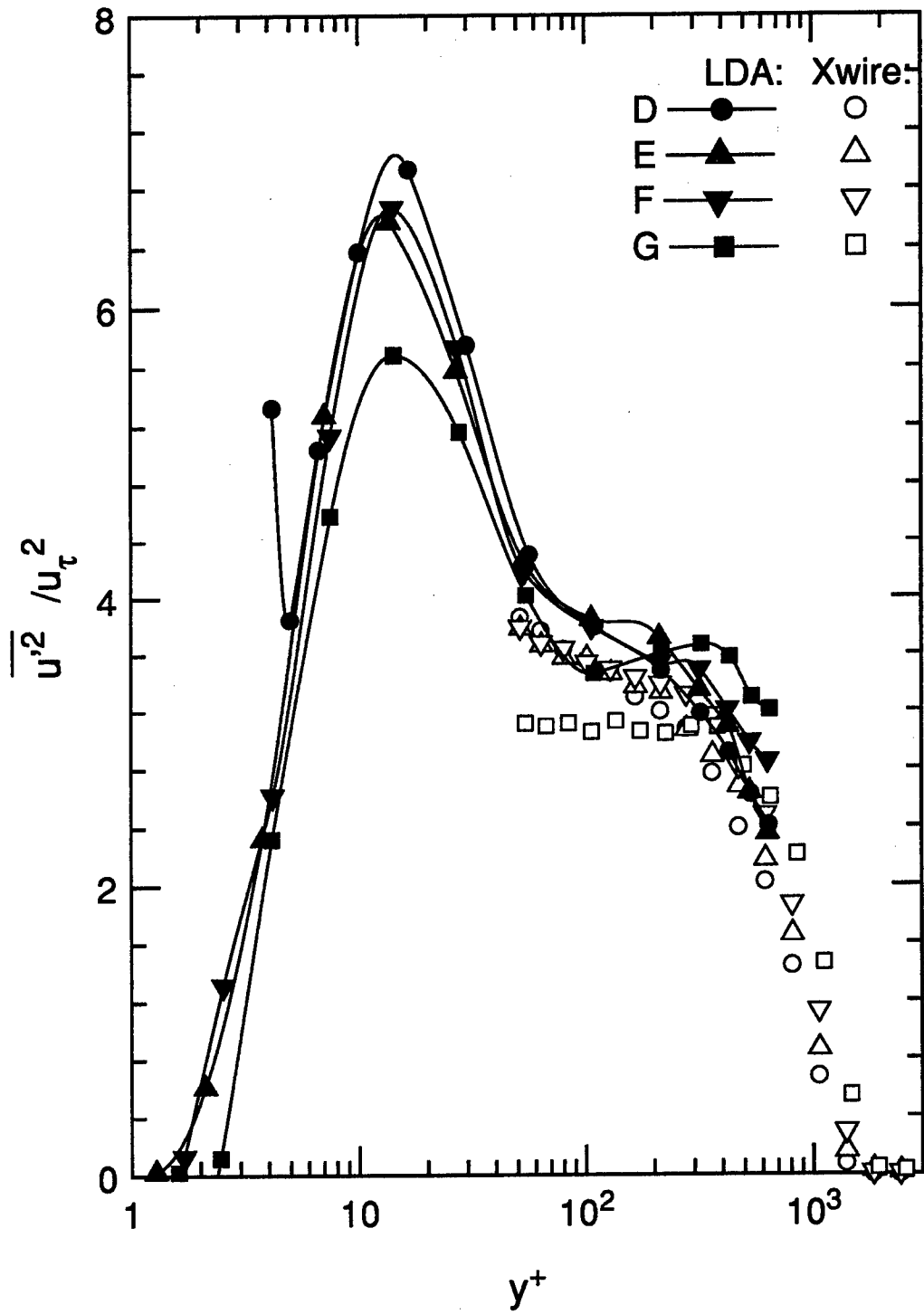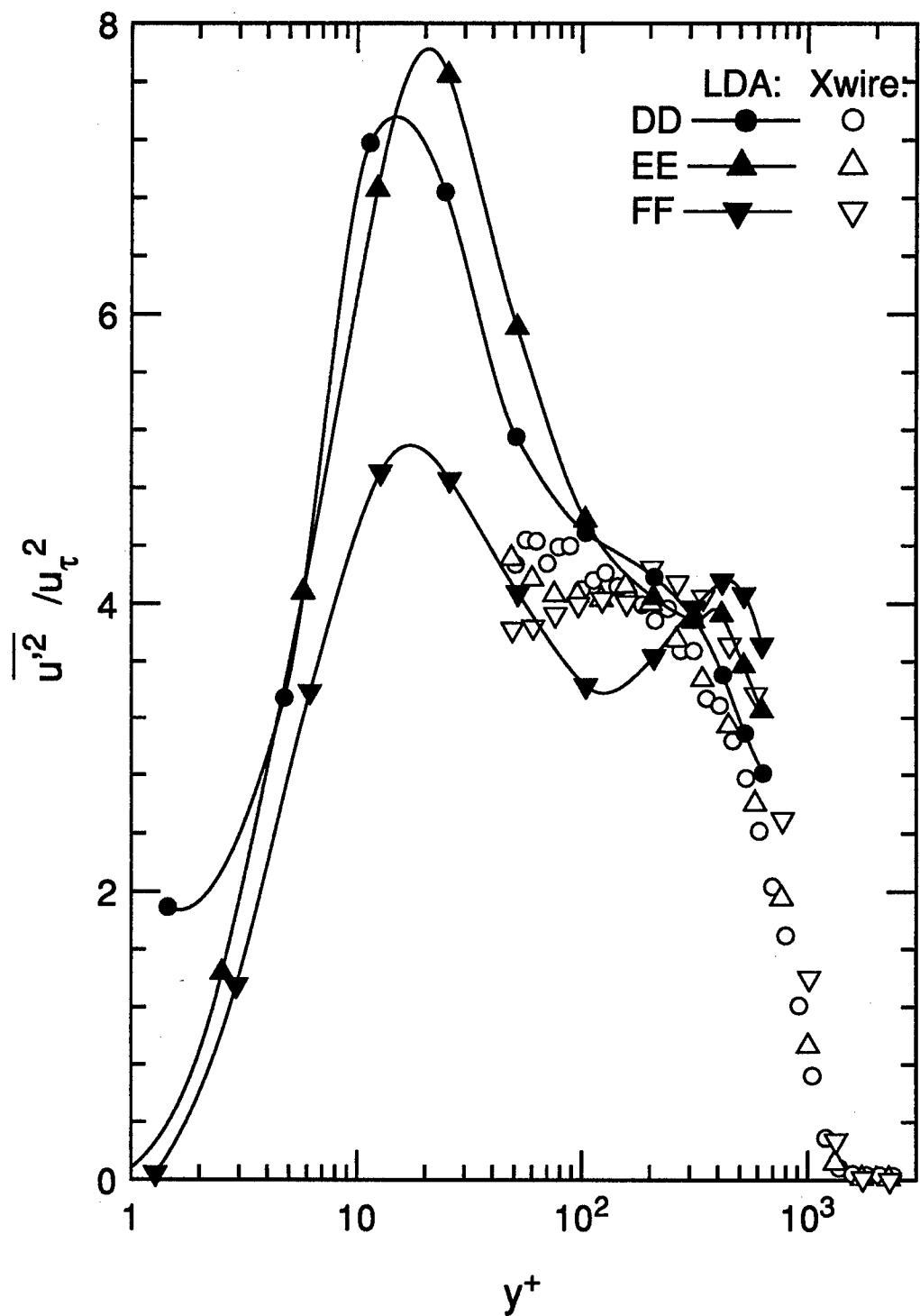
Figure 5.1. $\overline{u'^2}$ normal stress. $z = 0$.

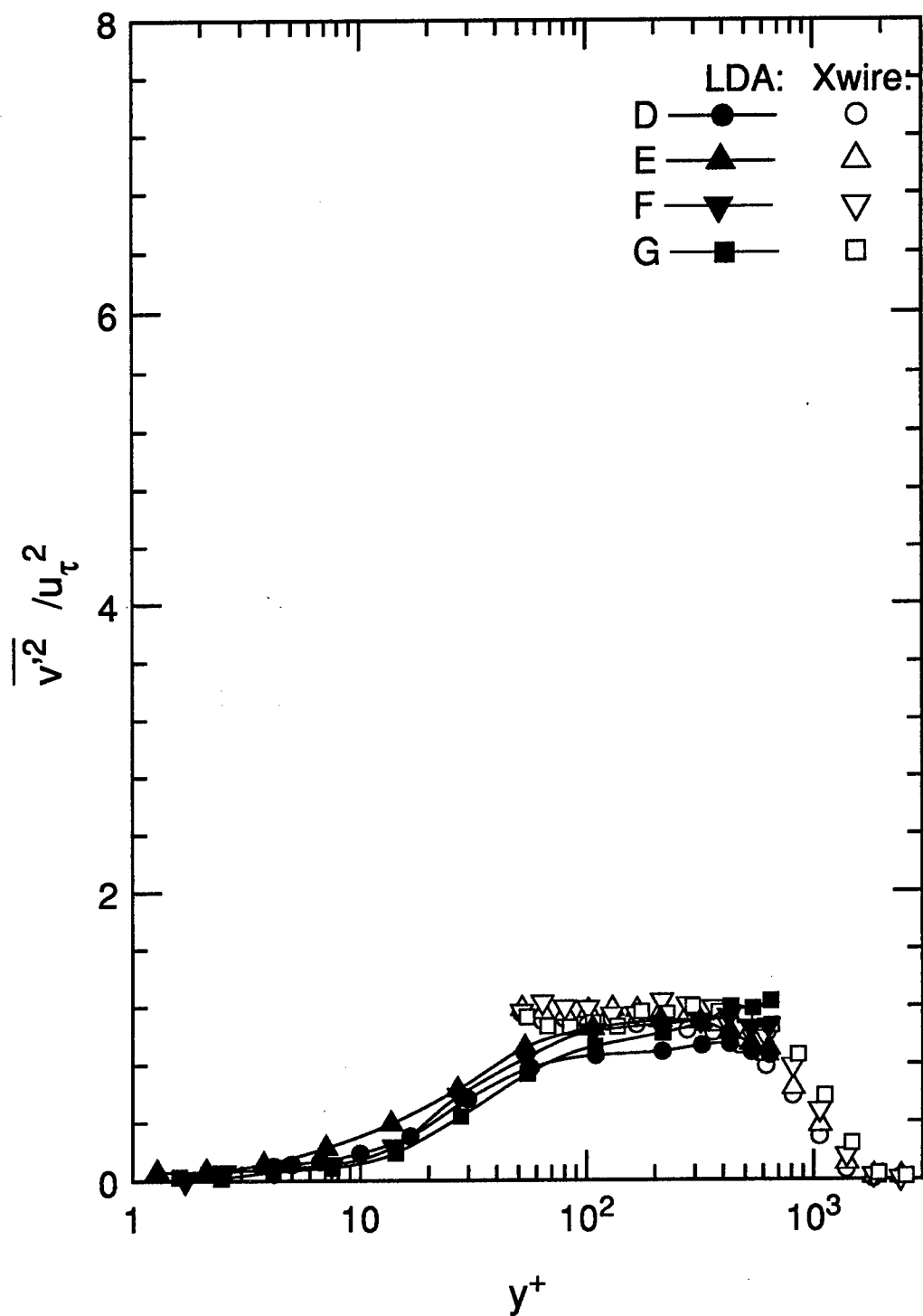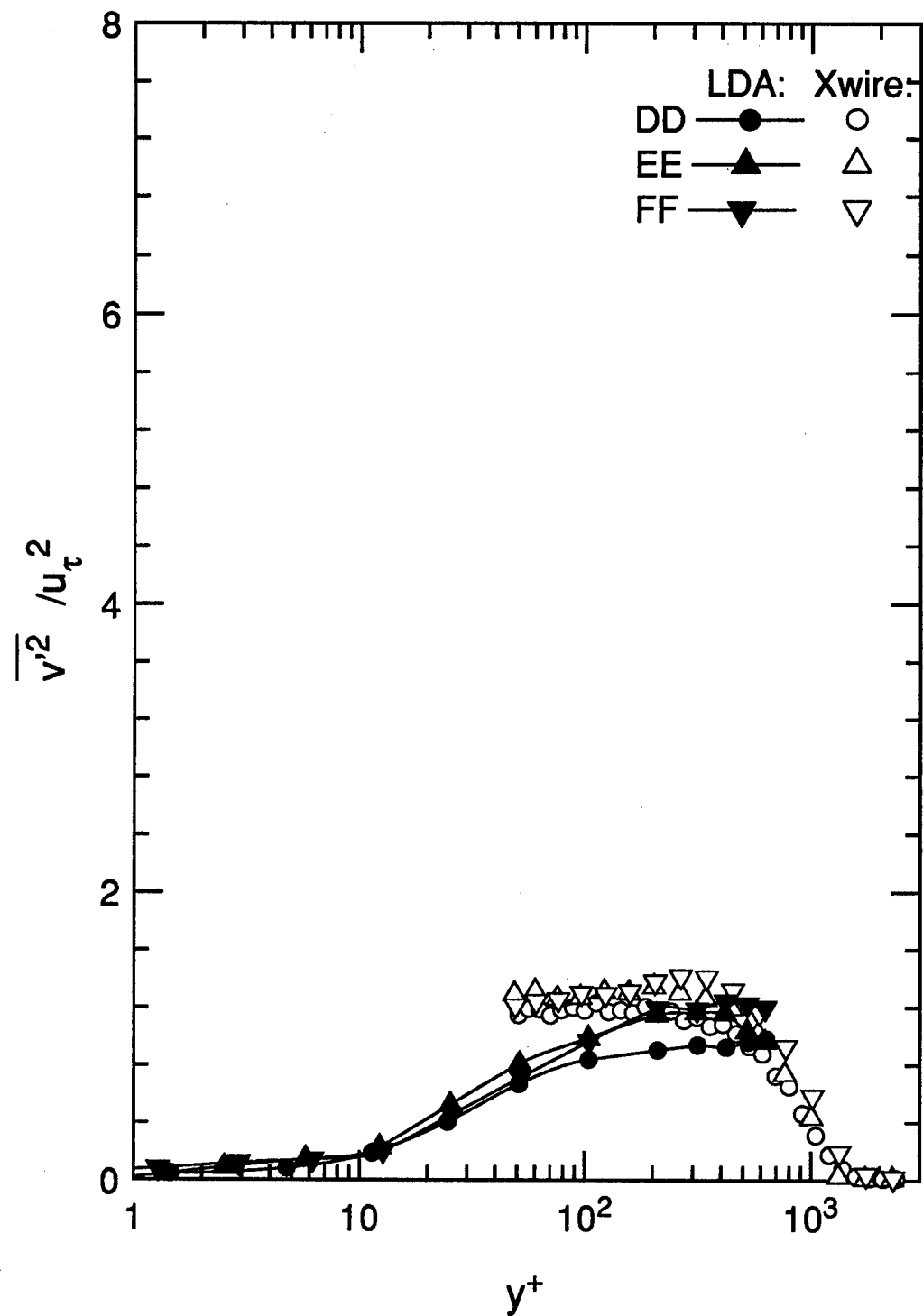Figure 5.2. $\overline{u'^2}$ normal stress. $z = -3.5$.

Figure 5.3. $\overline{v'^2}$ normal stress. $z = 0$.

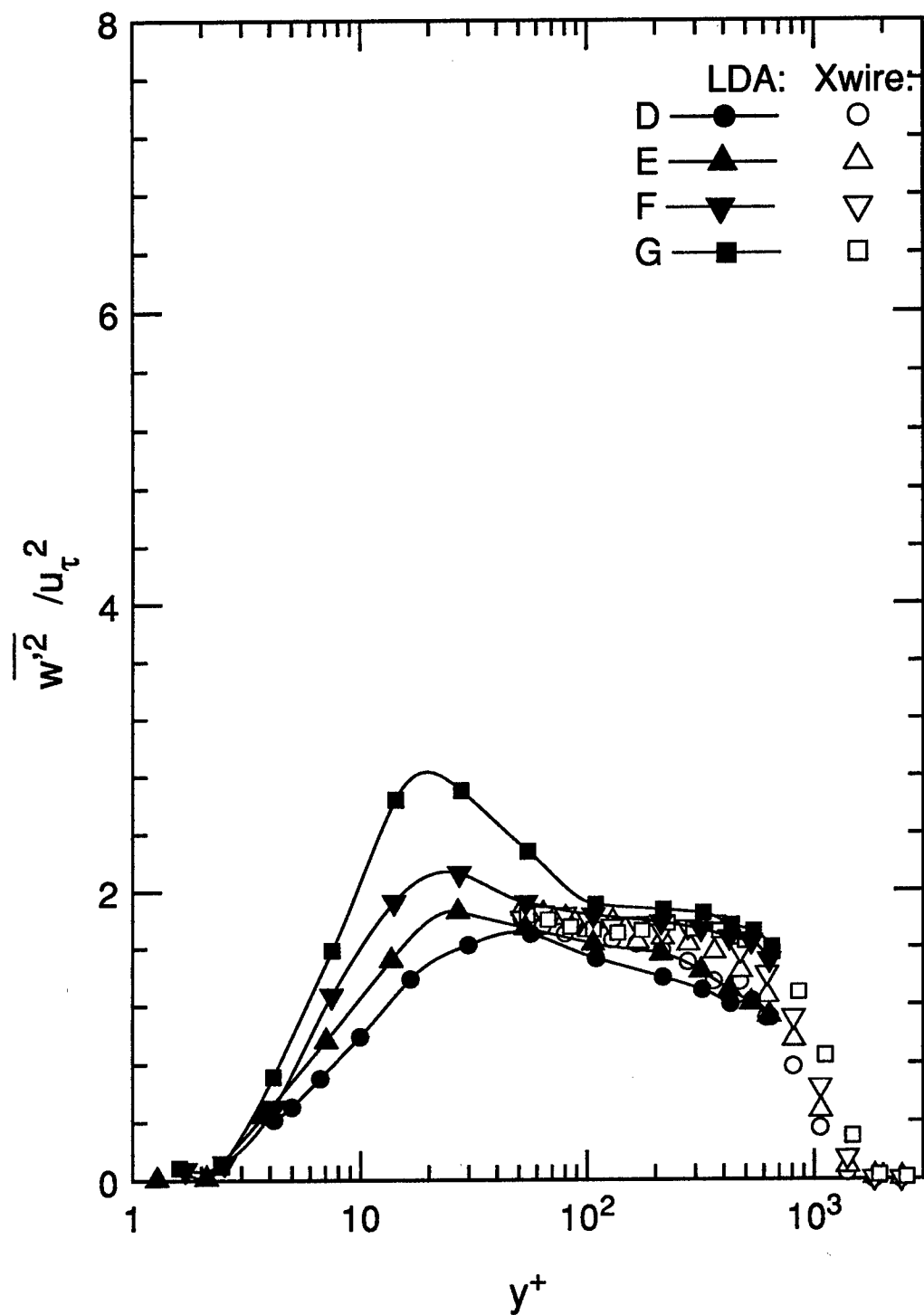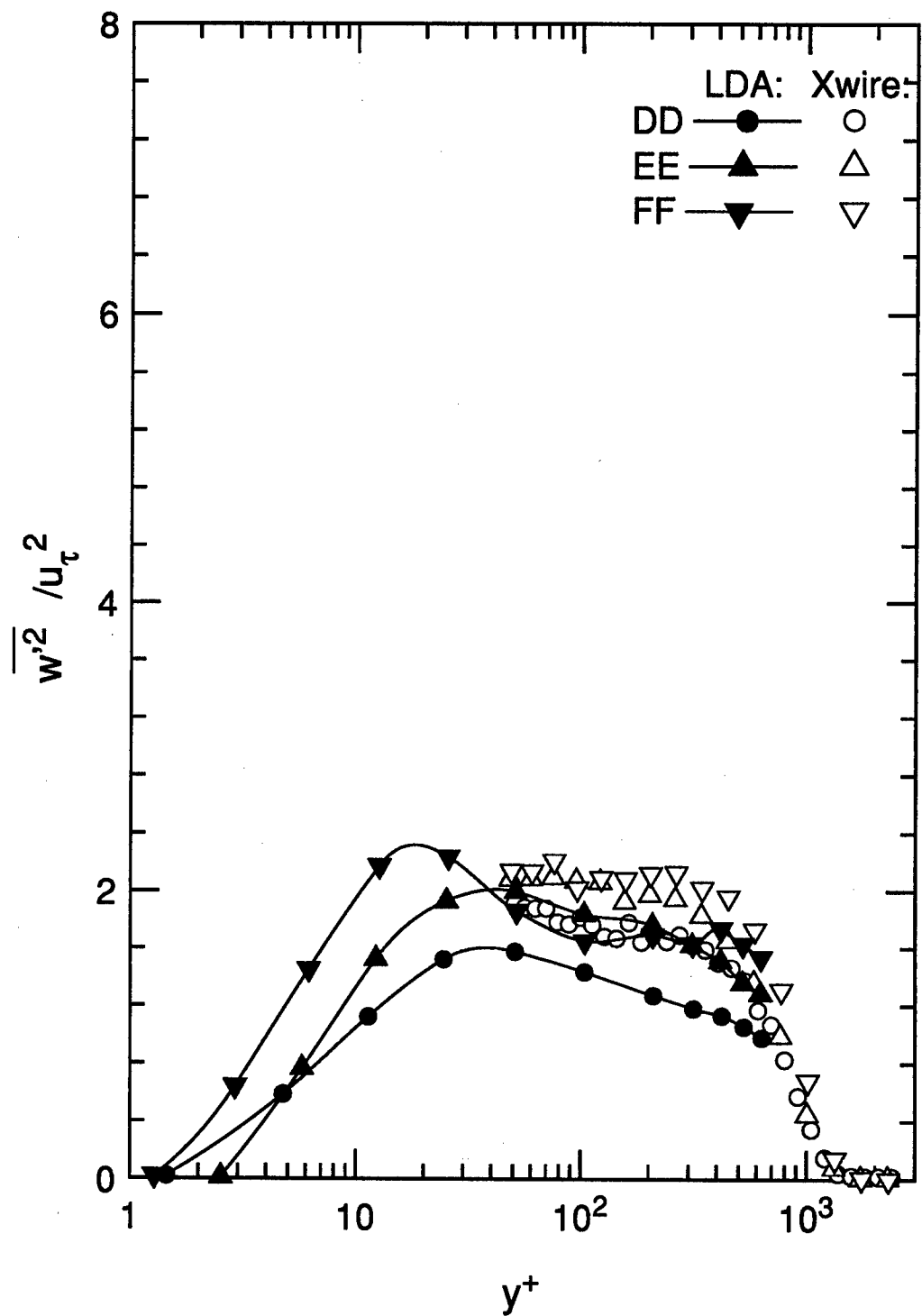Figure 5.4. $\overline{v'^2}$ normal stress. $z = -3.5$.

Figure 5.5. $\overline{w'^2}$ normal stress. $z = 0$.

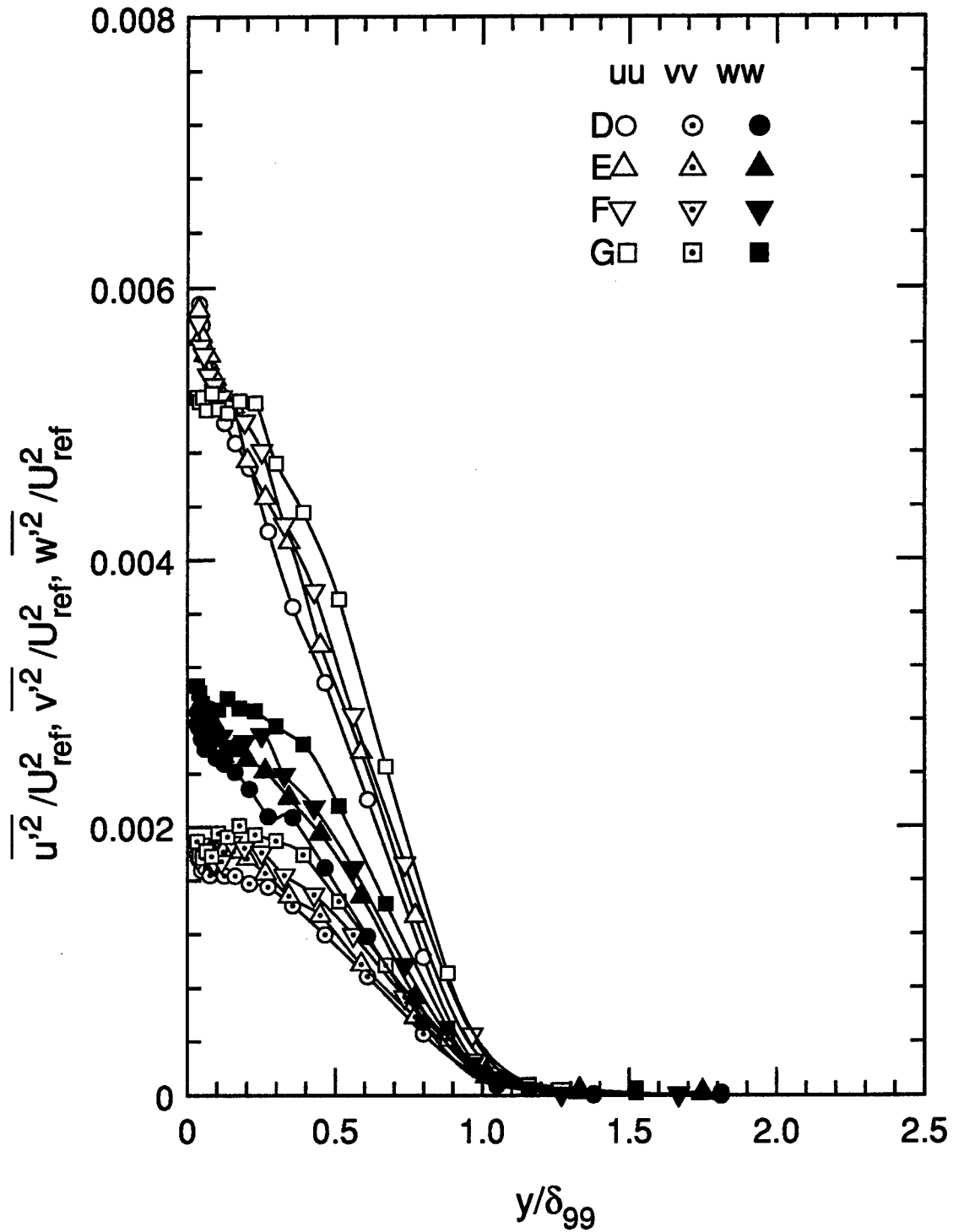Figure 5.6. $\overline{w'^2}$ normal stress. $z = -3.5$.

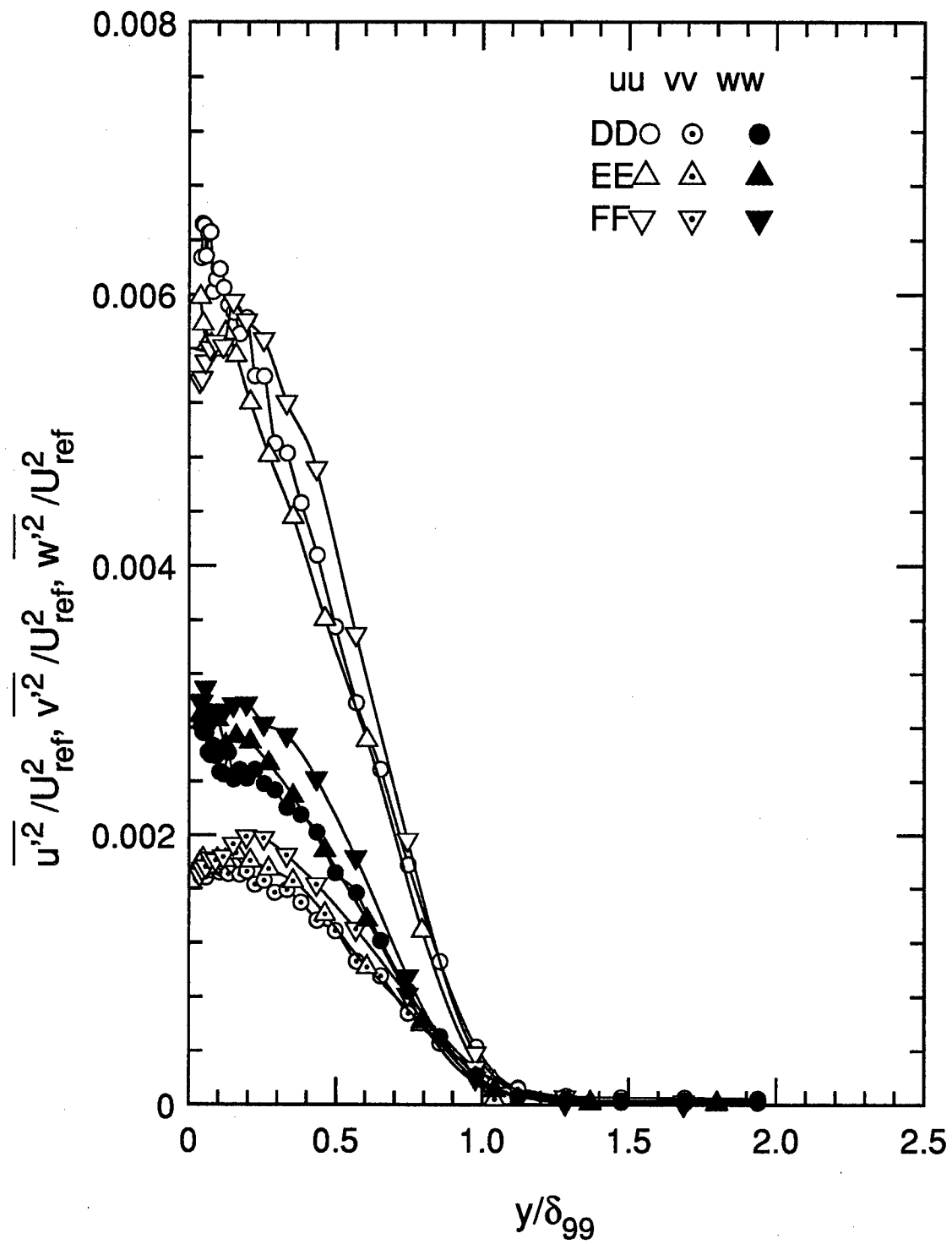Figure 5.7. Normal stresses measured by crosswire, normalized on U_{ref} and δ_{99}. $z = 0$.

Figure 5.8. Normal stresses measured by crosswire, normalized on U_{ref} and δ_{99}. $z = -3.5$.
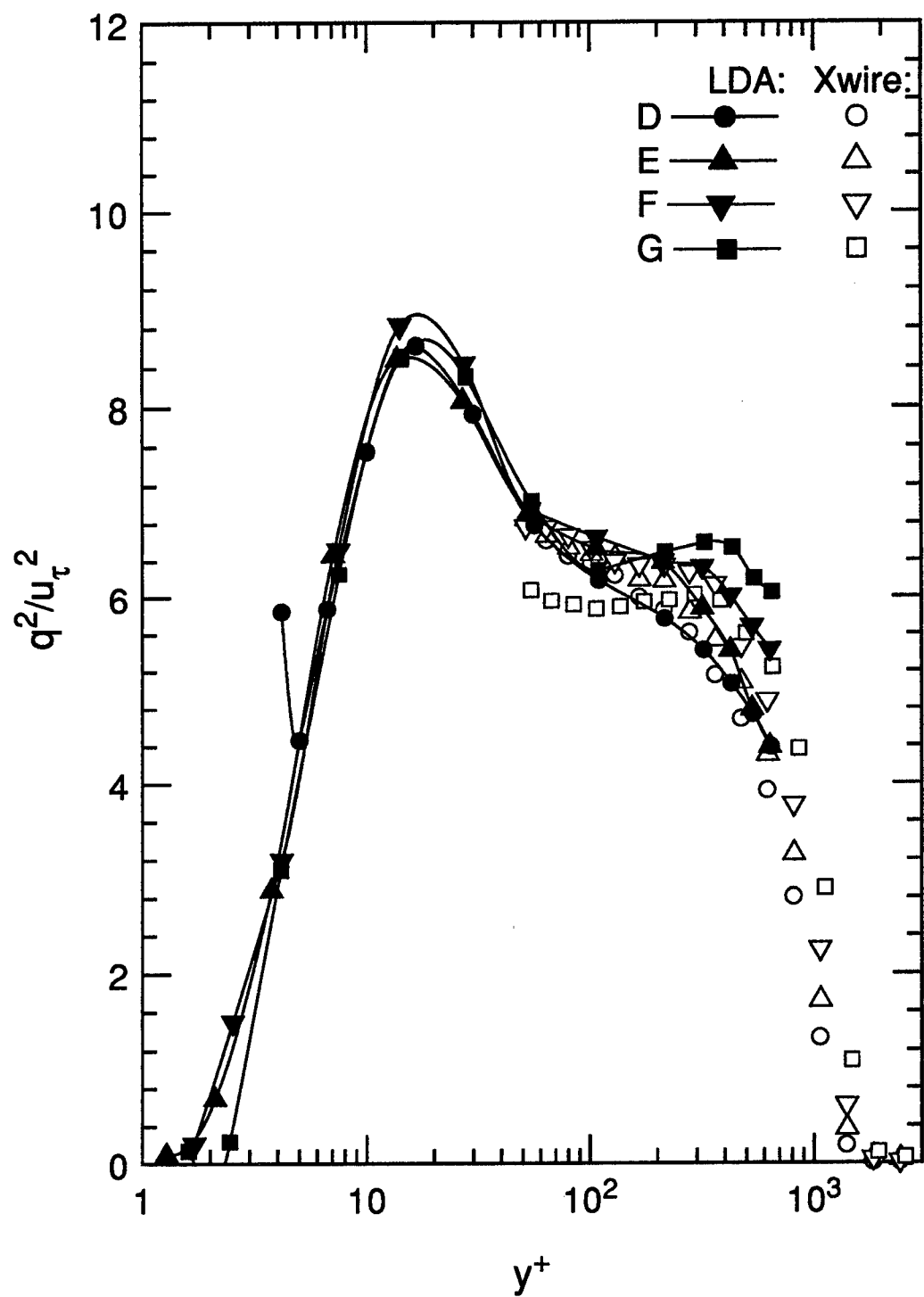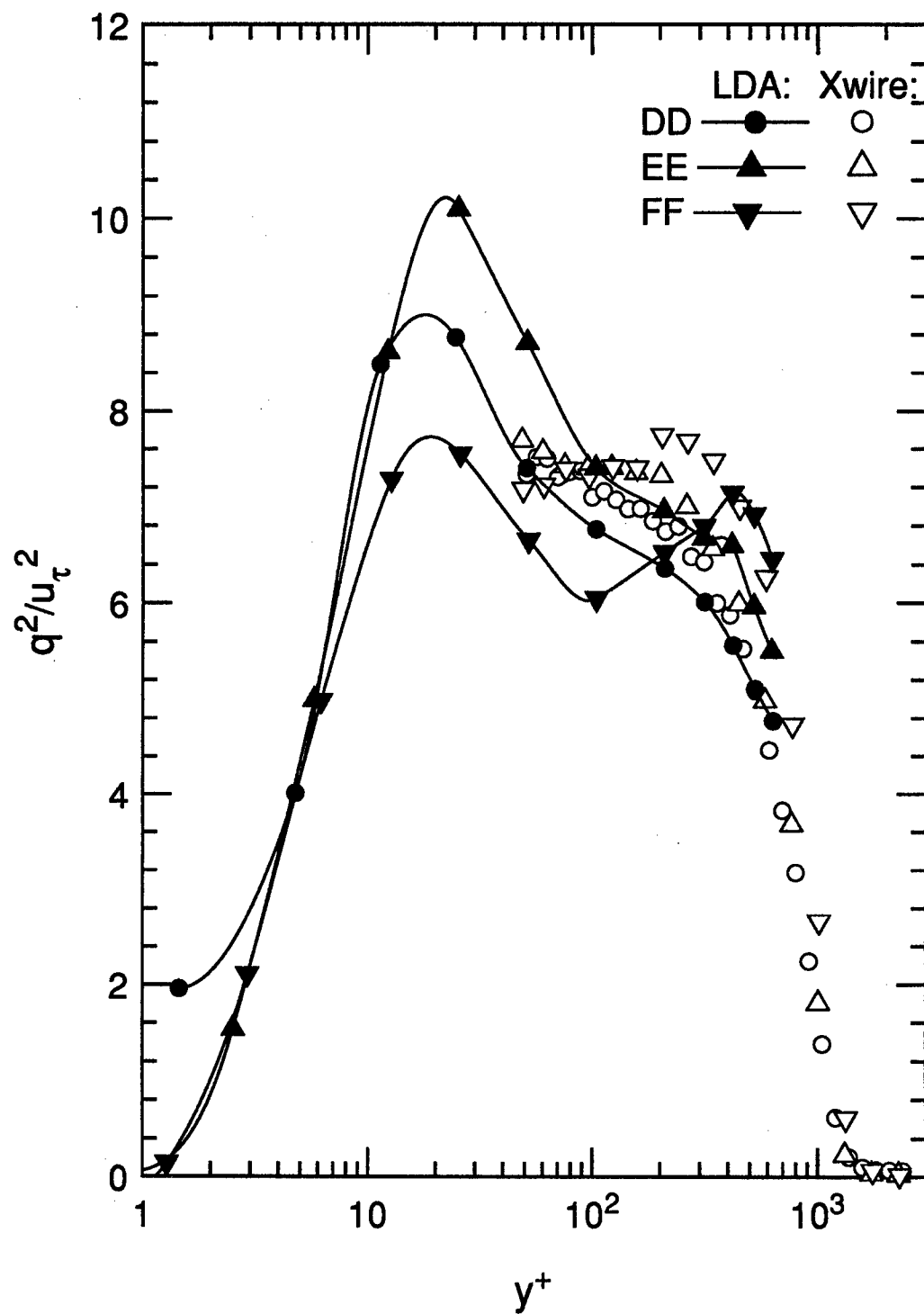
Figure 5.9. Turbulent kinetic energy. $z = 0$.
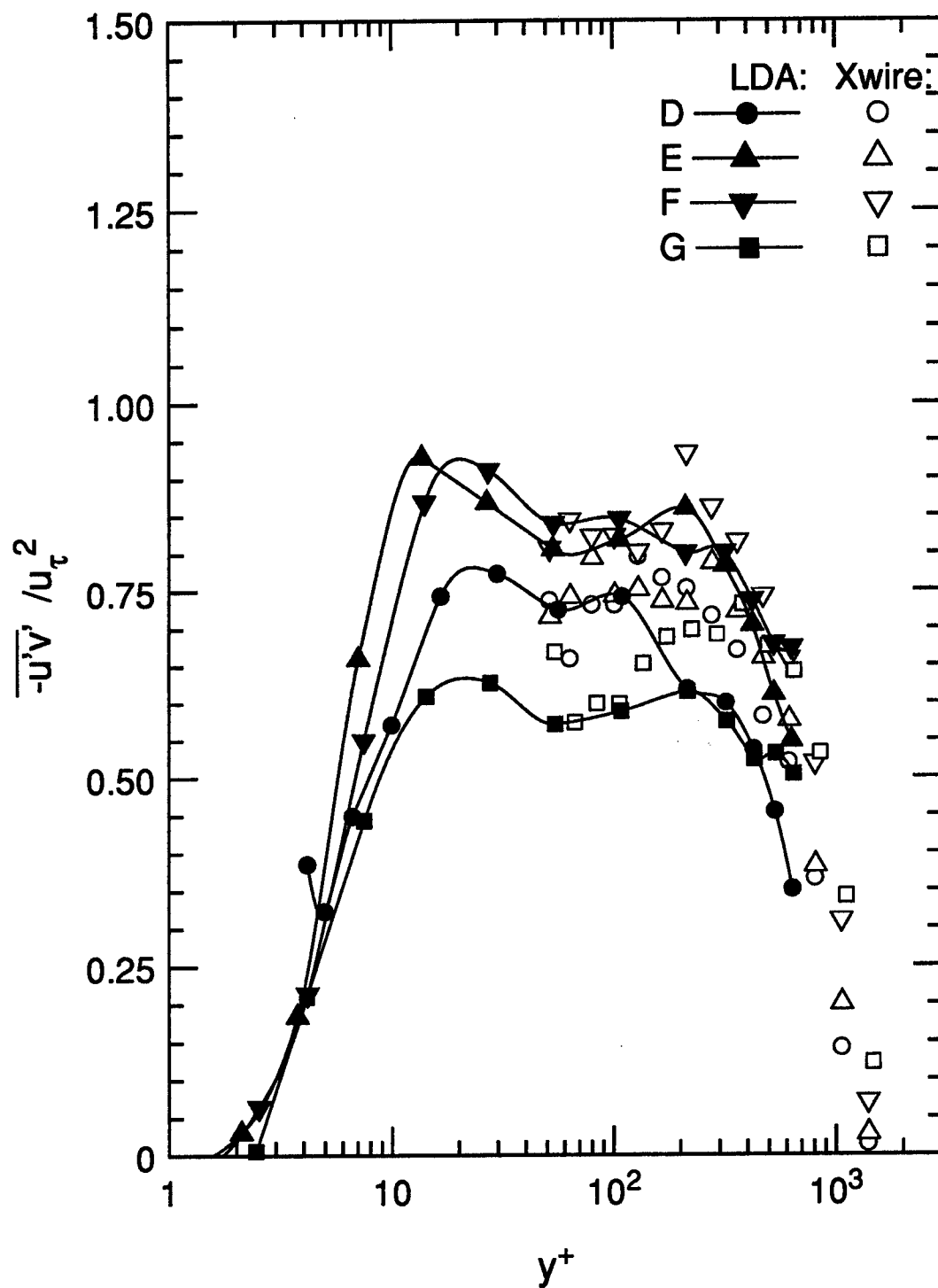
Figure 5.10. Turbulent kinetic energy. $z = -3.5$.

Figure 5.11. $-\overline{u'v'}$ shear stress. $z = 0$.
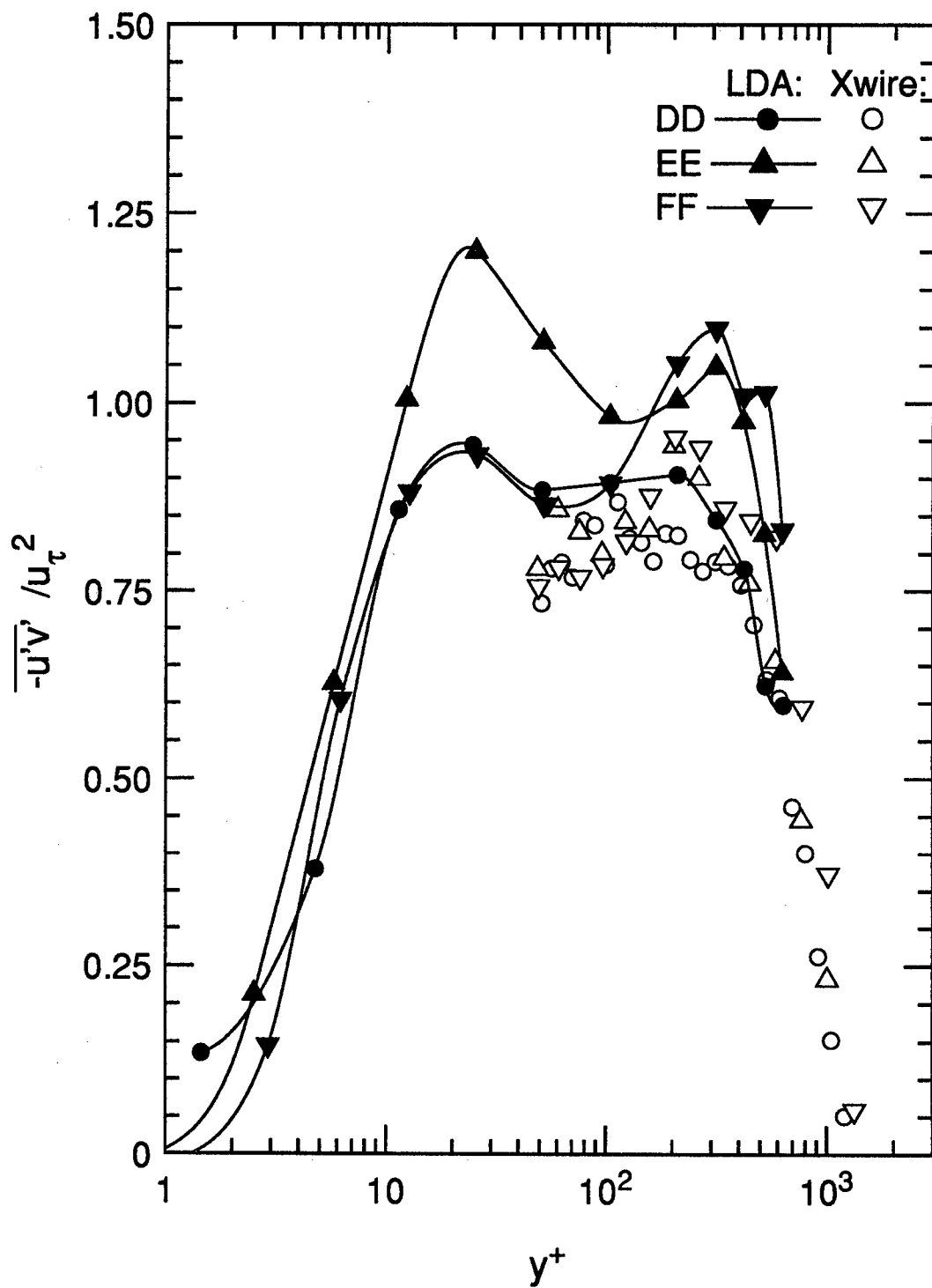
Figure 5.12. $-\overline{u'v'}$ shear stress. $z = -3.5$.
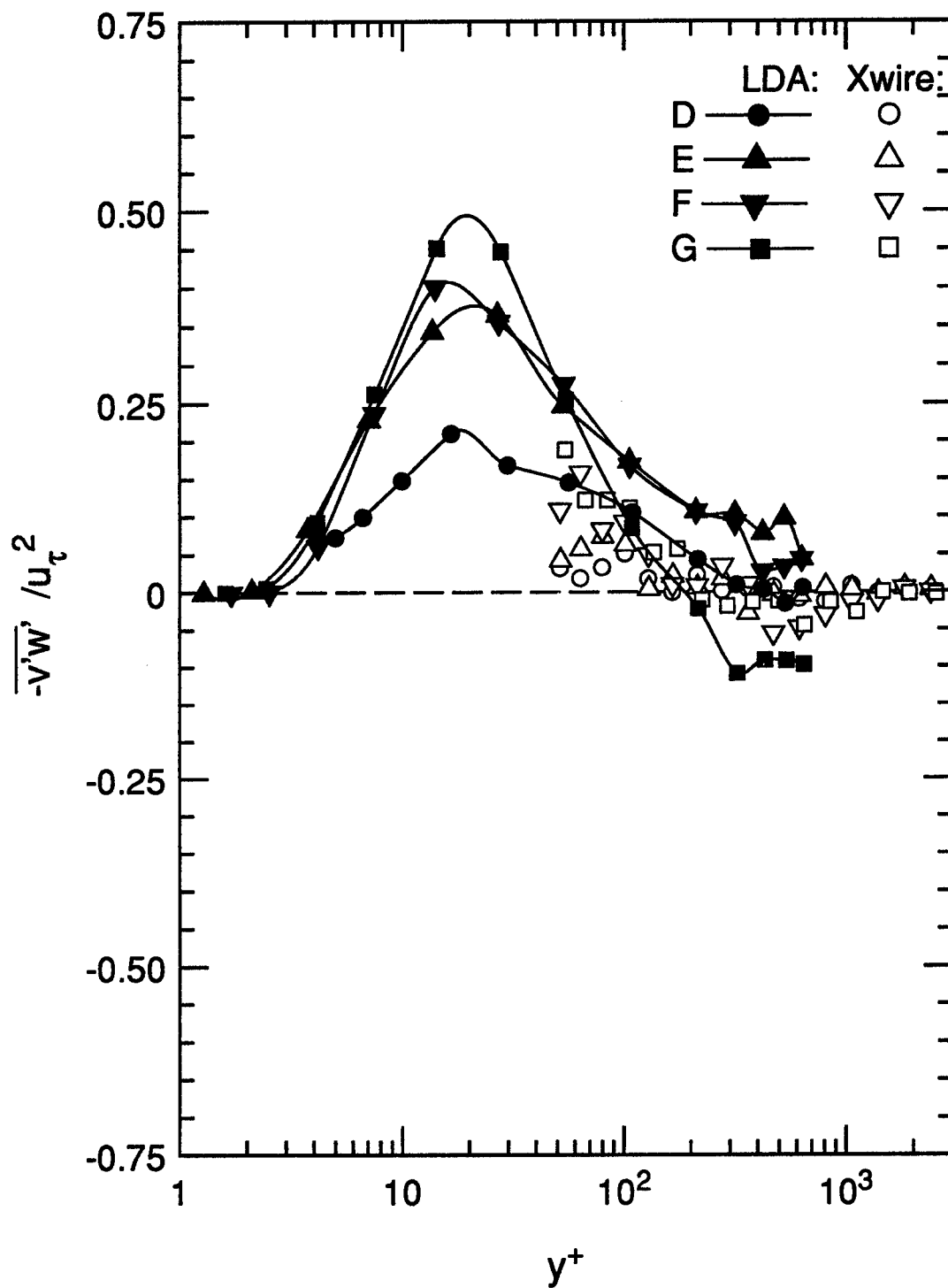
Figure 5.13. $-\overline{v'w'}$ shear stress. $z = 0$.
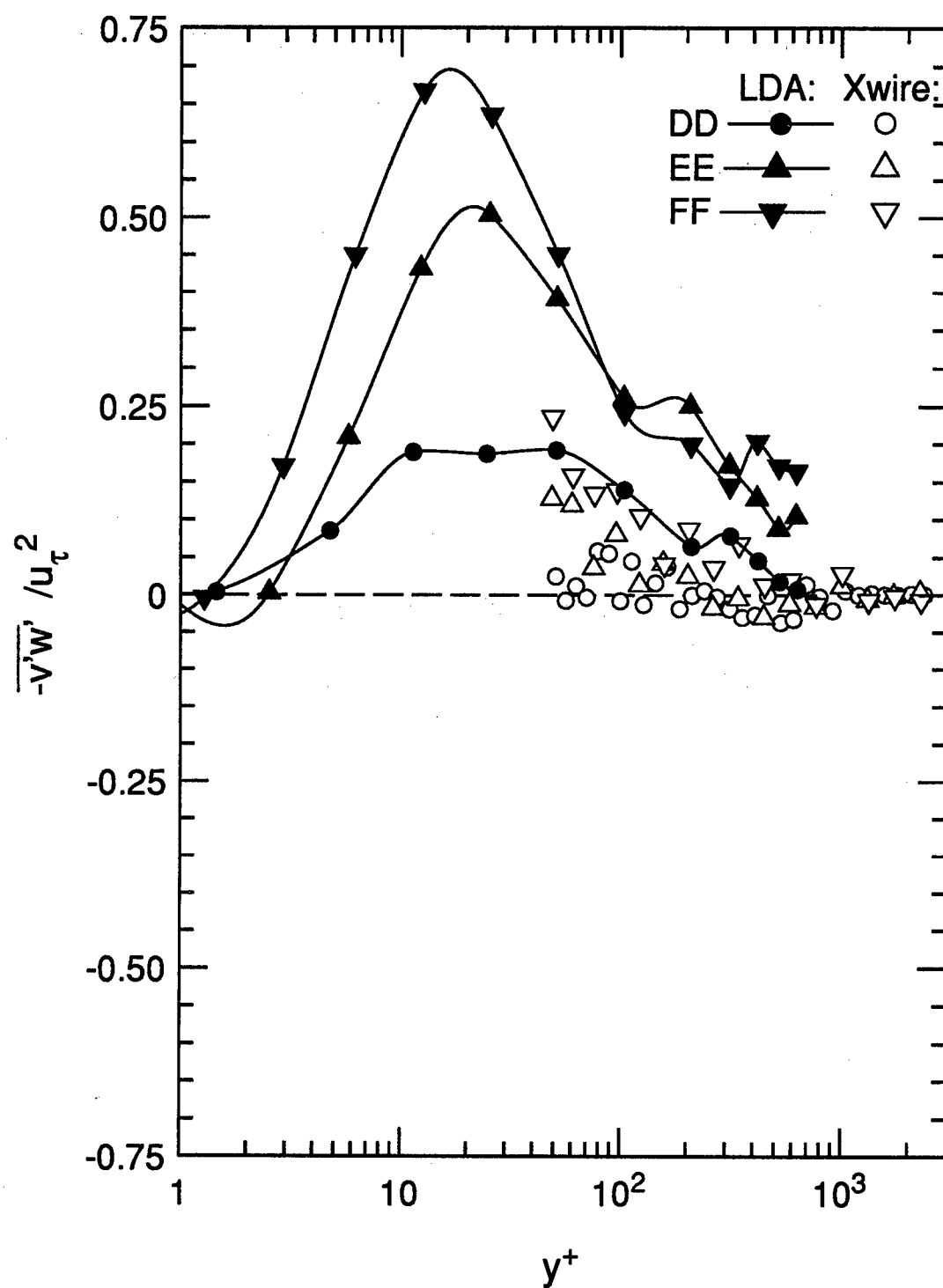
Figure 5.14. $-\overline{v'w'}$ shear stress. $z = -3.5$.
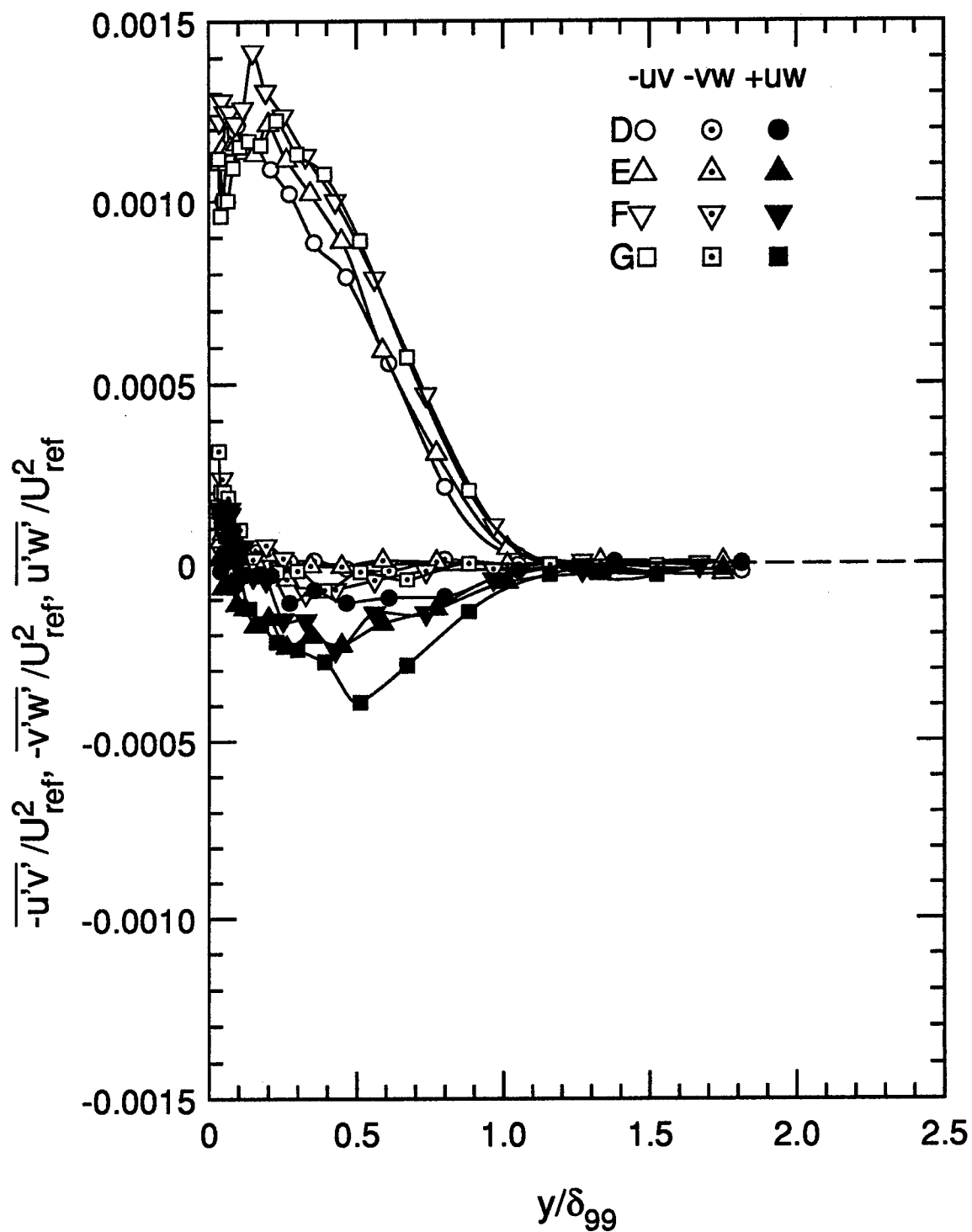
Figure 5.15. Shear stresses measured by crosswire, normalized on U_{ref} and δ_{99}. $z = 0$.
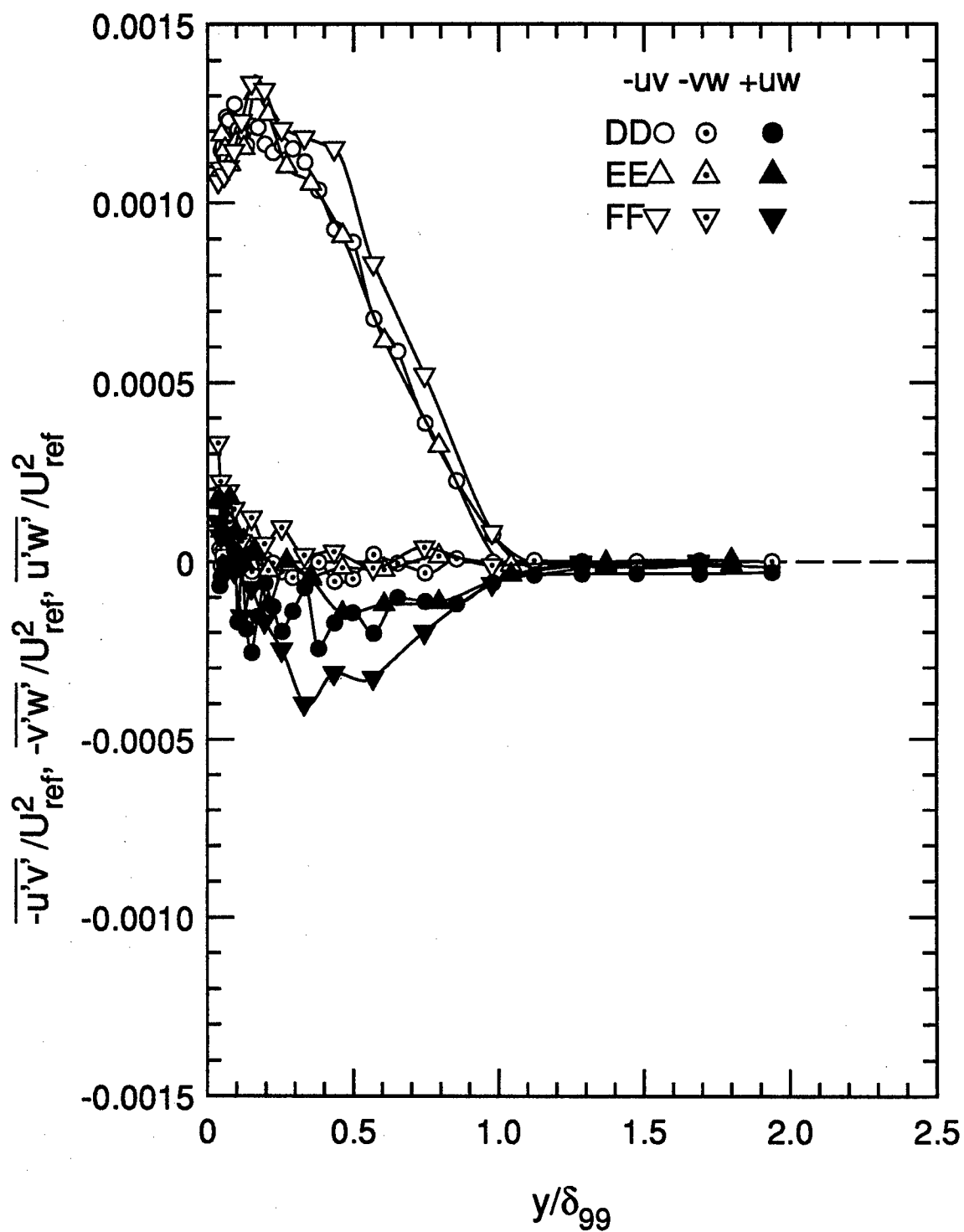
Figure 5.16. Shear stresses measured by crosswire, normalized on U_{ref} and δ_{99}. $z = -3.5$.
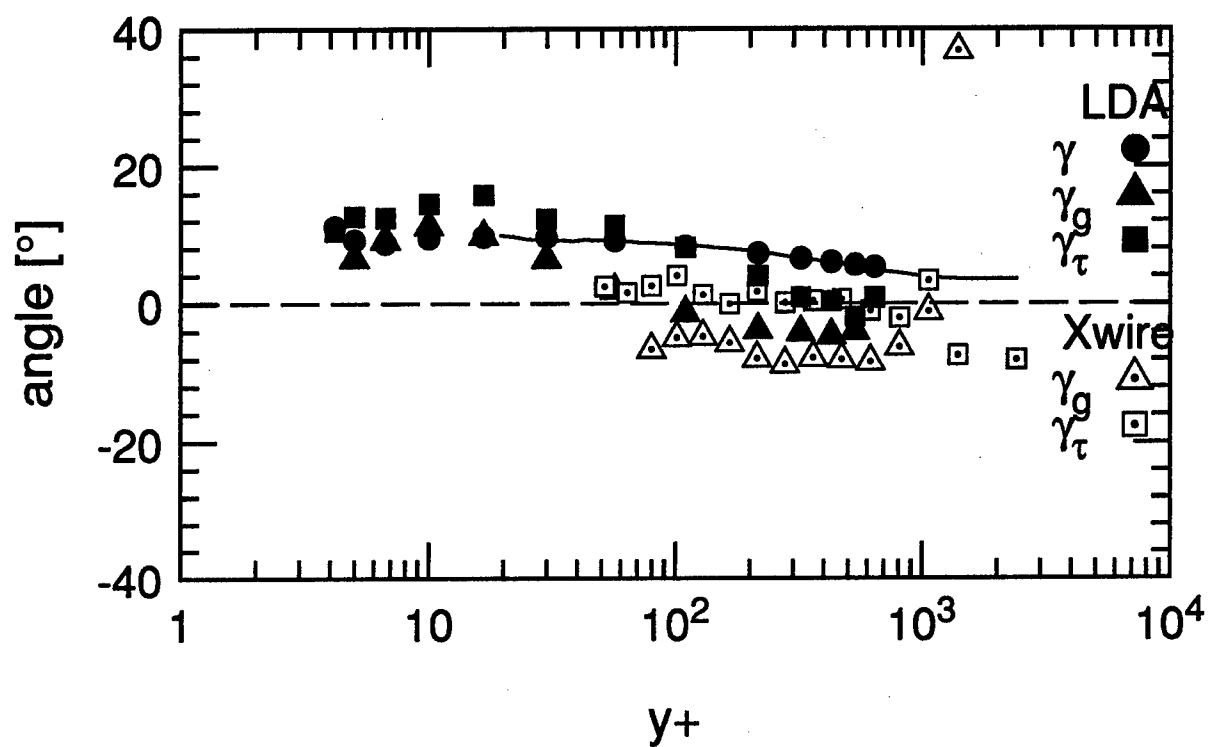
Figure 5.17. Flow angles, station D
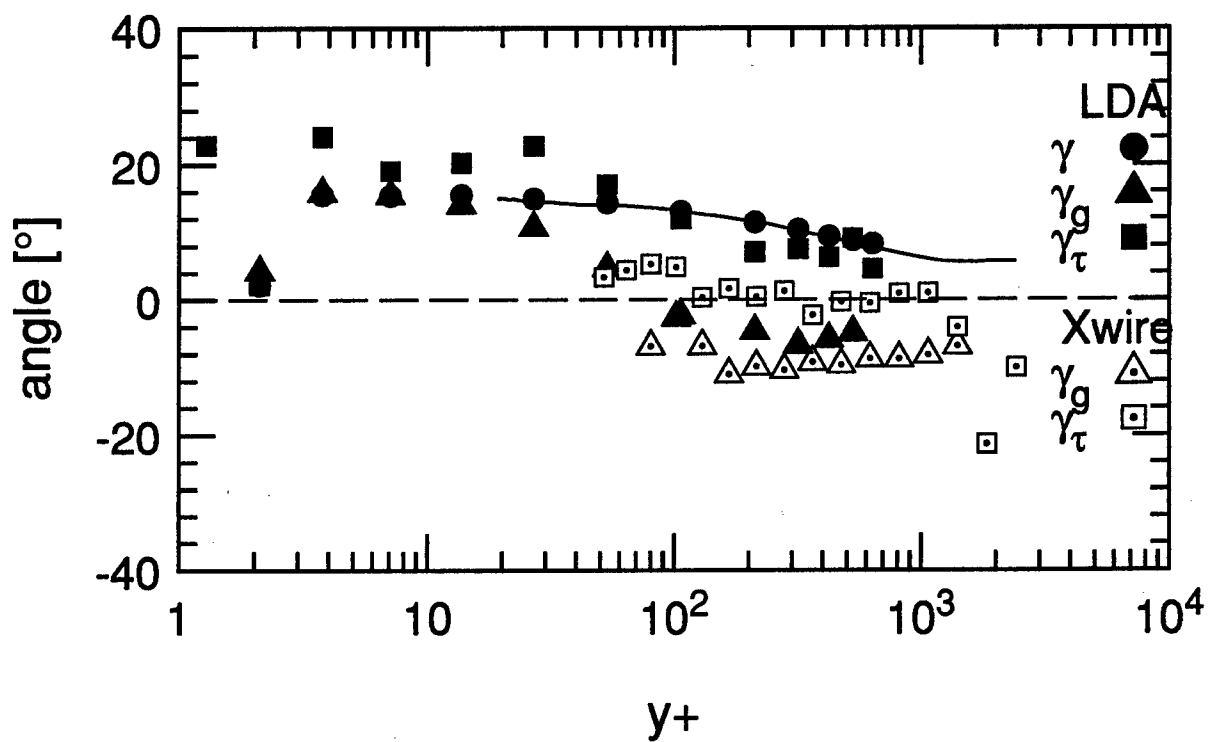
Figure 5.18. Flow angles, station E
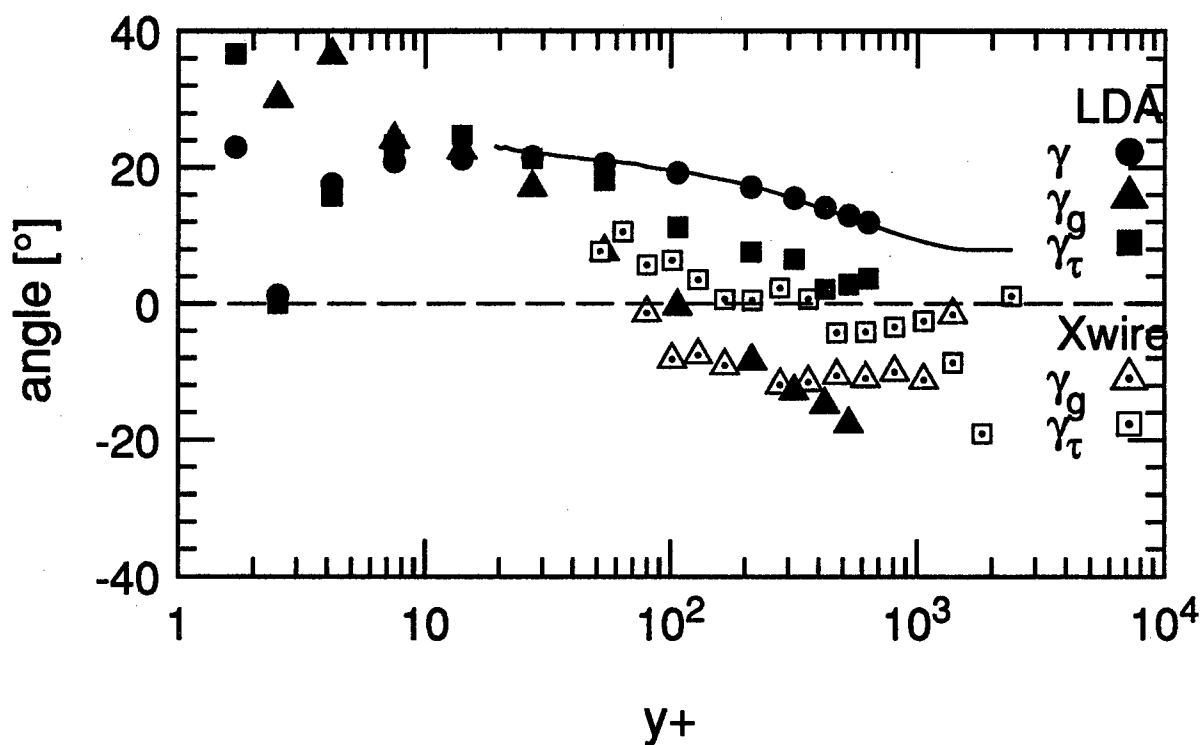
Figure 5.19. Flow angles, station F
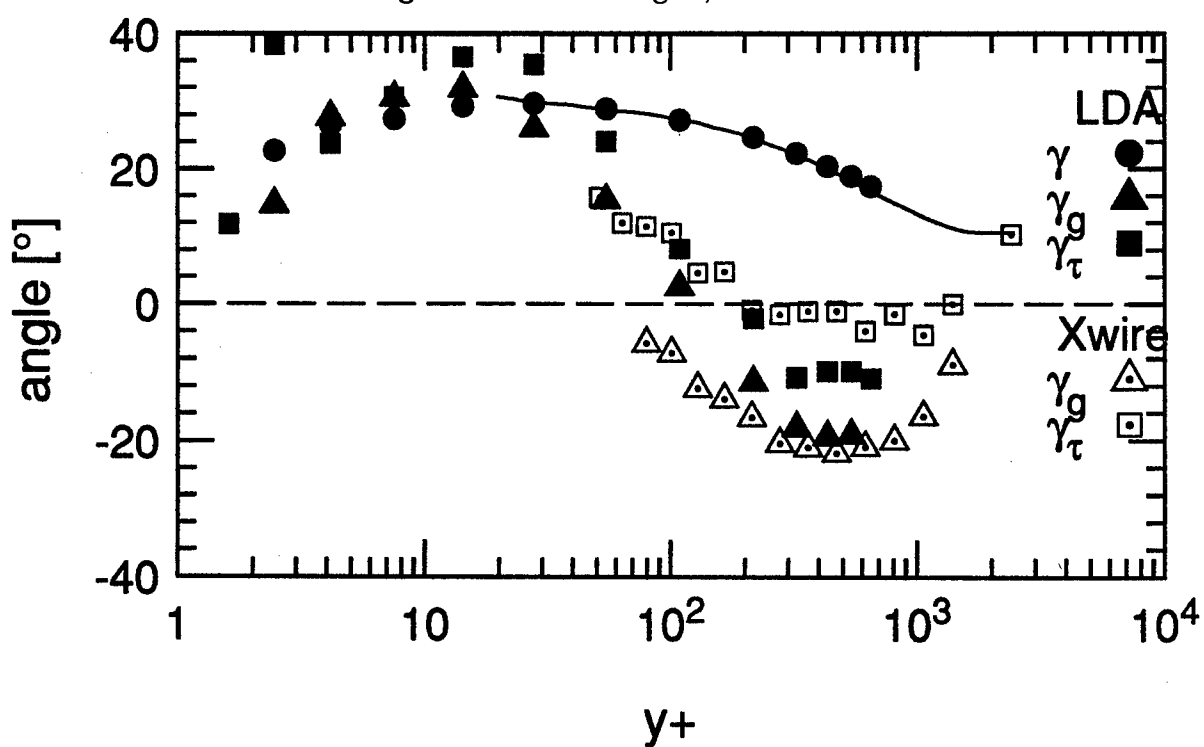
Figure 5.20. Flow angles, station G
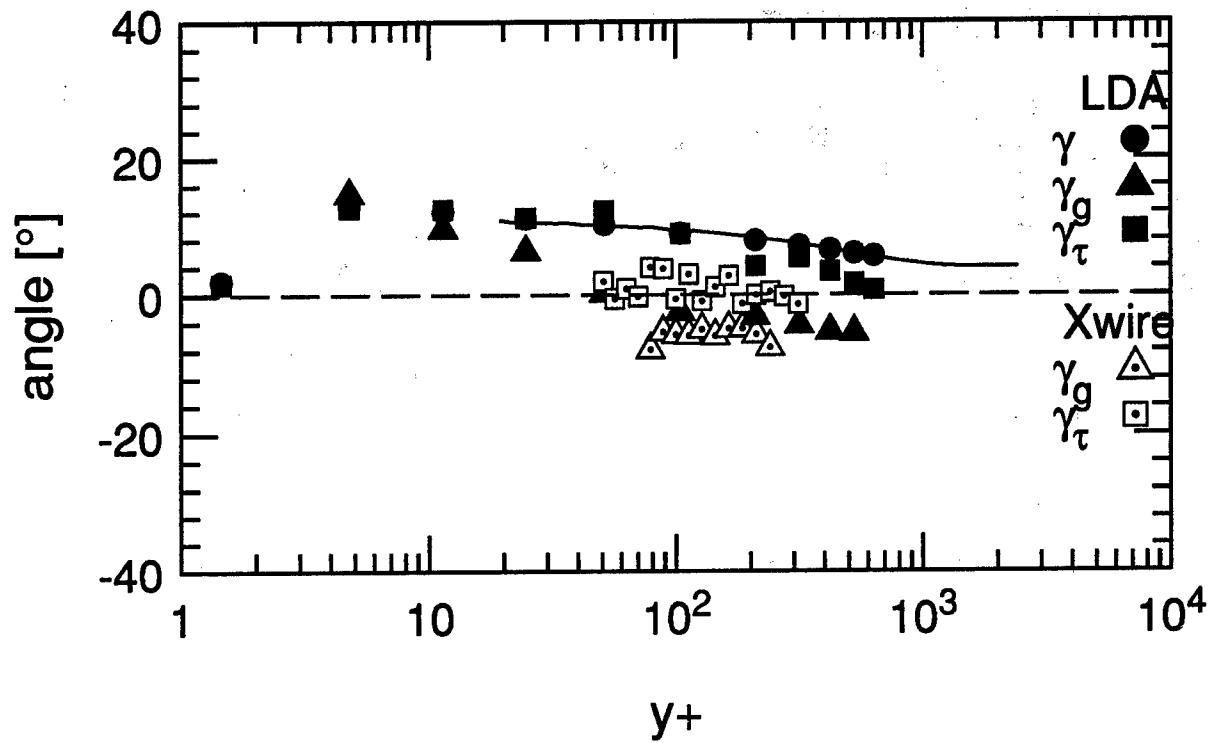
Figure 5.21. Flow angles, station DD
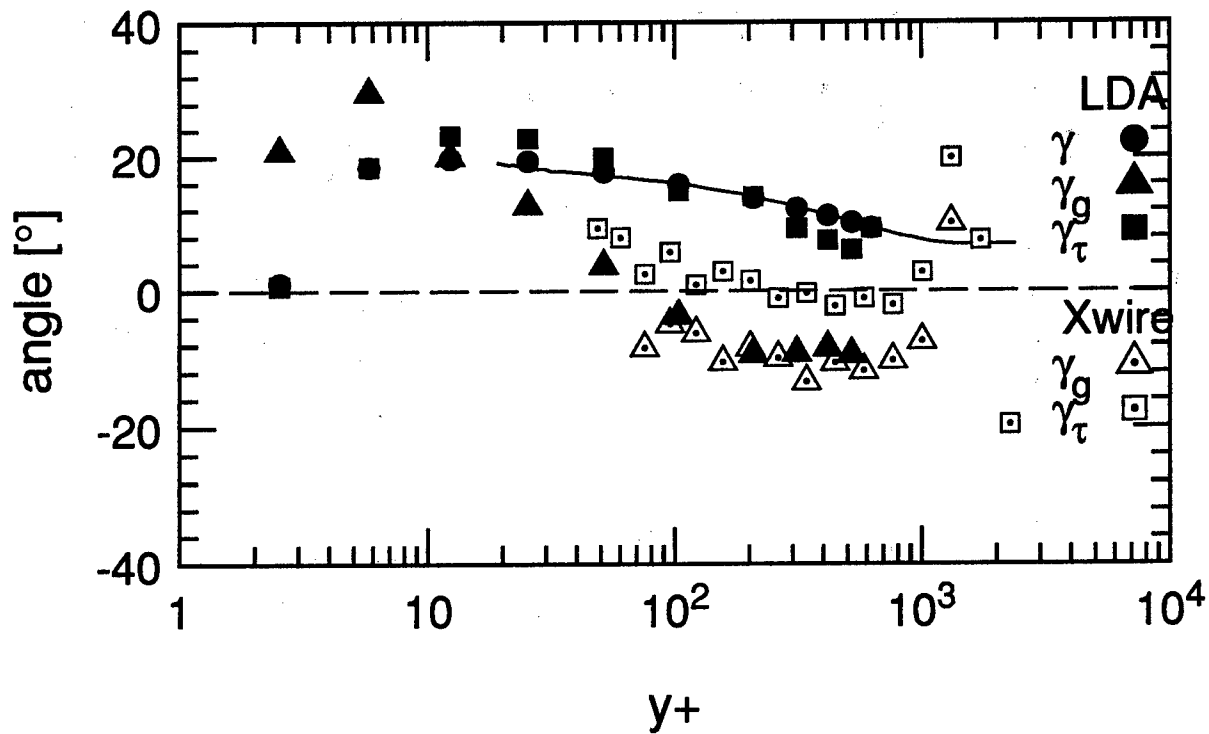
Figure 5.22. Flow angles, station EE
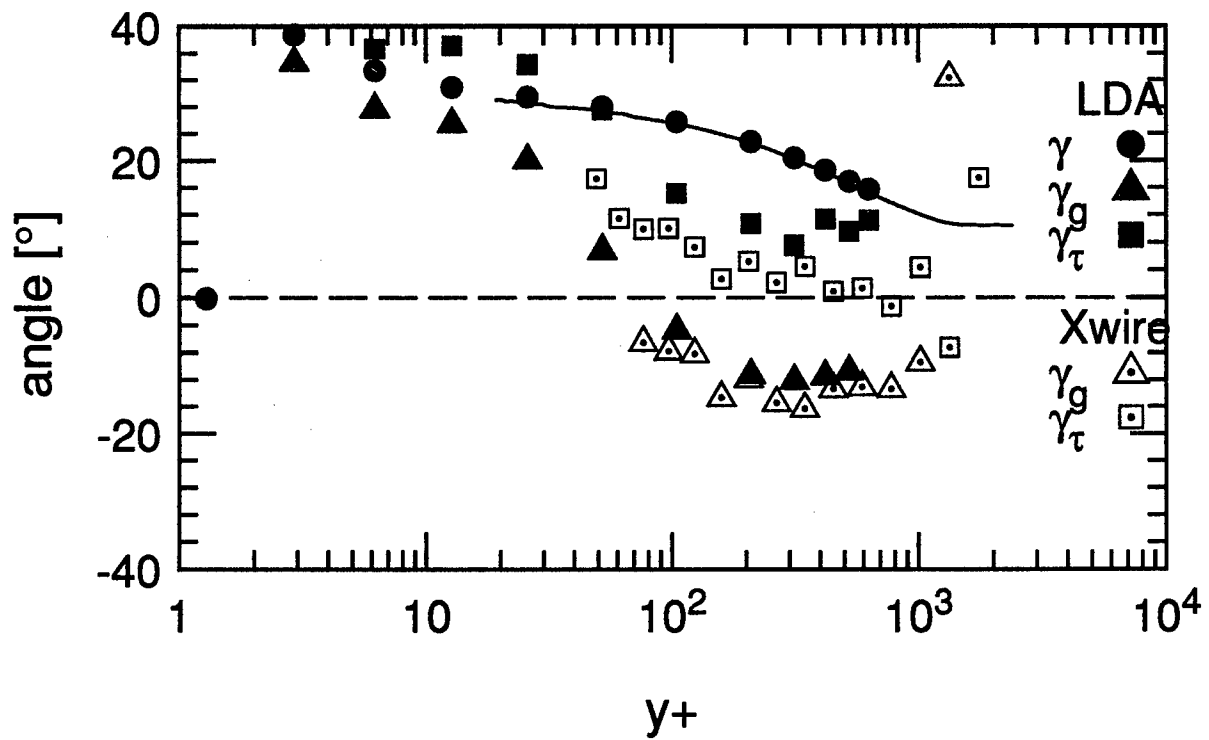
Figure 5.23. Flow angles, station FF
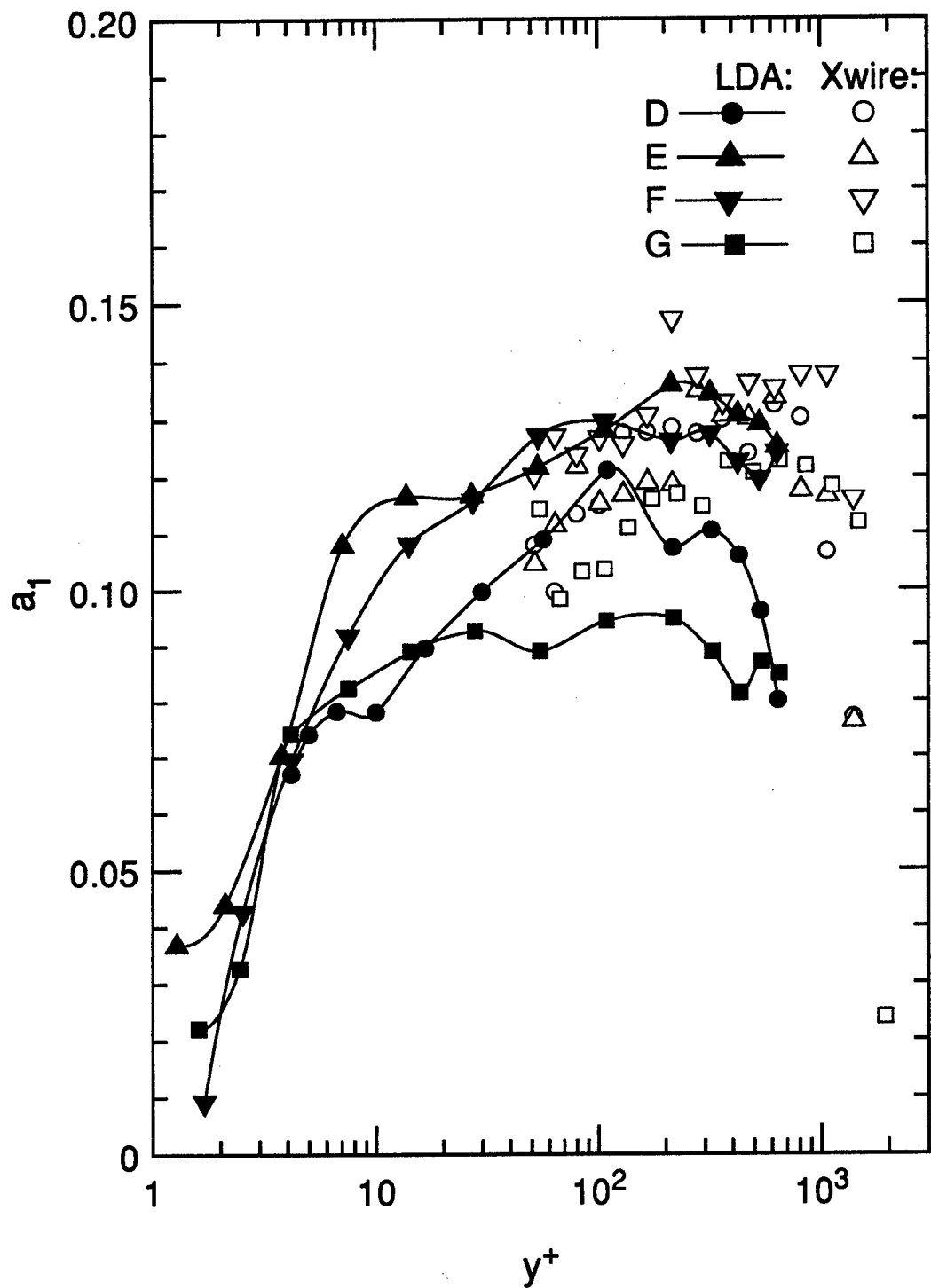
Figure 5.24. a_1 turbulence structure parameter. $z = 0$.
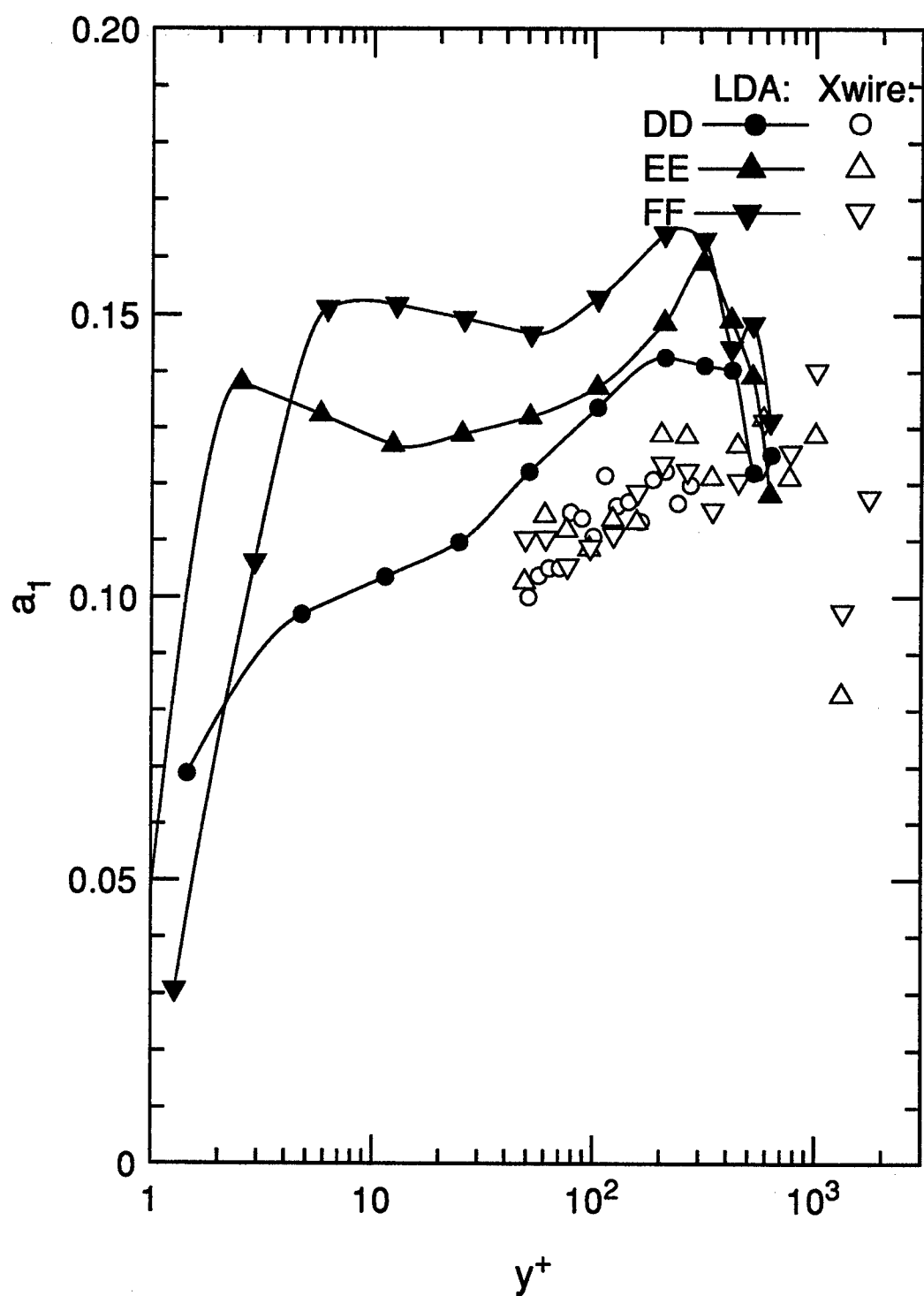
Figure 5.25. a_1 turbulence structure parameter. $z = -3.5$.
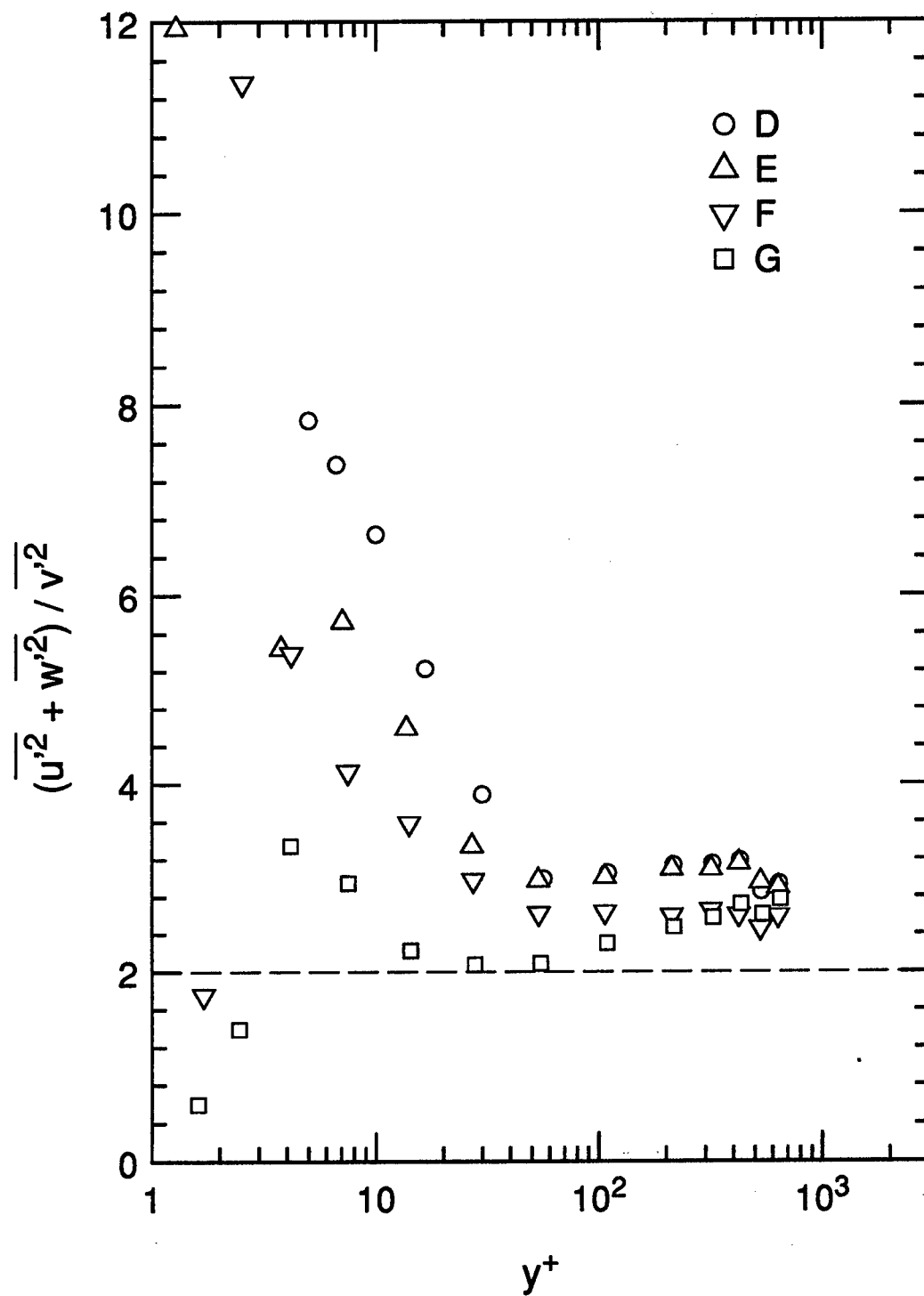
Figure 5.26. $(\overline{u'^2} + \overline{w'^2})/\overline{v'^2}$ turbulence structure parameter. $z = 0$.
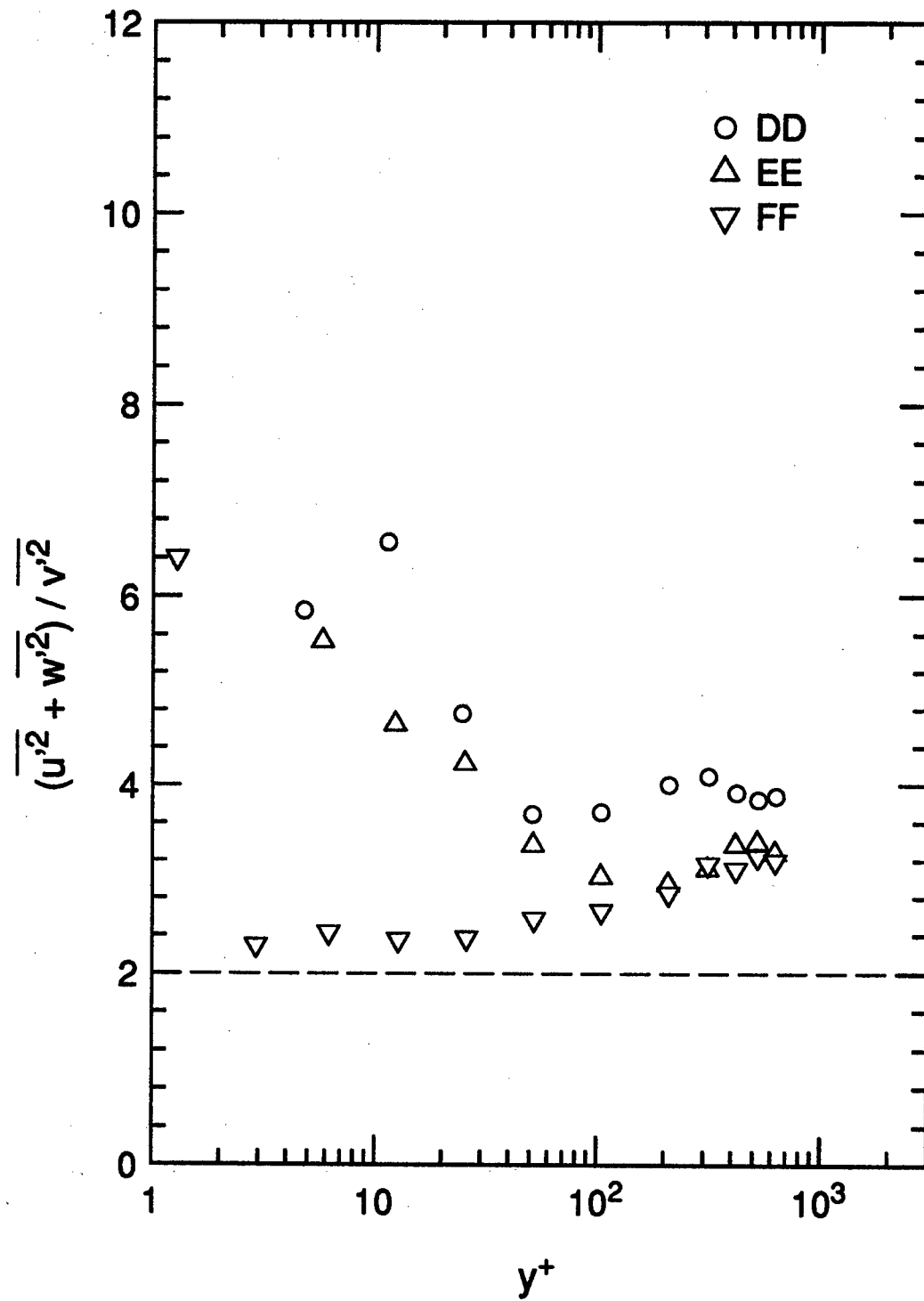
Figure 5.27. $(\overline{u'^2} + \overline{w'^2})/\overline{v'^2}$ turbulence structure parameter. $z = 0$.
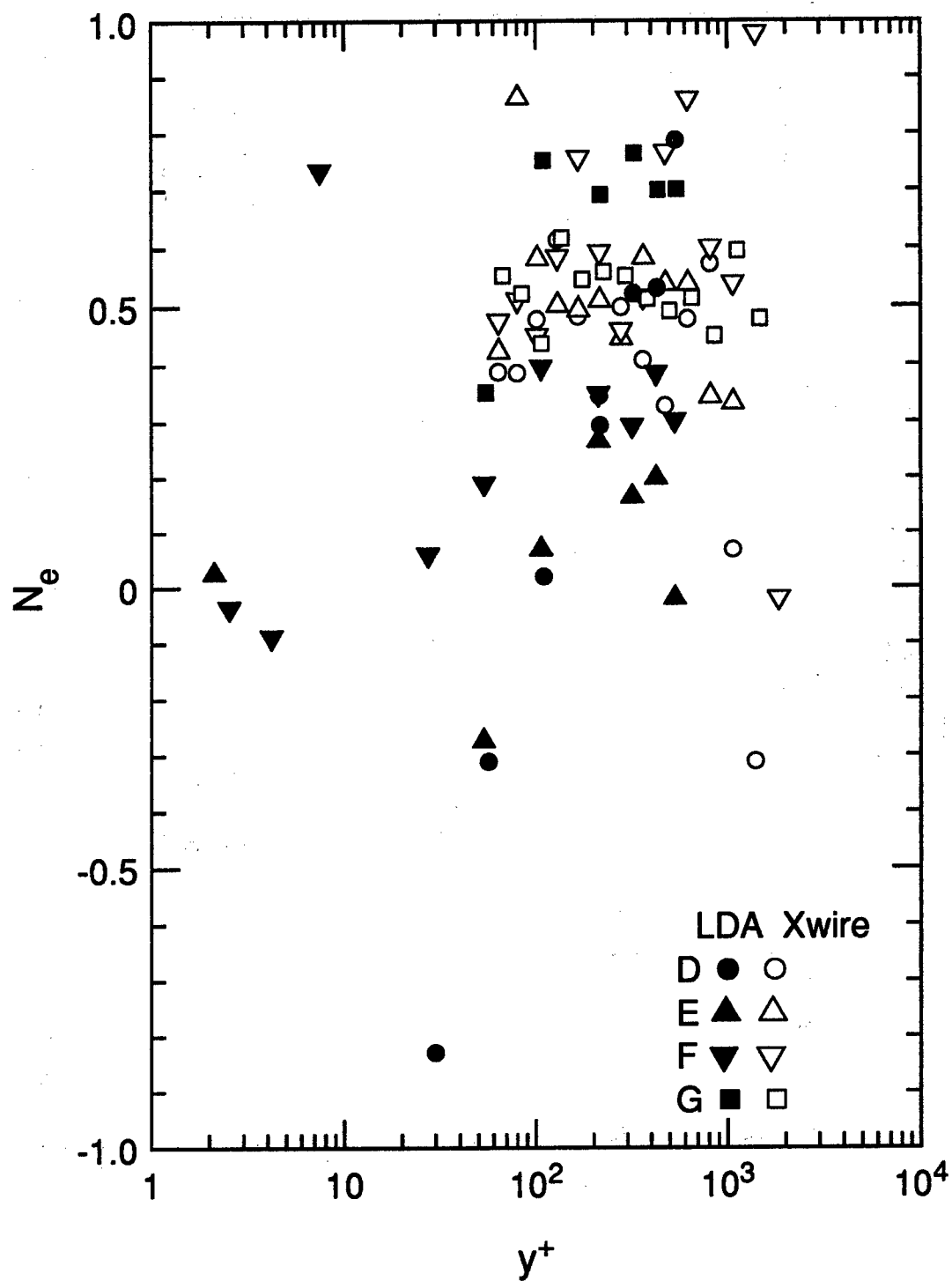
Figure 5.28. Eddy viscosity ratio N_e. $z = 0$.
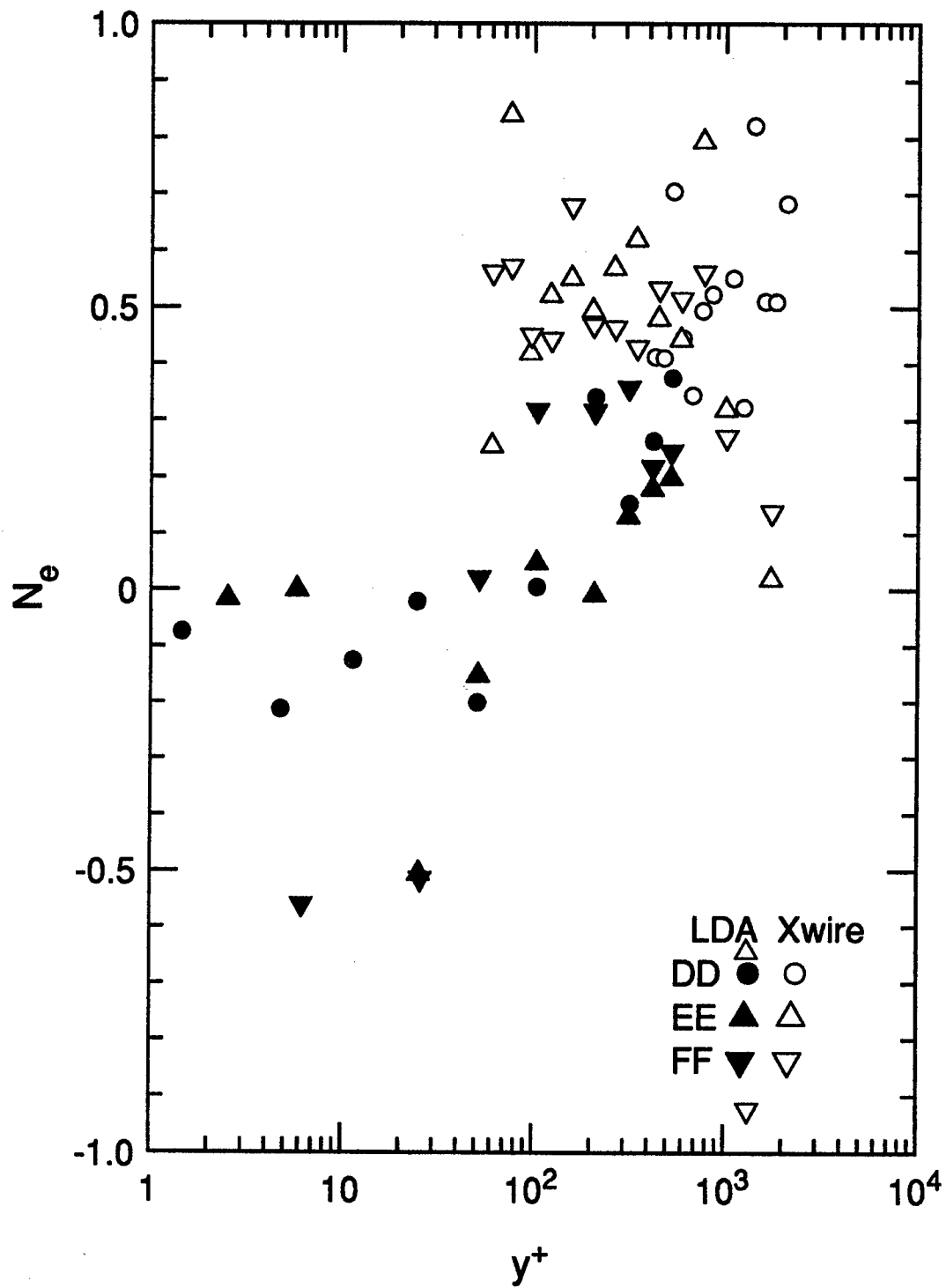
Figure 5.29. Eddy viscosity ratio N_e. $z = -3.5$.

Chapter 6

Reynolds Stress Transport

6.1 Overview

In this chapter we discuss the Reynolds stress transport equations and examine each term, evaluating it either directly from the data or indirectly, from equation balances. We also derive a transport equation for a_1 and evaluate its terms. Plots of the transport equation terms are presented at two stations in the three-dimensional boundary layer; one at the inception of three-dimensionality (station "D") and one where the flow is highly skewed (station "G"). We also present the vertical transport velocities for all stations where LDA data were acquired.

The transport equations for the Reynolds stresses are developed from the Navier-Stokes equations, by adding u_i times the u_j equation to u_j times the u_i equation:

$$\frac{D(u_i u_j)}{Dt} = u_i \frac{Du_j}{Dt} + u_j \frac{Du_i}{Dt} \tag{6.1}$$

Upon Reynolds averaging, we find for a steady flow:

$$
U_k \frac{\partial(-\overline{u_i' u_j'})}{\partial x_k} = \overbrace{\overline{u_i' u_k'}\frac{\partial U_j}{\partial x_k} + \overline{u_j' u_k'}\frac{\partial U_i}{\partial x_k}}^{\mathcal{P}_{ij}} \overbrace{- \frac{1}{\rho}\left[\overline{p'\left(\frac{\partial u_i'}{\partial x_j} + \frac{\partial u_j'}{\partial x_i}\right)}\right]}^{\Phi_{ij}} \overbrace{- 2\nu\overline{\frac{\partial u_i'}{\partial x_k}\frac{\partial u_j'}{\partial x_k}}}^{\mathcal{D}_{ij}}
$$

$$
+ \underbrace{\frac{\partial}{\partial x_k}\left[\frac{1}{\rho}\left(\overline{p' u_i'}\delta_{jk} + \overline{p' u_j'}\delta_{ik}\right) + \overline{u_i' u_j' u_k'} + \nu\frac{\partial \overline{u_i' u_j'}}{\partial x_k}\right]}_{\mathcal{J}_{ijk}} \tag{6.2}
$$

The first term represents the generation or "production" of $\overline{u_i' u_j'}$:

$$\mathcal{P}_{ij} \equiv \overline{u_i' u_k'}\frac{\partial U_j}{\partial x_k} + \overline{u_j' u_k'}\frac{\partial U_i}{\partial x_k} \tag{6.3}$$

The generation term represents the effects of the mean velocity gradients on the Reynolds stresses. It is also known as the Reynolds stress production. It is possible to directly measure the $\mathcal{P}_{ij}$ terms.

The second term is known as the pressure-strain redistribution term:

$$\Phi_{ij} \equiv \frac{1}{\rho}\left[\overline{p'\left(\frac{\partial u_i'}{\partial x_j} + \frac{\partial u_j'}{\partial x_i}\right)}\right] \tag{6.4}$$

It represents a tendency for the Reynolds stresses to become isotropic. We cannot measure the pressure fluctuations locally, nor can we measure their correlations with velocity gradients.

Next is the viscous destruction term

$$\mathcal{D}_{ij} \equiv 2\nu\overline{\frac{\partial u_i'}{\partial x_k}\frac{\partial u_j'}{\partial x_k}} \tag{6.5}$$

This is sometimes referred to as the dissipation rate.

The third-order diffusion term, representing the turbulent transport of the Reynolds stresses, is

$$\mathcal{J}_{ijk} \equiv \frac{1}{\rho}\left(\overline{p'u_i'}\delta_{jk} + \overline{p'u_j'}\delta_{ik}\right) + \overline{u_i'u_j'u_k'} + \nu\frac{\partial\overline{u_i'u_j'}}{\partial x_k} \tag{6.6}$$

Again, we cannot measure the terms containing p'. We also do not have the capability to measure the second derivatives of the Reynolds stresses with respect to x and z. We do measure most of the triple products, and can calculate their derivatives.

6.2 Methods of determining derivatives

In addition to the seven primary LDA profiles which we have been presenting, we acquired profiles at six secondary locations. The (x, z) coordinates of the profile locations used to calculate streamwise and spanwise derivatives are presented in table 6.1. To calibrate the LDA in places away from our pressure profiles, we interpolated the pressure field at the calibration height.

We use a central difference formula with secondary profiles 2 and 4 to calculate $\frac{\partial}{\partial z}$ derivatives, and with secondary profile 3 and the primary profile to calculate $\frac{\partial}{\partial x}$ derivatives. To calculate wall-normal derivatives, we use the parabolic derivative formula cited in the previous chapter. Second derivatives were calculated using the

related formula:

$$\left.\frac{\partial^2 f}{\partial y^2}\right|_{y=y_i} = 2\frac{(y_{i+1} - y_i)(f_{i-1} - f_i) - (y_{i-1} - y_i)(f_{i+1} - f_i)}{(y_{i-1} - y_i)^2(y_{i+1} - y_i) - (y_{i+1} - y_i)^2(y_{i-1} - y_i)} \tag{6.7}$$

6.2.1 Error estimates in derivatives

We estimate the error intrinsic to the central difference formula,

$$\left.\frac{\partial f}{\partial x}\right|_i = \frac{f_{i+1} - f_{i-1}}{2h} \tag{6.8}$$

where h is the distance between data points:

$$h = x_{i+1} - x_i = x_i - x_{i-1} \tag{6.9}$$

The error in this method is equal to $\frac{1}{6}h^2 f'''(x)$. To quantify the error, we use another method to calculate the third derivative with respect to x. Using the data at stations D, E, F, and G, we apply the formula below, for the third derivative for evenly spaced data points.

$$f'''(x) = \frac{f_1 - 3f_2 + 3f_3 - f_4}{\Delta x} \tag{6.10}$$

Upon calculating f''', we find that the error in $\frac{\partial U}{\partial x}$ from using equation 6.8 is on average 2.0% and never greater than 5%. Another issue in error is the small y offset of the various profiles. Near the wall, where the derivatives in y are large, we expect to see some error due to data acquired at very slightly different heights. We may be forced to ignore some of the points that are closest to the wall. We expect that the error $\frac{\partial U}{\partial z}$ should be comparable to the error in $\frac{\partial U}{\partial x}$, and that the errors in W and the Reynolds stresses will likewise be similar. Strictly, the central difference formulas apply to the center location between the four profile locations. Since the second derivatives are small, as evidenced by the slowly changing data presented in the previous chapters, we consider the calculated derivatives to be also valid at the primary profile locations.

When differentiating with respect to y there is potential for scatter in the data causing unreliable derivatives. The largest potential error in the Reynolds stress transport terms is due to inaccuracies in $\frac{\partial U}{\partial y}$ near the wall where the production terms are at their largest. We performed error analysis on $\frac{\partial U}{\partial y}$ based on the scatter we

predicted in Chapter 3. At $y^+ = 10$ the potential error in $\frac{\partial U}{\partial y}$ is 3% of the calculated $\frac{\partial U}{\partial y}$. At $y^+ = 100$ the absolute error is one fifth the size of the error at $y^+ = 10$, but represents a 10% error in the measured $\frac{\partial U}{\partial y}$. We are confident that the derivatives with respect to y are not overly contaminated by scatter, since the mean velocity gradient angle γ_g from LDA data in chapter 5 was observed to be quite smooth.

6.3 Turbulent kinetic energy transport

To derive the transport equation for turbulent kinetic energy, we take the trace of equation 6.2. Note that we use q^2 in place of k, so we are actually referring to the transport of twice the turbulent kinetic energy. By continuity, Φ_{ii} is zero in a constant-density, steady flow. Equation 6.2 therefore reduces to:

$$
\overbrace{U_k \frac{\partial \overline{u_i' u_i'}}{\partial x_k}}^{\text{advection}} = \overbrace{-2\, \overline{u_i' u_k'} \frac{\partial U_i}{\partial x_k}}^{\text{production}} + \overbrace{2\nu \overline{\frac{\partial u_i'}{\partial x_k} \frac{\partial u_i'}{\partial x_k}}}^{\text{dissipation}}
$$

$$
\overbrace{-\frac{\partial}{\partial x_k}\left[\frac{2}{\rho}\overline{p' u_i'}\delta_{ik} + \overline{u_i' u_i' u_k'} + \nu \frac{\partial \overline{u_i' u_i'}}{\partial x_k}\right]}^{\text{turbulent transport}} \tag{6.11}
$$

It is possible to measure most of the terms in equation 6.11, with the exception of the turbulent pressure fluctuation term and the $\mathcal{D}_{ii}$ term. We can indirectly determine the sum of the dissipation and pressure fluctuation terms by measuring the other terms in equation 6.11. When the pressure fluctuation is negligible, this provides an estimate of the dissipation.

To further simplify the turbulent transport term, we apply the thin shear layer assumptions. Thus, we assume that for the normal stresses, the second derivatives with respect to y are much larger than the second derivatives with respect to x and z. Further, we can confirm with our experimental data relations 6.12 through 6.15 below.

$$
\frac{\partial}{\partial x}\overline{u'^3} \ll \frac{\partial}{\partial y}\overline{u'^2 v'} \tag{6.12}
$$

$$\frac{\partial}{\partial x}\overline{u'v'^2} \quad \ll \quad \frac{\partial}{\partial y}\overline{v'^3} \tag{6.13}$$

$$\frac{\partial}{\partial z}\overline{v'^2w'} \quad \ll \quad \frac{\partial}{\partial y}\overline{v'^3} \tag{6.14}$$

$$\frac{\partial}{\partial z}\overline{w'^3} \quad \ll \quad \frac{\partial}{\partial y}\overline{v'w'^2} \tag{6.15}$$

$$\frac{\partial}{\partial z}\overline{u'^2w'} \quad \ll \quad \frac{\partial}{\partial y}\overline{u'^2v'} \tag{6.16}$$

$$\frac{\partial}{\partial x}\overline{u'w'^2} \quad \ll \quad \frac{\partial}{\partial y}\overline{v'w'^2} \tag{6.17}$$

We cannot directly check relations 6.16 and 6.17 but they are probably valid in any attached boundary layer. With these assumptions we can eliminate all but three terms of the turbulent transport.

Next we simplify the production term, following Pierce and Ezekewe (1976), who measured the stress gradients in a three-dimensional turbulent boundary layer and found that the role of $\overline{u'w'}$ in the production terms was significantly smaller than the role of $\overline{u'v'}$ and $\overline{v'w'}$. Our data show that the two terms $\overline{u'v'}\frac{\partial U}{\partial y}$ and $\overline{v'w'}\frac{\partial W}{\partial y}$ dominate the turbulent kinetic energy production.

With all the above simplifications, equation 6.11 is reduced to:

$$\overbrace{\left(U\frac{\partial}{\partial x} + V\frac{\partial}{\partial y} + W\frac{\partial}{\partial z}\right)q^2}^{advection} = \overbrace{-2\left(\overline{u'v'}\frac{\partial U}{\partial y}\right) - 2\left(\overline{v'w'}\frac{\partial W}{\partial y}\right)}^{production} + \overbrace{\mathcal{D}_{ii}}^{dissipation}$$

$$\underbrace{-\frac{\partial}{\partial y}(\overline{u'^2v'} + \overline{v'^3} + \overline{v'w'^2})}_{triple\ product\ transport} \underbrace{-\nu\left(\frac{\partial^2 q^2}{\partial y^2}\right)}_{viscous\ transport} \tag{6.18}$$

We have measured all of the terms in equation 6.18 with the exception of $\mathcal{D}_{ii}$, which we can infer from the balance of the remainder of the terms. Figures 6.1 and 6.3 show the transport terms for q^2 at stations D and G, plotted in "inner" coordinates. Since these quantities are usually seen in outer coordinates, we include figures 6.2 and 6.4, normalized on δ_{99} and u_τ. In these latter figures, we expand the vertical scale to examine the terms' behavior in the outer part of the boundary layer. The most striking feature of the turbulent kinetic energy transport terms is that the near-wall region dominates the figures.

The production term, measured directly, dominates the TKE transport. It is always larger than the advection and turbulent transport terms. The production is highest near the wall, which is expected since the velocity gradients and the shear stresses are both high near the wall. We should expect the production to drop to zero at the wall as the shear stresses drop to zero. This is evident at station G but not at station D, most likely due to noise near the wall. One indicator of the steepness of the drop-off is the ratio of production at $y^+ = 10$ to the production at $y^+ = 100$. For station D, this is approximately 20, and for station G, approximately 30. Station G exhibits higher production than station D at $y^+ = 10$ and lower production than station D at $y^+ = 100$. The direct numerical simulation of Moin *et al.* (1990) also found suppression of turbulent kinetic energy production. They found that with increasing spanwise pressure gradient imposed on a channel flow, the production of turbulent kinetic energy was suppressed significantly in the region $10 < y^+ < 40$.

The advection and turbulent transport terms are generally much smaller than the production and dissipation terms. These two smaller terms reach small (negative) peaks below $y^+ = 20$, with the advection reaching a peak closer to the wall than the turbulent transport. Spalart's (1988) two-dimensional boundary layer computation showed that advection should be negligible near the wall, while the turbulent transport reaches a negative peak around $y^+ = 10$. Around $y/\delta_{99} = 0.04$ ($y^+ = 50$) the turbulent transport at station D is markedly higher than at station G. The advection seems to diminish in the near-wall region and grow in the outer region as the flow develops. Growth in the advection term with increasing three-dimensionality was also seen by Schwarz and Bradshaw (1992).

The dissipation rate is inferred by the balance of the other terms, and since the turbulent transport and advection terms are small, $\mathcal{D}_{ii}$ essentially balances the production. This is especially true for station D above $y/\delta_{99} = 0.15$, as seen in figure 6.2.[1] When the dissipation is equal to the production , the turbulence is said to be in "local equilibrium." Station G does not exhibit local equilibrium to the extent that station D does, primarily due to the increased advection. Bradshaw and Pontikos

---

[1]The outermost point in figure 6.2 has been left off the plot, because of one anomalous $\overline{w'^2}$ measurement.

(1985) showed that though the the empirical relation

$$\epsilon = \frac{(\tau/\rho)^{3/2}}{0.1\,\delta_{99}} \qquad (6.19)$$

performs well in predicting the dissipation rate of turbulent kinetic energy for two-dimensional boundary layers, it underpredicts the dissipation rate for three-dimensional boundary layers. Littell and Eaton (1991) and Schwarz and Bradshaw (1992) also found that the above relation grossly underpredicts the dissipation rate in the region below $y/\delta_{99} \approx 0.4$. We add this relation to our data (doubling ϵ because we plot the transport of q^2) in figures 6.2 and 6.4. The relation underpredicts the dissipation at both stations. Near the wall we expect that there is some error in the dissipation due to the pressure-strain term being non-negligible. Spalart's two-dimensional boundary layer simulation showed a small peak — smaller than the peak in the turbulent transport — in the pressure-strain term around $y^+ = 3$.

In order to complete the individual normal stress transport equations, it is necessary to know the partition of the dissipation term. For large y^+, it is a reasonable approximation to assume equipartition, but near the wall that assumption breaks down. Thus, it appears that we have little prospect of learning about near-wall behavior of the transport of the individual normal stresses.

6.4 Shear stress transport

6.4.1 $-\overline{u'v'}$ transport

To evaluate the terms of the shear stress transport equations, we begin by returning to equation 6.2, setting $i = 1$ and $j = 2$.

$$\overbrace{\left(U\frac{\partial}{\partial x} + V\frac{\partial}{\partial y} + W\frac{\partial}{\partial z} \right)}^{advection} (-\overline{u'v'}) =$$

$$\overbrace{\left(\overline{u'^2}\frac{\partial}{\partial x} + \overline{u'v'}\frac{\partial}{\partial y} + \overline{u'w'}\frac{\partial}{\partial z} \right) V + \left(\overline{u'v'}\frac{\partial}{\partial x} + \overline{v'^2}\frac{\partial}{\partial y} + \overline{v'w'}\frac{\partial}{\partial z} \right) U}^{production}$$

$$\overbrace{-\frac{1}{\rho}\left[\overline{p'\left(\frac{\partial u'}{\partial y} + \frac{\partial v'}{\partial x} \right)} \right]}^{pressure-strain} \overbrace{- 2\nu\overline{\frac{\partial u'}{\partial x}\frac{\partial v'}{\partial x}} + \overline{\frac{\partial u'}{\partial y}\frac{\partial v'}{\partial y}} + \overline{\frac{\partial u'}{\partial z}\frac{\partial v'}{\partial z}}}^{dissipation} \qquad (6.20)$$

$$\overbrace{+\left[\frac{1}{\rho}\left(\frac{\partial \overline{p'u'}}{\partial y} + \frac{\partial \overline{p'v'}}{\partial x} \right) + \frac{\partial \overline{u'^2v'}}{\partial x} + \frac{\partial \overline{u'v'^2}}{\partial y} + \frac{\partial \overline{u'v'w'}}{\partial z} + \nu\left(\frac{\partial^2}{\partial x^2} + \frac{\partial^2}{\partial y^2} + \frac{\partial^2}{\partial z^2} \right)\overline{u'v'} \right]}^{turbulent \; transport}$$

Here we neglect the dissipation term entirely and use the balance of equation 6.20 to determine the pressure-strain term. As with the turbulent kinetic energy transport equation, we also neglect the pressure correlations in the turbulent transport terms. This implies that the term determined by the equation balance represents the sum of the pressure-strain term and the pressure transport term. Again using the thin shear layer assumptions, we can eliminate several other terms in equation 6.20, reducing it to:

$$\overbrace{\left(U\frac{\partial}{\partial x} + V\frac{\partial}{\partial y} + W\frac{\partial}{\partial z} \right)}^{advection} (-\overline{u'v'}) = \overbrace{\overline{v'^2}\frac{\partial U}{\partial y}}^{production} + \Phi_{12} + \overbrace{\frac{\partial \overline{u'v'^2}}{\partial y}}^{triple \; transport} + \overbrace{\nu\frac{\partial^2\overline{u'v'}}{\partial y^2}}^{visc. \; transport} \qquad (6.21)$$

Figures 6.5 and 6.6 represent the transport terms for $-\overline{u'v'}$ at station D; figures 6.7 and 6.8 show the transport terms for $-\overline{u'v'}$ at station G. Littell and Eaton (1991) observed that the production of $-\overline{u'v'}$ was concentrated nearer the wall for their disk boundary layer than for two-dimensional boundary layers. We do not observe this effect. In the near-wall region we observe a decrease in the production of $-\overline{u'v'}$ from station D to station G. The level of $-\overline{u'v'}$ production at station D is similar to that of Spalart (1988), which showed a peak value of 0.11 around $y^+ = 15$. Advection is

strongly enhanced at station G (see figure 6.8), so we infer that the pressure-strain term is reduced.

6.4.2 $-\overline{v'w'}$ transport

Making similar approximations in the $-\overline{v'w'}$ equation yields:

$$\overbrace{\left(U\frac{\partial}{\partial x} + V\frac{\partial}{\partial y} + W\frac{\partial}{\partial z}\right)(-\overline{v'w'})}^{\text{advection}} = \overbrace{\overline{v'^2}\frac{\partial W}{\partial y}}^{\text{production}} + \Phi_{23} + \overbrace{\frac{\partial\overline{v'^2w'}}{\partial y}}^{\text{triple transport}} + \overbrace{\nu\frac{\partial^2\overline{v'w'}}{\partial y^2}}^{\text{visc. transport}} \quad (6.22)$$

All the terms in equation 6.22 are zero for a two-dimensional boundary layer, and we should expect to see them growing as three-dimensionality increases. Figures 6.9 through 6.12 show the $-\overline{v'w'}$ transport equation terms. At station D, where the three-dimensionality has acted upon the near-wall turbulence only, we note that all the terms are essentially zero above $y/\delta_{99} = 0.08$. Station G exhibits transport of $-\overline{v'w'}$ throughout the measured region. The production term is positive from the wall to the y location of peak W and negative outboard of that point, where W is decreasing with y (see figure 6.12). The sign change does not show up in figure 6.11 becuase the negative is small compared to the positive peak. Figure 6.12 illustrates this change in sign of the production term.

6.5 a_1 transport

It is possible to combine the above transport equations to obtain a transport equation for the turbulence structure parameter a_1. Looking at the terms of this new transport equation may give us insight into the behavior of a_1. Recall that $a_1 = \frac{\tau}{\rho}/q^2$. Taking the material derivative of a_1,

$$D(a_1) = D\left(\frac{\tau}{\rho}/q^2\right) = \frac{1}{q^2}D\left(\frac{\tau}{\rho}\right) - \frac{1}{q^4}\frac{\tau}{\rho}D(q^2) \quad (6.23)$$

where

$$\frac{\tau}{\rho} = (\overline{u'v'}^2 + \overline{v'w'}^2)^{1/2} \quad (6.24)$$

Differentiating equation 6.24 and substituting into equation 6.23, we have

$$D(a_1) = \frac{1}{q^2 \frac{\tau}{\rho}} \left(-\overline{u'v'} D(-\overline{u'v'}) - \overline{v'w'} D(-\overline{v'w'}) \right) - \frac{\frac{\tau}{\rho}}{q^4} D(q^2) \qquad (6.25)$$

We expand the a_1 transport equation below, by substituting equations 6.18, 6.21 and 6.22 into equation 6.25.

$$\left(U \frac{\partial}{\partial x} + V \frac{\partial}{\partial y} + W \frac{\partial}{\partial z} \right) a_1 =$$

$$\overbrace{\left(2 \left(\frac{\tau}{\rho} \right)^2 - \overline{v'^2} q^2 \right) \frac{1}{q^4 \frac{\tau}{\rho}} \overbrace{\left(\overline{u'v'} \frac{\partial U}{\partial y} + \overline{v'w'} \frac{\partial W}{\partial y} \right)}^{production} - \frac{\overline{u'v'}}{q^2 \frac{\tau}{\rho}} \Phi_{12} - \frac{\overline{v'w'}}{q^2 \frac{\tau}{\rho}} \Phi_{23}}$$

$$-\frac{\frac{\tau}{\rho}}{q^4} \mathcal{D}_{ii} + \frac{\frac{\tau}{\rho}}{q^4} \left(\frac{\partial}{\partial y} \right) \overbrace{\left(\overline{u'^2 v'} + \overline{v'^3} + \overline{v'w'^2} \right)}^{triple\ product\ transport} - \frac{\overline{u'v'}}{q^2 \frac{\tau}{\rho}} \frac{\partial \overline{u'v'^2}}{\partial y} - \frac{\overline{v'w'}}{q^2 \frac{\tau}{\rho}} \frac{\partial \overline{v'^2 w'}}{\partial y}$$

$$+\nu \frac{\frac{\tau}{\rho}}{q^4} \overbrace{\left(\frac{\partial^2 q^2}{\partial y^2} \right)}^{viscous\ transport} - \nu \frac{\overline{u'v'}}{q^2 \frac{\tau}{\rho}} \frac{\partial^2 \overline{u'v'}}{\partial y^2} - \nu \frac{\overline{v'w'}}{q^2 \frac{\tau}{\rho}} \frac{\partial^2 \overline{v'w'}}{\partial y^2} \qquad (6.26)$$

In practice we evaluate the terms of equation 6.26 from the terms already plotted in figures 6.1 through 6.12. The figures show that the production decreases dramatically from station D to station G in the region below $y^+ = 30$. The reduced production may help to explain why we see the reduction of a_1 with three-dimensionality (as seen in Chapter 5). Station G exhibits strong advection in the outer data points, which arises from the strong $\overline{u'v'}$ advection at that station.

6.6 Vertical transport velocities

We also present the vertical transport velocities. These generally represent the ability of the turbulence to transport the Reynolds stresses in the $+y$ direction. They are defined as follows:

$$V_{q^2} \equiv \frac{\overline{u'^2 v'} + \overline{v'^3} + \overline{v'w'^2}}{\overline{u'^2} + \overline{v'^2} + \overline{w'^2}} \qquad (6.27)$$

$$V_{uv} \equiv \frac{\overline{u'v'^2}}{\overline{u'v'}} \qquad (6.28)$$

$$V_{vw} \equiv \frac{\overline{v'^2 w'}}{\overline{v' w'}} \tag{6.29}$$

We scale the vertical transport velocities on u_τ and present them in figures 6.17 through 6.22.

The vertical transport velocities plotted are negative very near the wall, and cross zero around $y^+ = 10$ to 20. This is in agreement with the near-wall behavior of two-dimensional boundary layers, as discussed by Bradshaw and Pontikos (1985). The triple products transport the shear stresses and turbulent kinetic energy away from regions of highest production centered around $y^+ = 10$. The direction of transport is toward the wall below $y^+ = 10$ and away from the wall above $y^+ = 10$.

The V_{q^2} profiles collapse very well in inner coordinates up to nearly $y^+ = 100$. All the profiles have a peak near $y^+ = 25$. Above $y^+ = 100$ there seems to be mild reduction in V_{q^2} with increasing three-dimensionality.

The vertical transport of $\overline{u'v'}$ reaches a local maximum near $y^+ = 25$, then decreases through $y^+ = 200$. As the three-dimensionality develops, V_{uv} is suppressed in this region. Station FF exhibits the greatest suppression of V_{uv}, with the $\overline{u'v'^2}$ triple product actually becoming positive. The vertical transport of $\overline{v'w'}$ is in general larger than V_{uv}, and is presented on an expanded scale. This trend was also observed by Flack and Johnston (1993). The V_{vw} curves are similar in shape to those of V_{uv}, and the further downstream stations also seem to have suppressed values of V_{vw}. Above $y^+ = 200$, the vertical transport velocities of the shear stresses exhibit considerable scatter, as the triple products and the shear stresses both approach zero.

	x'	z
D	10.5	0
D_2	11.0	−.5
D_3	11.5	0
D_4	11.0	+.5
G	21.0	0
G_2	21.5	−.5
G_3	22.0	0
G_4	21.5	+.5

Table 6.1. Secondary profile locations (dimensions in inches).

Figure 6.1. Terms of Re-stress transport equation for q^2, inner scaling. Station D.
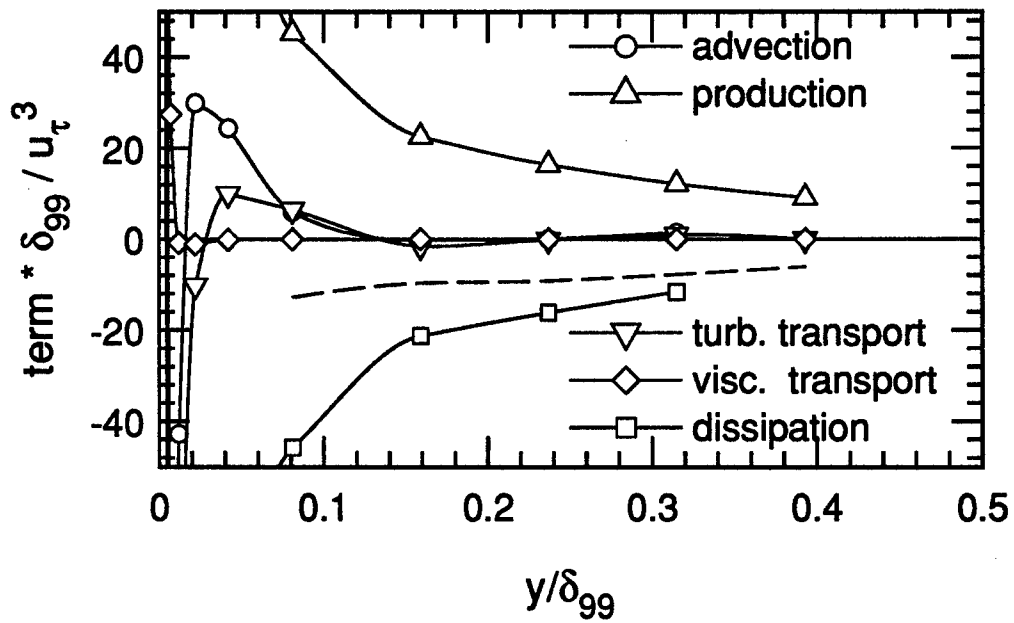
Figure 6.2. Terms of Re-stress transport equation for q^2, outer scaling. Dashed curve indicates two-dimensional dissipation rate correlation. Station D.
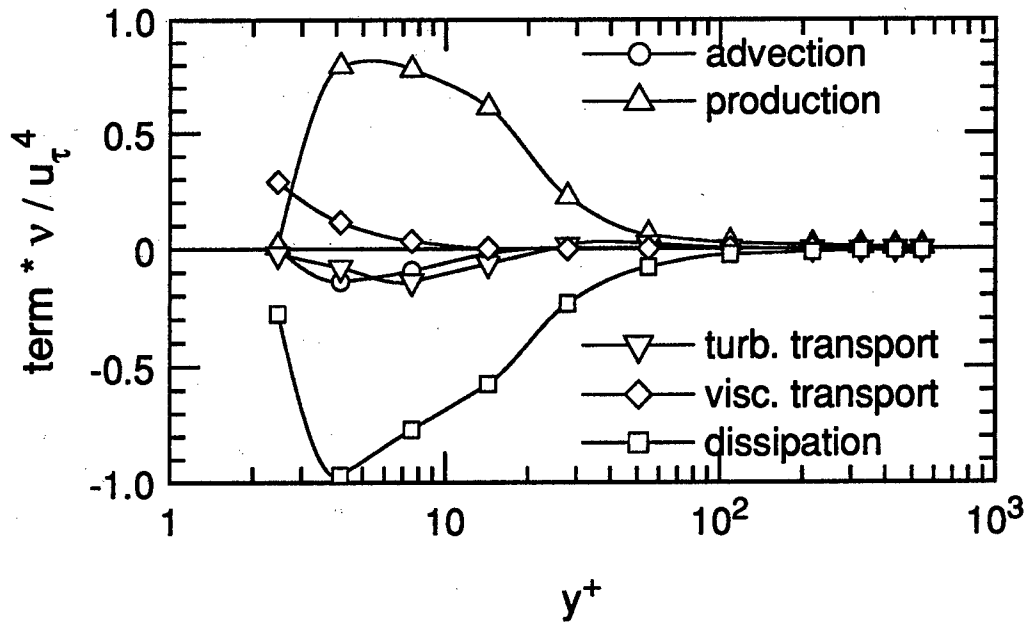
Figure 6.3. Terms of Re-stress transport equation for q^2, inner scaling. Station G.
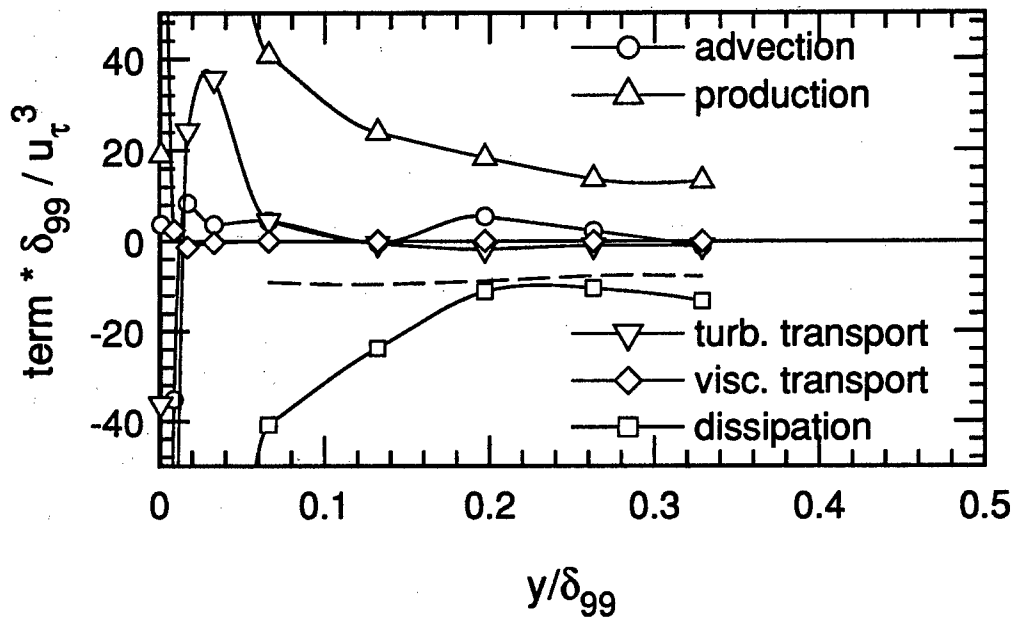
Figure 6.4. Terms of Re-stress transport equation for q^2, outer scaling. Dashed curve indicates two-dimensional dissipation-rate correlation. Station G.
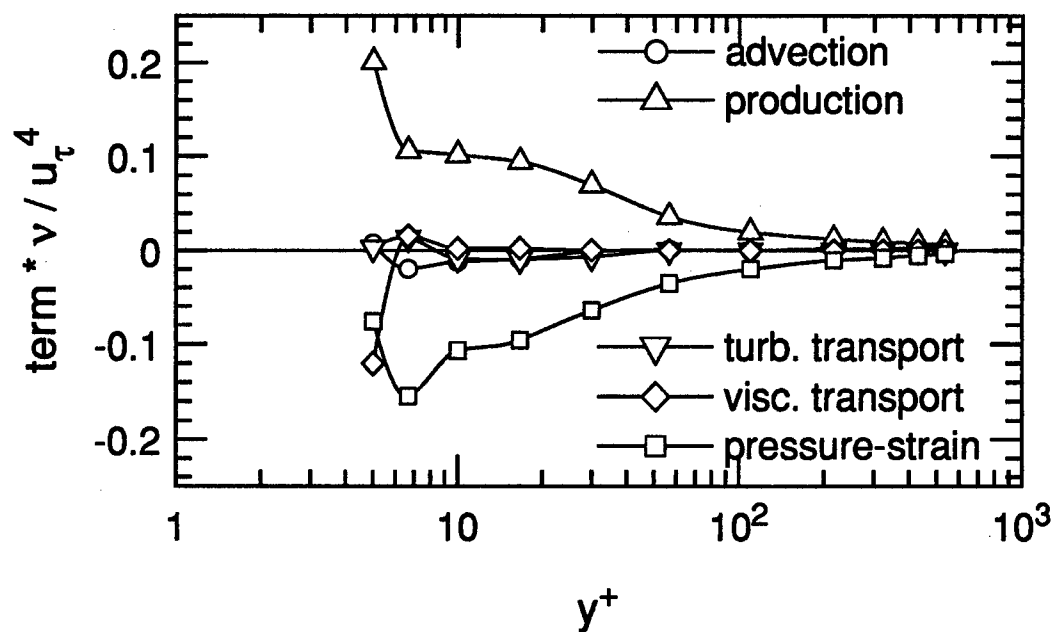
Figure 6.5. Terms of Re-stress transport equation for $\overline{u'v'}$, inner scaling. Station D.
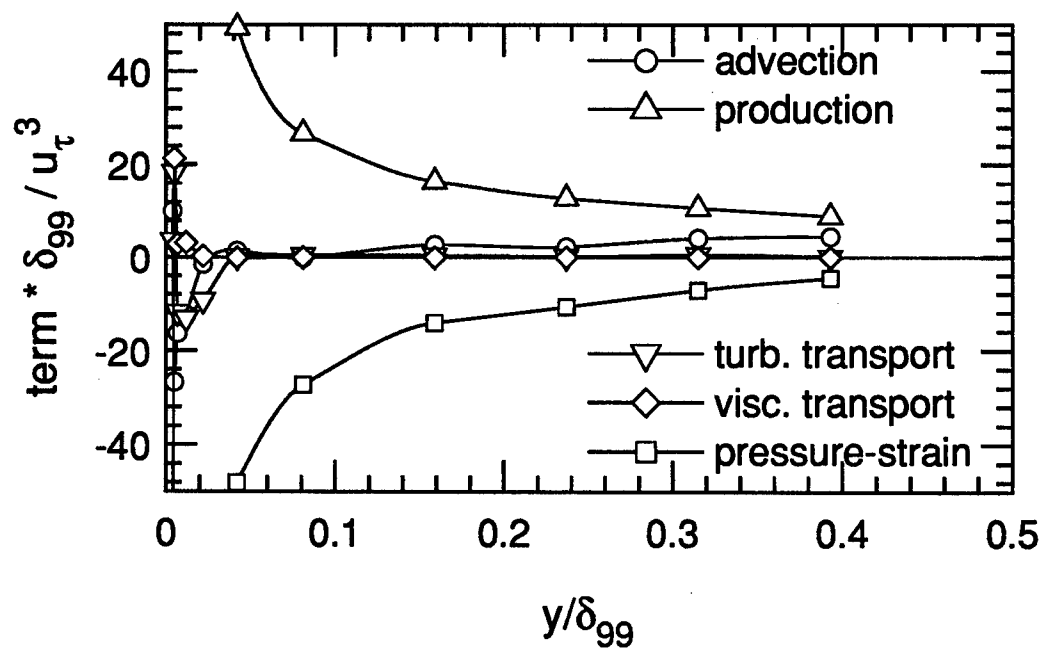
Figure 6.6. Terms of Re-stress transport equation for $\overline{u'v'}$, outer scaling. Station D.
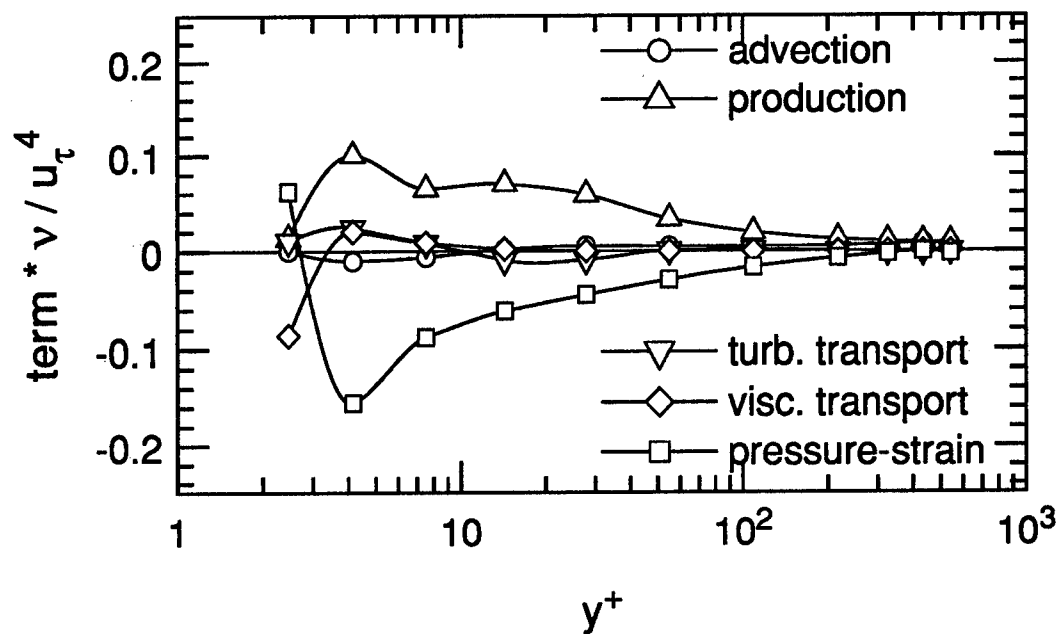
Figure 6.7. Terms of Re-stress transport equation for $\overline{u'v'}$, inner scaling. Station G.
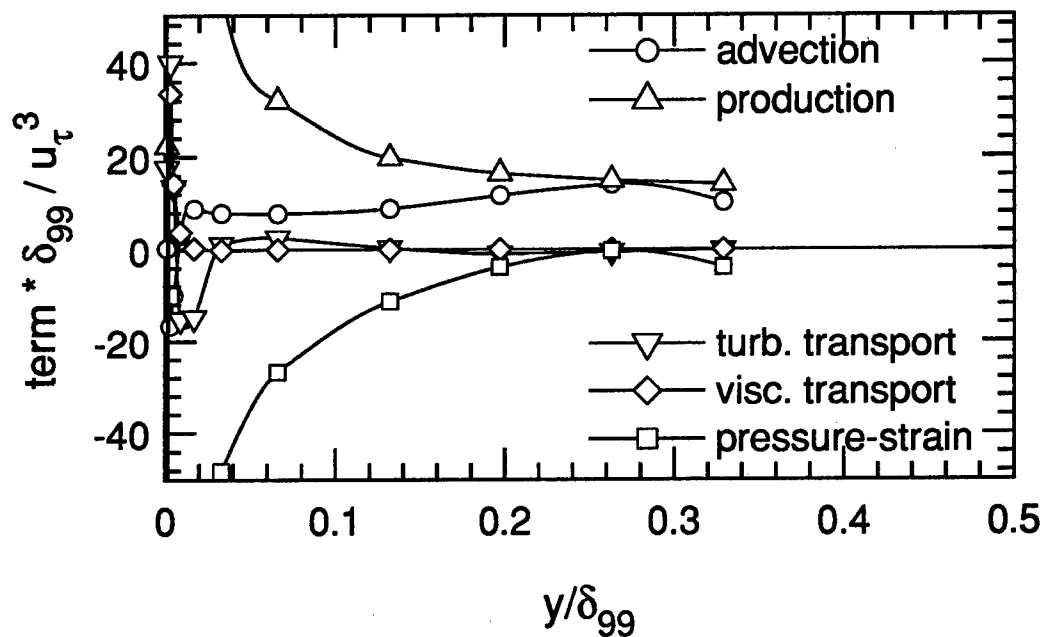
Figure 6.8. Terms of Re-stress transport equation for $\overline{u'v'}$, outer scaling. Station G.
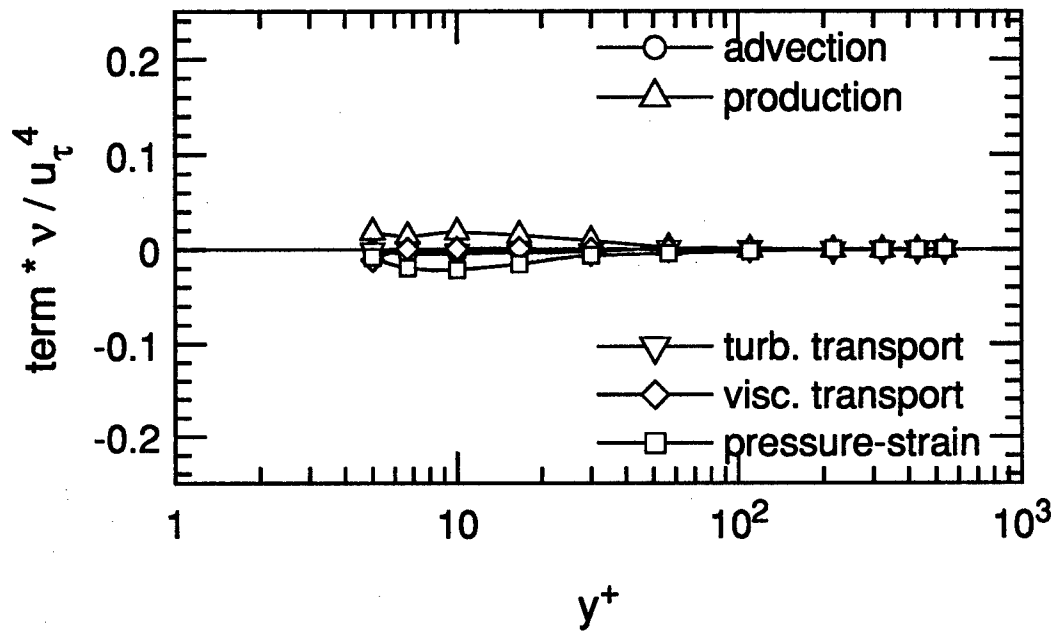
Figure 6.9. Terms of Re-stress transport equation for $\overline{v'w'}$, inner scaling. Station D.
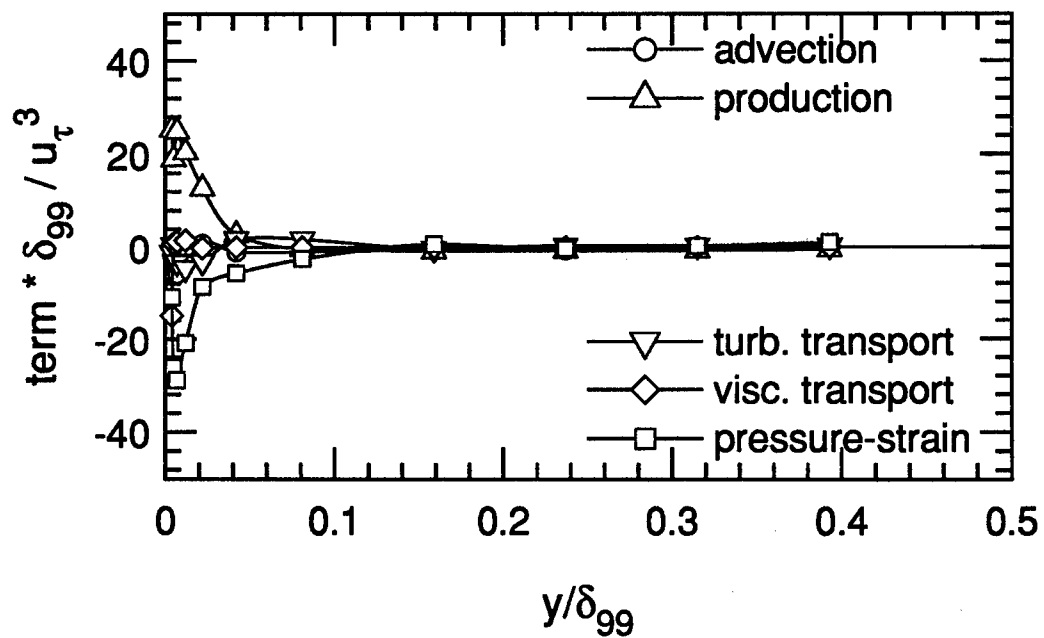
Figure 6.10. Terms of Re-stress transport equation for $\overline{v'w'}$, outer scaling. Station D.
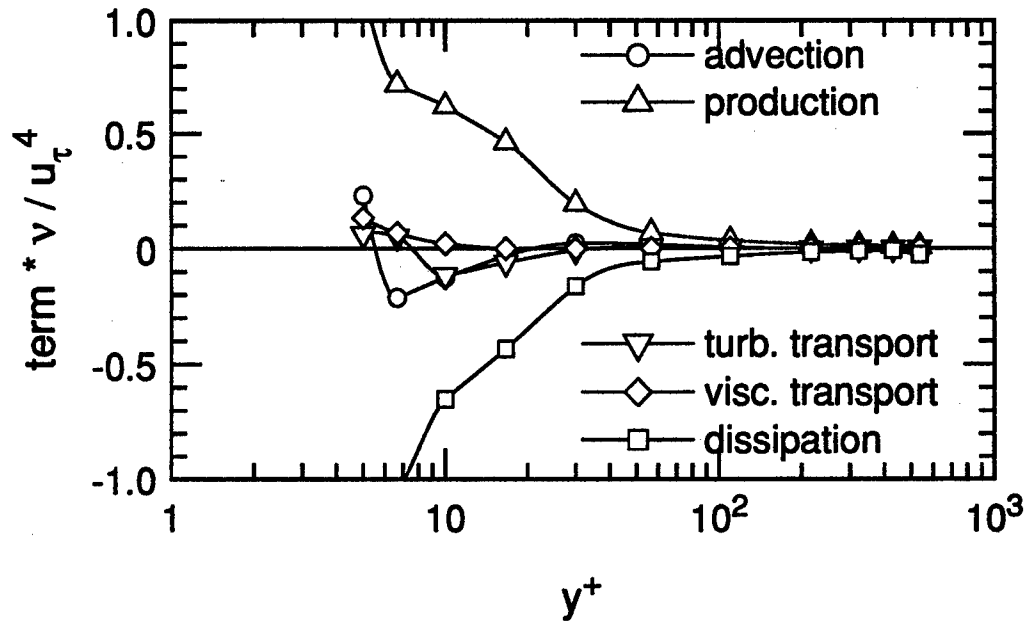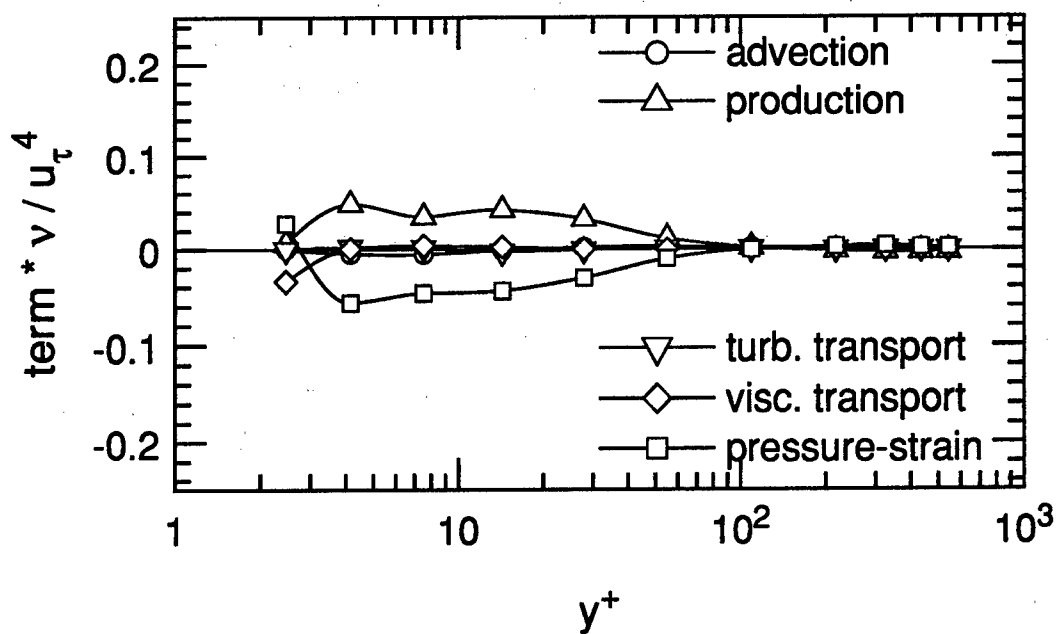
Figure 6.11. Terms of Re-stress transport equation for $\overline{v'w'}$, inner scaling. Station G.
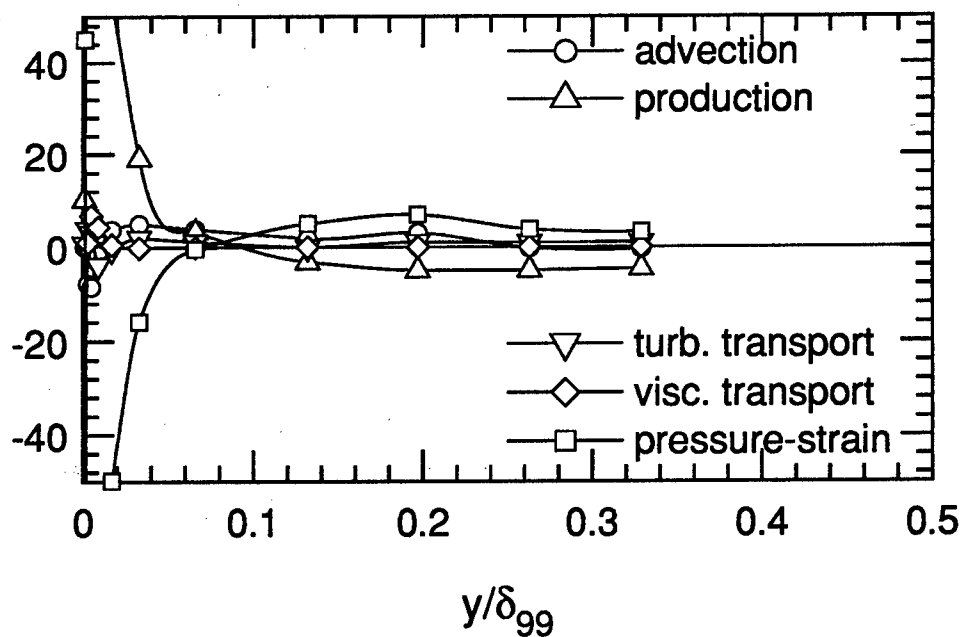
Figure 6.12. Terms of Re-stress transport equation for $\overline{v'w'}$, outer scaling. Station G.
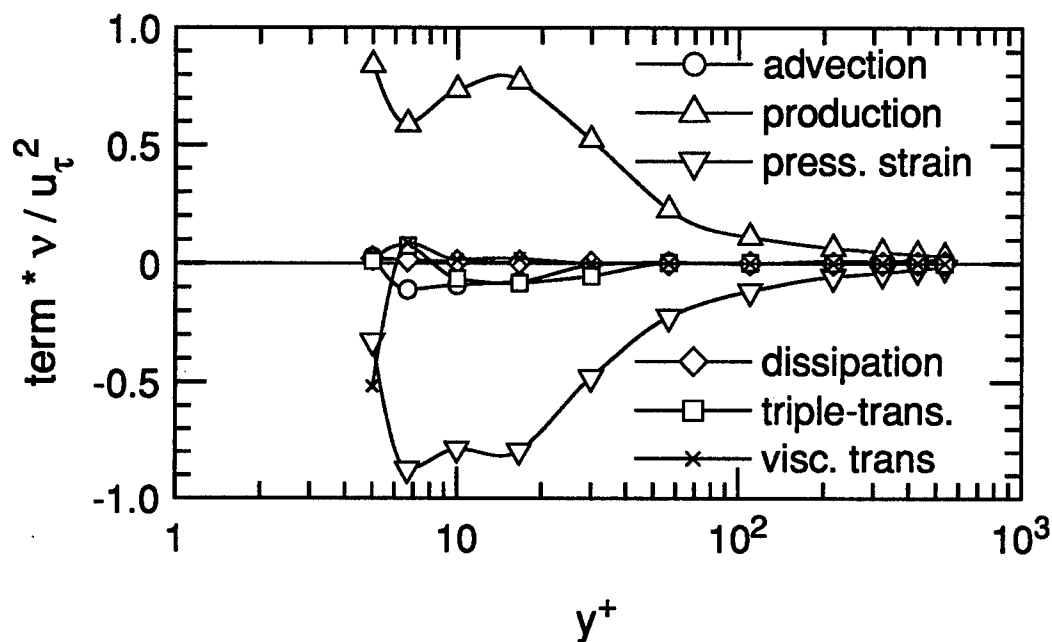
Figure 6.13. Terms of a_1 transport equation, inner scaling. Station D.
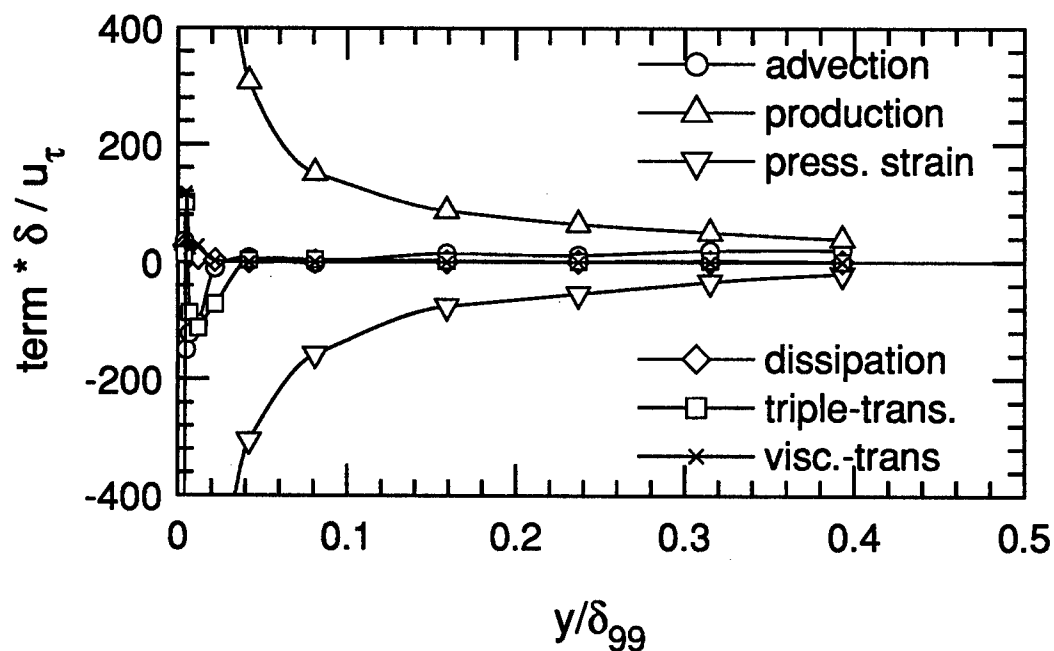
Figure 6.14. Terms of a_1 transport equation, outer scaling. Station D.
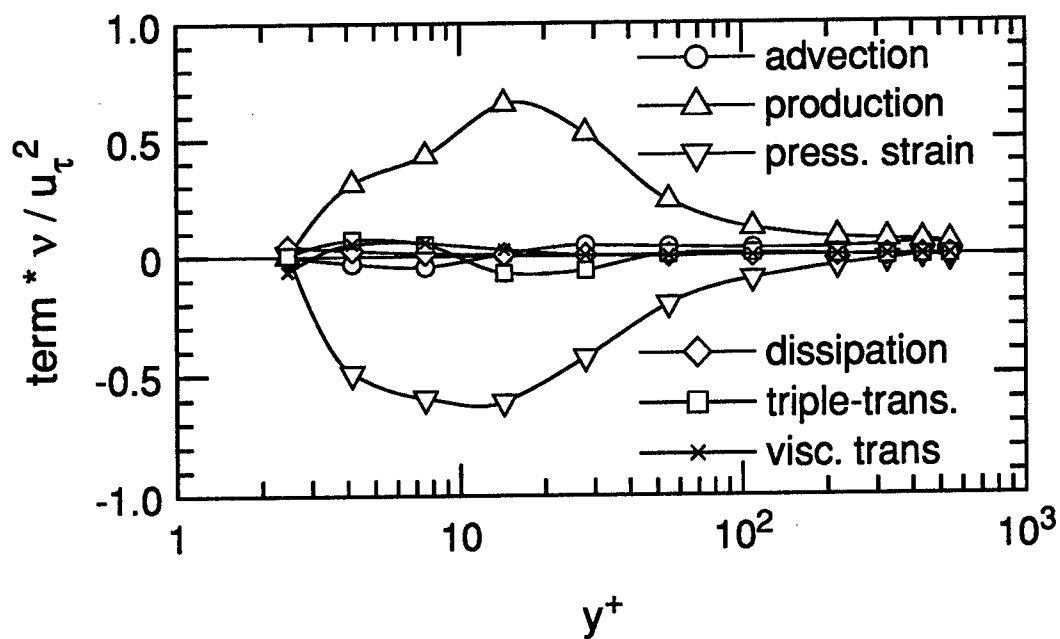
Figure 6.15. Terms of a_1 transport equation, inner scaling. Station G.
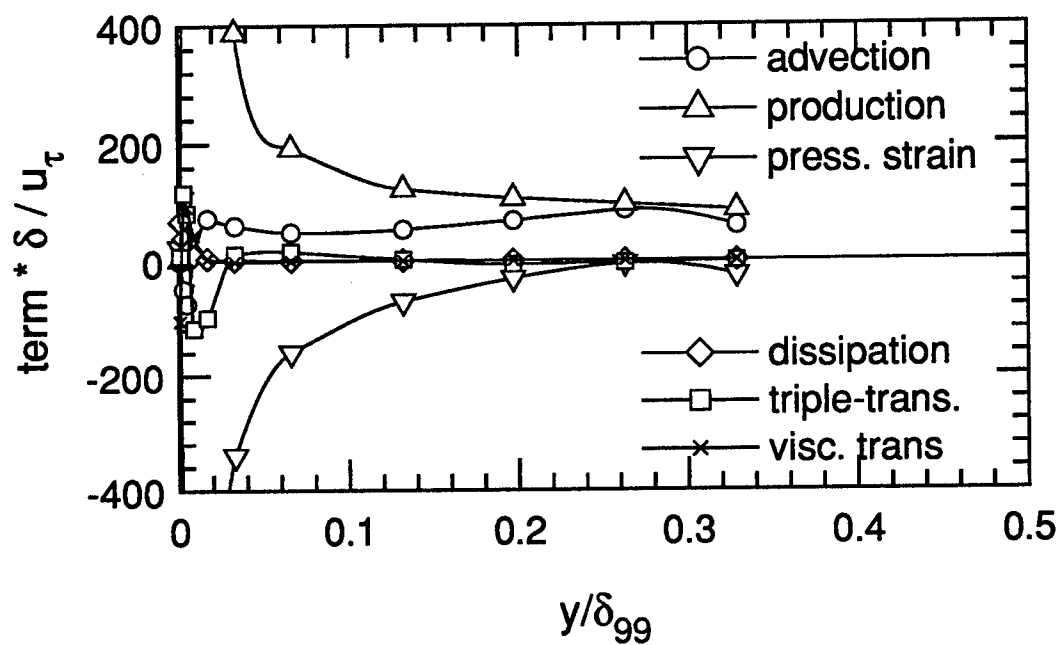
Figure 6.16. Terms of a_1 transport equation, outer scaling. Station G.
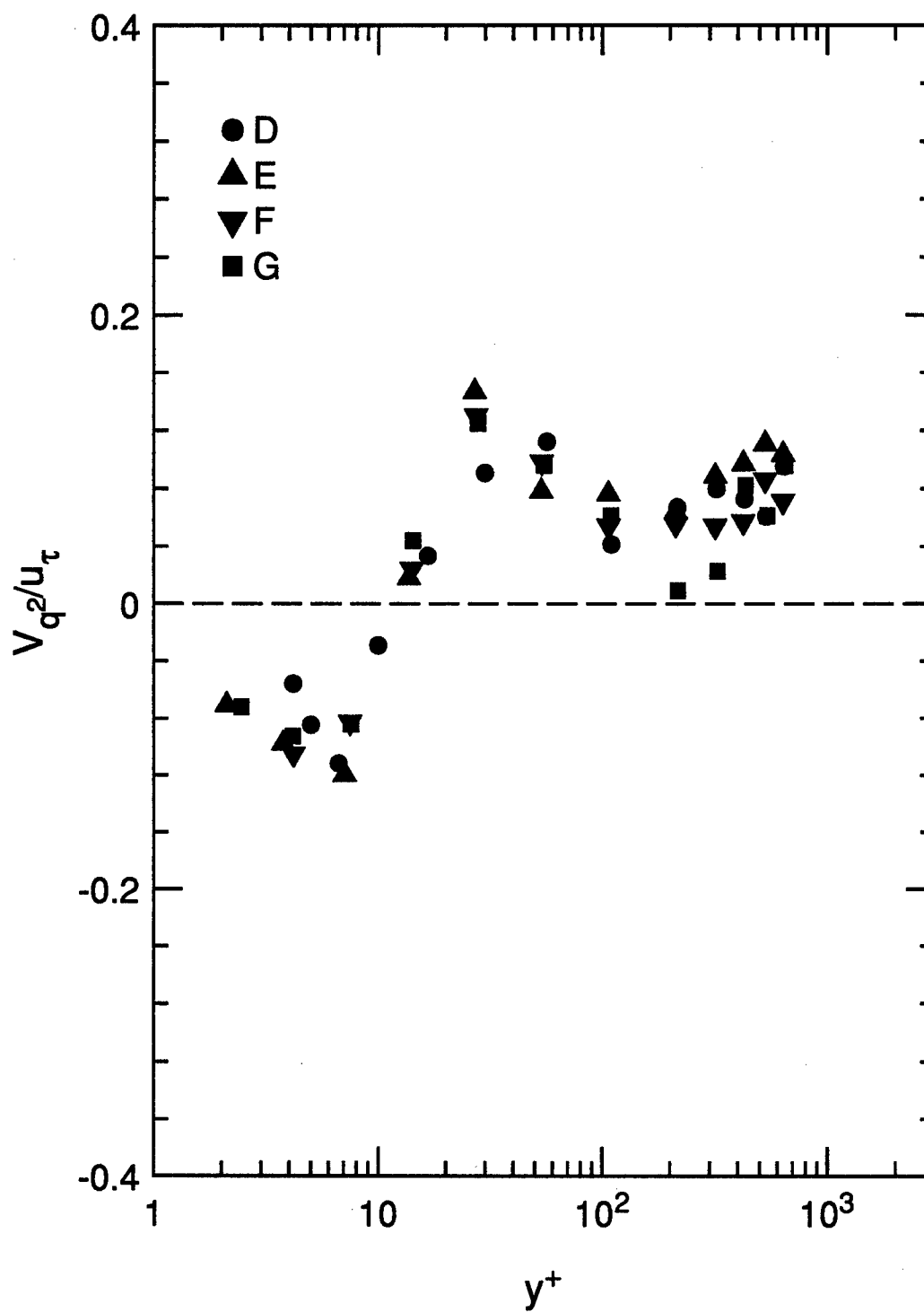
Figure 6.17. Vertical transport velocity for q^2. $z = 0$.
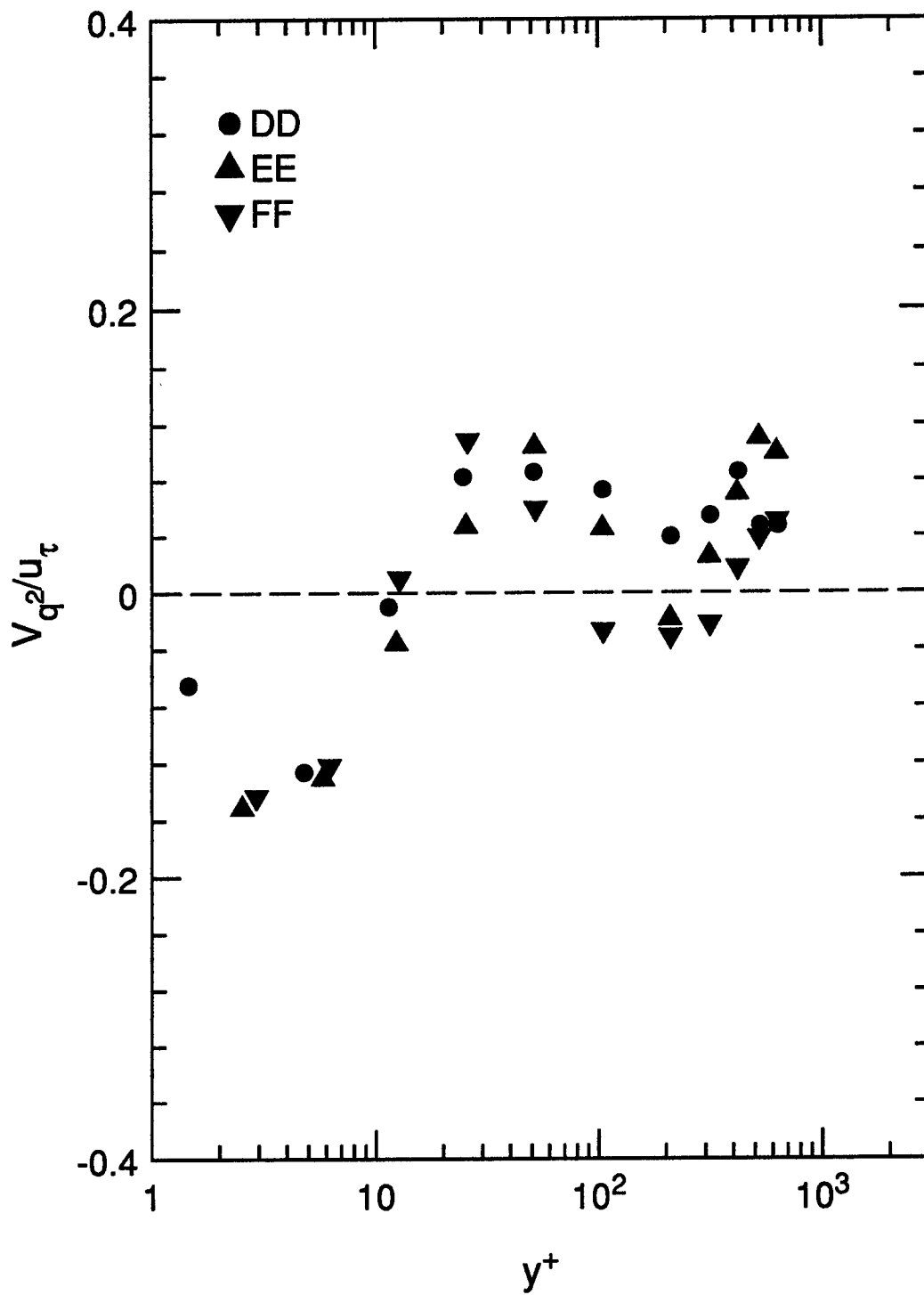
Figure 6.18. Vertical transport velocity for q^2. $z = -3.5$.
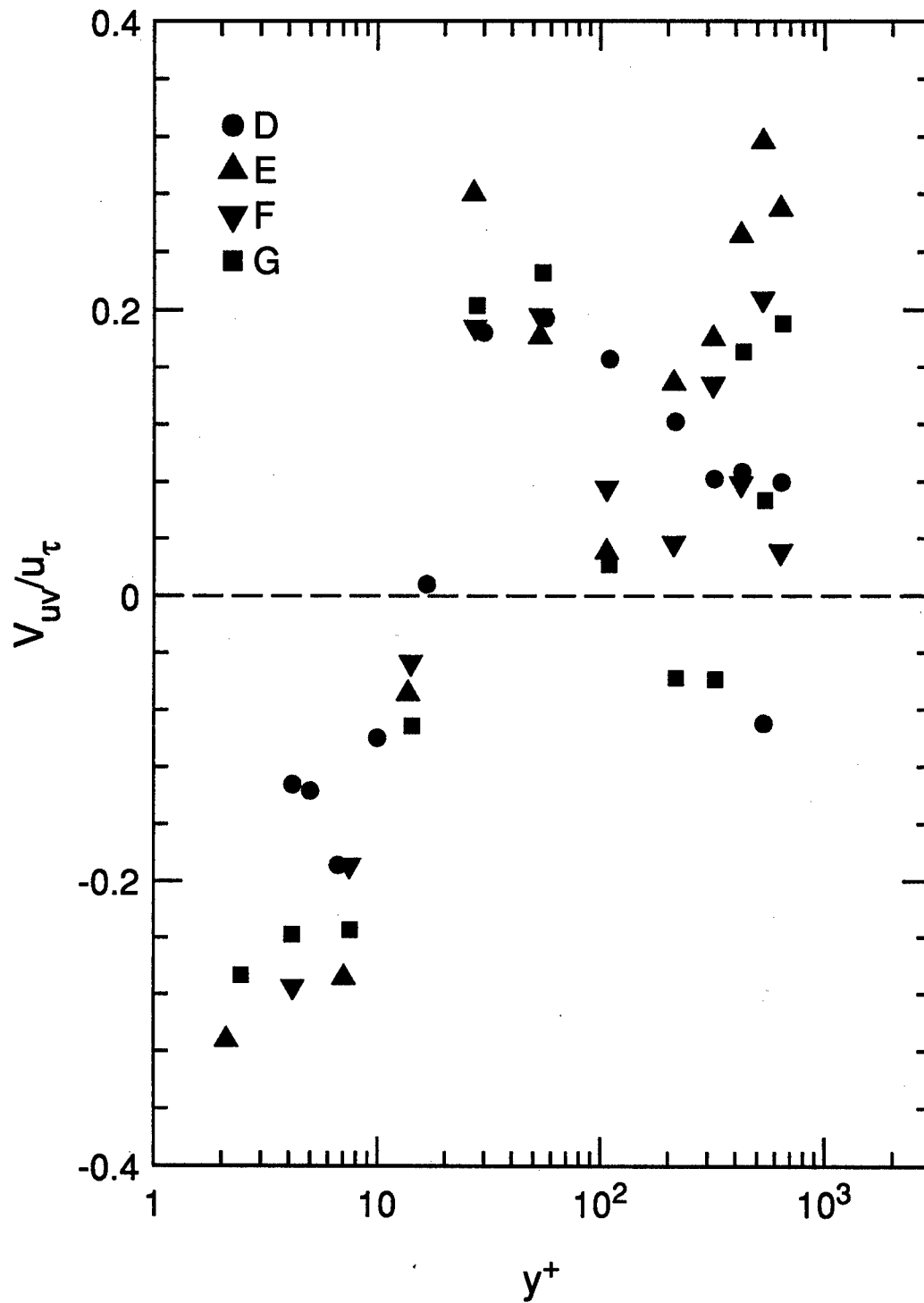
Figure 6.19. Vertical transport velocity for $\overline{u'v'}$. $z = 0$.
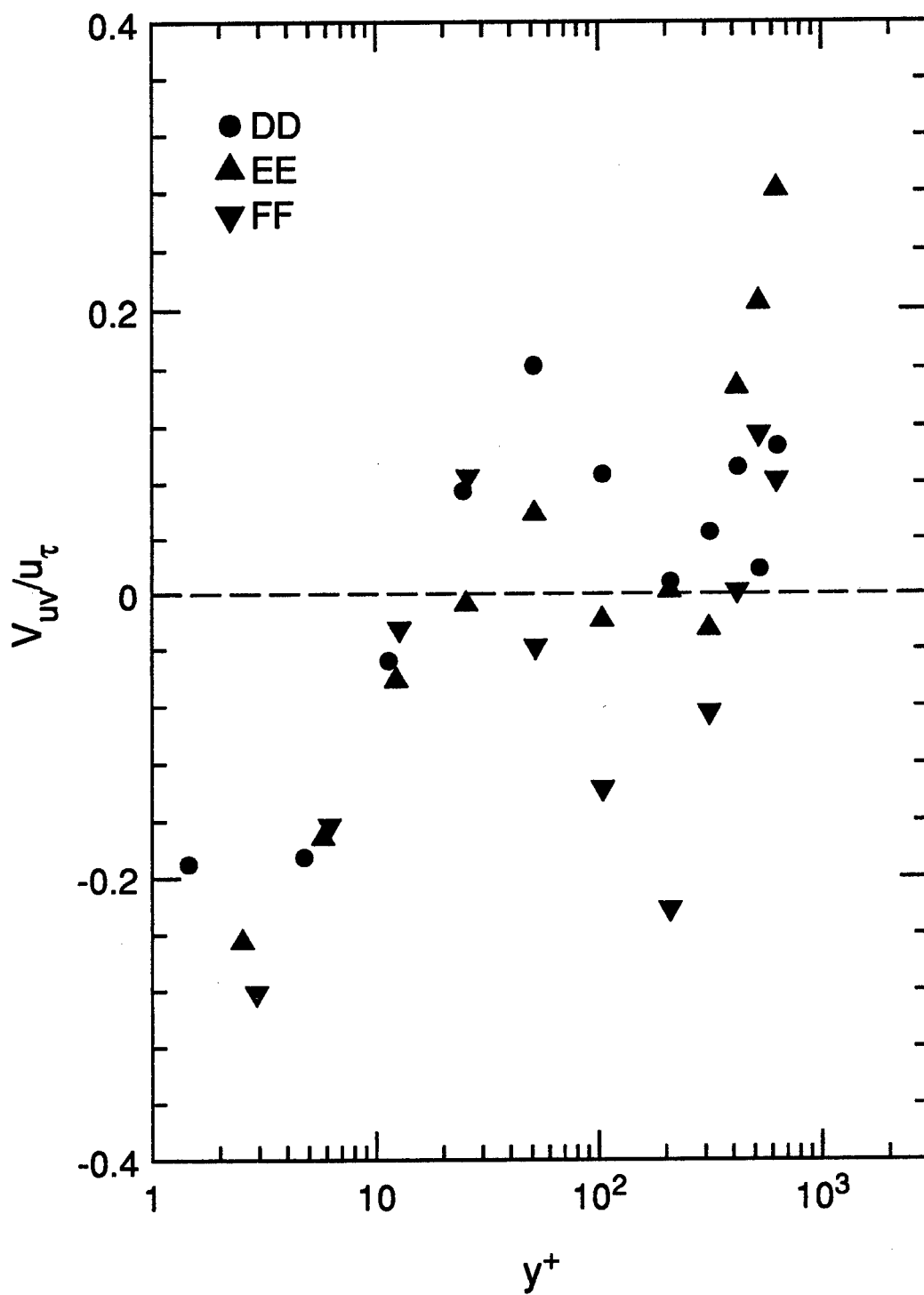
Figure 6.20. Vertical transport velocity for $\overline{u'v'}$. $z = -3.5$.
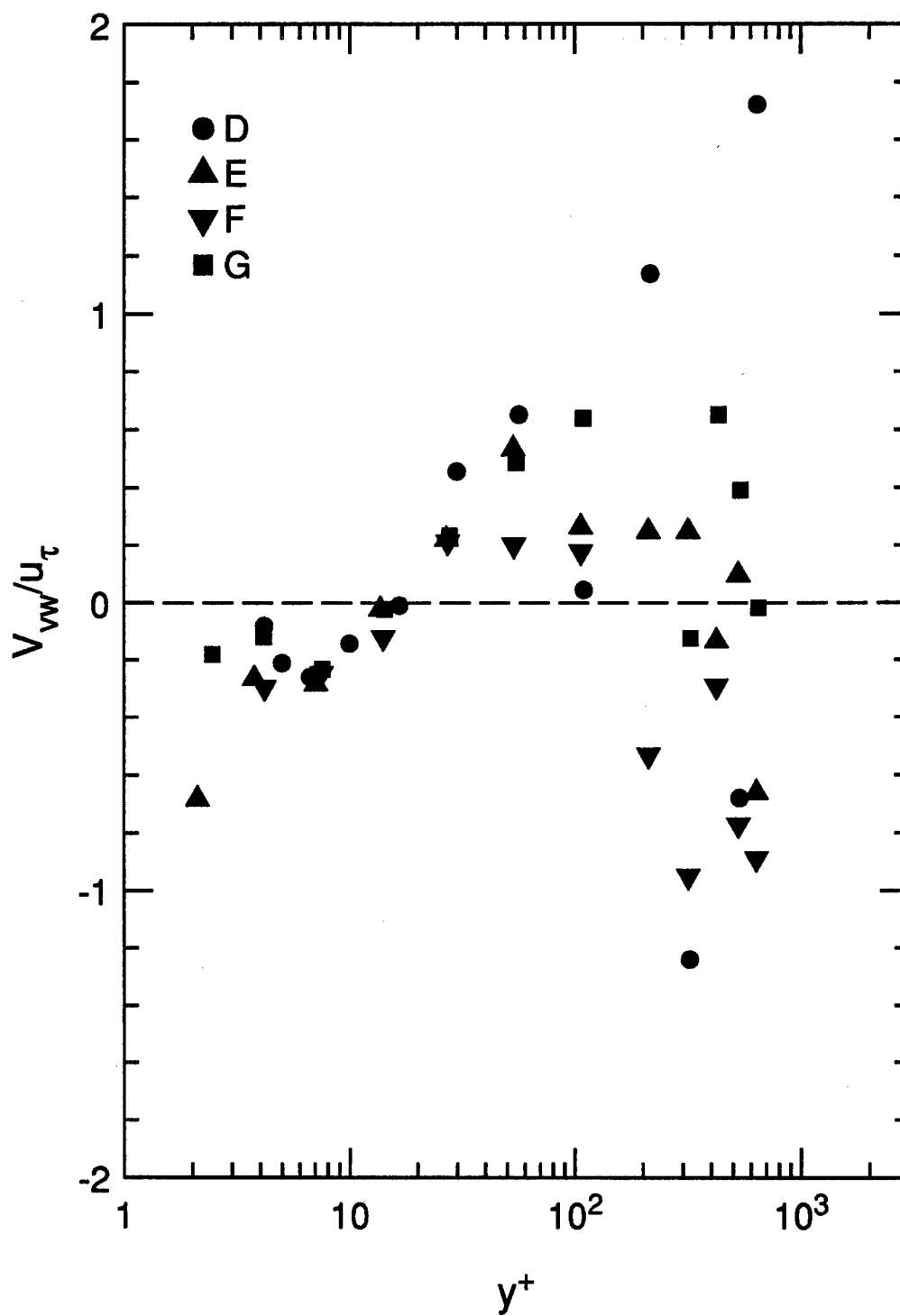
Figure 6.21. Vertical transport velocity for $\overline{v'w'}$. $z = 0$.
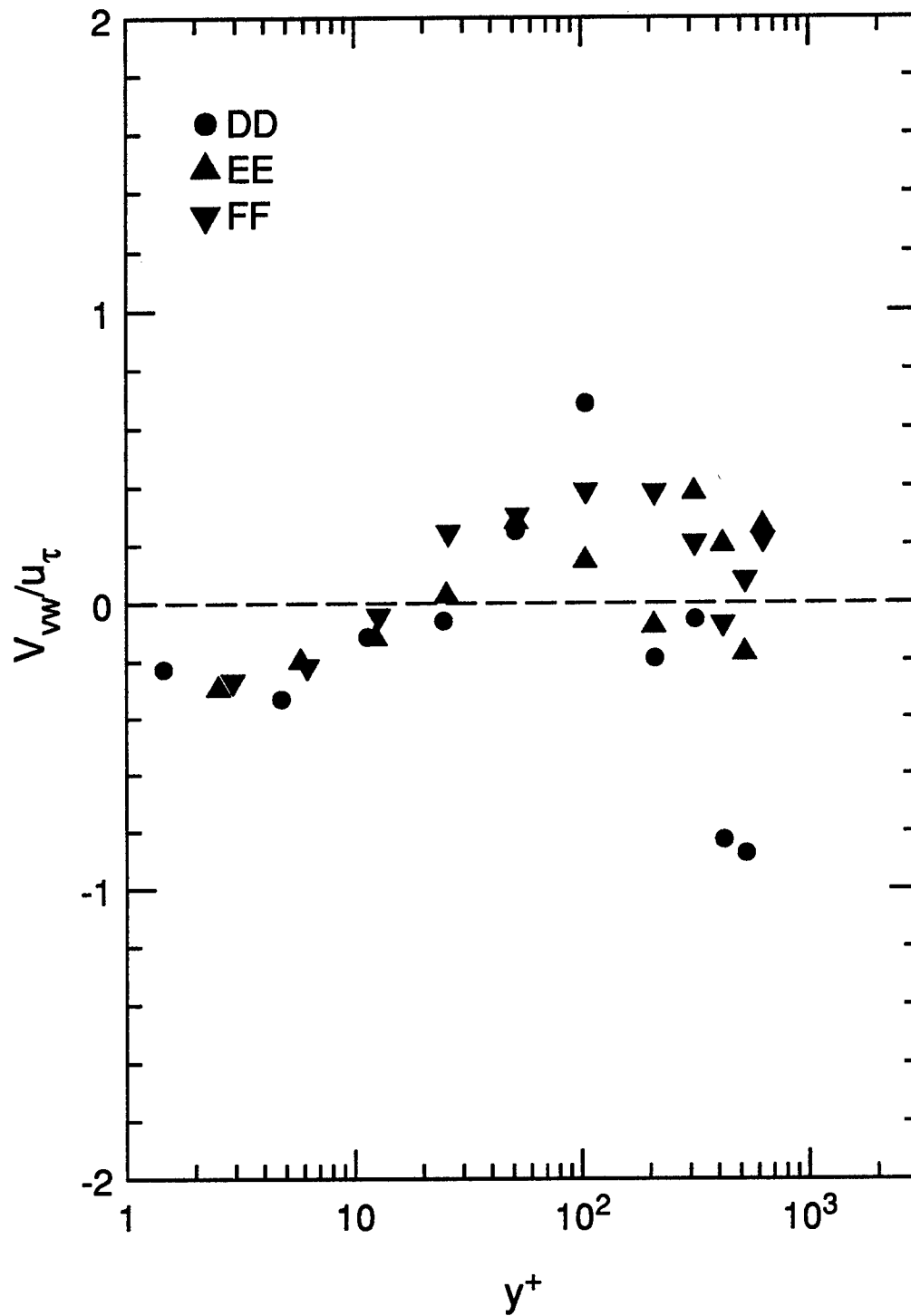
Figure 6.22. Vertical transport velocity for $\overline{v'w'}$. $z = -3.5$.

Chapter 7

Conclusions and Recommendations

7.1 Overview

We have measured the velocity field in a pressure-driven, three-dimensional boundary layer, at momentum thickness Reynolds numbers between 4000 and 5000. The flow was achieved by placing a 30 degree wedge in a straight duct in a wind tunnel. The boundary layer is dominated by a spanwise pressure gradient which produces up to 22 degrees of skewing across the layer. The furthest downstream measurement locations also experience a fairly strong favorable streamwise pressure gradient. A three-hole pressure probe was used to measure the mean flow, and the near-wall laser Doppler anemometer was used to fully investigate the near-wall flow. Crosswire data overlapped the LDA data to provide information about Reynolds stress behavior in the outer part of the boundary layer and to provide comparison to the LDA data.

The development of the near-wall LDA was a significant portion of this work. The LDA proved to provide accurate measurements of the mean flow and Reynolds stresses well below $y^+ = 10$. Special challenges arise due to a small measuring volume. Specifically, the fringe spacing varies along the measuring volume, necessitating calibration of the LDA for each run.

The near-wall data include mean velocity measurements, Reynolds stresses, and triple products, at seven primary profile locations and at six secondary profile locations. The secondary profile locations were used in the calculation of Reynolds stress transport equation terms.

7.2 Mean flow

The 30° wedge creates the pressure gradient to turn the flow, and the fairing on the top of the test section reduces the streamwise acceleration. The static pressure survey shows that the boundary layer grows under strong, increasing spanwise pressure gradient and relatively mild streamwise pressure gradient. The maximum spanwise pressure gradient, normalized by the boundary layer thickness, is $\left| \delta_{99} \frac{\partial C_p}{\partial z} \right| = 0.044$.

Fitting Q/Q_τ to the two-dimensional logarithmic law of the wall indicates fair agreement but not complete collapse. The downstream profiles tend to fall below the upstream curves in this normalization. This is primarily due to the effect of streamwise pressure gradient. Skin friction coefficients calculated from the fit to the law of the wall agree well with a correlation for two-dimensional boundary layers, at early stations. Later stations with strong streamwise pressure gradient show higher levels of skin friction.

The near-wall hodograph plots suggest that the flow may be collateral at the wall. That is, near the wall the spanwise velocity appears to be simply a scalar product of the streamwise velocity. The outer mean flow components exhibit more curvature than predicted by the inviscid Squire-Winter-Hawthorne theory.

7.3 Reynolds stresses and related quantities

The Reynolds normal stress profiles change slowly from the upstream two-dimensional boundary layer behavior. The $\overline{u'^2}$ profile shows a peak at approximately $y^+ = 10$, and drops off rapidly at the edge of the boundary layer. The more strongly 3D stations demonstrate suppressed levels of $\overline{u'^2}$ throughout the range $10 \leq y^+ \leq 200$. The $\overline{v'^2}$ profiles are shaped like two-dimensional profiles of $\overline{v'^2}$, changing very little as the flow develops. All of the profiles collapse very well in wall coordinates. The $\overline{w'^2}$ profiles change the most dramatically. Initially the profiles are typical of a two-dimensional boundary layer, with levels of $\overline{w'^2}$ intermediate between $\overline{v'^2}$ and $\overline{u'^2}$. However, as three-dimensionality becomes strong the $\overline{w'^2}$ profile grows a peak near $y^+ = 10$. The

increase in $\overline{w'^2}$ nearly makes up for the decrease in $\overline{u'^2}$ so the turbulent kinetic energy is only mildly suppressed in the near-wall region. Toward the outer edge of the boundary layer, q^2 grows as the Reynolds number increases.

The shear stresses are strongly affected by three-dimensionality. The streamwise shear stress $-\overline{u'v'}$ begins much like a two-dimensional boundary layer. With increasing three-dimensionality, it displays a marked decrease, by as much as 30%. The spanwise shear stress, which is zero in a two-dimensional boundary layer, grows to peak values as high as $0.65\ u_\tau^2$. Both components of the shear stress vector show collapse very near the wall ($y^+ < 10$) in inner coordinates, but they diverge above that region. The structural parameter a_1 is suppressed throughout most of the boundary layer, since the magnitude of the shear stress decreases more than does the magnitude of the turbulent kinetic energy. The $\overline{u'w'}$ stress was measured with the crosswire but not with the LDA. As is consistent with flow turned in this direction, $\overline{u'w'}$ is positive between the wall and $y^+ \approx 100$ and negative outboard of that.

The structural parameter $(\overline{u'^2} + \overline{w'^2})/\overline{v'^2}$, also invariant to coordinate rotation about the y axis, decreases from the wall outward to the edge of the boundary layer, as the turbulence approaches isotropy. Through the development of the three-dimensionality this quantity is reduced.

The angles of stress and strain are misaligned throughout most of the boundary layer, as should be expected based on the results of previous studies. In general the shear stress angle γ_τ lags the mean strain angle γ_g. This misalignment guarantees that an isotropic eddy viscosity model would perform poorly on this flow. Further, the quantity N_e varies throughout the flowfield, demonstrating that it would also be difficult to apply an anisotropic eddy viscosity model successfully. Near the wall, there is an exception. Around $y^+ = 10$ the angles γ_τ, γ_g, and γ nearly coincide. This further supports the concept that the flow is collateral at the wall.

7.4 Reynolds stress transport

Terms of the Reynolds stress transport equations are presented for two stations in the flow. The production of TKE appears to be reduced in the region $y^+ >$

20 by three-dimensionality, with greater reduction at greater distances from the wall. Turbulent transport (triple-product transport) seems to be reduced by three-dimensionality. Advection is increased in the outer part of the boundary layer, as found by other experimenters. An empirical dissipation relation that works well for two-dimensional boundary layers underestimates the dissipation rate of turbulent kinetic energy.

We observe a decrease in the production of $-\overline{u'v'}$ with three-dimensionality. All terms of the transport equation for $-\overline{v'w'}$ increase in magnitude with three-dimensionality.

A transport equation for a_1 has been derived. Its terms demonstrate a dramatic decrease in the production of a_1, consistent with the observed decrease in a_1.

The vertical transport velocities are also presented. The triple products transport the shear stresses and turbulent kinetic energy away from regions of highest production centered around $y^+ = 10$. The transport of q^2 is observed to be mildly suppressed above $y^+ = 100$ with increasing three-dimensionality. The vertical transport velocities of $-\overline{u'v'}$ and $-\overline{v'w'}$ are affected more strongly by three-dimensionality, with suppression evident throughout the boundary layer.

7.5 Recommendations

This study has provided insights into the behavior of the Reynolds stresses near the wall in a fairly strongly turned three-dimensional turbulent boundary layer. There are very few extant data for comparison to this study. Flack and Johnston (1993) found fairly different results with a much lower Reynolds number boundary layer, especially with respect to the issue of collateral flow at the wall and near-wall collapse of a_1. Experiments at yet higher Reynolds numbers will help the community to understand the "limiting" behavior (if any) of three-dimensionality.

We generated a flow dominated by spanwise pressure gradient, but we were not able to completely uncouple the effects of spanwise and streamwise pressure gradient. Although we do not expect these effects to interact simply, we would like to see more studies with three-dimensionality in the absence of streamwise pressure gradient.

The near-wall LDA generated high-quality data, but we believe that improvements

to the optical train could make data acquisition simpler and more reliable. One specific recommendation is that the distance between the Bragg cell and the transmitting lens be kept constant, which would make fringe variation less of a difficulty. A second recommendation is to measure u and w together, to reduce the uncertainties in the flow angles. This may necessitate using five beams to form the measuring volume instead of the existing three beams.

Appendix A

Crosswire Data Reduction

A.1 Introduction

The following discussion describes how the crosswire data were converted to velocities in the relevant coordinate systems. Assume we begin with the velocities from wire 1 and wire 2: U_1 and U_2, $\overline{u_1'^2}$ and $\overline{u_2'^2}$, and $\overline{u_1'u_2'}$. From the probe calibration, we have the angles of the two wires, Ψ_1 and Ψ_2. Note that $\Psi_2 < 0$.

A.2 First coordinate transformation

We first need to extract the velocities parallel and perpendicular to the probe stem, which we will call u^* and w^*. See figure A.1 for the orientation of these velocity components. Simple trigonometry yields:

$$
\begin{aligned}
u_1 &= u^* \cos \Psi_1 + w^* \sin \Psi_1 \\
u_2 &= u^* \cos \Psi_2 + w^* \sin \Psi_2
\end{aligned}
\tag{A.1}
$$

Solving for u^* and w^* gives:

$$
\begin{aligned}
u^* &= \frac{u_1 \sin \Psi_2 - u_2 \sin \Psi_1}{\cos \Psi_1 \sin \Psi_2 - \cos \Psi_2 \sin \Psi_1} \\
w^* &= \frac{u_2 \cos \Psi_1 - u_1 \cos \Psi_2}{\cos \Psi_1 \sin \Psi_2 - \cos \Psi_2 \sin \Psi_1}
\end{aligned}
\tag{A.2}
$$

We use equations A.3 to produce the velocities and Reynolds stresses in the coordinates of the probe tip. For each of the four orientations of the probe, we generate U^*, W^*, $\overline{u'^{*2}}$, $\overline{w'^{*2}}$, and $\overline{u'^*w'^*}$.

$$
\begin{aligned}
U^* &= (U_1 \sin \Psi_2 - U_2 \sin \Psi_1)/D \\
W^* &= (U_2 \cos \Psi_1 - U_1 \cos \Psi_2)/D
\end{aligned}
\tag{A.3}
$$

$$\overline{u'^{*2}} = (\overline{u_1'^2}\sin^2\Psi_2 + \overline{u_2'^2}\sin^2\Psi_1 - 2\overline{u_1'u_2'}\sin\Psi_1\sin\Psi_2)/D^2$$

$$\overline{w'^{*2}} = (\overline{u_1'^2}\cos^2\Psi_2 + \overline{u_2'^2}\cos^2\Psi_1 - 2\overline{u_1'u_2'}\cos\Psi_1\cos\Psi_2)/D^2$$

$$\overline{u'^*w'^*} = (\overline{u_1'u_2'}(\cos\Psi_1\sin\Psi_2 + \sin\Psi_1\cos\Psi_2) -$$
$$\overline{u_1'^2}\sin\Psi_2\cos\Psi_2 - \overline{u_2'^2}\sin\Psi_1\cos\Psi_1)/D^2$$

where

$$D = \cos\Psi_1\sin\Psi_2 - \cos\Psi_2\sin\Psi_1 \qquad (A.4)$$

A.3 Combining the probe orientations

The next step is to use the four probe orientations to put the velocities into one coordinate system aligned with the probe stem. Refer to figure A.2 for the probe orientations. For clarity in this figure, the circles indicate the "upstream" ends of the wires. As the figure indicates, we are rotating the probe tip and measuring u^* and w^*. In each orientation, u^* is the velocity along the probe stem and w^* is the velocity in the plane of the wires. Aligning the z axis parallel to the wall and the y axis normal to the wall, we have

$$w^* = w\cos\Phi + v\sin\Phi \qquad (A.5)$$

In position 1, $w^* = w$, and in position 3 $w^* = -v$. Therefore, we can extract most of the velocity components from these two positions. Position 1 yields U, W, $\overline{u'^2}$, $\overline{w'^2}$ and $\overline{u'w'}$. Position 3 adds $-V$, $\overline{v'^2}$, and $-\overline{u'v'}$. From positions 2 and 4 ($\Phi = -45°$ and $\Phi = -135°$) we have:

$$w_2^* = w\frac{\sqrt{2}}{2} - v\frac{\sqrt{2}}{2} \qquad (A.6)$$

$$w_4^* = -w\frac{\sqrt{2}}{2} - v\frac{\sqrt{2}}{2} \qquad (A.7)$$

Squaring and combining, we find

$$\overline{v'w'} = \frac{\overline{w_4'^{*2}} - \overline{w_2'^{*2}}}{2}. \qquad (A.8)$$

A.4 Second coordinate transform

The third step is to rotate the velocities and Reynolds stresses into the wind tunnel coordinate system. The probe is rotated at an angle γ from the tunnel x-axis. To rotate into tunnel coordinates we use the angle γ, and to rotate into local freestream coordinates we substitute $\gamma - \beta$ for the angle in the following equations. We denote the velocities in probe coordinates with the subscript 1 and the velocities in the new coordinates with subscript 2:

$$
\begin{aligned}
U_2 &= U_1 \cos\gamma - W_1 \sin\gamma & \text{(A.9)} \\
W_2 &= U_1 \sin\gamma + W_1 \cos\gamma \\
\overline{u_2'^2} &= \overline{u_1'^2}\cos^2\gamma + \overline{w_1'^2}\sin^2\gamma - 2\overline{u_1'w_1'}\sin\gamma\cos\gamma \\
\overline{w_2'^2} &= \overline{u_1'^2}\sin^2\gamma + \overline{w_1'^2}\cos^2\gamma + 2\overline{u_1'w_1'}\sin\gamma\cos\gamma \\
\overline{u_2'v_2'} &= \overline{u_1'v_1'}\cos\gamma - \overline{v_1'w_1'}\sin\gamma \\
\overline{v_2'w_2'} &= \overline{u_1'v_1'}\sin\gamma + \overline{v_1'w_1'}\cos\gamma \\
\overline{u_2'w_2'} &= (\overline{u_1'^2} - \overline{w_1'^2})\sin\gamma\cos\gamma + \overline{u_1'w_1'}(\cos^2\gamma - \sin^2\gamma)
\end{aligned}
$$

The final step is to do one further coordinate transform, for the grazing angle of the probe stem.
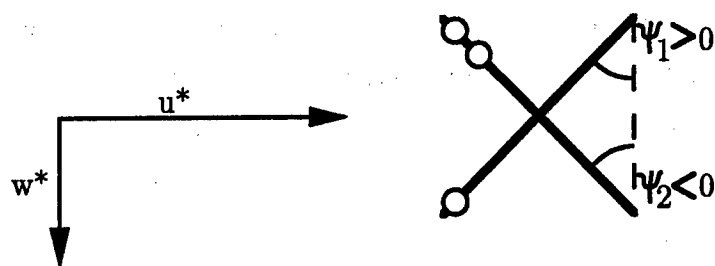
Figure A.1. Crosswire Ψ angles and flow orientation.
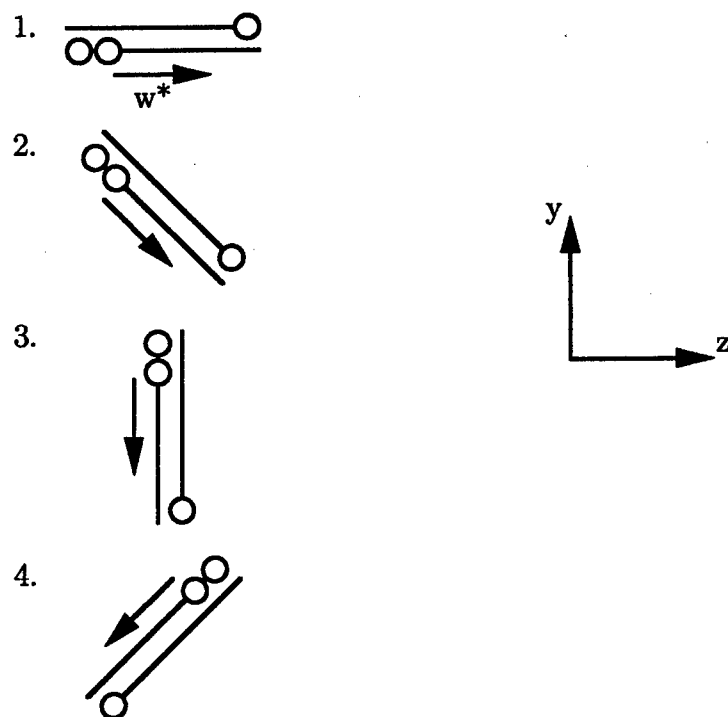
Figure A.2. Crosswire positions. 1: $\Phi = 0°$; 2: $\Phi = -45°$; 3: $\Phi = -90°$; 4: $\Phi = -135°$.

Appendix B

Small Angle Corrections for LDA Data

B.1 Angular dependence of velocities

The following discussion describes how to convert measured velocities from the LDA to relevant velocities through coordinate transformations. α_{41} represents the full crossing angle of the main beam with the 41 MHz beam, and α_{40} represents the full crossing angle of the main beam with the 40 MHz beam. The grazing angle of the main beam is represented by ϕ. See figure 3.8 for the orientations of the beams.

Let $a = \cos\frac{\alpha_{41}}{2}$; $b = \sin\frac{\alpha_{41}}{2}$; $c = \cos(\phi + \frac{\alpha_{40}}{2})$; $d = \sin(\phi + \frac{\alpha_{40}}{2})$, and mark the uncorrected quantities with tildes. The uv configuration gives

$$\tilde{u} = au + bw \tag{B.1}$$

$$\tilde{v} = cv - dw \tag{B.2}$$

and the vw configuration yields

$$\tilde{w} = aw - bu \tag{B.3}$$

$$\tilde{v}_2 = cv - du \tag{B.4}$$

B.2 Mean velocities

We solve the above equations for the mean quantities U, V, and W, disregarding the $\tilde{v}_2$ equation (B.4):

$$U = \frac{a\tilde{U} - b\tilde{W}}{a^2 + b^2} \tag{B.5}$$

$$W = \frac{a\tilde{W} + b\tilde{U}}{a^2 + b^2} \tag{B.6}$$

$$V = \frac{\tilde{V} + dW}{c} \tag{B.7}$$

B.3 Reynolds stresses

From the above equations we also get

$$\overline{\tilde{u}'^2} = a^2\,\overline{u'^2} + 2\,a\,b\,\overline{u'w'} + b^2\,\overline{w'^2} \tag{B.8}$$

$$\overline{\tilde{u}'\tilde{v}'} = a\,c\,\overline{u'v'} - a\,d\,\overline{u'w'} + b\,c\,\overline{v'w'} - b\,d\,\overline{w'^2} \tag{B.9}$$

$$\overline{\tilde{v}'^2}_1 = c^2\overline{v'^2} + d^2\overline{w'^2} - 2cd\overline{v'w'} \tag{B.10}$$

$$\overline{\tilde{w}'^2} = b^2\,\overline{u'^2} - 2\,a\,b\,\overline{u'w'} + a^2\,\overline{w'^2} \tag{B.11}$$

$$\overline{\tilde{v}'\tilde{w}'} = b\,d\,\overline{u'^2} - b\,c\,\overline{u'v'} - a\,d\,\overline{u'w'} + a\,c\,\overline{v'w'} \tag{B.12}$$

$$\overline{\tilde{v}'^2}_2 = c^2\overline{v'^2} + d^2\overline{u'^2} - 2cd\overline{u'v'} \tag{B.13}$$

We have for the Reynolds stresses six equations and six unknowns. However, we do not have a good way of measuring $\overline{u'w'}$ with this setup, so we expect the equations to be ill-conditioned if we try to solve for $\overline{u'w'}$. For now, we neglect contributions from $\overline{u'w'}$, since we cannot measure it, and eliminate the extra $\overline{v'^2}$ equation (B.13).

$$
\begin{bmatrix}
a^2 & 0 & 0 & 0 & b^2 \\
0 & ac & 0 & bc & -bd \\
0 & 0 & c^2 & -2cd & d^2 \\
bd & -bc & 0 & ac & 0 \\
b^2 & 0 & 0 & 0 & a^2
\end{bmatrix}
\begin{bmatrix}
\overline{u'^2} \\
\overline{u'v'} \\
\overline{v'^2} \\
\overline{v'w'} \\
\overline{w'^2}
\end{bmatrix}
\approx
\begin{bmatrix}
\overline{\tilde{u}'^2} \\
\overline{\tilde{u}'\tilde{v}'} \\
\overline{\tilde{v}'^2}_1 \\
\overline{\tilde{v}'\tilde{w}'} \\
\overline{\tilde{w}'^2}
\end{bmatrix}
\tag{B.14}
$$

Now neglect all terms containing b^2, d^2, and bd, since they are very small:

$$
\begin{bmatrix}
a^2 & 0 & 0 & 0 & 0 \\
0 & ac & 0 & bc & 0 \\
0 & 0 & c^2 & -2cd & 0 \\
0 & -bc & 0 & ac & 0 \\
0 & 0 & 0 & 0 & a^2
\end{bmatrix}
\begin{bmatrix}
\overline{u'^2} \\
\overline{u'v'} \\
\overline{v'^2} \\
\overline{v'w'} \\
\overline{w'^2}
\end{bmatrix}
\approx
\begin{bmatrix}
\overline{\tilde{u}'^2} \\
\overline{\tilde{u}'\tilde{v}'} \\
\overline{\tilde{v}'^2}_1 \\
\overline{\tilde{v}'\tilde{w}'} \\
\overline{\tilde{w}'^2}
\end{bmatrix}
\tag{B.15}
$$

We now solve for the actual Reynolds stresses:

$$\overline{u'^2} = \frac{1}{a^2}\overline{\tilde{u}'^2} \tag{B.16}$$

$$\overline{w'^2} = \frac{1}{a^2}\overline{\tilde{w}'^2} \tag{B.17}$$

$$\overline{u'v'} = \frac{1}{c(a^2+b^2)}(a\overline{\tilde{u}'\tilde{v}'} - b\overline{\tilde{v}'\tilde{w}'}) \tag{B.18}$$

$$\overline{v'w'} = \frac{1}{c(a^2+b^2)}(a\overline{\tilde{v}'\tilde{w}'} + b\overline{\tilde{u}'\tilde{v}'}) \tag{B.19}$$

$$\overline{v'^2} = \frac{1}{c^2}\left[\overline{\tilde{v}'^2}_1 + \frac{2d}{(a^2+b^2)}(a\overline{\tilde{v}'\tilde{w}'} + b\overline{\tilde{u}'\tilde{v}'})\right] \tag{B.20}$$

B.4 Triple products

We perform the same type of analysis for the triple products. The equations below are derived from equations B.1 through B.4.

$$\overline{\tilde{u}'^3} = a^3\,\overline{u'^3} + 3\,a^2\,b\,\overline{u'^2w'} + 3\,a\,b^2\,\overline{u'w'^2} + b^3\,\overline{w'^3} \tag{B.21}$$

$$\overline{\tilde{u}'^2\tilde{v}'} = a^2\,c\,\overline{u'^2v'} - a^2\,d\,\overline{u'^2w'} + 2\,a\,b\,c\,\overline{u'v'w'}$$
$$-2\,a\,b\,d\,\overline{u'w'^2} + b^2\,c\,\overline{v'w'^2} - b^2\,d\,\overline{w'^3} \tag{B.22}$$

$$\overline{\tilde{u}'\tilde{v}'^2} = a\,c^2\,\overline{u'v'^2} - 2\,a\,c\,d\,\overline{u'v'w'} + b\,c^2\,\overline{v'^2w'}$$
$$+a\,d^2\,\overline{u'w'^2} - 2\,b\,c\,d\,\overline{v'w'^2} + b\,d^2\,\overline{w'^3} \tag{B.23}$$

$$\overline{\tilde{v}'^3}_1 = c^3\,\overline{v'^3} - 3\,c^2\,d\,\overline{v'^2w'} + 3\,c\,d^2\,\overline{v'w'^2} - d^3\,\overline{w'^3} \tag{B.24}$$

$$\overline{\tilde{v}'^2\tilde{w}'} = -b\,d^2\,\overline{u'^3} + 2\,b\,c\,d\,\overline{u'^2v'} - b\,c^2\,\overline{u'v'^2}$$
$$+a\,d^2\,\overline{u'^2w'} - 2\,a\,c\,d\,\overline{u'v'w'} + a\,c^2\,\overline{v'^2w'} \tag{B.25}$$

$$\overline{\tilde{v}'\tilde{w}'^2} = -b^2\,d\,\overline{u'^3} + b^2\,c\,\overline{u'^2v'} + 2\,a\,b\,d\,\overline{u'^2w'}$$
$$-2\,a\,b\,c\,\overline{u'v'w'} - a^2\,d\,\overline{u'w'^2} + a^2\,c\,\overline{v'w'^2} \tag{B.26}$$

$$\overline{\tilde{w}'^3} = -b^3\,\overline{u'^3} + 3\,a\,b^2\,\overline{u'^2w'} - 3\,a^2\,b\,\overline{u'w'^2} + a^3\,\overline{w'^3} \tag{B.27}$$

$$\overline{\tilde{v}'^3}_2 = -d^3\,\overline{u'^3} + 3\,c\,d^2\,\overline{u'^2v'} - 3\,c^2\,d\,\overline{u'v'^2} + c^3\,\overline{v'^3} \tag{B.28}$$

As with the Reynolds stresses, we neglect contributions from all terms including both w and u. Also, the $\overline{\tilde{v}'^3}_2$ equation (B.28) is redundant. Again, we take out the

small terms — those that contain b^2, d^2, or bd, and the equations reduce to:

$$
\begin{bmatrix}
a^3 & 0 & 0 & 0 & 0 & 0 & 0 \\
0 & a^2c & 0 & 0 & 0 & 0 & 0 \\
0 & 0 & ac^2 & 0 & bc^2 & 0 & 0 \\
0 & 0 & 0 & c^3 & -3c^2d & 0 & 0 \\
0 & 0 & 0 & 0 & 0 & 0 & a^3 \\
0 & 0 & 0 & 0 & 0 & a^2c & 0 \\
0 & 0 & -bc^2 & 0 & ac^2 & 0 & 0
\end{bmatrix}
\begin{bmatrix}
\overline{u'^3} \\
\overline{u'^2v'} \\
\overline{u'v'^2} \\
\overline{v'^3} \\
\overline{v'^2w'} \\
\overline{v'w'^2} \\
\overline{w'^3}
\end{bmatrix}
\approx
\begin{bmatrix}
\overline{\tilde{u}'^3} \\
\overline{\tilde{u}'^2\tilde{v}'} \\
\overline{\tilde{u}'\tilde{v}'^2} \\
\overline{\tilde{v}'^3}_1 \\
\overline{\tilde{w}'^3} \\
\overline{\tilde{v}'\tilde{w}'^2} \\
\overline{\tilde{v}'^2\tilde{w}'}
\end{bmatrix}
\tag{B.29}
$$

Solve for the triple products:

$$\overline{u'^3} = \frac{1}{a^3}\overline{\tilde{u}'^3} \tag{B.30}$$

$$\overline{u'^2v'} = \frac{1}{a^2c}\overline{\tilde{u}'^2\tilde{v}'} \tag{B.31}$$

$$\overline{u'v'^2} = \frac{1}{(a^2+b^2)c^2}(a\overline{\tilde{u}'\tilde{v}'^2} - b\overline{\tilde{v}'^2\tilde{w}'}) \tag{B.32}$$

$$\overline{v'^3} = \frac{1}{c^3}\left(\overline{\tilde{v}'^3}_1 + \frac{3d}{a^2+b^2}(a\overline{\tilde{v}'^2\tilde{w}'} + b\overline{\tilde{u}'\tilde{v}'^2})\right) \tag{B.33}$$

$$\overline{v'w'^2} = \frac{1}{a^2c}\overline{\tilde{v}'\tilde{w}'^2} \tag{B.34}$$

$$\overline{v'^2w'} = \frac{1}{(a^2+b^2)c^2}(a\overline{\tilde{v}'^2\tilde{w}'} + b\overline{\tilde{u}'\tilde{v}'^2}) \tag{B.35}$$

$$\overline{w'^3} = \frac{1}{a^3}\overline{\tilde{w}'^3} \tag{B.36}$$

B.5 Effect of unknown $\overline{u'w'}$, $\overline{u'^2w'}$, $\overline{u'w'^2}$, $\overline{u'v'w'}$

The simplest solution to the problem of unknown $u - w$ correlations is to ignore contributions from them. We demonstrate below that this introduces small systematic errors. We tabulate the errors introduced by products of u and w on the Reynolds stresses and on the triple products, in table B.1 for $\phi = 6°$ and $\alpha_{40} = \alpha_{41} = 2°$. We see that the normal stresses $\overline{u'^2}$ and $\overline{w'^2}$ each have a contribution of $0.035\overline{u'w'}$ (of opposite sign). Since $\overline{v'^2}$ is not affected by $\overline{u'w'}$, the turbulent kinetic energy is not affected by $\overline{u'w'}$. The shear stresses will both be off by the amount $-0.123\overline{u'w'}$.

Figure B.1 illustrates the error in the shear stresses. At a profile location where $\overline{u'w'}$ is relatively large, we show $\overline{u'v'}$ and $\overline{v'w'}$, measured by the crosswire. These "actual" curves are the Reynolds shear stresses, which are not contaminated by $\overline{u'w'}$. We also plot $\overline{u'v'} - 0.123\overline{u'w'}$ and $\overline{v'w'} - 0.123\overline{u'w'}$, calculated from the crosswire data. These "simulated" curves represent the data the LDA should generate. Toward the outer edge of the boundary layer where $\overline{u'w'}$ is negative, we see that the magnitude of the shear stress will be slightly underreported by the LDA. In the inner part of the boundary layer, where $\overline{u'w'} > 0$, the LDA's reported shear stress magnitude will be larger than the actual value. The discrepancy is small over the y range represented in figure B.1.

Near the wall, we need to take a different approach to estimating the error due to $\overline{u'w'}$. It has been found by several researchers (Flack and Johnston (1993), Olcmen and Simpson (1994) and Spalart (1989)) that $\overline{u'w'}$ is largest at $y^+ \approx 15$. Therefore we will limit our discussion to $y^+ = 15$, which should represent the worst-case percentage error in the other Reynolds stresses. It can be shown that in any coordinate system (with y the wall-normal coordinate) there is an absolute limit on the magnitude of $\overline{u'w'}$. The reasoning is based on the fact that $\overline{u'^2}$ and $\overline{w'^2}$ are constrained to be positive for all orientations of the axes, and may be stated as $R_{23} \leq 1$, where

$$R_{23} \equiv \frac{\overline{u'w'}}{(\overline{u'^2})(\overline{w'^2})} \tag{B.37}$$

Looking again at station G, at $y^+ = 15$, we measured $\overline{u'^2} = 5.6u_\tau^2$ and $\overline{w'^2} = 2.5u_\tau^2$, so equation B.37 says that the maximum realizable $\overline{u'w'}$ at that point is $3.7u_\tau^2$. This is the most conservative estimate we can make for $\overline{u'w'}$. The largest possible error in $\overline{u'v'}$ and $\overline{v'w'}$ at station G is 12.3% of that, or $0.46u_\tau^2$. However, it is highly unlikely that the error will be that large.

Flack and Johnston (1993) found the near-wall $\overline{u'w'}$ stress to be largest around $y^+ = 15$. We compare our data at station G, $y^+ = 15$, to their "18°" profile at $y^+ = 15$. If we estimate that our $\overline{u'w'}$ has a value of $0.57u_\tau^2$, we find that the $u - w$ correlation coefficient R_{23} matches their data for any rotation of axes. Table B.2 indicates the stress quantities used to generate this estimate. This is a rough estimate for $\overline{u'w'}$. For three-dimensional turbulent boundary layers, near the wall,

$\overline{u'w'}$ increases from the wall as does $-\overline{u'v'}$, and the estimated $\overline{u'w'}$ quantity is almost as large as our measured $\overline{u'v'}$. Therefore, we take estimate conservatively that $\overline{u'w'} \approx -\overline{u'v'}$ when looking at the near-wall data. For two-dimensional boundary layers the error due to $\overline{u'w'}$ falls to zero.

The largest error in the triple products appears to be in $\overline{u'v'^2}$ and $\overline{v'^2w'}$. Other three-dimensional turbulent boundary layer experiments' triple products (c.f. Flack and Johnston (1993), Schwarz and Bradshaw (1992) and Flack (1995)) show the $\overline{u'v'w'}$ term to be significantly smaller than the $\overline{u'v'^2}$ term, but comparable in size to the $\overline{v'^2w'}$ term.

B.6 Changes of angles due to traversing

Elsewhere we discuss the changes in α_{40} and α_{41} due to the change in distance between focusing lens and Bragg cell as the system traverses in y. The parameters a,b,c, and d will change with distance from the wall, too. Tabulated in table B.3 are the amount of change of each of these parameters over a 22 mm range. We see that they do not change enough to warrant including this variation in the data reduction scheme.

Quantity	Systematic error
$\overline{u'^2}$	$+0.035\ \overline{u'w'}$
$\overline{v'^2}$	-none-
$\overline{w'^2}$	$-0.035\ \overline{u'w'}$
$\overline{u'v'}$	$-0.123\ \overline{u'w'}$
$\overline{v'w'}$	$-0.123\ \overline{u'w'}$
$\overline{u'^3}$	$+0.051\ \overline{u'w'^2}$
$\overline{u'^2v'}$	$0.122\ \overline{u'^2w'}\ -\ 0.035\ \overline{u'v'w'}$
$\overline{u'v'^2}$	$0.245\ \overline{u'v'w'}$
$\overline{v'^3}$	-none-
$\overline{v'^2w'}$	$0.245\ \overline{u'v'w'}$
$\overline{v'w'^2}$	$0.122\ \overline{u'^2w'}\ +\ 0.035\ \overline{u'v'w'}$
$\overline{w'^3}$	$-0.051\ \overline{u'w'^2}$

Table B.1. Effect of correlations of u and w on the measured Reynolds stresses and triple products.

Stress	Flack & Johnston	station G
$\overline{u'^2}$	$6.5u_\tau{}^2$	$5.6u_\tau{}^2$
$\overline{w'^2}$	$3.0u_\tau{}^2$	$2.5u_\tau{}^2$
$\overline{u'w'}$	$0.7u_\tau{}^2$	n/a

Table B.2. Quantities at $y^+ = 15$, from Flack and Johnston (1993), and from our station G.

Parameter	% change
a	0.001%
b	3.3%
c	0.007%
d	0.47%

Table B.3. Change in angle parameter over y range of LDA.
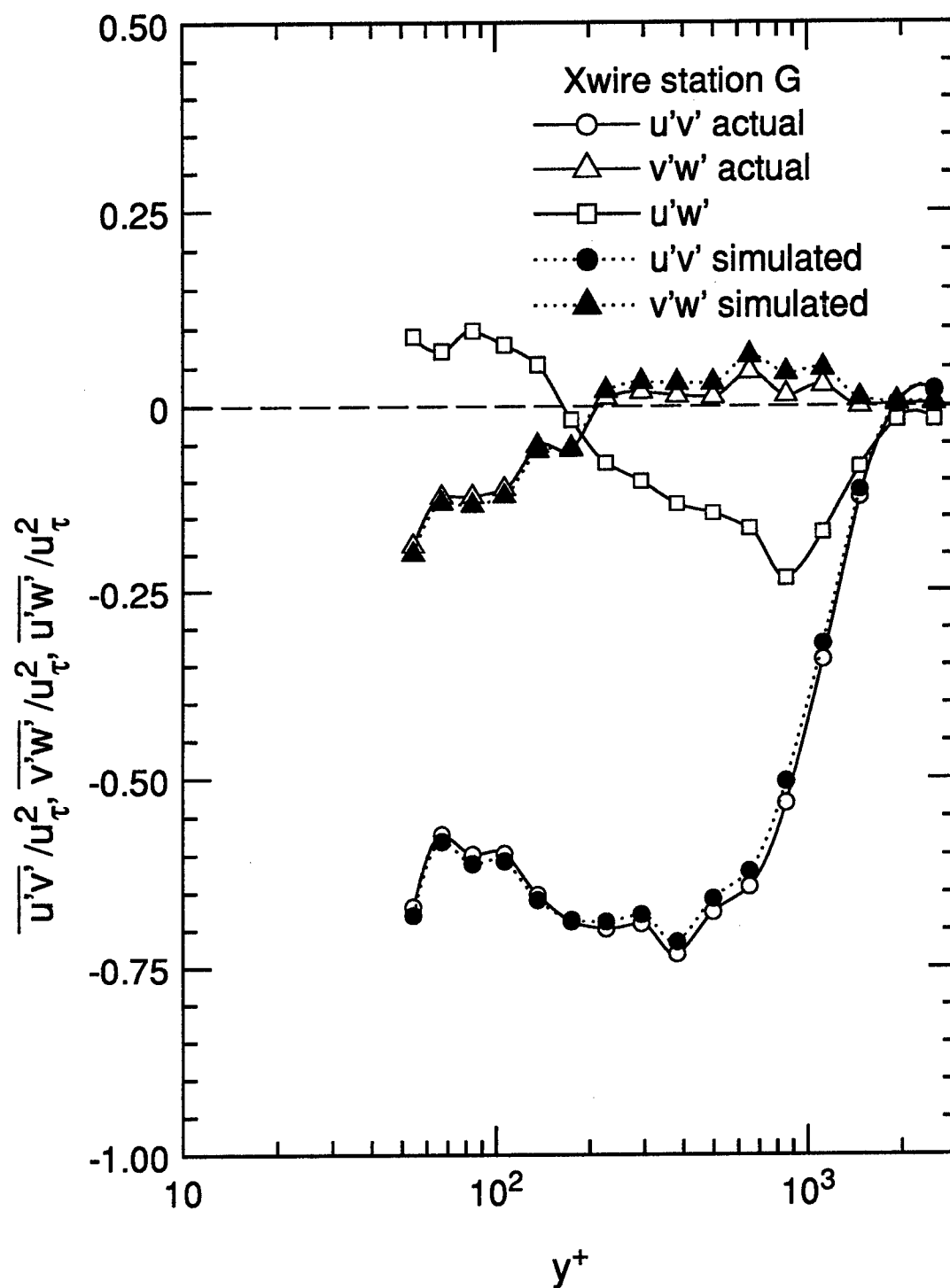
Figure B.1. Shear stresses at station G measured by the crosswire, and streamwise and spanwise shear stresses reduced by 0.123 $\overline{u'w'}$.

Appendix C

Error Due to Finite Measuring Volume

C.1 Analysis

Any instrument necessarily has finite extent, and we analyze here the effect of a measuring volume's finite extent in the y direction on the measured velocities and Reynolds stresses. These errors are manifested where there are velocity gradients, so in wall-bounded turbulent flows they are highest near the wall.

We analyze the effect of velocity gradients in one direction, since $\frac{\partial}{\partial y} \gg \frac{\partial}{\partial x}$ for boundary layer flows. For this analysis, we consider the center of the measuring volume to be at $y = y_0$. The individual data samples are $u_i = u(y_i, t_i)$, while the velocities we desire to measure are $u = u(y_0, t_i)$ The probability that any given sample occurs at a height $y = y_i$ is represented by the distribution function

$$P(y_i) = m(y_i - y_0) \tag{C.1}$$

The function m is everywhere ≥ 0, and it integrates to 1. In addition m is assumed to be symmetric about 0, and zero outside the measuring volume. A representative such function would be:

$$m(y_i - y_0) = \begin{cases} 1/d & \text{for} \quad |y_i - y_0| \leq d/2 \\ 0 & \text{for} \quad |y_i - y_0| > d/2 \end{cases} \tag{C.2}$$

where d is the measuring volume diameter.

C.1.1 Mean velocity error

We begin the analysis by examining the measured U:

$$U_{meas} = \frac{1}{N} \sum_{i=1}^{N} u_i, \tag{C.3}$$

where N is the number of samples. Expressing u_i in a Taylor series expansion about $y = y_0$,

$$u_i = u(y_i, t_i) = u(y_0, t_i) + (y_i - y_0) \left.\frac{\partial u}{\partial y}\right|_{y_0, t_i} + \frac{(y_i - y_0)^2}{2} \left.\frac{\partial^2 u}{\partial y^2}\right|_{y_0, t_i} + \dots \quad (C.4)$$

Substituting equation C.4 into C.3 we get

$$U_{meas} = \frac{1}{N} \left[\sum_{i=1}^{N} u(y_0, t_i) + \sum_{i=1}^{N} (y_i - y_0) \left.\frac{\partial u}{\partial y}\right|_{y_0, t_i} + \sum_{i=1}^{N} \frac{(y_i - y_0)^2}{2} \left.\frac{\partial^2 u}{\partial y^2}\right|_{y_0, t_i} \right] \quad (C.5)$$

If there are enough samples, the two random variables y_i and t_i are independent, and therefore separable. It can be shown that

$$\sum_{i=1}^{N} f(y_0, t_i) \, g(y_i - y_0) = N\overline{f}(y_0) \int_{-\infty}^{\infty} m(y_j - y_0) \, g(y_j - y_0) \, dy_j \quad (C.6)$$

Applying equation C.6 to equation C.5 and recognizing that the first summation term in equation C.5 is simply U,

$$U_{meas} = U + \left.\frac{\partial U}{\partial y}\right|_{y_0} \underbrace{\int_{-\infty}^{\infty} m(y_j - y_0) \, (y_j - y_0) \, dy_j}_{I_0}$$
$$+ \frac{1}{2} \left.\frac{\partial^2 u}{\partial y^2}\right|_{y_0} \underbrace{\int_{-\infty}^{\infty} m(y_j - y_0) \, (y_j - y_0)^2 \, dy_j}_{I_1} \quad (C.7)$$

We define the intergrals I_0 and I_1 as indicated above. It is clear that since we defined m to be symmetric about zero, I_0 is zero. Therefore the result is:

$$U_{meas} = U + \frac{1}{2} \frac{\partial^2 U}{\partial y^2} \cdot I_1 \quad (C.8)$$

C.1.2 Reynolds shear stress

We expand upon the previous section to describe the error in the Reynolds shear stress $\overline{u'v'}$.

The shear stress is evaluated using the following formula:

$$\overline{u'v'}_{meas} = \frac{1}{N} \sum_{i=1}^{N} u_i v_i - U_{meas} V_{meas} \quad (C.9)$$

Again, we expand the sum via Taylor series:

$$\frac{1}{N}\sum_{i=1}^{N}u_iv_i = \frac{1}{N}\sum_{i=1}^{N}(uv)_{y_0,t_i} + (y_i - y_0)\left(\frac{\partial(uv)}{\partial y}\right)_{y_0,t_i} + \frac{(y_i - y_0)^2}{2}\left(\frac{\partial^2(uv)}{\partial y^2}\right)_{y_0,t_i} + \cdots$$
(C.10)

and replace sums with integrals as we did in the previous section, noting that $I_0 = 0$.

$$\frac{1}{N}\sum_{i=1}^{N}u_iv_i = \frac{1}{N}\sum_{i=1}^{N}uv + \frac{I_1}{2}\left(\frac{\overline{\partial^2 uv}}{\partial y^2}\right)$$
(C.11)

$$= \frac{1}{N}\sum_{i=1}^{N}uv + \frac{I_1}{2}\left(\frac{\partial^2\overline{u'v'}}{\partial y^2} + V\frac{\partial^2 U}{\partial y^2} + U\frac{\partial^2 V}{\partial y^2} + 2\frac{\partial U}{\partial y}\frac{\partial V}{\partial y}\right)$$
(C.12)

Now we expand the second term of equation C.9 based on the results of the previous section (equation C.8).

$$U_{meas}V_{meas} = \left(U + \frac{1}{2}\frac{\partial^2 U}{\partial y^2}\cdot I_1\right)\left(V + \frac{1}{2}\frac{\partial^2 V}{\partial y^2}\cdot I_1\right)$$
(C.13)

Substituting equations C.12 and C.13 into equation C.9 we have

$$\overline{u'v'}_{meas} = \frac{1}{N}\sum_{i=1}^{N}uv + \left(\frac{\partial^2\overline{u'v'}}{\partial y^2} + V\frac{\partial^2 U}{\partial y^2} + U\frac{\partial^2 V}{\partial y^2} + 2\frac{\partial U}{\partial y}\frac{\partial V}{\partial y}\right)\frac{I_1}{2}$$
$$- \left(UV + \left(V\frac{\partial^2 U}{\partial y^2} + U\frac{\partial^2 V}{\partial y^2}\right)\frac{I_1}{2} + \frac{1}{4}\frac{\partial^2 U}{\partial y^2}\frac{\partial^2 V}{\partial y^2}I_1^2\right)$$
(C.14)

Collecting the terms and recognizing that the RHS contains the definition of $\overline{u'v'}$,

$$\overline{u'v'}_{meas} = \overline{u'v'} + \left(\frac{\partial^2\overline{u'v'}}{\partial y^2} + 2\frac{\partial U}{\partial y}\frac{\partial V}{\partial y}\right)\frac{I_1}{2} - \frac{1}{4}\frac{\partial^2 U}{\partial y^2}\frac{\partial^2 V}{\partial y^2}I_1^2$$
(C.15)

C.1.3 Normal stresses

We may simply replace v in equation C.15 with u to find the error in the normal stress $\overline{u'^2}$.

$$\overline{u'^2}_{meas} = \overline{u'^2} + \left(\frac{\partial^2\overline{u'^2}}{\partial y^2} + 2\left(\frac{\partial U}{\partial y}\right)^2\right)\frac{I_1}{2} - \frac{1}{4}\left(\frac{\partial^2 U}{\partial y^2}\right)^2 I_1^2$$
(C.16)

C.1.4 Worst case I_1

The sample estimate of m in equation C.2 is fairly crude. It represents an equal probability across the the measuring volume. This is a worst case scenario, since the true distribution will have a higher value in the center of the measuring volume and thus will have a lower moment. Let us evaluate the integral I_1 for the distribution function $m(y_i - y_0)$ given by equation C.2.

$$I_1 = \int_{-\infty}^{\infty} m(y_j - y_0)(y_j - y_0)^2 \, dy_j = \int_{-d/2}^{d/2} \frac{1}{d}\eta^2 d\eta = \frac{d^2}{12} \qquad \text{(C.17)}$$

Recalling that d has units of length (measuring volume diameter), we see that the error estimates do turn out dimensionally correct. We note, also, that it makes sense to call terms with I^2 small.

Finally, applying the worst case I_1 and scaling velocities on u_τ and lengths ν/u_τ ($d^+ \equiv d\frac{u_\tau}{\nu}$), we get:

$$\frac{U_{meas} - U}{u_\tau} \approx \frac{\partial^2 U^+}{\partial y^{+2}} \frac{d^{+2}}{24} \qquad \text{(C.18)}$$

$$\frac{\overline{u'v'}_{meas} - \overline{u'v'}}{u_\tau^2} \approx \left(\frac{\partial^2 \overline{u'v'}^+}{\partial y^{+2}} + 2\frac{\partial U^+}{\partial y^+}\frac{\partial V^+}{\partial y^+} \right) \frac{d^{+2}}{12} \qquad \text{(C.19)}$$

$$\frac{\overline{u'^2}_{meas} - \overline{u'^2}}{u_\tau^2} \approx \left(\frac{\partial^2 \overline{u'^2}^+}{\partial y^{+2}} + 2\left(\frac{\partial U^+}{\partial y^+}\right)^2 \right) \frac{d^{+2}}{12} \qquad \text{(C.20)}$$

It is clear that the error goes as the square of the diameter of the measuring volume.

C.2 Application

In order to evaluate the finite measuring volume errors, we must use either reliable data, analytical expressions, or numerical simulations for the velocity profiles. Here we choose to use Spalart's (1988) two-dimensional boundary layer simulation. The data were numerically differentiated and then used to evaluate equations C.18 to C.20. Two probe diameters were considered, $d^+ = 1$ representing the present LDA system; $d^+ = 4$ representing more typical LDA systems. Figure C.1 shows that mean velocity errors are insignificant with the present LDA but can be as large as 6% with

a larger LDA. Similar trends are observed for the normal stress, plotted in figure C.2, and the shear stress in figure C.3. Clearly the finite measurement volume makes no significant contribution to the uncertainty in the present case but would have been a major factor if we had used a conventional LDA.
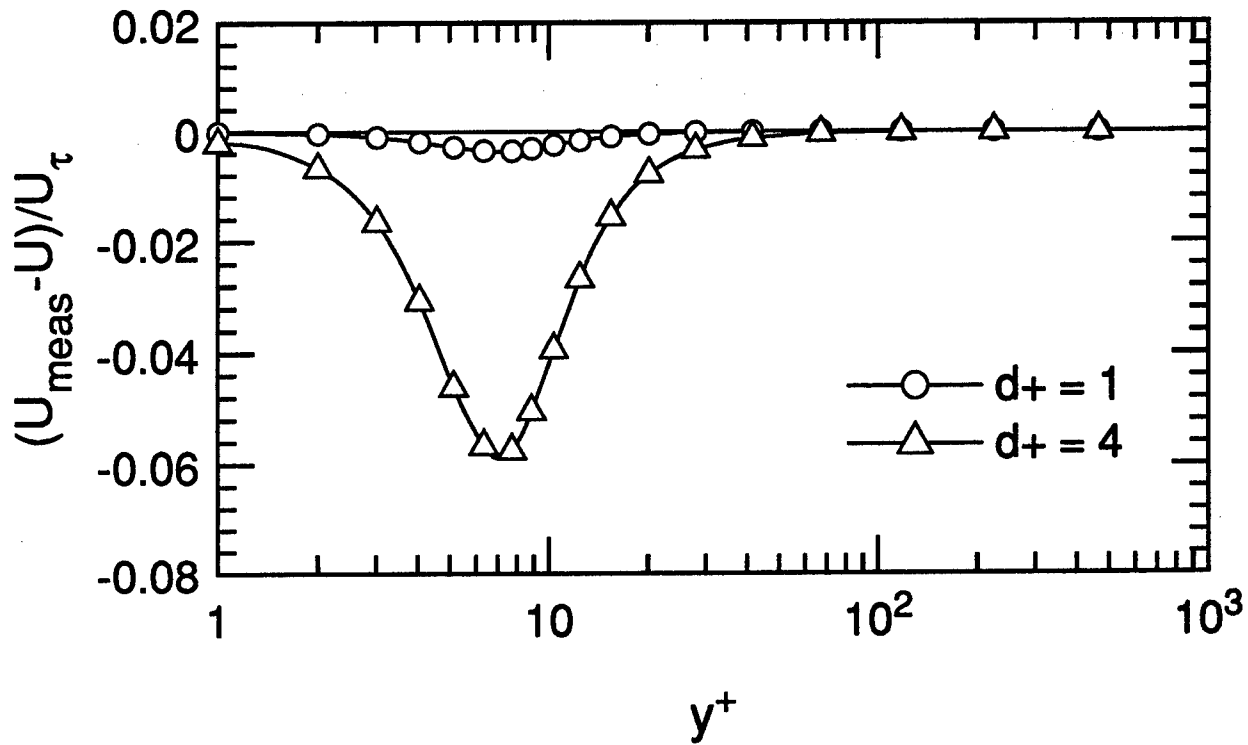
Figure C.1. Error in U due to finite volume size. Scaled on u_τ.
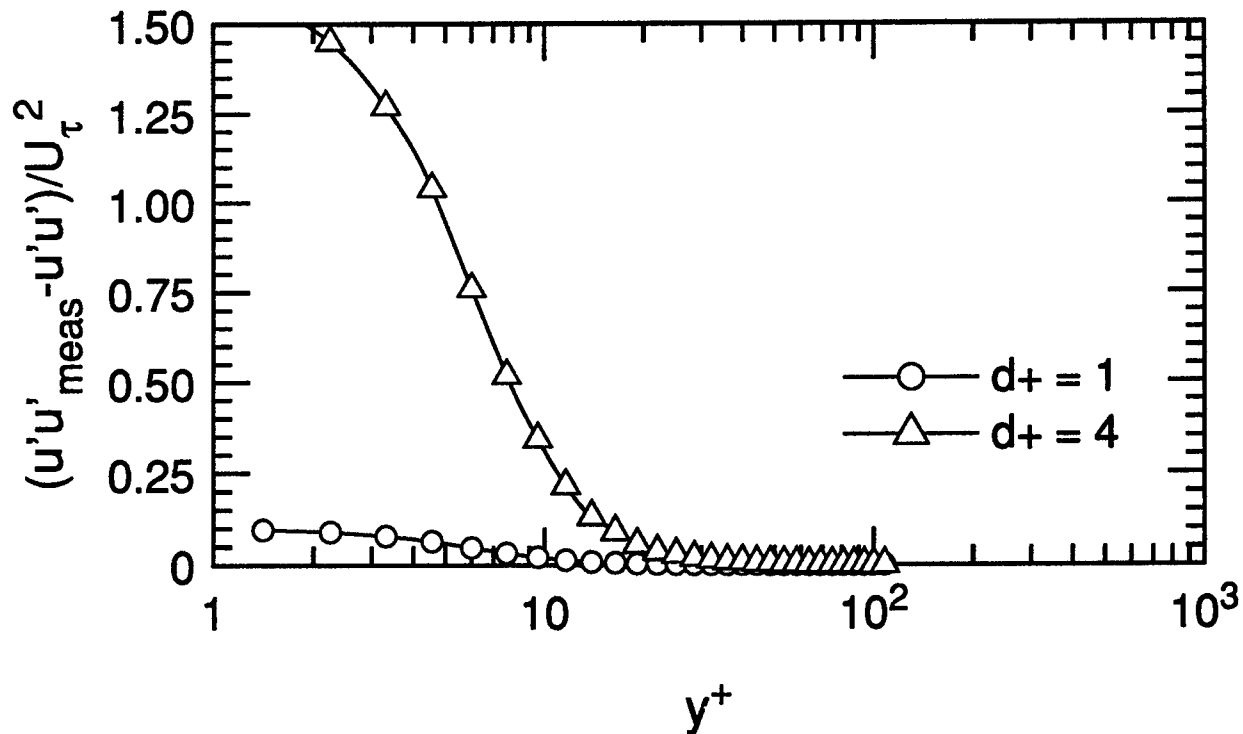
Figure C.2. Error in $\overline{u'^2}$ due to finite volume size. Scaled on u_τ.
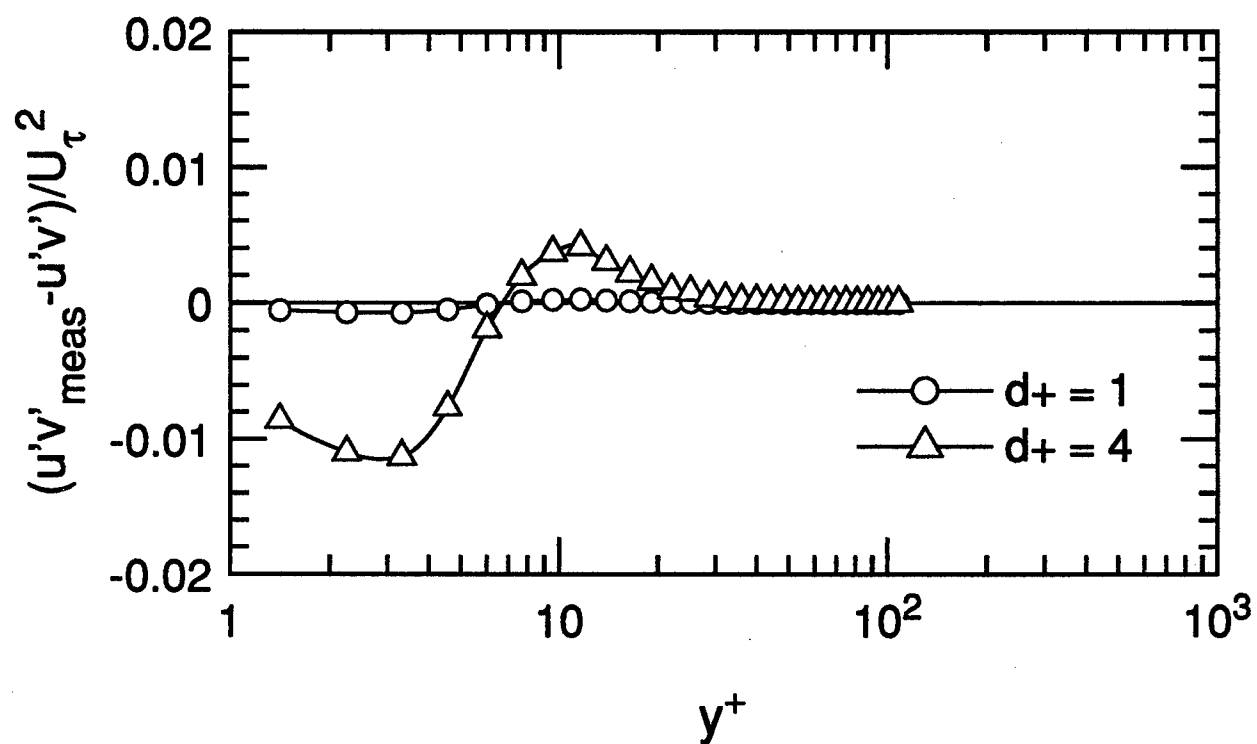
Figure C.3. Error in $\overline{u'v'}$ due to finite volume size. Scaled on u_τ.

Appendix D

Data Archives

All the data presented in this document are available on IBM or Macintosh format floppy disk from Professor John K. Eaton at the Mechanical Engineering Department of Stanford University. The files include the LDA, hotwire and pressure probe data, in ASCII format. The hotwire data include mean velocity and Reynolds stresses. The LDA data include the mean velocity, the $\overline{u'^2}$, $\overline{v'^2}$, $\overline{w'^2}$, $\overline{u'v'}$ and $\overline{v'w'}$ Reynolds stresses, and the $\overline{u'^3}$, $\overline{u'^2v'}$, $\overline{u'v'^2}$, $\overline{v'^3}$, $\overline{v'^2w'}$, $\overline{v'w'^2}$, and $\overline{w'^3}$ triple products. Included with the data files is a text file README.TXT which describes the contents in further detail.

References

Abramowitz, M. & Stegun, I.A., ed. (1965) *Handbook of Mathematical Functions*, National Bureau of Standards Applied Mathematics Series **55**.

Adams, E.W. & Eaton, J.K. (1988) "An LDA study of the backward-facing step flow, including the effects of velocity bias," *ASME J. Fluids. Engng.*, **110**, pp. 275–282.

Adams, E.W., Eaton, J.K. & Johnston, J.P. (1984) "An examination of velocity bias in a highly turbulent separated and reattaching flow," in *Laser Anemometry in Fluid Mechanics*, pp. 21–37, Ladoan — Instituto Superior Técnico 1096 Lisboa Codex - Portugal.

Anderson, S.D. & Eaton, J.K. (1987) "An experimental investigation of pressure driven three-dimensional turbulent boundary layers," Thermosciences Div., Stanford University, Stanford, CA, Report MD-49.

Anderson, S.D. & Eaton, J.K. (1989) "Reynolds stress development in pressure-driven three-dimensional turbulent boundary layers," *J. Fluid Mech.*, **202**, pp.263–264.

Barlow, R.S. & Johnston, J.P. (1985) "Structure of turbulent boundary layers on a concave surface," Thermosciences Div., Stanford University, Stanford, CA, Report MD-47.

Baskaran, V., Pontikis, Y.G., & Bradshaw, P. (1989) "Experimental investigation of three-dimensional turbulent boundary layers on 'infinite' swept curved wings," *J. Fluid Mech.*, **211**, pp. 95–122.

Bassom, A.P. & Hall, P. (1991) "Vortex instabilities in three-dimensional boundary layers: the relationship between Görtler and crossflow vortices," *J. Fluid Mech.*, **232**, pp. 647–680.

Bettelini, M.S.G. & Fanneløp, T.K. (1993) "Systematic comparison of mathematically simple turbulence models for three-dimensional boundary layers," *AIAA Journal*, **31**,

No. 6, pp. 999–1006.

Bissonnette, L.R. & Mellor, G.L. (1974) "Experiments on the behaviour of an axisymmetric turbulent boundary layer with a sudden circumferential strain," *J. Fluid Mech.*, **63**, pp. 369–413.

van den Berg, B. (1988) "A European collaborative investigation of the three-dimensional turbulent shear layers of a swept wing," presented at AGARD FDP Symposium, Cesme, Turkey.

Bradshaw, P. (1967) "The turbulence structure of equilibrium boundary layers," *J. Fluid Mech.*, **29**, pp. 635–645.

Bradshaw, P. & Pontikos, N.S. (1985) "Measurements in the turbulent boundary layer on an 'infinite' swept wing," *J. Fluid Mech.*, **159**, pp. 105–130.

Bradshaw, P. & Sendstad, O. (1990) "Structure of three-dimensional boundary layers," *Proceedings of the Summer Program 1990*, pp. 75–84, Center for Turbulence Research.

Bradshaw, P. & Terrell, M.C. (1969) "The response of a turbulent boundary layer on an 'infinite' swept wing to the sudden removal of pressure gradient," *NPL Aero Report* No. 1305.

Chesnakas, C.J. & Simpson, R.L. (1992) "An investigation of the three-dimensional turbulent flow in the cross-flow separation region of a 6:1 prolate spheroid," *6th Intl. Symposium on Applications of Laser Techniques to Fluid Mechanics*, Jul. 20–23, 1992, Lisbon, Portugal.

Chesnakas, C.J. & Simpson, R.L. (1994) "Three-dimensional turbulence structure in the vicinity of a 3-D separation," *ASME Winter Annual Meeting*, Nov. 6–11, 1994, Chicago, Illinois.

Chiang, C., & Eaton, J.K. (1993) "An experimental investigation of corotating disks and single disk flow structure," Thermosciences Div., Stanford University, Stanford, CA, Report MD-62.

Cline, C. & Deutsch, S. (1993) "On elevated RMS levels in wall-bounded turbulent flows

when measured by laser Doppler velocimetry," *Experiments in Fluids*, **15**, pp. 130–132.

Cousteix, J. (1986) "Three-dimensional and unsteady boundary layer computations," *Ann. Rev. Fluid Mech.*, **18**, pp. 173–196.

Dechow, R. & Felsch, K.O. (1977) "Measurements of the mean velocity and of the Reynolds stress tensor in a three-dimensional turbulent boundary layer induced by a cylinder standing on a flat wall," *1st Turbulent Shear Flow Symposium*, Apr. 18–20, 1977, University Park, Pennsylvania.

Degani, A.T., Smith, F.T. & Walker, J.D.A. (1992) "The three-dimensional turbulent boundary layer near a plane of symmetry," *J. Fluid Mech.*, **234**, pp. 329–360.

Degani, A.T., Smith, F.T. & Walker, J.D.A. (1993) "The structure of a three-dimensional turbulent boundary layer," *J. Fluid Mech.*, **250**, pp. 43–68.

Driver, D.M., & Hebbar, S.K. (1987) "Experimental study of a three-dimensional shear-driven turbulent boundary layer," *AIAA Journal*, **25**, no. 1, pp. 35–42.

Driver, D.M., & Johnston, J.P. (1990) "Experimental study of a three-dimensional shear-driven turbulent boundary layer with streamwise adverse pressure gradient," Thermosciences Div., Stanford University, Stanford, CA, Report MD-57. (Also published as NASA Tech. Memorandum 102211.)

Durst, F., Melling, A. & Whitelaw, J.H. (1981) *Principles and Practice and Laser Doppler Anemometry*, Academic Press, London.

Durst, F. & Müller, R. (1988) "Determination of the measuring position in laser-Doppler anemometry," *Experiments in Fluids*, **6**, pp. 105–110.

Durst, F., Müller, R., & Naqwi, A.A. (1992) "Semiconductor laser Doppler anemometer for applications in aerodynamics research," *AIAA Journal*, **30**, no. 4, pp. 1033–1038.

Eaton, J.K. (1991) "Turbulence structure and heat transfer in three-dimensional boundary layers," *9th Symp. on Energy Engineering Sciences*, Argonne, May 1991.

Eaton, J.K. (1994) "The effects of mean flow three dimensionality on turbulent boundary layer structure," AIAA paper 94-2225, presented Colorado Springs, Colorado, June

193

1994.

Edwards, R.V., ed. (1987) "Report of the special panel on statistical particle bias problems in laser anemometry," *ASME J. Fluids. Engng.*, **109**, pp. 89–93.

Elsenaar, A., & Boelsma, S.H. (1974) "Measurements of the Reynolds stress tensor in a three-dimensional turbulent boundary layer under infinite swept wing conditions," *NLR TR* 74095 U.

Fernholz, H.H. & Vagt, J.-D. (1981) "Turbulence measurements in an adverse-pressure-gradient three-dimensional turbulent boundary layer along a circular cylinder," *J. Fluid Mech.*, **111**, pp. 233–269.

Flack, K.A. & Johnston, J.P. (1993) "Near-wall investigation of three-dimensional turbulent boundary layers," Thermosciences Div., Stanford University, Stanford, CA, Report MD-63.

Flack, K.A. & Johnston, J.P. (1993) "Experimental study of a detaching three-dimensional turbulent boundary layer," *International Conference on Near-Wall Turbulent Flows*, Tempe, Arizona, March 15–18, 1993.

Flack, K.A. (1995) Private communication.

Flack, K.A. & Johnston, J.P. (1995) "Near-wall structure of three-dimensional turbulent boundary layers," *10th Turbulent Shear Flow Symposium*, University Park, August 14–16, 1995.

Fleming, G.A. & Kuhlman, J.M. (1994) "Experimental investigation of fringe divergence errors in laser velocimetry measurements," *AIAA Journal*, **32**, No. 10, pp. 2030–2035.

Fleming, J. & Simpson, R.L. (1994) "Experimental investigation of the near wall flow structure of a low Reynolds number 3-D turbulent boundary layer," AIAA paper 94-0649, presented Reno, Nevada, January 1994.

Fontaine, A.A. & Deutsch, S. (1995) "Three-component, time-resolved velocity statistics in the wall region of a turbulent pipe flow," *Experiments in Fluids*, **18**, No. 3, pp. 168–173.

Gad-el-Hak, M. & Bandyopadhyay, P.R. (1993) "Reynolds number effects in wall-bounded turbulent flows," **submitted** *Applied Mechanics Reviews.*

Gleyzes, C., Maciel, Y., Cousteix, J., Gooden, J.H.M., Reinders, W., & Van Den Berg, B.(1993) "Three-dimensional turbulent flow around the Garteur swept wing. Selected features," *9th Symposium on Turbulent Shear Flows*, Aug. 16–18, 1993, Kyoto, Japan.

Gould, R.D. & Loseke, K.W. (1993) "A comparison of four velocity bias correction techniques in laser Doppler velocimetry," *ASME J. Fluids. Engng.*, **115**, pp. 508–514.

Ha, S.-M. & Simpson, R.L. (1993) "An experimental investigation of a three-dimensional turbulent boundary layer using multiple-sensor probes," *9th Symposium on Turbulent Shear Flows*, Aug. 16–18, 1993, Kyoto, Japan.

Hanson, S. (1973) "Broadening of the measured frequency spectrum in a differential laser anemometer due to interference plane gradients," *J. Phys. D: Appl. Phys.*, **6**, pp. 164–171.

Horowitz, P.& Hill, W. (1989) *The Art of Electronics - 2nd ed.*, Cambridge University Press, Cambridge, UK.

Johansson, A.V. & Alfredsson, P.H. (1983) "Effects of imperfect spatial resolution on measurements of wall-bounded turbulent shear flows," *J. Fluid Mech.*, **137**, pp. 409–421.

Johansson, T.G. & Karlsson, R.I., (1989) "The energy budget in the near-wall region of a turbulent boundary layer," Adrian, R.J. /etal, ed., *Applications of Laser Anemometry to Fluid Mechanics*, Springer-Verlag, Berlin 1989, pp. 3–22.

Johnson, D.A. (1988) "Laser Doppler anemometry," NASA Tech. Memorandum 100072.

Johnson, D.A. (1990) "Simultaneous multivelocity component laser Doppler velocimetry using one digital frequency processor," *Rev. Sci. Instrum.*, **61**, No. 7, in 'notes', pp. 1989–1990.

Johnson, D.A. & Abrahamson, S.D. (1989) "Near- wall, three-dimensional turbulence measurements: A challenge for laser velocimetry," *Eighth International Congress on Applications of Lasers and Electro-Optics*, Orlando, Florida, October 15–20, 1989.

Johnson, D.A. & Brown, J.D. (1990) "A laser Doppler velocimeter approach for near-wall three- dimensional turbulence measurements," *Fifth International Symposium on Applications of Laser Techniques to Fluid Mechanics*, July 9–12, 1990, Lisbon.

Johnston, J.P. (1960) "On the three-dimensional turbulent boundary layer generated by secondary flow," *ASME Journal of Basic Engineering*, March 1960, pp. 233–248.

Johnston, J.P. (1970) "Measurements in a three-dimensional turbulent boundary layer induced by a swept, forward-facing step," *J. Fluid Mech.*, **42**, pp. 823–844.

Johnston, J.P. (1976) "Experimental studies in three-dimensional turbulent boundary layers," *Stanford Univ., Dept. Mech. Eng. Thermosciences Div. Rep.* MD-34.

Johnston, J.P. & Flack, K.A. (1994) "Advances in three-dimensional turbulent boundary layers with emphasis on the wall-layer regions," *Stanford Univ., Dept. Mech. Eng. Thermosciences Div. Rep.* MD-67.

Kays, W.M. & M.E. Crawford (1980) *Convective Heat and Mass Transfer - 2nd ed.*, McGraw-Hill, New York.

Kim, J., Moin, P. & Moser, R. (1987) "Turbulence statistics in fully developed channel flow at low Reynolds number," *J. Fluid Mech.*, **177**, pp. 133–166.

King, L.V. (1914) "On the convection of heat from small cylinders in a stream of fluid: Determination of the convection constants of small platinum wires with applications to hot-wire anemometry," *Phil. Trans. Roy. Soc. A* **214**, pp. 373–432

Klein, M.V. & Furtak, T.E. (1986) *Optics*, Wiley, New York.

Klewicki, J.C., Murray, J.A., & Falco, R.E. (1994) "Vortical motion contributions to stress transport in turbulent boundary layers," *Physics of Fluids*, **6**, No. 1, pp.277–286.

Kreplin, H.-P. & Stäger, R. (1993) "Measurements of the Reynolds-stress tensor in the three-dimensional boundary layer of an inclined body of revolution," *9th Symposium on Turbulent Shear Flows*, Aug. 16–18, 1993, Kyoto, Japan.

Launder, B.E. (1988?) "Turbulence modelling of three-dimensional shear flows," *AGARD CP-438*, pp. 26-1–26-20.

Liang, Q.X. (1990) "A visual study of the coherent structure of the turbulent boundary layer in flow with adverse pressure gradient," *J. Fluid Mech.*, **215**, pp. 101–124.

Littell, H.S. & Eaton, J.K. (1991) "An experimental investigation of the three-dimensional boundary layer on a rotating disk," Thermosciences Div., Stanford University, Stanford, CA, Report MD-60.

Littell, H.S. & Eaton, J.K. (1991) "Experimental investigation of the three-dimensional boundary layer on a rotating disk," *8th Turbulent Shear Flow Symposium*, Sept. 9–11, 1991, Munich.

Littell, H.S. & Eaton, J.K. (1994) "Turbulence characteristics of the boundary layer on a rotating disk," *J. Fluid Mech.*, **266**, pp. 175-207.

Lohmann, R.P. (1976) "The response of a developed turbulent boundary layer to local transverse surface motion," *ASME J. Fluids. Engng.*, **98**, pp. 355–363.

Menna, J.D. & Pierce, F.J. (1988) "The mean flow structure around and within a turbulent junction or horseshoe vortex — Part I: The upstream and surrounding three-dimensional turbulent boundary layer," *ASME J. Fluids. Engng.*, **110**, pp. 406–414.

Moin, P., Shih, T.-H., Driver, D. & Mansour, N.N. (1990) "Direct numerical simulation of a three-dimensional turbulent boundary layer," *Physics of Fluids A*, **2**, No. 10, pp.1846–1853.

Müller, U.R. (1982) "Measurement of the Reynolds stress and the mean-flow field in a three-dimensional pressure-driven boundary layer," *J. Fluid Mech.*, **119**, pp. 121–153.

Müller, U.R. (1982b) "On the accuracy of turbulence measurements with inclined hot wires," *J. Fluid Mech.*, **119**, pp. 155-172.

Murlis, J., Tsai, H.M., & Bradshaw, P. (1982) "The structure of turbulent boundary layers at low Reynolds numbers," *J. Fluid Mech.*, **122**, pp. 13–56.

Nash, J.F. & Patel, V.C., (1972) *Three-Dimensional Turbulent Boundary Layers*, SBC Books.

Naqwi, A.A. & Reynolds, W.C. (1991), "Measurement of turbulent wall velocity gradients

using cylindrical waves of laser light," *Experiments in Fluids*, **10**, pp. 257–266.

Nelson, C.F., Eaton, J.K. & Koga, D.J. (1990) "Measurement and control of the unsteady, separated flow downstream of an oscillating spoiler," Thermosciences Div., Stanford University, Stanford, CA, Report MD-59.

Ölçmen, M.S. & Simpson, R.L. (1992) "Perspective: On the near wall similarity of three-dimensional turbulent boundary layers," *ASME J. Fluids. Engng.*, **114**, pp. 487–495.

Ölçmen, M.S. & Simpson, R.L. (1993) "Evaluation of algebraic eddy-viscosity models in three-dimensional turbulent boundary layer flows," *AIAA Journal*, **31**, No. 9, pp. 1545–1554.

Ölçmen, M.S. & Simpson, R.L. (1994) "A 5-velocity-component laser-Doppler velocimeter for measurements of a three-dimensional turbulent boundary layer," *7th Intl. Symposium on Applications of Laser Techniques to Fluid Mechanics*, Jul. 11–14, 1994, Lisbon, Portugal.

Özcan, O. (1988) "Three-component LDA measurements in a turbulent boundary layer," *Experiments in Fluids*, **6**, pp. 327–334.

Pierce, F.J. & Duerson, S.H. Jr. (1975) "Reynolds stress tensors in an end-wall three-dimensional channel boundary layer," *ASME J. Fluids. Engng.*, **97**, No. 4, pp. 618–620.

Pierce, F.J. & East, J.L. Jr. (1971) "Near-wall collateral flow in three-dimensional turbulent boundary layers," *AIAA Journal*, **10**, No. 3, pp. 334–336.

Pierce, F.J. & Ezekewe, C.I. (1976) "Measured $\overline{uw}$ stress gradients in a three-dimensional turbulent boundary layer," *ASME J. Fluids. Engng.*, **98**, No. 4, pp 768–770.

Pierce, F.J. & Harsh, M.D. (1988) "The mean flow structure around and within a turbulent junction or horseshoe vortex — Part II: The separated and junction vortex flow," *ASME J. Fluids. Engng.*, **110**, pp. 415–423.

Pierce, F.J. & McAllister, J.E. (1982) "Measurements in a pressure-driven and a shear-driven three-dimensional turbulent boundary layer," *IUTAM Three- Dimensional Turbulent Boundary Layers Symposium*, March 29 – April 1, 1982, Berlin.

Pompeo, L., Bettelini, M.S.G., & Thomann, H. (1993) "Laterally strained turbulent boundary layers near a plane of symmetry," *J. Fluid Mech.*, **257**, pp.507–532.

Purtell, L.P. & Klebanoff, P.S. (1981) "Turbulent boundary layer at low Reynolds number," *Phys. Fluids*, **24**, pp. 802–811.

Robinson, S.K. (1991) "Coherent motions in the turbulent boundary layer," *Ann. Rev. Fluid Mech.*, **23**, pp. 601–639.

Rotta, J.C. (1977) "A family of turbulence models for three-dimensional thin shear layers," *1st Turbulent Shear Flow Symposium*, Apr. 18–20, 1977, University Park, Pennsylvania.

Schlichting (1960) *Boundary Layer Theory - 4th ed.*, McGraw-Hill, New York.

Schwarz, W.R. & Bradshaw, P. (1992) "Three-dimensional turbulent boundary layer in a 30 degree bend: experiment and modelling," Thermosciences Div., Stanford University, Stanford, CA, Report MD-61.

Schwarz, W.R. & Bradshaw, P. (1993) "Measurements in a pressure-driven three-dimensional turbulent boundary layer during development and decay," *AIAA Journal*, **31**, No. 7, pp. 1207–1214.

Schwarz, W.R. & Bradshaw, P. (1994) "Term-by-term tests of stress-transport turbulence models in a three-dimensional turbulent boundary layer," *Physics of Fluids*, **6**, No. 2, pp.986–998.

Sendstad, O. & Moin, P. (1991) "On the mechanics of 3-D turbulent boundary layers", *8th Turbulent Shear Flow Symposium*, Sept. 9–11, 1991, Munich.

Sendstad, O. & Moin, P. (1992) "The near-wall mechanics of three-dimensional turbulent boundary layers," Thermosciences Div., Stanford University, Stanford, CA, Report TF-57.

Shizawa, T. & Eaton, J.K. (1991) "Turbulence measurements for a longitudinal vortex interacting with a three-dimensional turbulent boundary layer," AIAA paper 91-0732, presented Reno, Nevada, January 1991.

Simonich, J.C. & Moffat, R.J. (1982) "Local measurements of turbulent boundary layer

Pompeo, L., Bettelini, M.S.G., & Thomann, H. (1993) "Laterally strained turbulent boundary layers near a plane of symmetry," *J. Fluid Mech.*, **257**, pp.507–532.

Purtell, L.P. & Klebanoff, P.S. (1981) "Turbulent boundary layer at low Reynolds number," *Phys. Fluids*, **24**, pp. 802–811.

Robinson, S.K. (1991) "Coherent motions in the turbulent boundary layer," *Ann. Rev. Fluid Mech.*, **23**, pp. 601–639.

Rotta, J.C. (1977) "A family of turbulence models for three-dimensional thin shear layers," *1st Turbulent Shear Flow Symposium*, Apr. 18–20, 1977, University Park, Pennsylvania.

Schlichting (1960) *Boundary Layer Theory - 4th ed.*, McGraw-Hill, New York.

Schwarz, W.R. & Bradshaw, P. (1992) "Three-dimensional turbulent boundary layer in a 30 degree bend: experiment and modelling," Thermosciences Div., Stanford University, Stanford, CA, Report MD-61.

Schwarz, W.R. & Bradshaw, P. (1993) "Measurements in a pressure-driven three-dimensional turbulent boundary layer during development and decay," *AIAA Journal*, **31**, No. 7, pp. 1207–1214.

Schwarz, W.R. & Bradshaw, P. (1994) "Term-by-term tests of stress-transport turbulence models in a three-dimensional turbulent boundary layer," *Physics of Fluids*, **6**, No. 2, pp.986–998.

Sendstad, O. & Moin, P. (1991) "On the mechanics of 3-D turbulent boundary layers", *8th Turbulent Shear Flow Symposium*, Sept. 9–11, 1991, Munich.

Sendstad, O. & Moin, P. (1992) "The near-wall mechanics of three-dimensional turbulent boundary layers," Thermosciences Div., Stanford University, Stanford, CA, Report TF-57.

Shizawa, T. & Eaton, J.K. (1991) "Turbulence measurements for a longitudinal vortex interacting with a three-dimensional turbulent boundary layer," AIAA paper 91-0732, presented Reno, Nevada, January 1991.

Simonich, J.C. & Moffat, R.J. (1982) "Local measurements of turbulent boundary layer

heat transfer on a concave surface using liquid crystal," Thermosciences Div., Stanford University, Stanford, CA, Report HMT-35.

Spalart, P.R. (1988) "Direct simulation of a turbulent boundary layer up to $R_\theta = 1410.$," *J. Fluid Mech.*, **187**, pp. 61–98.

Spalart, P.R. (1989) "Theoretical and numerical study of a three-dimensional turbulent boundary layer," *J. Fluid Mech.*, **205**, pp. 319–340.

Spalding, D.B. (1961) "A single formula for the law of the wall," *J. Applied Mech.* **28**, pp. 455–457.

Squire, H.B. & Winter, K.G. (1951) "The secondary flow in a cascade of airfoils in a nonuniform stream," *Journal of the Aeronautical Sciences*, **18**, No. 4, pp. 271–277.

Thomann, H. (1994) "Diverging solutions of the boundary-layer equations near a plane of symmetry," *AIAA Journal*, **32**, no. 9, pp. 1923–1924.

Townsend, A.A. (1980) "The response of sheared turbulence to additional distortion," *J. Fluid Mech.*, **98**, pp. 171–191.

Westphal, R.V., Ligrani, P.M. & Lemos, F.R (1988) "Development of subminiature multi-sensor hot-wire probes," NASA Tech. Memorandum 100052.

White, F.M. (1974) *Viscous Fluid Flow*, McGraw-Hill, New York.

Young, A.D., & Maas, J.N. (1936) "The behaviour of a pitot tube in a transverse total-pressure gradient," *Cambridge University Aeronautical Laboratory Reports and Memoranda* No. 1770.